Imperial College London

Flow boiling in horizontal pipes: integral measurements, optical diagnostics, and numerical simulations

Hannah Rosina Moran

July 2021

Department of Chemical Engineering

Imperial College London

Submitted in part fulfilment of the requirements for the degree of
Doctor of Chemical Engineering of Imperial College London
and the Diploma of Imperial College London

Dedication

To my parents

Who inspire, love and support me without fail

Statement of Originality

I, Hannah R. Moran, certify that the material presented in this thesis is the result of my own original research. Where information has been derived from other sources, I confirm that this has been properly indicated and the source suitably referenced.

Copyright Declaration

This dissertation is a description of the work carried out by the author in the Department of Chemical Engineering, Imperial College London, under the supervision of Prof. Omar K. Matar and Prof. Christos N. Markides. Except where acknowledged, the content is the original work of the author and no portion of it has been submitted in support of an application for a degree at any other university. The copyright of this thesis rests with the author and unless otherwise indicated its contents are licensed under a Creative Commons Attribution Non-Commercial 4.0 International Licence (CC BY-NC). Researchers are free to copy, distribute or transmit the thesis in any medium or format on the condition that the the author is credited and that they do not use it, or any of derivative works, for commercial purposes. For any reuse or redistribution, researchers must make clear to others the licence terms of this work and where work is adapted the changes must be indicated and described. The permission of the copyright holder must be sought for uses of this work that are not included in this licence or permitted under UK Copyright Law.

Abstract

Flow boiling in horizontal pipes is the heat transfer mechanism central to a wide variety of applications including refrigeration systems, high-temperature heat pumps, organic Rankine cycle systems and concentrating solar power plants operating in the direct steam generation mode. Refrigerants such as R245fa often serve as the working fluid in these applications, but few studies have been published investigating flow boiling of R245fa in pipes of sizes above the micro-scale. There is a lack of detailed data available with high spatial and temporal resolution for boiling flows, which could enhance fundamental understanding of the hydrodynamic and thermal behaviour and aid effective design and operation of heat transfer systems. Numerical simulation of boiling flows can complement detailed experimental data, but it presents a complex computational challenge, particularly in macro-scale geometries.

This work presents experimental and numerical investigations towards a full description of flow boiling. A bespoke experimental facility was constructed for flow boiling of R245fa in a horizontal 12.6 mm pipe, and an experimental database has been populated with measurements of pressure drops, heat transfer coefficients and flow patterns. Laser-induced fluorescence and particle image velocimetry techniques were also developed and successfully applied in this facility, providing detailed spatio-temporally resolved interfacial property, phase distribution and liquid-phase velocity-field data. Predictive methods in the literature are compared to experimental data and improvements suggested based on the optical measurements of interface location.

Numerical simulations of elongated bubble flow provide new insights into the effects of buoyancy and inertia on bubble shape and dynamics. A new theoretical model for the film thickness around the bubble is presented and compared to experimental data. A phase change model is validated in OpenFOAM for growth of a small bubble, and is then used to simulate stratified flow based on a set of experimental conditions from this work.

Acknowledgements

I would like to express my gratitude towards my supervisors Prof. Omar K. Matar and Prof. Christos N. Markides for their guidance and support, and for all the insights and learnings they have shared with me throughout the years of my Ph. D. They have been committed to developing me both as a researcher and as a person and provided me with a wealth of opportunities. I would also like to acknowledge the funding sources that have made this work possible, including Mrs. Marit Mohn for supporting my scholarship and generously offering an extension when I needed it. The Department for International Development (DFID) supported this work through the Royal Society-DFID Africa Capacity Building Initiative, along with the UK Engineering & Physical Sciences Research Council (EPSRC) through the PREMIERE (EP/T000414/1) Programme Grant.

This work would not have been possible without the guidance of Dr. Mirco Magnini who initiated me in the ways of OpenFOAM and patiently guided me to the publication of my first paper. Similarly Dr. Victor Voulgaropoulos, who was a fount of knowledge on experimental techniques and spent many hours explaining to me the intricacies of laser diagnostics and image processing. I am also grateful to Dr. Shunsuke Yamada and Dr. Andrey Cherdantsev for their expert guidance on the implementation of experimental techniques and for their input to some very enjoyable collaborations. I would like to thank my fellow Ph. D. students Dr. Stuart Wright and Dr. Jae Sik An for passing on their knowledge of the inner workings of lab 111A and Dr. Assen Batchvarov and Gabriel Farah for answering my many CFD-related questions. I must also mention my masters students Akhil, Dimitri, Ali and Josh, who provided extra pairs of hands for much of the lab work on FLOBOF whilst producing excellent projects of their own. The Imperial HPC OpenFOAM Slack channel has been a welcome source of virtual support during the last year, particularly Felipe Huerta whose Wednesday morning focus sessions have kept me on track.

I want to thank all the members of the Matar Fluids Group and Clean Energy Processes Laboratory for their collaboration and company, with a special appreciation of my fellow occupants of RODH 338 for providing distraction, conversation and friendship, particularly my long-suffering desk buddy Assen. My Ph. D. experience would have been much less enjoyable without Chloe Armour, Dr. Anton Firth, Seb Green, Emily Manchester, Dr. Brett Parkinson, Nixon Sunny and Oliver Watson, who through our coffee breaks, lunches, nimmt sessions, nights out and weekends away, and from here on out, are much-valued friends. Hannah Tiernan has helped to keep me sane with our many cycling trips and has taught me the restorative value of putting the world to rights with a good friend during an early morning bike ride.

Outside of the Imperial bubble I would like to thank my housemates Emma and Jessie who have been there (with matching outfits, of course) through all the highs and lows of these Ph. D. years. Also Lizzi, my oldest and dearest friend and greatest cheerleader. I am so grateful to be a part of Girlguiding, which has allowed me to share my experiences as a chemical engineer with girls and young women, and has been a much-needed escape from the lab to unit meetings, camping trips and international expeditions. Last but in no means least, I would like to thank my parents Cath and Tom for their constant support of every decision I make, and in every experience I go through. They have always believed in me unwaveringly and their love and encouragement have made me the woman I am today.

Nomenclature

A	area	m^2
AR	aspect ratio	[-]
b	Hele-Shaw cell radius	m
Bo	Bond number	[-]
Ca	capillary number	[-]
Co	confinement number	[-]
c_p	heat capacity	J/kg.K
Cv	convection number	[-]
d	diameter	m
E	bubble extension	m
F	frequency	Hz
Fr	Froude number	[-]
G	mass flux	$kg/m^2.s$
g	gravitational acceleration	m/s^2
H	dimensionless film thickness	[-]
h	film thickness	m
h	heat transfer coefficient	$W/m^2.K$

h_{lv}	latent heat of vaporisation	J/kg
I	current	A
k	thermal conductivity	W/m.K
L	length	m
M	molecular weight	kg/mol
MARD	mean relative deviation	%
$\dot{m}$	mass flow rate	kg/s
MGI	mean grayscale intensity	[-]
MRD	mean relative deviation	%
n	refractive index	[-]
Nu	Nusselt number	[-]
P	power	W
p	pressure	Pa
P_{iD}	dimensionless liquid interface length	[-]
Q	heat rate	W
q	heat flux	$\mathrm{W/m^2}$
R	resistance	Ω
r	radius	m
Re	Reynolds number	[-]
R_{g}	universal gas constant	J/mol.K
S	Slip ratio	[-]
St	Stanton number	[-]
T	temperature	K

t	time	s
U	velocity	m/s
u	streamwise velocity component	m/s
V	voltage	V
$\dot{V}$	volumetric flow rate	m^3/s
Var	variance	
w	width	m
We	Weber number	[-]
x	vapour quality	[-]
X_{tt}	Lockhart-Martinelli parameter	[-]
y	vertical direction coordinate	m
z	axial (streamwise) direction coordinate	m

Greek symbols

α	inclination angle	rad
α	phase volume fraction	[-]
β	thermal expansion coefficient	1/K
ϵ	emissivity	[-]
γ	interfacial tension	N/m
μ	dynamic viscosity	Pa.s
ν	kinematic viscosity	m^2/s
ρ	density	kg/m^3
σ	standard deviation	
τ	time constant	s

θ	angle	rad
ε	void fraction	[-]

Subscripts and superscripts

+	top
−	bottom
amb	ambient
b	bubble
cap	capillary
crit	critical
d	drainage
equiv	equivalent
exp	experimental
fric	frictional
grav	gravitational
ht	heated
h	horizontal
IA	intermittent-annular transition
ins	insulation
int	interface
i	inside
LD	liquid dimensionless
l	liquid
max	maximum

min minimum

m mixture

o outside

pred predicted

ref reference

sat saturation point

sa spatial acceleration

sc subcooling

strat stratified

s superficial

tc thermocouple

VD vapour dimensionless

v vapour

w wall

Acronyms

1-D two-dimensional

2-D two-dimensional

3-D three-dimensional

A annular

BBLIF brightness-based laser-induced fluorescence

CSP concentrating solar power

D dryout

DAQ data acquisition device

DSG direct steam generation

FLOBOF Flow Boiling Facility

I intermittent

ID inside diameter

LIF laser-induced fluorescence

M mist

ORC organic Rankine cycle

P&ID piping and instrumentation diagram

PIV particle image velocimetry

PLIF planar laser-induced fluorescence

PTC parabolic trough collector

RI refractive index

RMSE root mean square error

S stratified

SW stratified-wavy

Slug+SW slug plus stratified-wavy

VOF volume of fluid

Contents

1 Introduction **32**

1.1 Motivation 32

1.2 Objectives 33

1.3 Outline 35

1.4 Publications 36

2 Background and Theory **37**

2.1 Predictive methods in boiling flows 38

2.1.1 Flow patterns 38

2.1.2 Pressure drop in boiling flows 47

2.1.3 Heat transfer coefficient in boiling flows 51

2.2 Experimental investigations of boiling flows 57

2.2.1 Overview of experimental flow boiling studies 57

2.2.2 Optical measurement techniques in boiling flows 64

2.3 Numerical investigations towards boiling flows 66

2.3.1 Elongated bubble flow 66

2.4 Summary 72

3 Experimental Methods **74**

3.1 Experimental design 74

3.2 Description of the experimental facility 75

3.2.1 Flow loop 75

3.2.2 Heated test section 78

3.2.3 Visualisation section 78

3.2.4 Safety considerations 80

3.3 Description of integral measurement techniques 80
3.3.1 Temperature 81
3.3.2 Pressure 82
3.3.3 Pressure drop 82
3.3.4 Flow rate 82
3.4 Data reduction for integral measurements 83
3.4.1 Mass flux 83
3.4.2 Heat flux 83
3.4.3 Heat transfer coefficient 84
3.4.4 Vapour quality 85
3.4.5 Pressure drop 85
3.4.6 Uncertainty analysis 86
3.5 Description of optical measurement techniques 88
3.5.1 High-speed imaging for flow pattern identification 88
3.5.2 Combined PLIF and PIV technique 88
3.5.3 Combined BBLIF and PLIF technique 90
3.6 Image processing 91
3.6.1 High-speed imaging for flow pattern identification 91
3.6.2 PLIF and PIV for stratified, stratified-wavy and slug flows 94
3.6.3 BBLIF and PLIF for annular flows 98
3.7 Test fluid 101
3.7.1 Property analysis 102
3.8 Facility commissioning and validation 105
3.8.1 Single phase validation of integral measurements 105
3.8.2 Single phase validation of PIV measurements 105

4 Computational Methods **108**
4.1 Numerical model for multiphase flow 108
4.1.1 Problem description 108
4.1.2 Numerical method 110
4.1.3 Simulation set-up 112
4.2 Numerical model for multiphase flow with phase change 116
4.2.1 Problem description 116

4.2.2 Numerical method . . . 118
4.2.3 Simulation set-up . . . 122

5 Integral Measurements 125
5.1 Experimental parameter ranges . . . 125
5.2 Flow patterns . . . 126
5.3 Pressure drop . . . 131
5.3.1 Experimental data . . . 131
5.3.2 Comparisons with pressure drop predictions . . . 132
5.4 Heat transfer . . . 137
5.4.1 Experimental data . . . 137
5.4.2 Comparisons with heat transfer coefficient predictions . . . 141
5.5 Summary . . . 148

6 Detailed Spatio-temporally Resolved Measurements 150
6.1 Stratified flow . . . 150
6.1.1 Velocity field and interface information . . . 151
6.1.2 Heat transfer effects . . . 154
6.1.3 Heat transfer coefficient prediction . . . 155
6.2 Stratified-wavy flow . . . 156
6.2.1 Velocity field information . . . 156
6.2.2 Interface statistics and heat transfer effects . . . 157
6.2.3 Wave characteristics . . . 161
6.3 Slug flow . . . 164
6.3.1 Velocity fields . . . 166
6.3.2 Slug frequency . . . 167
6.3.3 Vapour bubble velocity . . . 171
6.4 Annular flow . . . 173
6.5 Summary . . . 178

7 Numerical Simulations Towards Flow Boiling 181
7.1 Inertial and buoyancy effects on flow of elongated bubbles in horizontal pipes 182
7.1.1 Theoretical predictions . . . 182
7.1.2 Model validation . . . 184

7.1.3 Buoyancy effects . . . 185
7.1.4 Inertial effects . . . 193
7.1.5 Film thickness predictive method comparison to experimental data 198
7.2 Flow boiling model development . . . 200
7.2.1 Phase change model validation in micro-channels . . . 201
7.2.2 Simulation of experimental conditions . . . 206
7.3 Summary . . . 213

8 Conclusion **215**
8.1 Overview of thesis achievements . . . 215
8.2 Recommendations for future work . . . 218

Bibliography **221**

A Temperature Measurement Corrections and Calculations **250**
A.1 Thermocouple response times . . . 250
A.2 Thermocouple conduction errors . . . 251
A.3 Calibration . . . 252
A.4 Inside wall temperature calculation . . . 253

B Supplementary Material for Computational Results **257**
B.1 Pressure profiles for the inertia-free case . . . 257

List of Figures

2.1 Flow patterns in horizontal gas-liquid flow based on the Alves [19] classification. . . . 39

2.2 Flow pattern map of Kattan et al. [31] (solid black lines) compared to that of Steiner [30] (dashed red lines) for R245fa at $p_{\text{sat}} = 1.7\,\text{bar}$ and the conditions $q = 14\,\text{kW/m}^2$, $G = 330\ \text{kg/m}^2\text{.s}$. . . . 42

2.3 Flow pattern map of Wojtan et al. [36] for R245fa at $p_{\text{sat}} = 1.7\,\text{bar}$ and the conditions $q = 14\,\text{kW/m}^2$, $G = 330\ \text{kg/m}^2\text{.s}$. . . . 43

3.1 Simplified flow diagram of Flow Boiling Facility (FLOBOF). Measurement locations for temperature, pressure and differential pressure are indicated by T, P and DP respectively. . . . 76

3.2 Detailed P&ID of FLOBOF. . . . 77

3.3 Schematic of the heated test section. Measurement locations for temperature, pressure and differential pressure are indicated by T, P and DP respectively. . . . 78

3.4 Photograph of the visualisation section. . . . 79

3.5 Photograph of graticule target inside the visualisation section. . . . 80

3.6 Photograph showing attachment of unsheathed thermocouples to the wall. 81

3.7 Camera arrangement for qualitative flow visualisation. . . . 88

3.8 Camera arrangement for combined PLIF and PIV. . . . 89

3.9 Camera arrangement for combined BBLIF and PLIF. . . . 91

3.10 Example high-speed image used for flow pattern identification, with selection area for grayscale intensity analysis illustrated between the red lines (not to scale). . . . 92

3.11 Example mean grayscale intensity (MGI) signals plotted against acquisition time t for different flow patterns. . . . 95

3.12 Values of Var/$\overline{MGI}$ for intermittent and annular flow patterns. 95
3.13 Example images at each stage of the image processing procedure. 97
3.14 Example images of calibration target inserted into the liquid flooded pipe in (a) raw and (b) binarised form. The centres of the circles on the target are exactly 1 mm apart. 97
3.15 Image calibration for BBLIF and PLIF with (a) example images of calibration target in the liquid-flooded pipe captured by the PLIF camera (top) and BBLIF camera (bottom) - see Fig. 3.9 for arrangement. (b) Brightness calibration with stable liquid film captured by PLIF camera (top) and BBLIF camera (bottom). 98
3.16 Image intensity as a function of film height with calibration data points (blue circles) and Eq. (3.22) fitted to the data (solid line) and adjusted for evaporation to a vapour quality of 0.15 (dashed line) as an example. 100
3.17 Illustrations of the maximum bubble pressure method: (a) describes the formation, growth and detachment of a gas bubble at the capillary tip; (b) shows an optical microscope image used to characterise the capillary tip; (c) shows a sample pressure trace against time t, where the peaks of $p_{\max}$ have been identified and correspond to the point of maximum bubble size and subsequent detachment. 104
3.18 Representative data collected using the maximum bubble pressure method for R245fa with a dye concentration of 7.5 ppm. The gradient of the line in (a) is equal to ρg, and gives $\rho = 1386\,\mathrm{kg/m^3}$, 0.5 % lower than the theoretical density of pure refrigerant at the same conditions. In (b) the temperature-corrected surface tension values are plotted against immersion depth z, with the literature value indicated by the dashed line. 105
3.19 Single phase liquid flow velocity profiles from PIV measurements normalised by maximum velocity and pipe diameter (blue crosses) and theoretical predictions (red dashed line) for (a) laminar and (b) turbulent flows. 106
3.20 Mass flux G calculated based on PIV measurements versus flowmeter measurements for single phase liquid flow. The solid black line represents $G_{\mathrm{PIV}} = G_{\mathrm{flowmeter}}$, whilst the red dashed line represents $G_{\mathrm{PIV}} = G_{\mathrm{flowmeter}} \pm 10\%$. 107

4.1 Sketches of an elongated gas bubble flowing in a horizontal tube filled with liquid, and notation used in this work. (a) Two-dimensional bubble profile extracted on a vertical centreline plane, where $x = 0$. (b) Bubble cross-sectional profile extracted on an arbitrary x-y plane. In (a), position 'K' indicates the most upstream point of the bubble interface; position 'F' identifies the location of the lowest point of the bubble interface, which in this work is selected as the location where the film thicknesses are measured. 109

4.2 Illustration of the x-y cross-section of the computational mesh. The core consists of a square rod of size $0.5r \times 0.5r$ meshed with uniform cubes, outside of which the mesh is gradually refined radially towards the wall. At the wall, the size of the elements along the radial and circumferential directions are denoted as Δ_r and Δ_θ, respectively. For the mesh depicted here, $\Delta_r = 0.0041r$ and $\Delta_\theta = 0.105r$. 113

4.3 Mesh independence study for conditions $\mathrm{Ca_l} = 0.024$, $\mathrm{Bo} = 0.42$, and $\mathrm{Re_l} = 1$: (a) bubble profile on a vertical centreline plane ($x = 0$) and (b) bubble cross-sectional shape at the location F (see Fig. 4.1). The geometric details of the meshes and corresponding values of the top film thickness at F are reported in Tab. 4.1. 114

4.4 Mesh independence study for conditions $\mathrm{Ca_l} = 0.024$, $\mathrm{Bo} = 0.42$, and $\mathrm{Re_l} = 750$: (a) bubble profile on a vertical centreline plane ($x = 0$) and (b) bubble cross-sectional shape at the location F (see Fig. 1 in the article). The geometric details of the meshes and corresponding values of the top film thickness at F are reported in Tab. 4.1. 115

4.5 Sketch (not to scale) of the simulation set-up for flow boiling in a square micro-channel. The channel width is $w = 229\,\mu\mathrm{m}$ and flow is from left to right. 117

4.6 Sketch (not to scale) of the simulation set-up for flow boiling in geometry based on FLOBOF. The pipe diameter is $d = 12.6\,\mathrm{mm}$ and flow is from left to right. The cross-section on the right shows the computational mesh. . . 118

5.1 Flow patterns captured in FLOBOF using high-speed imaging. 127

5.2 Flow pattern map with G vs. x axes summarising all experimental data points for $p_{\text{sat}} = 1.7\,\text{bar}$, with the inset showing a logarithmic x-axis for better visualisation of the data at low x. 128

5.3 Flow pattern map summarising all experimental data points, $p_{\text{sat}} = 1.7\,\text{bar}$, with transition lines and flow pattern regions according to method of Wojtan et al. [36] for the conditions $q = 14\,\text{kW/m}^2$, $G = 330$ kg/m^2.s. 129

5.4 Flow pattern map summarising all experimental data points, $p_{\text{sat}} = 1.7\,\text{bar}$, with transition lines and flow pattern regions according to the method of Zürcher et al. [49] calculated for the conditions $q = 14\,\text{kW/m}^2$, $G = 330$ kg/m^2.s. 130

5.5 Flow pattern map summarising all experimental data points and a range of transition curves, $p_{\text{sat}} = 1.7\,\text{bar}$. The Costa-Patry and Thome [51] curve was generated for $q = 14\,\text{kW/m}^2$. 131

5.6 Frictional pressure drop as a function of vapour quality for a range of mass flux conditions. 132

5.7 Comparison of predicted and experimental frictional pressure drops using a selection of predictive methods. The solid lines represent $\Delta p_{\text{pred}} = \Delta p_{\text{exp}}$, the black dashed lines $\Delta p_{\text{pred}} = \Delta p_{\text{exp}} \pm 30\%$, and the red dashed lines $\Delta p_{\text{pred}} = \Delta p_{\text{exp}} \pm 50\%$. 134

5.8 Comparison of predicted and experimental frictional pressure drops using a selection of predictive methods, presented as the ratio of predicted to experimental frictional pressure drop as a function of vapour quality. . . . 135

5.9 Stanton number as a function of vapour quality for a range of heat flux conditions. 139

5.10 Heat transfer coefficient vs. vapour quality for a range of heat flux conditions and two mass flux conditions. 140

5.11 Comparison of predicted and experimental frictional heat transfer coefficients using a selection of predictive methods. The solid lines represent $h_{\text{pred}} = h_{\text{exp}}$, the black dashed lines $h_{\text{pred}} = h_{\text{exp}} \pm 30\%$, and the red dashed lines $h_{\text{pred}} = h_{\text{exp}} \pm 50\%$. 143

5.12 Ratio of predicted to experimental frictional heat transfer coefficients plotted against vapour quality using a selection of predictive methods. 144

5.13 Ratio of predicted to experimental frictional heat transfer coefficients plotted against experimental heat transfer coefficient for data in the nucleate boiling dominant zone. 147

6.1 Time-averaged velocity information for two stratified flow conditions with the following experimental parameters: (a,b) $G = 32\,\mathrm{kg/m^2.s}$, $q = 1.9\,\mathrm{kW/m^2}$, $x = 0.21$; (c,d) $G = 97\ \mathrm{kg/m^2.s}$, $q = 1.1\,\mathrm{kW/m^2}$, $x = 0.04$. The velocity fields (a,c) have the colour scale $u = 0$–u_{max}. The velocity profiles (b,d) were spatially-averaged over the streamwise direction, with the red dashed line showing the velocity profile as predicted according to the Yiantsios and Higgins [219] method, and are presented with $\langle u \rangle$ normalised by u_{max} and y normalised by the interface height y_{int}. 152

6.2 Streamwise velocity profiles, averaged over the streamwise direction and time, for stratified flow with $q = 1.7\,\mathrm{kW/m^2}$ at a range of mass fluxes, with the vertical direction y scaled by the corresponding interface height y_{int} for each case. 154

6.3 Stratified angle calculated using the Biberg [46] method, as utilised by Wojtan et al. [36], compared to that measured experimentally using PLIF. The dashed line represents $\theta_{\mathrm{strat,pred}} = \theta_{\mathrm{strat,exp}}$. 156

6.4 Instantaneous liquid-phase velocity fields from a stationary frame of reference in stratified wavy flows with the conditions (a) $G = 73\ \mathrm{kg/m^2.s}$, $q = 2.6\,\mathrm{kW/m^2}$, $x = 0.13$ and (b) $G = 70\ \mathrm{kg/m^2.s}$, $q = 3.4\,\mathrm{kW/m^2}$, $x = 0.17$. The pipe inside diameter is $d = 12.6\,\mathrm{mm}$. The interface is identified with the black line and the length of the arrows represents the magnitude of the velocity vector, whilst the colour map in the background represents the magnitude of the velocity in the streamwise direction, z. . . 158

6.5 Probability density functions of film thickness normalised by the mean film thickness over all frames and pixels for each set of experimental conditions. Red lines represent stratified flow and blue lines represent stratified-wavy flow, with colour grading corresponding to heat flux. 159

6.6 Stanton number ($\mathrm{St} = h/Gc_{p,\mathrm{l}}$) vs. (a) mean interface height $\langle \bar{y}_{\mathrm{int}} \rangle$ and (b) interfacial roughness $y_{\mathrm{int,RMS}}/\langle \bar{y}_{\mathrm{int}} \rangle$ for stratified and stratified-wavy flows. . 161

6.7 Probability density functions of the wave radii of curvature r_{curv} for (a) peaks and (b) troughs. Red lines represent stratified flow and blue lines represent stratified-wavy flow, with colour grading corresponding to heat flux. An inset is provided in (a) expanding the $r_{\text{curv,p}} = 0$–0.3 mm region. . 163

6.8 (a) Ensemble averaged velocity field and (b) corresponding profiles under waves for $0.9 < r_{\text{curv}} < 1$ at the conditions $G = 68\,\text{kg/m}^2\text{.s}$, $q = 2.3\,\text{kW/m}^2$. The velocity profiles were extracted at the centre of the wave for the streamwise and vertical velocities, u and v respectively. 165

6.9 (a) Ensemble averaged velocity field and (b) corresponding profiles under troughs for $0.9 < r_{\text{curv}} < 1$ at the conditions $G = 68\,\text{kg/m}^2\text{.s}$, $q = 2.3\,\text{kW/m}^2$. The velocity profiles were extracted at the centre of the trough for the streamwise and vertical velocities, u and v respectively. 165

6.10 Representative high speed images (top row) with the detected interface marked with a red line and corresponding masked instantaneous velocity fields (bottom row) in a stationary frame of reference for slug flow at the conditions $G = 460$ kg/m^2.s, $q = 7.9\,\text{kW/m}^2$. Images and velocity fields are shown at the (a) tail, (b) middle and (c) nose of a vapour bubble. . . . 168

6.11 (a) Interface height versus time and (b) corresponding fast Fourier transform displayed as amplitude versus frequency at the $z = 12.5\,\text{mm}$ location in the stationary frame of reference of the high-speed images, for slug flow at the conditions $G = 460\,\text{kg/m}^2\text{.s}$, $q = 7.9\,\text{kW/m}^2$. 169

6.12 Effect of slug frequency F_{slug} on heat transfer, illustrated by plotting the Stanton number $\text{St} = h/Gc_{p,\text{l}}$, to normalise for the differing mass fluxes, against slug frequency. The different heat flux conditions are indicated by different marker symbols and colours. 170

6.13 Predicted versus experimental slug frequency for predictive methods proposed by Gregory and Scott [235] and Al-Safran [236]. The black dashed line indicates equality of the predicted and experimental values. 171

6.14 Interface height versus time at the $z = 0\,\text{mm}$ (solid black line) and $z = 25\,\text{mm}$ (dashed blue line) locations in the stationary frame of reference of the high-speed images, for slug flow at the conditions $G = 460\,\text{kg/m}^2\text{.s}$, $q = 7.9\,\text{kW/m}^2$. 172

6.15 Vapour bubble velocity u_{b} versus superficial mixture velocity u_{m} for slug flow. The different heat flux conditions are indicated by different marker symbols and colours. 173

6.16 Example instantaneous PLIF (top) and BBLIF (bottom) images in a stationary frame of reference for annular flow with the conditions (a) $G = 440$ kg/m^2.s, $q = 26\,\mathrm{kW/m^2}$ and (b) $G = 510$ kg/m^2.s, $q = 21\,\mathrm{kW/m^2}$. . . . 174

6.17 Fraction ϕ of (a) erroneous film thickness-time pairs after filtering and (b) film thickness values above the 5 mm cut-off value as functions of superficial liquid Reynolds number $Re_{\mathrm{s,l}} = G(1-x)d/\mu_{\mathrm{l}}$. 175

6.18 Example plot of film thickness y_{int} versus time t extracted at the midpoint of the BBLIF frame for annular flow at the conditions $G = 440$ kg/m^2.s, $q = 23\,\mathrm{kW/m^2}$. 176

6.19 Probability density functions of the film thickness y_{int} in annular flow for all experimental conditions investigated with BBLIF, with colour grading by heat flux. 177

6.20 (a) Mean film thickness $\langle \bar{y}_{\mathrm{int}} \rangle$ and (b) film thickness standard deviation σ as a function of superficial liquid Reynolds number $\mathrm{Re_{s,l}}$, separated by heat flux conditions, for annular flow conditions investigated using BBLIF. . . . 178

6.21 The effect of film statistics for annular flow on heat transfer, represented by Stanton number $\mathrm{St} = h/Gc_{p,\mathrm{l}}$ versus (a) mean film thickness $\langle \bar{y}_{\mathrm{int}} \rangle$ and (b) film thickness standard deviation σ, separated by heat flux conditions. 179

7.1 Comparison of the effect of the bubble capillary number and Bond number on the top and bottom film thicknesses with the experimental work of Atasi et al. [169]. The results of both 2-D and 3-D numerical simulations are reported. The dashed line represents the prediction of H using the Aussillous and Quéré [161] correlation, Eq. (2.25), i.e. in the $\mathrm{Bo} = 0$ case. . 185

7.2 (a) Profile of an elongated bubble obtained with a numerical simulation for $\mathrm{Ca_l} = 0.024$ and $\mathrm{Bo} = 0.42$ ($\mathrm{We_l} \ll 1$), flow is from left to right; (b-d) corresponding contour plots of the vertical component of the velocity in the liquid film, at selected cross-sections along the bubble; (e) corresponding bubble profile (not to scale) in the $x = 0$ plane. 187

7.3 Systematic analysis of the impact of the Bond number for the negligible inertia case ($We_l \ll 1$) on the (a) bubble profile on a vertical centreline plane ($x = 0$), (b) on the bubble cross-sectional shape at the location F (see Fig. 4.1), and (c) on the bubble cross-sectional aspect-ratio AR measured at the same location. In (a), flow is from left to right. The capillary number of the liquid in (a) and (b) is $Ca_l = 0.024$. 188

7.4 Impact of the Bond and capillary numbers ($We_l \ll 1$) on the (a) top (H^+) and bottom (H^-) liquid film thicknesses and (b) bubble advancing speed. In (a), the solid lines represent the predictions for the top film thickness given by Eqs. (7.1) and (7.2), while the dashed lines identify the predictions for the bottom thickness obtained with Eqs. (7.1) and (7.3). In (b), the lines identify the predictions extracted by applying Eq. (7.4) with $\overline{H}$ calculated based on the simulation data (solid lines), and with $\overline{H}$ predicted based on Eqs. (7.1)−(7.3) for H^+ and H^-, and Aussillous and Quéré [161] correlation for H^h (dashed lines). 189

7.5 Impact of the Bond and capillary numbers ($We_l \ll 1$) on the (a) average liquid film drainage velocity and (b) top (α^+) and bottom (α^-) bubble inclination angles. Red and blue lines identify the predictions obtained using (a) Eq. (7.6) with $\sin\theta = 1$, and (b) Eq. (2.29), with H^h based on simulation data (solid lines) or Aussillous and Quéré [161] correlation (dashed lines). The black solid lines identify the scaling laws extracted from the analysis of the minimum film thickness trends in Fig. 7.6. 191

7.6 (a) Circumferential evolution of the liquid film thickness on the channel cross-section at the location F for $Ca_l = 0.024$ and different Bond numbers ($We_l \ll 1$), and (b) top and minimum liquid film thickness at F as a function of Bond and capillary numbers. In (a), $\theta = 0$ corresponds to the top of the channel, see Fig. 4.1. 193

7.7 Systematic analysis of the impact of the Reynolds number on the (a) bubble profile on a vertical centreline plane ($x = 0$), (b) on the bubble cross-sectional shape at the location F, and (c) on the bubble cross-sectional aspect-ratio measured at the same location. In (a) and (b), conditions are $Ca_l = 0.024$ and $Bo = 0.42$. 195

7.8 Systematic analysis of the impact of the Reynolds number on the (a) bubble profile on a vertical centreline plane ($x = 0$), (b) on the bubble cross-sectional shape at the location F, and (c) on the bubble cross-sectional aspect-ratio measured at the same location. In (a) and (b), conditions are $\mathrm{Ca_l} = 0.051$ and $\mathrm{Bo} = 0.42$. 196

7.9 Systematic analysis of the effect of the Reynolds number on the (a-c) top and bottom liquid film thickness, and (d-f) on the top and bottom bubble inclination. The liquid capillary number is fixed to $\mathrm{Ca_l} = 0.024$. 197

7.10 Systematic analysis of the effect of the Reynolds number on the (a-c) top and bottom liquid film thickness, and (d-f) on the top and bottom bubble inclination. The liquid capillary number is fixed to $\mathrm{Ca_l} = 0.051$. 198

7.11 Probability density function of interface height y_{int} corresponding to Fig. 6.11a for slug flow at the conditions $G = 460$ kg/m^2.s, $q = 7.9\,\mathrm{kW/m^2}$. The red dashed line indicates the rightmost local minimum, below which the probability density function is integrated to estimate the film thickness under the vapour bubble, h^-. 199

7.12 Predictions of film thickness under vapour bubbles, h^-, using Eq. (7.3) against the corresponding experimental film thicknesses in slug flow at the conditions $G = 300$–460 kg/m^2.s, $q = 5.3$–$7.9\,\mathrm{kW/m^2}$. The black dashed line represents $h^-_{\mathrm{pred}} = h^-_{\mathrm{exp}}$, whilst the red dashed lines indicate $h^-_{\mathrm{pred}} = h^-_{\mathrm{exp}} \pm 30\,\%$. 200

7.13 Initial temperature conditions extracted along the central $x = 0$ plane for 4 different simulations as described in Table 7.1. 202

7.14 Development of equivalent bubble diameter d_{equiv} from boiling in a 229 µm square micro-channel with time t for cases with different initial temperature conditions, as described in Table 7.1, with comparison to the experimental data of Mukherjee et al. [152] (blue crosses). The flow conditions are $\mathrm{Re_l} = 100$ and $\mathrm{Ca_l} = 0.0006$. 204

7.15 Visualisation of bubble growth from boiling in a 229 µm square micro-channel for simulation 4 (see Table. 7.1 and Fig. 7.13), coloured by the local evaporation rate. Channel dimensions are in metres and empty regions within the bubble identify dry vapour regions. The flow conditions are $\mathrm{Re_l} = 100$ and $\mathrm{Ca_l} = 0.0006$. 205

7.16 Development of equivalent bubble diameter d_{equiv} from boiling in a 229 µm square micro-channel with time t for different computational meshes, as described in Table 7.2. The flow conditions are $\mathrm{Re_l} = 100$ and $\mathrm{Ca_l} = 0.0006$ and the initial temperature condition corresponds to simulation 4 in Table 7.1. 206

7.17 Visualisation of simulation of flow boiling in a 12.6 mm pipe at the conditions $G = 32$ kg/m^2.s, $q = 1.9\,\mathrm{kW/m^2}$ after 4.5 s of simulation time. Flow is from left to right. The contour of the vapour liquid interface is shown above the liquid-phase streamwise velocity field along the central plane of the pipe. The axial coordinate is in m and velocity u is in m/s. 208

7.18 Spatially averaged interface height, $\bar{y}_{\mathrm{int}}$, development with time t from the flow boiling simulation (solid black line) compared to the experimental mean interface height (dashed blue line) for stratified flow at the conditions $G = 32$ kg/m^2.s, $q = 1.9\,\mathrm{kW/m^2}$. 208

7.19 Temporally and spatially averaged streamwise velocity profiles from the experiment (blue circles) and simulation (red squares) with the conditions $G = 32$ kg/m^2.s, $q = 1.9\,\mathrm{kW/m^2}$. The horizontal lines indicate the mean interface height from the experiment (blue dashed line) and the simulation (red dotted line). 209

7.20 Temperature field extracted along the central plane of the pipe (left) and in the cross-section at the $z = 16d$ location (right) after 4.5 s of simulation time for stratified flow at the conditions $G = 32$ kg/m^2.s, $q = 1.9\,\mathrm{kW/m^2}$. The interface is shown by the white contour line. The axial coordinate is in metres and temperature, T, is in K. 210

7.21 Temporal development of (a) the mean heat transfer coefficient and (b) the ratio of the heat transfer coefficients at the bottom and top of the pipe in simulations of stratified flow at the conditions $G = 32$ kg/m^2.s, $q = 1.9\,\mathrm{kW/m^2}$. In (b) the blue dashed line indicates the mean heat transfer coefficient ratio obtained in the corresponding experiment. 211

A.1 Errors in raw thermocouple temperature readings due to conduction heat losses along the thermocouple wire. 252

A.2 Diagram of thermal bath set-up for thermocouple calibration. Measurements are in mm. 253

A.3 Thermocouple calibration data at one recorded temperature alongside the fitted line and 95 % confidence intervals as applied to the whole calibration temperature range. 254

A.4 Control volume evaluated for solution of one-dimensional heat transfer in pipe walls. Q is heat flow measured in W, and Q''' is the heat input per unit volume, V. 255

B.1 Streamwise pressure profiles along the (a,c) channel axis and (b,d) channel bottom ($x = 0$, $y = -r$). 258

B.2 Streamwise pressure drop induced by the bubble, calculated along the channel axis. As a reference, Bretherton's theoretical model in the absence of gravity (Bo = 0) predicts $\Delta p/(\gamma/r) = 4.52(3\mathrm{Ca})^{2/3} = 0.89$ and 1.57 for, respectively, bubble capillary numbers Ca = 0.029 ($\mathrm{Ca_l} = 0.024$) and Ca = 0.068 ($\mathrm{Ca_l} = 0.051$). 259

List of Tables

2.1 Summary of studies mapping horizontal gas-liquid flows 40

2.2 Summary of experimental flow boiling studies in horizontal macro-scale pipes. 60

3.1 Fixed errors in measured quantities. 86

3.2 Experimental uncertainties. Percentage uncertainties pertain to the measured value. 87

3.3 Experimental parameters of considered refrigerants. Fluid property data from various sources [199–202]. 102

4.1 Geometrical details of the meshes tested and corresponding values of the top film thickness evaluated at F, for the simulation cases illustrated in Fig. 4.3 and 4.4. Δ_r and Δ_θ denote the radial and circumferential size of the mesh elements at the wall (see Fig. 4.2), while Δ_z indicates the longitudinal extension of the cell, which is constant across each mesh. The top film thickness H^+ is evaluated at the location F (see Fig. 4.1). 116

5.1 Experimental parameter ranges. 126

5.2 Summary of the discrepancies between the predicted and experimental pressure drops in terms of the the mean relative deviation (MRD) and mean absolute relative deviation (MARD). 133

5.3 Summary of the discrepancies between the predicted and measured heat transfer coefficients in terms of the mean relative deviation (MRD) and mean absolute relative deviation (MARD). 145

5.4 Summary of discrepancies between the predicted and measured pool boiling heat transfer coefficients in terms of mean relative deviation (MRD) and mean average relative deviation (MARD). 146

6.1 Stratified flow experimental parameters and results for the heat flux condition $q = 1.7\,\mathrm{kW/m^2}$, including the Reynolds numbers at the pipe inlet, and for the liquid phase at the measurement location, $\mathrm{Re_{l,in}} = \mathrm{Gd}/\mu_\mathrm{l}$ and $\mathrm{Re_l} = (\mathrm{G}(1-\mathrm{x})/(1-\varepsilon))\mathrm{d}/\mu_\mathrm{l}$ respectively. 153

7.1 Initial temperature conditions for different simulation test cases in a 229 µm channel. In the thermal boundary layer the condition $T = T_\mathrm{sat}$ is set. The bottom and side walls of the channel are subject to the condition $T_\mathrm{wall} = 375.25\,\mathrm{K}$. 202

7.2 Mesh parameters. 205

Chapter 1

Introduction

1.1 Motivation

Boiling flows in horizontal pipes are present in evaporators, boilers and heat exchangers in a wide variety of applications. For example, refrigerants such as R245fa are used as the working fluid in organic Rankine cycle (ORC) systems for the generation of electrical power from low-temperature thermal energy sources [1, 2] such as solar heat [3, 4], or for waste heat recovery [5, 6]. These fluids can also be used in high-temperature heat pumps, or in cooling and refrigeration systems. Identification of the most accurate predictive methods for flow pattern, pressure drop and heat transfer is essential for design engineers to select the most appropriate correlations for their system and optimise the design parameters accordingly. In ORC systems heat exchangers dominate the total investment cost [7, 8], with the evaporator alone accounting for at least a third of the total cost in systems with an n-alkane-type working fluid such as R245fa [9, 10]. Since the cost of a heat exchanger is directly related to the heat transfer area, accurate prediction of heat transfer performance is vital. The heat transfer area will also affect the footprint of the heat exchanger, which has further cost implications in terms of equipment size and space.

The understanding of boiling flows is also important for effective design and operation of concentrating solar power (CSP) plants operating in the direct steam generation (DSG) mode [11]. In this application, water boils directly inside the solar collector tube, rather than in a secondary circuit. As in all boiling flow applications, the development of a transient two-phase flow makes reliable control and operation of the system challenging, and the flow pattern within the boiling flow can have a significant impact on the system per-

formance. Stratified flow in these solar collector tubes can result in large circumferential temperature gradients [12, 13], which can in turn cause bending of the tubes and severe, and costly, damage to the system. Accurate prediction of the heat transfer in the desired flow regimes, through use of appropriate correlations, is also key to the design of these systems, since under- or over-sizing can result in inefficiencies and associated cost penalties. In industrial applications, flow-pattern specific models can be prohibitively complex to implement, but detailed measurements of these boiling flows could enable identification of areas for improvement and simplification.

The operational costs of all flow boiling systems are affected by the power requirements of the pump, although the capital cost of the pump is relatively small compared to that of the heat exchangers [9, 10]. It is thus also important to understand the most accurate predictive methods for pressure drop of boiling flows, as investigated in this work.

Many experimental studies have presented the investigation of boiling of various fluids in horizontal pipes of a wide range of diameters. However, there is a relative scarcity of data for R245fa in pipe diameters above the 'mini' scale (i.e. $d > 3\,\text{mm}$ [14]) and validation of the many predictive methods available for flow pattern, pressure drop and heat transfer coefficient in these flows is required. The literature also lacks detailed spatio-temporally resolved information for these flows, including the interfacial dynamics, phase distribution and velocity fields. Advanced laser-based diagnostic techniques exist that have been employed to study both isothermal and heated two-phase flows without phase change, and there is scope for these methods to be developed for application to boiling flows as well. This detailed data could reveal insights into the thermohydraulic behaviour of boiling flows, and provide validation cases for numerical simulations. Such simulations of boiling flow, particularly in macro-scale pipes, require accurate modelling of multi-phase flow with heat transfer, phase change and often turbulence, resulting in complex simulations that must be thoroughly validated.

1.2 Objectives

This work seeks to address the literature gaps regarding flow boiling in horizontal pipes identified in the previous section. Experimental and numerical investigations will aim to provide new data and insights into R245fa boiling flows across a range of flow patterns in

pipes with diameters above the micro-scale.

The experimental work in this study is based on the development of optical measurement techniques for boiling flows to provide detailed spatio-temporally resolved measurements of velocity fields and phase distributions. These techniques build on laser-diagnostic methods based on particle image velocimetry and laser-induced fluorescence, which have been employed successfully to measure multiphase flows without phase change [15–17]. To take such measurements, a new experimental facility was required in which the temperature and pressure drop measurements typical of the flow boiling literature could be taken alongside quantitative optical measurements. These requirements formed the basis of the design, construction, commissioning and validation of the new facility. It was also necessary to develop bespoke data and image processing algorithms to obtain meaningful results from the experimental measurements. Experimental pressure drops and heat transfer coefficients could be used to assess the applicability of predictive methods in the literature to R245fa flow boiling at the macro-scale, whilst high-speed imaging could be used to identify flow patterns and validate existing flow pattern maps.

The numerical investigations presented in the thesis aim to work towards a full numerical model of flow boiling at the experimental conditions in this work. First, existing models of adiabatic elongated bubble flow in micro-channels require extension to geometries and flow conditions in which inertial and buoyancy effects become significant. Then, heat transfer and phase change models can be added and validated for bubble development in micro-scale boiling flows, before increasing the size of the computational geometry to the scale of the experimental facility developed for this work. The simulation of this geometry allows for direct comparison of experimental and computational results, whilst further comparisons can be made across different geometries through consideration of predictive methods against both data sets.

The main objectives of this work can be summarised as follows:

- Construct a dedicated experimental facility for flow boiling of the refrigerant R245fa with capabilities for optical flow measurements using laser diagnostic techniques such as particle image velocimetry and planar laser-induced fluorescence.

- Build an experimental data bank of both integral temperature and pressure drop measurements and full space- and time-resolved flow measurements for diabatic vapour-liquid boiling flows in horizontal pipes.

- Assess the applicability of predictive methods in the literature for flow pattern, pressure drop and heat transfer coefficient to R245fa boiling flows in macro-scale geometries.

- Use computational methods to perform a parametric study of inertial and buoyancy effects on elongated bubble flow and develop an accurate predictive method for liquid film thickness around the bubble.

- Validate a phase change model using the open-source computational fluid dynamics software OpenFOAM for growth of a small bubble.

- Simulate the experimental geometry at selected flow conditions and compare the two sets of results.

1.3 Outline

This thesis is structured in eight chapters. A brief introduction has been given in this chapter, along with the objectives of the work. A literature review is presented in Chapter 2 where the state of the art and underlying theory are discussed. The development of predictive methods in boiling flows is discussed, and relevant experimental and computational techniques from the multiphase flow literature are described. The experimental methods employed in this work are described in detail in Chapter 3, including the data and image processing procedures. Chapter 4 provides information on the numerical methods used to perform computational fluid dynamics simulations of multiphase and boiling flows.

In Chapter 5, the results of integral measurements of the pressure drop and heat transfer coefficient are presented and discussed. Predictive methods for flow pattern, pressure drop and heat transfer coefficient are compared to the experimental data. Detailed spatio-temporally resolved measurements of velocity fields and interface location are presented in Chapter 6. Velocity profiles and interface statistics are analysed and linked to the heat transfer performance. Chapter 7 details the development of numerical simulations of flow boiling, starting from an investigation into the effects of inertia and buoyancy on elongated bubble flow. A phase change model is validated for the growth of a small vapour bubble at the wall in a boiling flow, then preliminary simulations of the experimental geometry

and conditions are discussed. Finally, Chapter 8 summarises the main conclusions of the thesis and gives recommendations for further work.

1.4 Publications

Peer-reviewed journal articles published by the author of this thesis include:

- R. Bale and H.R. Moran. Reflections on Peer Facilitation of Graduate Teaching Assistant Training. Journal of Perspectives in Applied Academic Practice, 8(1):157-162, 2020

- H.R. Moran, M. Magnini, C.N. Markides and O.K. Matar. Inertial and buoyancy effects on the flow of elongated bubbles in horizontal channels. International Journal of Multiphase Flow, 135:103468, 2021

- H.R. Moran, D. Zogg, V. Voulgaropoulos, W.J. Van den Bergh, J. Dirker, J.P Meyer, O.K. Matar and C.N. Markides. An experimental study of the thermohydraulic characteristics of flow boiling in horizontal pipes: Linking spatiotemporally resolved and integral measurements. Applied Thermal Engineering, 194:117085, 2021

- H.R. Moran, K.S. Pervunin, O.K. Matar and C.N. Markides, Laser-based diagnostics of slug flow boiling in a horizontal pipe. Submitted to Interfacial Phenomena and Heat Transfer, 2021

- J. Dirker, W.J. Van den Bergh, H.R. Moran, C.N. Markides, J.P Meyer. Influence of inlet vapour quality perturbations on the transient response of flow-boiling heat transfer. International Journal of Heat and Mass Transfer, 170:121017, 2021

- W.J. Van den Bergh, H.R. Moran, J. Dirker, C.N. Markides, J.P. Meyer. Effect of low heat and mass fluxes on the boiling heat transfer coefficient of R245fa. International Journal of Heat and Mass Transfer, 180:121743, 2021

Chapter 2

Background and Theory

The literature on the topic of flow boiling is extensive, with a large number of applications including heat pumps, petrochemical plant reboilers, water-tube and fire boilers, water-cooled nuclear reactors, refrigeration and air-conditioning systems [18] and, more recently, direct steam generation (DSG) solar collectors. Flow boiling research is mainly motivated by applications in refrigeration systems or the nuclear space, the latter being based primarily on subcooled boiling of water, as in pressurised water reactors (PWRs). Driven by the need for accurate predictive methods for flow boiling in refrigeration systems, there have been a large number of experimental studies with refrigerants, many of which have proposed flow pattern maps, and pressure drop and heat transfer correlations.

The numerical study of flow boiling is dominated by micro-channel flows, which have important applications in the removal of high heat fluxes from micro-electronic devices. Numerical studies in larger channels require greater computational power due to the complexity of cases involving turbulent flow with heat transfer and phase change. In a number of studies, flow boiling has been approached from the case of evaporation of a vapour bubble in a liquid flow.

In this section, the theory and literature surrounding experimental and numerical investigations of flow boiling in horizontal pipes are discussed. The development of predictive methods describing boiling flows is considered, along with the applicability and accuracy of such methods across changing flow conditions. The range of both experimental and numerical methods used to study boiling flows is introduced, along with techniques from other types of studies that could be applied to boiling flows to provide new insights into the thermal and hydrodynamic phenomena.

2.1 Predictive methods in boiling flows

A horizontal boiling flow can be characterised by its flow pattern, pressure drop and heat transfer performance, by means of the heat transfer coefficient. This section explores the development of predictive methods for these characteristics in the literature.

2.1.1 Flow patterns

2.1.1.1 Flow pattern classification

During flow boiling, liquid vaporises and this vapour exists with the liquid in a variety of structures known as flow patterns. The formation of these flow patterns depends on the fluid properties, flow conditions, and phase fraction. In horizontal pipes the distribution of the vapour and liquid phases is also affected by gravity, resulting in complex asymmetrical flow structures not present in vertical boiling flows. Various flow pattern classifications have been proposed, but in the literature of horizontal gas-liquid flow the patterns discussed are generally those proposed by Alves [19], or some variation on these. The forms of these different flow patterns are represented in Fig. 2.1 and are defined as follows:

- *Stratified*: The gas and liquid phases flow in two layers separated by a smooth interface. This patterns occurs at very low velocities of both phases.

- *Wavy*: In this pattern, waves travelling in the direction of flow form at the interface as the gas velocity increase.

- *Slug*: Large liquid slugs travel behind bubbles large enough to span the pipe diameter. This pattern occurs as gas velocity increases above that of wavy flow, causing waves to lift and form a slug.

- *Plug*: This pattern consists of elongated gas bubbles separated from the pipe wall by a thin, draining liquid film. Buoyancy effects cause the bubbles to travel towards the top of the pipe.

- *Bubbly*: Isolated gas bubbles move in a continuous liquid phase. This pattern occurs at moderate liquid and gas velocities and low void fractions.

- *Annular*: A continuous liquid film flows in an annulus along the the pipe wall, with a gas core at the centre, which may contain entrained droplets. The liquid film will be thicker towards the bottom of the pipe and may not be continuous around the whole circumference. This pattern occurs at high gas velocities and void fractions.

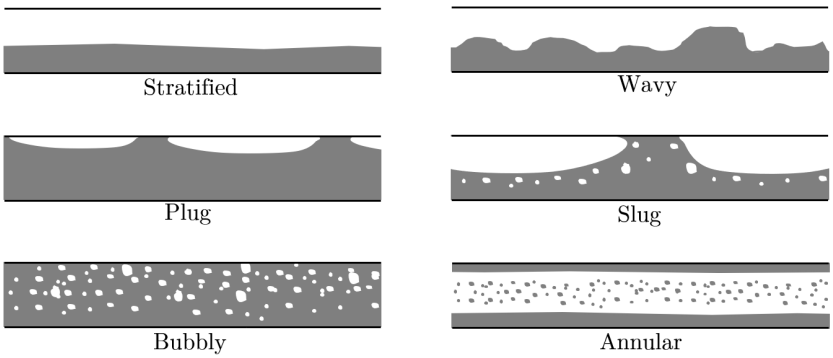


Figure 2.1: Flow patterns in horizontal gas-liquid flow based on the Alves [19] classification.

As liquid boils in a heated pipe, some combination of the flow patterns shown in Fig. 2.1 will occur, where the gas phase is the vapour phase associated with the liquid. Development of these flow patterns is influenced by departures from hydrodynamic and thermodynamic equilibrium, and the order in which, and indeed if, the different flow patterns appear is largely influenced by the heat flux, liquid temperature and flow rate. The local flow pattern is also highly dependent on the phase fraction and relative velocities of the two phases.

2.1.1.2 Flow pattern maps

Since flow pattern can influence the pressure drop and heat transfer in boiling flows, it is essential to be able to predict the expected flow pattern regime under operational conditions. This is most commonly done by means of a flow map, where areas on a graph represent different flow patterns. The axes of such graphs are often superficial phase velocities, sometimes adjusted for fluid properties and/or flow parameters, or dimensionless numbers that attempt to generalise the flow map. Studies mapping horizontal gas-liquid flows have been summarised in Table 2.1, beginning with early studies mapping adiabatic flows and moving into more recent studies mapping heated flows with phase change.

Some of the earliest investigations into two-phase gas-liquid flows in horizontal pipes were those of Bergelin and Gazeley [20] and Kosterin [21], both using air and water as the

Table 2.1: Summary of studies mapping horizontal gas-liquid flows

Publication	Conditions	Fluids	Pipe inside diameters
Bergelin and Gazeley [20]	Adiabatic	Air-water	1 in
Kosterin [21]	Adiabatic	Air-water	1, 2, 3 and 4 in
Baker [22]	Adiabatic	Air-water, natural gas-oil	4.026, 5.937, 7.75 and 10.136 in
Hoogendoorn [23]	Adiabatic	Air-water, air-oil	24-140 mm
Hoogendoorn and Buitelaar [24]	Adiabatic	Freon-11 vapour-water	15 mm
Scott [25]	Adiabatic	Air-water, air-oil	Data from others
Mandhane et al. [26]	Adiabatic	Gas-oil, data bank	0.5 - 6 in (UC multiphase pipe flow data bank)
Taitel and Dukler [27]	Adiabatic	Universal	0.5 - 5.9 in
Hashizume [28]	Adiabatic	Refrigerant liquid-vapour	10 mm
Dukler and Taitel [29]	Diabatic	Universal	Universal
Steiner [30]	Adiabatic	Refrigerant liquid-vapour	Universal
Kattan et al. [31–33]	Adiabatic & diabatic	Refrigerant liquid-vapour	12.0 mm
Zürcher et al. [34]	Diabatic	Refrigerant liquid-vapour	10.92 mm
Thome and El Hajal [35]	Diabatic	Refrigerant liquid-vapour	8, 12, 14 mm
Wojtan et al. [36, 37]	Diabatic	Refrigerant liquid-vapour	13.84 mm
Cheng et al. [38]	Diabatic	CO2 liquid-vapour	0.6-10 mm
Grauso et al. [39]	Adiabatic & diabatic	Refrigerant liquid-vapour	6 mm

test fluids. Baker [22] used this data and that of Alves [19] to create a flow map plotting gas mass-velocity against the liquid-to-gas mass-velocity ratio in the feed. Baker's map [22] is widely used, particularly in the petrochemical industries. Scott [25] modified the Baker [22] flow map to improve agreement with the data of Hoogendoorn [23] and Govier and Omer [40].

The shape and relative sizes of the areas on the Scott flow map change somewhat

for other test fluids, and change rapidly as the pipe diameter decreases below 1 in, so despite the wide-ranging use of this map as a reference, it is not universally applicable. Al-Sheikh et al. [41] defined a variety of dimensionless groups and used two-phase flow data from the AGA-API Data Bank to assess the suitability of various combinations of these for mapping flow regimes. They concluded that no pair of dimensionless numbers was capable of characterising all flow patterns and all data. Work by Mandhane et al. [26] based on the UC Multiphase Pipe Flow Data Bank also concluded that accounting for the effects of the physical properties of fluids using any of the previously proposed physical property parameters gave no improvement in flow map applicability. This highlights the difficulty of producing a universal flow pattern map, and reinforces the need for clear boundaries of applicability in flow map reporting.

The first reporting of an accurate analysis of flow pattern transitions in horizontal adiabatic two-phase gas-liquid flow using a physically based model was presented by Taitel and Dukler [27], who used a theoretical basis for the selection of flow map coordinates that predict the effect of pipe size, fluid properties and inclination angle on the transition boundaries. The combination of different pairs of flow parameters for different flow transitions in this flow map removed the assumption in other flow maps that all transitions can be described by the same pair of parameters.

Steiner [30] modified the map of Taitel and Dukler [27] and validated their new map with additional experimental data. However, this flow map is only applicable to adiabatic flows, and flow boiling is usually achieved by application of heating to the pipe wall. Adiabatic flow maps are not suitable for accurate predictions of flow patterns in heated pipes [42]. Dukler and Taitel [29] modified the Taitel and Dukler [27] map for diabatic flows by altering one of the dimensionless flow parameters to account for heating. Kattan et al. [31] used the Steiner [30] map as the basis for a new diabatic two phase flow map by applying various modifications. The most notable of these was the implementation of coordinates of mass velocity (or mass flux) vs. vapour quality, making it simpler to identify and follow the development of flow patterns during the evaporation process at different mass fluxes. It also improved the readability of the map, making it a more useful research and design tool. However, removing the Taitel and Dukler [27] coordinates removed the universal applicability of the flow map. Kattan et al. [31] used their new diabatic flow map to correctly identify 96.2 % of flow pattern data for five refrigerants tested over a wide

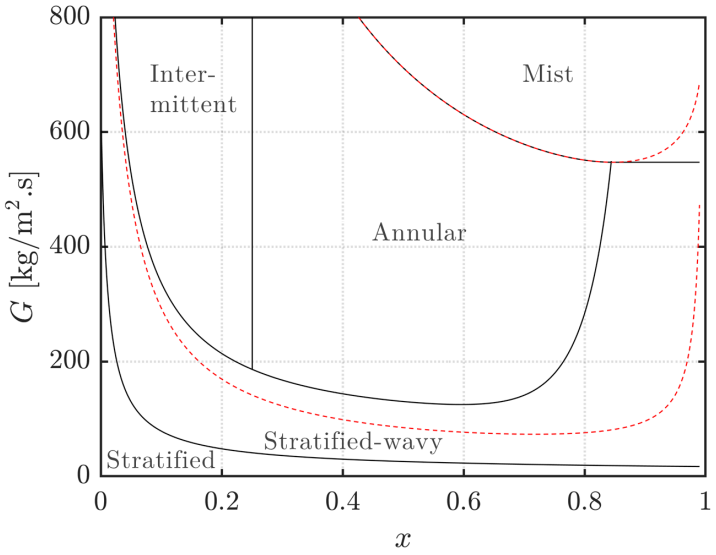


Figure 2.2: Flow pattern map of Kattan et al. [31] (solid black lines) compared to that of Steiner [30] (dashed red lines) for R245fa at $p_{\text{sat}} = 1.7\,\text{bar}$ and the conditions $q = 14\,\text{kW/m}^2$, $G = 330\ \text{kg/m}^2\text{.s}$.

range of pressures, vapour qualities and mass fluxes. A comparison of the Steiner [30] and Kattan et al. [31] flow maps is shown in Fig. 2.2 for a given set of conditions. The map is divided into five different flow patterns: 'stratified', 'stratified-wavy', 'intermittent', 'annular', and 'mist' flow; and the transition lines are calculated based on fluid properties and experimental conditions. The map must therefore be generated for each specific test fluid, saturation condition, pipe diameter and heat flux, so the resulting map takes into account the effect of all of these parameters but is not applicable across multiple data points.

Wojtan et al. [36] later further divided the 'stratified-wavy' class, adding 'slug' as well as 'slug and stratified-wavy' flow patterns to the map. These adjustments gave a more accurate prediction of flow patterns below the wavy flow transitional mass flux, and improved the identification of dryout inception in accordance with experimental data [36, 37]. Kundu et al. [43] reported a reasonably good fit of experimental data for flow boiling of R134a and R407C to the corresponding Wojtan et al. [36] flow map, although the spread of their experimental data highlights the difficulty of determining transition boundaries empirically. An example of the Wojtan et al. [36] flow map is shown in Fig. 2.3.

The calculation procedure for the flow pattern transition lines according to Wojtan et al. [36] begins with calculating the geometrical parameters ε, A_{LD}, A_{VD}, θ_{strat}, h_{LD} and

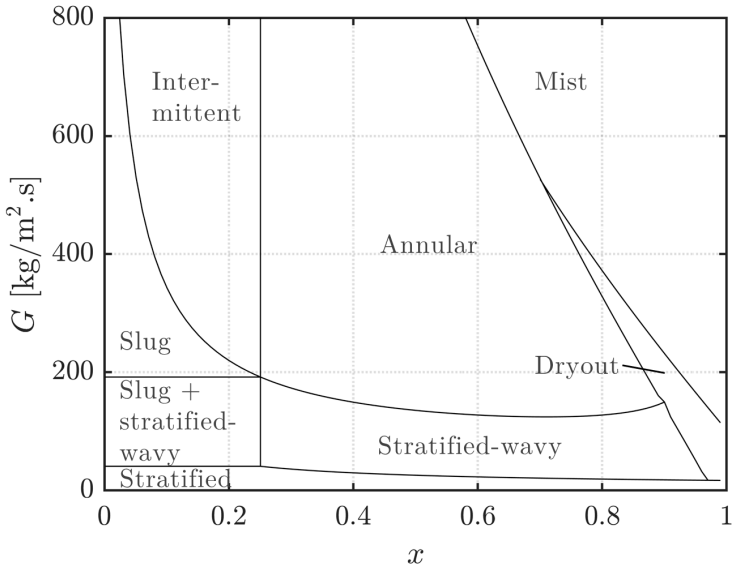


Figure 2.3: Flow pattern map of Wojtan et al. [36] for R245fa at $p_{\text{sat}} = 1.7\,\text{bar}$ and the conditions $q = 14\,\text{kW/m}^2$, $G = 330\ \text{kg/m}^2\text{.s}$.

P_{iD}. ε is the void fraction calculated using the Steiner [44] formulation of the Rouhani and Axelsson [45] drift flux void fraction correlation:

$$\varepsilon = \frac{x}{\rho_{\text{v}}}\left[(1+0.12(1-x))\left(\frac{x}{\rho_{\text{v}}}+\frac{1-x}{\rho_{\text{l}}}\right)+\frac{1.18(1-x)[g\gamma(\rho_{\text{l}}-\rho_{\text{v}})]^{0.25}}{G\rho_{\text{l}}^{0.5}}\right]^{-1} \tag{2.1}$$

The dimensionless liquid and vapour cross sectional areas, A_{LD} and A_{VD}, are defined based on the cross-sectional area of the heated section, A, as:

$$A_{\text{LD}} = \frac{A(1-\varepsilon)}{d_{\text{i}}^2}; \qquad A_{\text{VD}} = \frac{A\varepsilon}{d_{\text{i}}^2} \tag{2.2}$$

The dimensionless liquid height h_{LD} and dimensionless liquid interface length P_{iD} are expressed as a function of the stratified angle θ_{strat}, which can be calculated using an approximation proposed by Biberg [46] in terms of ε to avoid the need for solution by iteration.

$$h_{\text{LD}} = 0.5\left(1-\cos\left(\frac{2\pi-\theta_{\text{strat}}}{2}\right)\right) \tag{2.3}$$

$$P_{\text{iD}} = \sin\left(\frac{2\pi-\theta_{\text{strat}}}{2}\right) \tag{2.4}$$

$$\theta_{\text{strat}} = 2\pi - 2\left\{\begin{array}{c}\pi(1-\varepsilon)+\left(\frac{3\pi}{2}\right)^{1/3}\left[1-2(1-\varepsilon)+(1-\varepsilon)^{1/3}-\varepsilon^{1/3}\right] \\ -\frac{1}{200}(1-\varepsilon)\varepsilon[1-2(1-\varepsilon)][1+4((1-\varepsilon)^2+\varepsilon^2)]\end{array}\right\} \tag{2.5}$$

The vertical intermittent to annular boundary is generally assumed to occur at a fixed value of the Martinelli parameter, $X_{\mathrm{tt}} = \left(\frac{1-x}{x}\right)^{0.875}\left(\frac{\rho_{\mathrm{v}}}{\rho_{\mathrm{l}}}\right)^{0.5}\left(\frac{\mu_{\mathrm{l}}}{\mu_{\mathrm{v}}}\right)^{0.125} = 0.34$, which is solved to give the corresponding vapour quality $x = x_{\mathrm{IA}}$.

The stratified-wavy to intermittent/annular transition line is calculated using the equation proposed by Kattan et al. [31] as follows:

$$G_{\mathrm{wavy}} = \left\{ \frac{16A_{\mathrm{VD}}^3 g d_{\mathrm{i}} \rho_{\mathrm{l}} \rho_{\mathrm{v}}}{x^2\pi^2(1-(2h_{\mathrm{LD}}-1)^2)^{0.5}} \left[\frac{\pi^2}{25h_{\mathrm{LD}}^2}\left(\frac{\mathrm{We}}{\mathrm{Fr}}\right)_{\mathrm{l}}^{-1} + 1 \right] \right\}^{0.5} + 50 \tag{2.6}$$

where the ratio of the liquid Weber and Froude numbers is calculated as $(\mathrm{We}/\mathrm{Fr})_{\mathrm{l}} = gd_{\mathrm{i}}^2\rho_{\mathrm{l}}/\gamma$, γ is the surface tension. Wojtan et al. [36] then divided the stratified-wavy area under this line into three regions such that:

- The slug region is defined as $G > G_{\mathrm{wavy}}(x_{\mathrm{IA}})$;
- The slug + stratified-wavy region meets the criteria $G_{\mathrm{strat}} < G < G_{\mathrm{wavy}}(x_{\mathrm{IA}})$ and $x < x_{\mathrm{IA}}$;
- The stratified-wavy region is then given by $x \geq x_{\mathrm{IA}}$.

The stratified to stratified-wavy transition line is calculated using the equation proposed by Kattan et al. [31]:

$$G_{\mathrm{strat}} = \left\{ \frac{226.3^2 A_{\mathrm{LD}} A_{\mathrm{VD}}^2 \rho_{\mathrm{v}}(\rho_{\mathrm{l}}-\rho_{\mathrm{v}})\mu_{\mathrm{l}} g}{x^2(1-x)\pi^3} \right\}^{1/3} \tag{2.7}$$

with the additional condition that $G_{\mathrm{strat}} = G_{\mathrm{strat}}(x_{\mathrm{IA}})$ at $x < x_{\mathrm{IA}}$.

The transition curves for annular to dryout and dryout to mist were modified by Wojtan et al. [36] to match their experimentally-observed dryout inception point and have the form:

$$G_{\mathrm{dryout}} = \left[\frac{1}{0.235}\left(\ln\left(\frac{0.58}{x}\right) + 0.52\right)\left(\frac{d}{\rho_{\mathrm{v}}\gamma}\right)^{-0.17}\left(\frac{1}{gd\rho_{\mathrm{v}}(\rho_{\mathrm{l}}-\rho_{\mathrm{v}})}\right)^{-0.37} \times \left(\frac{\rho_{\mathrm{v}}}{\rho_{\mathrm{l}}}\right)^{-0.25}\left(\frac{q}{q_{\mathrm{crit}}}\right)^{-0.70} \right]^{0.926} \tag{2.8}$$

$$G_{\text{mist}} = \left[\frac{1}{0.0058} \left(\ln \left(\frac{0.61}{x} \right) + 0.57 \right) \left(\frac{d}{\rho_{\text{v}} \gamma} \right)^{-0.38} \left(\frac{1}{g d \rho_{\text{v}} (\rho_{\text{l}} - \rho_{\text{v}})} \right)^{-0.15} \times \left(\frac{\rho_{\text{v}}}{\rho_{\text{l}}} \right)^{0.09} \left(\frac{q}{q_{\text{crit}}} \right)^{-0.27} \right]^{0.943} \tag{2.9}$$

where the critical heat flux is calculated according to Kutateladze [47]:

$$q_{\text{crit}} = 0.131 \rho_{\text{v}}^{0.5} h_{\text{lv}} (g(\rho_{\text{l}} - \rho_{\text{v}})\gamma)^{0.25} \tag{2.10}$$

Further modifications have been made to the flow map of Wojtan et al. [36] in studies by Cheng et al. [38] and Grauso et al. [39]. Cheng et al. [38] modified the intermittent to annular and annular to dryout transition curves and proposed new dryout to mist transition curves, adding a bubbly flow criterion and developing an updated flow boiling heat transfer model based on their flow map. This new flow map captured their CO_2 flow boiling data very well. Grauso et al. [39] observed that the Wojtan et al. [36] flow map predicted the dryout transition at an erroneously high heat flux, although it showed good agreement with predictions of the slug-intermittent transition. The intermittent to annular transition was found to be dependent on mass flux, which Wojtan et al. [36] had not accounted for. Nasr et al. [48] compared experimental observations of horizontal flow boiling of R-600a to the case-specific flow maps of Wojtan et al. [36] and Kattan et al. [31] and found that they correctly predicted the flow patterns of 77 % and 88 % of experimental results respectively.

Zürcher et al. [49] investigated the application of the Kattan et al. [31] flow map to ammonia boiling in a 14 mm ID horizontal tube. They proposed empirical corrections to the G_{strat} transition curve, which was observed to be too low, and the G_{wavy} transition curve, which was observed to be too high at high vapour qualities. Like Kattan et al. [31], they also grouped the slug + stratified-wavy and slug flow patterns into one section of the map, and stratified-wavy and stratified flow patterns into another section. The modified

Zürcher et al. [49] transition lines are calculated as follows for horizontal tubes:

$$G_{\text{strat}} = \left\{ \frac{226.3^2 A_{\text{LD}} A_{\text{VD}}^2 \rho_{\text{v}} (\rho_{\text{l}} - \rho_{\text{v}}) \mu_{\text{l}} g}{x^2 (1-x) \pi^3} \right\}^{1/3} + 20x \tag{2.11}$$

$$G_{\text{wavy}} = \left\{ \frac{16 A_{\text{VD}}^3 g d_{\text{i}} \rho_{\text{l}} \rho_{\text{v}}}{x^2 \pi^2 (1-(2h_{\text{LD}}-1)^2)^{0.5}} \left[\frac{\pi^2}{25 h_{\text{LD}}^2} (1-x)^{F_1} \left(\frac{\text{We}}{\text{Fr}} \right)_{\text{l}}^{F_2} + 1 \right] \right\}^{0.5} + 50 - 75 e^{-[(x^2-0.97)^2/x(1-x)]} \tag{2.12}$$

where the parameters F_1 and F_2 are empirical coefficients that account for the effect on heat flux on dryout.

It can also be useful to consider specifically the transition from slug/bubble based flow to annular/intermittent type flows, i.e. the G_{wavy} transition line. Ong and Thome [50] defined the transition line as:

$$x_{\text{wavy}} = 0.047 \text{Co}^{0.05} \left(\frac{\mu_{\text{v}}}{\mu_{\text{l}}} \right)^{0.7} \left(\frac{\rho_{\text{v}}}{\rho_{\text{l}}} \right)^{0.6} \frac{\text{Re}_{\text{v}}{}^{0.8}}{\text{We}_{\text{l}}{}^{0.91}} \tag{2.13}$$

where Co is the confinement number, defined as $\text{Co} = (1/d_{\text{i}}) \cdot \sqrt{\gamma/(g(\rho_{\text{L}} - \rho_{\text{V}}))}$.

Costa-Patry and Thome [51] proposed the equation:

$$x_{\text{wavy}} = 425 \left(\frac{\rho_{\text{v}}}{\rho_{\text{l}}} \right)^{0.1} \frac{\text{Bo}^{1.1}}{\text{Co}^{0.5}} \tag{2.14}$$

where the boiling number is defined as $\text{Bo} = q/(h_{\text{lv}} G)$. This transition prediction formed part of a flow pattern-based predictive method for heat transfer in micro-channel boiling flow of several refrigerants including R245fa.

Barbieri et al. [52] assessed the applicability of various flow maps to experimental data for R134a boiling in tubes of 6.2–12.6 mm ID. They found the Kattan et al. [31] flow map to give the best fit but proposed an alternative intermittent to annular transition to the fixed value of x_{IA} used by Kattan et al. [31] and Wojtan et al. [36] given by:

$$G_{\text{IA}} = \frac{(3.75 X_{\text{tt}}^{2.40} \rho_{\text{l}}^2 g d_{\text{i}})^{0.5}}{(1-x)} \tag{2.15}$$

2.1.2 Pressure drop in boiling flows

The pressure gradient in a pipe is composed of the frictional, acceleration and gravitational pressure gradients:

$$\left(\frac{\mathrm{d}p}{\mathrm{d}z}\right) = \left(\frac{\mathrm{d}p}{\mathrm{d}z}\right)_{\mathrm{fric}} + \left(\frac{\mathrm{d}p}{\mathrm{d}z}\right)_{\mathrm{acc}} + \left(\frac{\mathrm{d}p}{\mathrm{d}z}\right)_{\mathrm{grav}} \tag{2.16}$$

In horizontal flows the gravitational pressure drop can be neglected. The spatial acceleration pressure drop can be calculated according to the method of Collier and Thome [18]:

$$\Delta p_{\mathrm{sa}} = G^2 \left\{ \left[\frac{(1-x)^2}{(1-\varepsilon)\rho_{\mathrm{l}}} + \frac{x^2}{\varepsilon \rho_{\mathrm{v}}} \right]_{\mathrm{out}} - \left[\frac{(1-x)^2}{(1-\varepsilon)\rho_{\mathrm{l}}} + \frac{x^2}{\varepsilon \rho_{\mathrm{v}}} \right]_{\mathrm{in}} \right\} \tag{2.17}$$

Many correlations exist for the calculation of two-phase frictional pressure drops, and can be separated into two main groups: homogeneous models and separated flow models. The majority of predictive methods fall into the latter category since the assumptions required for a homogeneous model are not applicable to boiling flows. Although not as widely developed or utilised due to their complexity, other predictive methods follow a phenomenological approach based on the flow pattern. An overview of all three types of method is given in this section.

2.1.2.1 Homogeneous models for two-phase flow

In comparison to two-phase flows, pressure drop in single-phase flows, particularly in simple geometries such as a horizontal pipe, is relatively simple to predict to an acceptable degree of accuracy. It then follows logically that many of the earliest approaches to two-phase pressure drop prediction utilised a homogeneous flow model which is based on the following assumptions:

1. The two phases are thoroughly mixed and may be treated as a single phase;
2. The liquid and vapour phases have equal velocities;
3. The two phases are in thermodynamic equilibrium;
4. A suitable single-phase friction factor can be defined for two-phase flow.

Two-phase pressure drop correlations based on the homogeneous model include those of Cicchitti et al. [53] and McAdams et al. [54], although the model of Beggs and Brill

[55] incorporates inclination angle correction and some consideration of the two-phase flow pattern for a more accurate prediction. More recently, Awad and Muzychka [56] developed a homogeneous model incorporating a new definition of the two-phase viscosity based on an analogy with thermal conductivity of porous media. However, Cioncolini and Thome [57] compared correlation predictions to adiabatic pressure drop data and found that the Awad and Muzychka [56] model gave percentage errors similar to or larger than earlier models. In plain tubes, homogeneous models do not give the most accurate pressure drop predictions [58], and are generally only applicable when the mixing assumption holds, i.e. at high velocities [59], or at high pressures [60].

2.1.2.2 Separated flow models

Separated flow models for pressure drop in two-phase flows consider the phases to be artificially segregated into two single-phase streams. Martinelli and Nelson [61] were the first to apply this separated model, with their work being later simplified and developed into a correlation by Lockhart and Martinelli [62]. Each phase flowing in a channel is assumed to occupy a distinct portion of the cross sectional area, with a frictional pressure drop described by conventional single-phase equations. The method reasons that the total frictional pressure drop in the channel must therefore equal that in both the liquid and vapour phases, which are each the product of a single phase pressure drop for that phase alone and a two-phase multiplier, i.e.

$$\Delta p_{\text{fric}} = \Delta p_{\text{fric,i}} \cdot \Phi_{\text{i}}^2 \tag{2.18}$$

where $\Delta p_{\text{fric,i}}$ is the frictional pressure drop of phase 'i' and Φ_{i} is the relevant two-phase multiplier.

However, the Lockhart and Martinelli [62] model does not accurately predict two-phase pressure drop and has been subsequently modified by many researchers. Grönnerud [63] expanded this approach further to specifically cover refrigerants, obtaining good results for some fluids and flows [64, 65]. However, the Grönnerud [63] model did not account for surface tension effects and was modified by Friedel [66] to fit a large experimental database. The resulting model has the form:

$$\phi_{\text{L,total}}^2 = A_1 + \frac{3.24 A_2 A_3}{\text{Fr}^{0.045}\text{We}^{0.035}}, \tag{2.19}$$

where A_1, A_2 and A_3 are empirical functions of the vapour quality and individual phase densities, viscosities and friction factors.

The extensive basis for the model means the Friedel [66] method is often found to be one of the most reliable for pressure-drop predictions for refrigerant flows over a wide range of conditions [67, 68]. However, large deviations have been reported for air-water applications [69], since the surface tensions of refrigerants and water are significantly different, and the small exponent of the Weber number does not address this. Also, it is not generally recommended for applications with high liquid to gas viscosity ratios (i.e. $\mu_{\mathrm{L}}/\mu_{\mathrm{V}} > 1000$) [70, 71], or at low vapour qualities [71]. Various authors have made further modifications to these correlations in order to improve their applicability to specific fluids and geometries (e.g. [72, 73]).

To address the shortcomings of the Friedel [66] model, Müller-Steinhagen and Heck [71] proposed a separated flow correlation based on the pressure drops of the respective single phase flows, creating an empirical extrapolation between liquid and vapour frictional pressure drops using the Blasius friction factor formula that is applicable for $0 < x < 1$. The correlation provides good predictions across different pipe diameters [68, 72] and for a wide range of refrigerants [64]. Xu and Fang [72] improved the Müller-Steinhagen and Heck [71] correlation for small diameter channels by introducing the Laplace constant La to account for surface tension and gravitational influences, proposing a frictional pressure drop equation of the form

$$\Delta p_{\mathrm{fric}} = \{Y^2 x^3 + (1-x)^{1/3}[1 + 2x(Y^2 - 1)]\}[1 + 1.54(1-x)^{0.5}\mathrm{La}^{1.47}] \tag{2.20}$$

where $Y = \sqrt{(\Delta p/\Delta L)_{\mathrm{v}}/(\Delta p/\Delta L)_{\mathrm{l}}}$ determined using the Fang et al. [74] friction factor.

2.1.2.3 Flow pattern-specific models

Although not as widely developed or utilised due to their complexity, other predictive methods follow a phenomenological approach based on the flow pattern.

Chawla [75] was an early developer of flow pattern-specific pressure drop models. Their work led to the VDI-Wärmeatlas method [76], an empirical separated flow model defining two flow types: dispersed vapour phase and continuous vapour phase. However, large deviations for this correlation in comparison to experimental data were reported [71]. The Chawla [75] method was extended by Olujic [77] for application to high vapour

and low liquid velocity conditions, giving a new correlation of the form

$$\left(\frac{\Delta p}{\Delta L}\right)_{\text{fric}} = \left(\frac{\Delta p}{\Delta L}\right)_{\text{v}} \left[1 + \frac{(1-x)}{x\varphi(\rho_{\text{L}}/\rho_{\text{V}})}\right]^{2.375} \tag{2.21}$$

where φ is the two phase flow parameter given by Olujic [77] and is a function of various independent variables including mass flux, vapour quality and pipe diameter. In their assessment of experimental data against two phase pressure drop predictions, Ferguson and Spedding [78] found that the Olujic [77] correlation had particular value for wavy, slug and annular flow patterns. However, an analysis of pressure drop predictions by Odeh et al. [12] for DSG collectors specifically found that the Martinelli and Nelson [61] correlation gave better agreement with experimental data than that of Olujic [77].

Bandel [79] divided two phase flow into three regions: annular flow, stratified flow and the transition region. They then developed separate pressure drop equations for each region, but the applicability of this method is limited for flow boiling since it does not account for the interfacial structures between regimes. Müller-Steinhagen and Heck [71] recommended the Bandel [79] correlation for accuracy, but criticised its lengthy and complicated application, lauding their own correlation as being more convenient whilst maintaining sufficient accuracy.

Quibén and Thome [80] undertook a comprehensive review of existing two-phase pressure drop correlations and concluded that none of them gave adequate predictions of experimental data, since they each exhibit some or all of the following deficiencies:

- Flow pattern effects are not accounted for, yet these are particularly important at low flow rates where stratification effects are significant, and at high vapour qualities where dryout effects are significant.
- The influence of interfacial waves is not explicitly accounted for.
- The upper dry perimeter in stratified flows is not accounted for.
- The introduction of the local void fraction into the method neglects the use of actual phase velocities.
- Annular flows are represented by tubular flow expressions.
- The peak (or its location or magnitude) in the pressure gradient at high vapour

qualities is not captured, and the pressure gradient trend against vapour quality is not well represented.

- They do not extend across an acceptable range of vapour qualities.

To address these deficiencies, Quibén and Thome [81] developed a new two-phase frictional pressure drop prediction method, taking the interfacial structure between phases into account by following a phenomenological approach. They used the flow map of Wojtan et al. [36] to provide the corresponding interfacial structure and developed a model that treats each flow pattern separately whilst ensuring a smooth transition at the interface. Interfacial phenomena were incorporated through an interfacial friction factor which is calculated uniquely for each flow pattern. A comparison of this new model to the experimental database concluded that it is successful in predicting the pressure drop and capturing the various trends in the data. However, this is a much more complicated model to use than those of Martinelli and Nelson [61] and Müller-Steinhagen and Heck [71], which have been shown to provide adequate pressure drop predictions for boiling flows at the conditions in DSG collectors [12, 82], subject to acceptance of a certain degree of deviation. When using two-phase pressure drop models there is thus a trade off between the easy implementation but lower accuracy and varying applicability of empirical models, and the complicated nature but elevated accuracy and applicability of a phenomenological model based on flow patterns.

2.1.3 Heat transfer coefficient in boiling flows

The heat transfer coefficient in boiling flows has the form:

$$h = \frac{q}{T_{\text{wall}} - T_{\text{sat}}} \tag{2.22}$$

where q is the heat flux applied to the pipe walls. Various predictive methods for this heat transfer coefficient exist in the literature, and those applicable to boiling flow are discussed in this section.

2.1.3.1 Flow boiling mechanisms

As discussed in Section 2.1.1, various flow patterns develop as liquid boils in a horizontal tube. During this development, the heat transfer is governed by different mechanisms.

Whilst the flow is entirely in the liquid phase, heat transfer occurs by single phase convective heat transfer to the liquid phase, which may be described by standard convective heat transfer models as temperature of the liquid rises towards its saturation temperature. Bubbles will first start to appear before the bulk flow temperature reaches the saturation point, in a regime known as subcooled nucleate boiling. Eventually, the bulk flow will reach the saturation temperature and the heat transfer mechanism becomes that of saturated nucleate boiling. Here, the bulk flow temperature remains constant at the saturation temperature and an ever-increasing amount of vapour forms. If a vapour core is formed the flow will enter the annular flow regime, where the heat transfer mechanism is forced convective heat transfer through the liquid film. Subsequently, dryout occurs and heat transfer is by convection to either the liquid or the vapour, depending on the wall wetting. There is a large difference in heat transfer coefficient between wetted and non-wetted areas of a tube, and if a stratified flow pattern develops this results in an asymmetrical heat transfer between the top and the bottom of the tube.

2.1.3.2 Pool boiling correlations

The heat transfer behaviour in the nucleate boiling zone can be described by pool boiling correlations. These are not a function of vapour quality or mass flux, so should not be affected by the large proportional uncertainties these parameters introduce in flow boiling correlations, but are simply dependent on the fluid and pipe properties, and on empirical constants. The thermophysical property-based method of Stephan and Abdelsalam [83] was developed using data for pool boiling of a range of fluids including water, refrigerants, hydrocarbons and cryogenic fluids, with different sets of dimensionless numbers employed for heat transfer coefficient prediction in each fluid group. However, Halon et al. [84] found this correlation to give a poor prediction of heat transfer coefficient for pool boiling of R245fa on a heated plate, finding deviations of up to 157 % and suggesting that it overestimates the effects of heat flux and saturation temperature.

Other correlations are based on reduced pressure ($p_{\mathrm{red}} = p_{\mathrm{sat}}/p_{\mathrm{crit}}$) to avoid the uncertainties involved in the estimation of thermophyscial properties. Gorenflo [85] developed such a method in which a reference heat transfer coefficient is scaled according to the ratios of desired conditions to a set of reference conditions for reduced pressure, surface temperature and heat flux. However, this method is dependent upon an accurate ref-

erence heat transfer coefficient for the fluid in question, and the list of fluids for which reference values are provided is by no means exhaustive. Gorenflo and Kenning [86] provided a modified and improved version of the [85] correlation, but this is still dependent on several fluid specific correction factors and reference values.

The Cooper [87] correlation follows a similar approach by utilising the reduced pressure, molecular weight and surface roughness, but uses empirically determined multipliers and exponents rather than scaling from reference values. This approach still requires accurate knowledge of the surface roughness, although the reader is advised to use a value of 1 µm when it is not known definitively. Other authors [18] have recommended the Cooper [87] correlation for applications in which the thermophysical fluid properties are not well-defined, but the lack of experimental validation across a wide range of conditions results in large uncertainties.

Ribatski and Jabardo [88] developed a correlation in a very similar format to that of Cooper [87], but incorporated an empirical constant that accounts for the effects of the pipe material. They listed values of this constant for brass, copper and steel, which are the most commonly used pipe materials in flow boiling experiments. The correlation of Mostinski [89] did not include surface roughness in its calculation, instead depending solely on the reduced pressure and heat flux.

Jung et al. [90] proposed a correlation that was based on those of Cooper [87] and Stephan and Abdelsalam [83] but incorporated thermophysical properties into the equation. They tuned the empirical constants based on data for 8 different refrigerants across a range of vapour pressures and achieved a mean deviation of less than 7 % when comparing the resulting correlation to their data set.

2.1.3.3 Flow boiling correlations

Methods for predicting the two-phase (tp) heat transfer coefficient in boiling flows typically consider the contributions of the two thermal mechanisms of nucleate boiling (nb) and convective boiling (cb) in the following format:

$$h_{\mathrm{tp}} = \left[(S h_{\mathrm{nb}})^n + (F h_{\mathrm{cb}})^n \right]^{1/n} \tag{2.23}$$

where S and F are multipliers of the nucleate and convective boiling terms respectively. Typically, it is the calculation of these multipliers and the value of n that differ between

correlations.

The Chen [91] correlation forms the basis of many more recent predictive methods, and sets $n = 1$ in Eq. 2.23 to use both nucleate and convective boiling contributions in a superposition approach. This correlation is widely validated and recommended, but has a number of limitations, the most significant of which for this review being that it is only valid for vertical flow. Shah [92] used a large amount of experimental data from multiple studies to improve the Chen [91] correlation and extend its validity to horizontal flow boiling. This was achieved through the introduction of various criteria and adoption of an enhancement-factor approach, whereby effectively $n \to \infty$ and Eq. 2.23 yields the larger of the two h values. A Froude number criterion was employed to determine whether the wall is wetted, and a convection number, similar to the Lockhart-Martinelli parameter, used to determine whether the boiling mechanism is purely nucleate or convective. The boiling number was also introduced to the convective term. The Shah [92] correlation has been reported to give good predictions for R245fa boiling [93] and condensation [94] in horizontal pipes.

Kandlikar [95] further developed the Shah [92] model, simplifying the implementation and modifying the nucleate to convective boiling transition criteria. They introduced the fluid specific parameter F_{fl} to the nucleate boiling term to improve the fit to a flow boiling database of over 5000 data points for ten different fluids. The resulting correlation gave mean deviations of 15.9 % and 18.8 % for water and refrigerant data respectively, which are lower than those of other correlations, but not significantly. However, the Kandlikar [95] model is one of the most widely used enhancement factor-type correlations, although various others have been developed more recently to fit new experimental data sets [96–98].

Some models employ an enhancement-factor approach, whereby effectively $n \to \infty$ and Eq. 2.23 yields the larger of the two h values. These models include a method for determining the larger h and an appropriate multiplier. An early example of this is the Shah [92] correlation which offered an improvement on that of Chen [91] when applied to horizontal tubes and has been reported to give good predictions for R245fa boiling [93] and condensation [94]. Kandlikar [95] further developed the Shah [92] model, simplifying the implementation and modifying the nucleate to convective boiling transition criteria. This model is one of the most widely used enhancement-factor-type correlations, although

various others have been developed more recently [96–98].

Gungor and Winterton [99] also developed a correlation based on the Chen [91] method. They discarded the convection number discretisation in the Shah [92] correlation but employed a similar Froude number criterion similar to account for situations in which the horizontal tube wall is not wetted, specifying additional multipliers for the convective and nucleate boiling terms that are functions of Froude number. They also replaced the convective boiling factor F from the Chen [91] correlation with the factor E, which is an empirical function of the boiling number and the Lockhart-Martinelli parameter. Gungor and Winterton [99] compared their, and other, correlations to an experimental databank and found that their correlation gave predictions of a similar accuracy to that of Shah [92], although their correlation requires fewer calculations and is thus simpler to implement. Guo et al. [93] reported this to be the most accurate of eight common correlations when applied to R245fa boiling in a 10 mm ID horizontal tube.

Setting $n > 1$ in Eq. 2.23 results in an asymptotic approach to two-phase heat transfer coefficient prediction. Liu and Winterton [100] were early adopters of such an approach using similar multipliers to Gungor and Winterton [99]. They discarded the boiling number in order to allow application to subcooled boiling, introducing instead a Prandtl number dependence, but obtained similar accuracies to Kandlikar [95]. Wattelet et al. [101] developed a two-phase multiplier for the convective term using a modified Lockhart-Martinelli parameter, and used a Froude number correction similar to that of Gungor and Winterton [99] to account for a decrease in the available heat transfer area in stratified wavy flow at low mass flux. They reported that the resulting correlation predicted annular and stratified-wavy data well. Yuan et al. [102] also developed an asymptotic model for annular flow specifically, whilst Guo et al. [103] modified the Liu and Winterton [100] correlation for boiling flows of R245fa and an R134a/R245fa mixture in smooth horizontal tubes of 3 mm inside diameter.

Numerous studies have since compared the predictions of the aforementioned correlations with experimental data with varying results. Lee et al. [104] conducted experiments with hydrocarbon refrigerants and R22 inside horizontal copper tubes with inside diameters 9.5 and 12.7 mm and compared their heat transfer data to the correlations of Shah [92], Kandlikar [95] and Gungor and Winterton [99], with the Kandlikar [95] correlation providing the best predictions. Wang et al. [105] compared experimental data for propane

boiling in 6 mm ID horizontal copper tubes to various well-known correlations, including those of Shah [92] and Kandlikar [95], and concluded that the Liu and Winterton [100] correlation gave the best predictions with a mean absolute relative deviation below 10 %. Nasr et al. [48] performed experiments with R600a in a 8.7 mm ID horizontal copper tube and recommended the Gungor and Winterton [99] correlation above others. Even in these relatively similar experimental studies the most accurate heat transfer correlation is not always the same, indicating the difficulty of selecting an appropriate predictive method. Often experimental studies will compare a number of correlations and select the best fit for further modification and empirical tailoring to the data.

2.1.3.4 Flow pattern-specific heat transfer models

Other investigators have attempted to develop models valid for a wider range of conditions through a flow pattern-based approach, since flow pattern can have a significant effect on flow boiling heat transfer. Across the intermittent flow regime the heat transfer coefficient will increase with vapour quality, but this effect is typically more pronounced in the annular regime as the vapour core develops [33]. When partial dryout occurs and the flow pattern moves to stratified-wavy the heat transfer coefficient drops sharply and continues to decrease towards a fully vapour flow. Heat transfer is best in annular flow where the wall is completely wetted, and a peak in heat transfer coefficient occurs at the onset of partial dryout. In reality, the heat transfer coefficient will vary circumferentially around the tube, most significantly in stratified flow patterns where there is liquid in the bottom of the pipe and vapour in the top, and the liquid heat transfer coefficient is larger. There will also be circumferential variations in the annular flow regime, since gravitational effects result in a thicker annulus at the bottom of the tube than the top.

Whilst some of the correlations discussed in Section 2.1.3.3 attempted to account for the effects of a stratified flow pattern, they are typically empirical and do not include any flow pattern information [106]. In particular, the Froude criterion employed by some correlations is not effective in predicting the onset of stratified flow patterns in horizontal tubes. Therefore, more recent research has attempted to develop flow pattern-based heat transfer models. The first comprehensive model was put forward by Kattan et al. [33] utilising their flow map [31] and the asymptotic heat transfer model of Steiner and Taborek [107]. The model uses the flow map to identify the local flow pattern, then

provides methods for calculating the heat transfer coefficients in the annular, intermittent, stratified-wavy and stratified flow regimes. Such a model requires a parameter linking the stratified and stratified-wavy flow configuration to that of annular flow. Defining a stratified angle, θ_{strat} and a dry angle, θ_{dry}, is a convenient way to do this, where it is assumed that in the stratified-wavy regime a thin liquid film of uniform thickness partially wets the tube. The calculation of the heat transfer coefficient for each flow pattern is then based on this definition of the flow structure, along with the void fraction and flow characteristics. Intermittent flow is modelled as annular flow, since the authors found similar heat transfer coefficient vs. vapour quality data trends for the two flow patterns. This model was developed for flow boiling of pure R134a and R123 and other refrigerant mixtures in horizontal tubes of 10.9 and 12.0 mm ID, although the database did not include heat transfer coefficient data for the stratified, bubbly or mist flow regimes.

Zürcher et al. [49] found the Kattan et al. [33] method to give accurate predictions when applied to the boiling of ammonia in horizontal tubes, but later added a new criterion for the onset of nucleate boiling informed by their flow boiling experiments with R134a, R407C and ammonia [34]. They also showed that the heat transfer coefficient predictions for the stratified wavy regime were not as accurate as those for the annular regime.

Wojtan et al. [37] used their new flow pattern map [36] to modify the dry angle calculation and obtained significant improvements in the heat transfer coefficient prediction in the stratified wavy regimes compared to their experimental data for boiling of R22 and R410A in horizontal tubes. They also extended the model of Kattan et al. [33] by developing new predictive methods for heat transfer in the dryout and mist flow regimes. Cheng et al. [38] further extended the model of Wojtan et al. [37] for flow boiling of CO_2.

2.2 Experimental investigations of boiling flows

2.2.1 Overview of experimental flow boiling studies

Many experimental studies have been undertaken to investigate flow boiling in horizontal tubes. A selection of such studies from recent decades are summarised in Table 2.2, and the results from a number of these have already been discussed in Section 2.1. Table 2.2 provides a representative snapshot of the flow boiling literature, and an effort has been made to avoid duplication of works using the same test facility, combining entries where

possible. In many of these studies, heat transfer and pressure drop data were collected to validate, modify and improve upon existing flow pattern maps and predictive correlations. The studies included in Table 2.2 are limited to those involving macro-scale pipes, i.e. $d_i > 3\,\text{mm}$ [14], since the flow-governing phenomena are different at smaller scales where gravity is not significant. The boiling heat transfer mechanism can also be affected by the pipe size; in a 7.49 mm inside diameter pipe, Balachander et al. [108] found nucleate boiling to be dominant, whilst in a 38.5 mm inside diameter pipe Zhang et al. [109] found convective boiling to be dominant and suggested that this may be due to the larger pipe size. Passos et al. [110] also found that the dominant heat transfer mechanisms in pipes of inside diameters of 6.5 mm and 10.7 mm were nucleate boiling and convective boiling, respectively.

A large amount of research has been conducted into the flow boiling of refrigerants for use in refrigeration systems. Studies into water boiling have been mainly focussed on subcooled boiling, and are not included in Table 2.2, although the rise of DSG PTC technology has encouraged more experimental research into water flow boiling [42, 109]. There is much variation in test section length in the studies in Table 2.2. Jung et al. [111] state that a long test section is necessary to eliminate entry-length effects and to take measurements over a range of vapour qualities. They do not give quantitative guidance on what constitutes 'long' but their test section had a length to inside diameter ratio of 880. Cho and Tae [112] found that the effect of flow disturbance from the inlet on heat transfer disappeared after a length of 48 diameters, although this study was for microfin tubes. A number of the studies used a preheater to partially evaporate the flow before the test section; this reduces the heated test section length necessary to achieve a given vapour quality at the outlet, but the two phase flow at the inlet may require a longer development length. Test sections were heated electrically or by some form of heat exchanger. Electric heating supplies a constant heat flux to the pipe wall, and therefore to the test fluid, and is a convenient method of doing so. The counter-current double pipe, or tube in tube, heat exchanger was recommended by Kattan et al. [33] as the preferred heating method for realistic study of the heat transfer coefficient for boiling of a refrigerant mixture, which is likely to be why a number of researchers have chosen this method. Also, Shin et al. [113] suggested that electrical heating is not appropriate for stratified flows or flows with partial dry out.

Most of the studies in Table 2.2 used multiple thermocouples or platinum resistance thermometers to measure the outside temperature of the test section pipe wall. Often these were arranged in a number of stations along the length of the test section, with multiple thermocouples circumferentially at each station, the most common arrangement of which being four thermocouples at 90° intervals around the pipe. Alternatively, Hardik et al. [65] used an infrared thermal camera to measure wall temperature which has the advantage of providing local temperature measurements with high spatial and temporal resolution but is much more difficult and costly to implement than thermocouples. The pressure drop along and mass flow rate through the test sections were also measured in most of the studies, with test section inlet and outlet conditions also recorded.

The test fluids of choice in the studies in Table 2.2 have changed over time with the introduction of new, less environmentally damaging, refrigerants. R245fa is one of these newer refrigerants and is attracting increasing research interest due to its dominance [114] as a working fluid in organic Rankine cycle (ORC) systems for the generation of electrical power from low-temperature thermal energy sources [1, 2] such as solar heat [3, 4], or for waste heat recovery [5, 6]. However, there is a relative scarcity of data in the literature for R245fa boiling in macro-scale pipes, with the majority of R245fa studies to date focussing on mini- and micro-channels [115–118], vertical tubes [119], or condensation [120, 121].

Table 2.2: Summary of experimental flow boiling studies in horizontal macro-scale pipes.

Study	Test fluid	d_i mm	Test length m	Pipe material	Heating method	Test section inlet	Mass flux kg/m^2 s	Heat flux kW/m^2	Visualisation
[111, 122, 123]	R22/R114, R12/R152a	9.1	8 (2× 4 m + U-bend)	Stainless steel	Electrical - DC current	Subcooled liquid	250-720	10-45	Sight glasses
[113]	R22, R32, R134a, R290, R600a, R32/R134a, R290/R600a, R32/R125	7.7	5.9	Stainless steel	DC heating	Two-phase (x = 0-0.4)	265-583	10-30	Sight glasses
[124]	R22/R407C	6.5	1.3	Not specified, 'smooth'	Double pipe heat exchanger, water	Two-phase	100-400	5-20	Sight glass + microcamera
[31–33]	R134a, R123, R402a, R404a, R502	10.92, 12	2 × 3.013	Copper	Double pipe heat exchanger, water	Two-phase	100-300	4-25	Sight glasses + video
[125]	R32, R134a, R32/134a, R407C	7.75	5.9	Stainless steel	DC heating	Two-phase	240-1060	4-30	None
[126]	Isceon 59, R407C and R404A	9.52 (OD)	4	Copper	Double pipe heat exchanger, water	Subcooled liquid	270-310	27-42	Sight glasses
[127]	R404a, R407c	12.7	2	Copper	Electrical tape heating	Two-phase	100-300	5-20	Sight glasses

Study	Test fluid	d_i mm	Test length m	Pipe material	Heating method	Test section inlet	Mass flux kg/m^2 s	Heat flux kW/m^2	Visualisation
[34, 49]	R134a, R407C, ammonia	10.92, 12	2 × 3.013	Copper	DC heating	Two-phase	100-300	2-5	Sight glasses + video
[110]	R407C	6.5, 10.7	1.5	Copper	Electrically heated brass shell	Two-phase	200-300	10, 20	None
[97, 128]	R22, R134a, R410a, R404a, R407c, R507, R417a	6	6	Stainless steel	DC heating	Saturated liquid	200-1100	3.5-47	Sight glasses + video
[36, 37]	R22, R410a	8, 13.84	2.035, 2.026	Copper	Double pipe heat exchanger, water	Two-phase	70-300	21-57.5	Glass tube with laser sheet + CCD camera
[129]	R22, R134a, R125, R410a	8	1.6	Not specified	Double pipe heat exchanger, water	Two-phase	200-600	9-53	None
[108]	R134a, R404a	7.49	10	Copper	Double pipe heat exchanger, acetone	Saturated liquid	57-102	4-18	None
[39]	R1234ze(E), R134a	6.0	0.78	Stainless steel	DC heating	Two-phase	146-530	5.0-20.4	Visualisation section + high-speed video
[105]	Propane	6	1.55	Copper	Thin-film electric heaters on tube surface	Two-phase	62-104	11.7-87.1	Sight glasses
[43]	R134a R407C	7	1.2	Copper	Flexible heating wire	Two-phase	100-400	3-10	Sight glasses

Study	Test fluid	d_i mm	Test length m	Pipe material	Heating method	Test section inlet	Mass flux kg/m^2 s	Heat flux kW/m^2	Visualisation
[130]	R1234ze(E), R600a, L-41b	8	2.4	Copper	Electrical heating tape	Two-phase	200-400	5-10	None
[48]	R600a	8.7	1.1	Copper	Electrical resistance heaters	Two-phase	130-180	10-27	Sight glass with illumination
[69, 131]	R600a, R1234ze(E)	6	4 × 0.05	Copper	Thin-film electric heaters on copper blocks around tube	Two-phase	67-258	10.6-75	Sight glasses
[65]	R123	5.5, 7.5, 9.5, 12	0.5, 1	Copper	DC heating	Subcooled liquid	262-1650	25-337	Sight glass
[132]	R134a	5	2.035	Stainless steel	Joule effect	Subcooled liquid	200-400	3.9-47	Sight glass
[133]	R134a	8.62, 9.52	1.1	Copper	Resistance wire	Two-phase	290-381	10-15	Sight glass
[134]	R1234yf	3.2, 4.8, 6.4, 8.0	Copper	Resistance wire	Two-phase	200-400	0-14	None	
[135]	R245fa	10	2	Stainless steel	Joule effect	Two-phase	192-386	10-36	Visualisation section + high-speed camera
[136]	R32	6.0, 8.0	0.2	Stainless steel	DC heating	Two-phase	146-507	2.4-41.2	None

Study	Test fluid	d_i mm	Test length m	Pipe material	Heating method	Test section inlet	Mass flux kg/m^2 s	Heat flux kW/m^2	Visualisation
[137]	R245fa	5.8		Copper	Electrical heating	Two-phase	50-240	5.65-14.87	Sight glass + high-speed camera
[93]	R134a, R245fa, R134a/R245fa	10	2	Copper	Electrical heating wire	Two-phase	100-300	6-24	None

2.2.2 Optical measurement techniques in boiling flows

A number of the studies in Table 2.2 employed sight glasses at one or both ends of the test section to observe flow patterns, sometimes combined with a camera to capture photographs or videos of the flow. Nasr et al. [48] used a flow pattern visualisation method developed by Jassim et al. [138] where a diffuse white film pigmented with evenly spaced black stripes is placed behind the sight glass and illuminated with a stroboscope, and images are captured by a web camera. Wojtan et al. [36, 37] illuminated a cross-section of the flow with a laser sheet and recorded high-speed images from which they detected the vapour-liquid interface and thus extracted information on the dry angle and void fraction using a method developed by Ursenbacher et al. [139]. Aside from these works, the studies in Table 2.2 have taken relatively simple measurements. There has been no attempt to measure detailed velocity profiles of the flow, local temperatures of the flow itself or film thicknesses. Laser-based optical measurement techniques could be employed to take such measurements, although such techniques have not been widely applied to boiling flows, particularly under saturated boiling conditions.

Estrada-Perez and Hassan [140] employed particle tracking velocimetry (PTV) to investigate turbulent subcooled boiling in vertical rectangular channels with a hydraulic diameter of 10 mm. In PTV, the flow is seeded with reflective particles and illuminated by a laser sheet, with high-speed images of the illuminated region captured by a high-speed camera. The motion of individual particles is then tracked between frames to provide a measurement of the velocity field in the fluid. Estrada-Perez and Hassan [140] used such measurements to calculate flow properties such as velocities, turbulence intensities and Reynolds stresses. Hassan et al. [141] developed the experimental techniques further by using infrared thermography alongside PTV. In infrared thermography, an infrared camera is used to measure the temperature field, usually of the heated wall rather than the flow itself. This allows for calculation of local heat transfer coefficients with high spatial and temporal resolution, and Hassan et al. [141] combined the two techniques to assess the impact of heating on the Reynolds stresses.

Su et al. [142] and Kossolapov et al. [143] also applied infrared thermometry techniques to subcooled boiling flows specifically to investigate the impact of surface roughness on the boiling process. The resulting temperature and heat flux distributions obtained using a high-speed infrared camera could be correlated to bubble nucleation sites using corre-

sponding images from backlit high-speed video of the surface. Particle image velocimetry (PIV) is a laser-diagnostic technique similar to PTV, but the flow is seeded with particles at a much higher density and the mean displacement of groups of particles between frames is tracked to provide an estimate of the velocity field. Particle image velocimetry (PIV) has been used in pool boiling experiments alongside IR thermometry [144] to provide detailed measurements of the phase, temperature and velocity fields on and above the boiling surface. Such measurements provide a useful benchmark for nucleate boiling simulations. Voulgaropoulos et al. [145] combined PIV and PTV with infrared thermometry and two-colour laser-induced fluorescence (2cLIF) to investigate the velocity and temperature fields around a bubble during its nucleation. In laser induced fluorescence techniques a fluorescent dye is typically added to the flow, which is then excited using a laser at the appropriate wavelength. A high-speed camera is used to capture the fluorescence and the resulting images can be processed to provide data on phase distribution [146], temperature fields [147] or local component concentration [148] depending on the specific experimental aims and set-up. Voulgaropoulos et al. [145] were able to obtain detailed spatio-temporally resolved measurements of the temperature and velocity fields, and observe the coupling of these during a bubble nucleation event.

Whilst there is little evidence in the literature of application of laser-based diagnostic techniques described in this section to horizontal boiling flows in horizontal pipes, these methods have been employed successfully to investigate two-phase flows in similar geometries. Morgan et al. [149] used high-speed simultaneous planar laser-induced fluorescence (PLIF), PIV and PTV to obtain detailed spatiotemporally resolved measurements of flow characteristics of two-phase liquid-liquid flows in a horizontal transparent circular tube of 27.6 mm ID. Measured values included phase distribution, in-situ phase fraction, interface level and droplet size distribution, and measurements were made for different flow regimes, including stratified and dispersed flow.

Zadrazil et al. [150] and Zadrazil and Markides [15] used PLIF and a combination of PIV and PTV techniques to study isothermal downwards co-current gas-liquid flows in annular flow in a 32.4 mm ID pipe. Velocity fields and kinetic energy profiles in the liquid film, and data on the film thickness, interface and wave statistics, and gas entrainment into the liquid were obtained. The annular flows studied had liquid Reynolds numbers in the range 306 to 1532 and gas liquid numbers in the range 0 to 84 600. Cherdantsev

et al. [17] developed a brightness-based laser-induced fluorescence (BBLIF) technique to measure the film thickness in annular flows in the same facility, comparing the results to measurements taken using a conventional PLIF technique.

Charogiannis et al. [151] presented a 'thermographic particle velocimetry' technique capable of the simultaneous measurement of two-dimensional surface temperature and velocity at the interface of multiphase flows. The flow was seeded with highly reflective particles of a different emissivity to the fluid, and the signals from the particles were captured using an infrared camera. The technique was developed for the study of gravity-driven liquid-film flows over inclined heated substrates, but could be applied to any flow with a sufficient density difference between the two phases.

2.3 Numerical investigations towards boiling flows

There are not a large number of studies in the literature regarding flow boiling in macro-scale channels due to the computational complexity of such a case where heat transfer, phase change and often turbulence must be considered. There is more work available on flow boiling in micro-channels, driven by applications in removal of high heat fluxes from micro-electronic devices, although availability of experimental data with which to compare these models is low due to the difficulty of obtaining quantitative measurements of velocity fields in the micro-scale. In some studies, flow boiling has been approached from the case of evaporation of a vapour bubble in a liquid flow [152–155]. As such, the theoretical and numerical study of elongated bubbles will be discussed in the following section, with a view to reaching a complete flow boiling model by adding the necessary degrees of complexity to an adiabatic elongated bubble flow.

2.3.1 Elongated bubble flow

As well as providing a start point for flow boiling simulations in this work, elongated bubble flow in liquid-filled channels is relevant to a wide variety of industries, being of interest in a range of heat and mass transfer as well as lubrication problems. The research on elongated bubble flow problems is motivated by applications such as treatment of pulmonary disorders, enhanced oil recovery [156], boiling flows in refrigeration [157] and concentrating solar power [158].

2.3.1.1 Adiabatic bubble flow

In adiabatic bubble flows, an elongated bubble travels at a speed U_b in a channel in which liquid flows at an average velocity U_l (with $U_\mathrm{b} > U_\mathrm{l}$), and has density, viscosity and surface tension of ρ_l, μ_l, and γ, respectively. The flow can be characterised by the following dimensionless numbers: the Reynolds number $\mathrm{Re} = \rho_\mathrm{l} U d/\mu_\mathrm{l}$, where d is the diameter of the circular cross-section of the channel with corresponding radius $r = d/2$, which describes the relative magnitudes of the inertial and viscous forces; the capillary number $\mathrm{Ca} = \mu_\mathrm{l} U/\gamma$, which describes the relative magnitude of the viscous and interfacial tension forces; and the Bond number $\mathrm{Bo} = \rho_\mathrm{l} g r^2/\gamma$, where g is the gravitational acceleration, which describes the relative magnitude of the buoyancy and interfacial tension forces. Elongated bubble flow has been widely studied in micro-channels, where inertial and buoyancy effects are often negligible, i.e. $(\mathrm{Bo}, \mathrm{Re}) \ll 1$. In this regime, an axisymmetric liquid film separates the bubble from the tube wall. Bretherton [159] developed the classical theoretical prediction of the thickness of this liquid film, applying lubrication theory to find that, for flows where $(\mathrm{Ca_b}, \mathrm{Re_b}) \ll 1$ (and neglecting buoyancy effects), the liquid film thickness h scales with $\mathrm{Ca_b}^{2/3}$ as follows:

$$H = h/r = 1.34\mathrm{Ca_b}^{2/3} \tag{2.24}$$

where H is the film thickness non-dimensionalised by the characteristic length of the channel cross-section, the radius r for a circular capillary. Taylor [160] carried out experiments at higher $\mathrm{Ca_b}$ using very viscous fluids and found that as $\mathrm{Ca_b} \to 2$, H approaches an asymptotic value of approximately 1/3.

Various improvements to the Bretherton [159] model have been suggested to expand its range of applicability. Aussillous and Quéré [161] showed that the validity of Eq. (2.24) could be extended to larger capillary numbers ($\mathrm{Ca_b} \approx 1$) by replacing r with $r - ch$, where c is an empirical constant, to account for the effect of a thick film on the curvature of the front meniscus of the bubble. The modified film thickness relationship compared well with their experimental liquid film thickness data when setting $c = 2.5$, giving the following equation:

$$H = \frac{1.34\mathrm{Ca_b}^{2/3}}{1 + 3.35\mathrm{Ca_b}^{2/3}} \tag{2.25}$$

For finite $\mathrm{Re_b}$, inertial effects become significant and a modification to Eq. (2.25) that

takes these into account is required. The impact of inertia on liquid film thickness in micro-tubes was investigated numerically and experimentally by Kreutzer et al. [162], whose results showed a similar trend to the numerical results of Heil [163]. Han and Shikazono [164] performed experiments at higher $\mathrm{Ca_b}$ and $\mathrm{Re_b}$, observing that at these conditions the effect of inertia cannot be neglected. They applied a scaling analysis to obtain a relation of the following form for $\mathrm{Re_b} < 2000$:

$$H = \frac{1.34\mathrm{Ca_b}^{2/3}}{1 + 3.35\mathrm{Ca_b}^{2/3} + f(\mathrm{Ca_b}, \mathrm{Re_b}) - g(\mathrm{We_b})} \tag{2.26}$$

where $\mathrm{We_b}$ is the bubble Weber number, defined as $\mathrm{We_b} = \rho U_\mathrm{b}^2 d/\gamma = \mathrm{Re_b Ca_b}$. They obtained empirical coefficients through fitting of experimental data and reported film thickness predictions with $\pm$ 15 % accuracy. The experimental and numerical results of Khodaparast et al. [165] exhibited close agreement to those of Han and Shikazono [164].

The studies discussed so far were all conducted in micro-tubes and therefore did not consider the effect of buoyancy, which may begin to be significant in tubes of diameters slightly above 1 mm or where $\mathrm{Bo} \ll 1$ [166, 167]. In a horizontal tube buoyancy acts by elevating the bubble above the channel centreline, thus developing a circumferential asymmetry of the liquid film, where the top film becomes thinner than the bottom film. Jensen et al. [168] studied the effect of gravity on the propagation of an air finger within a horizontal Hele-Shaw cell. By applying a theoretical analysis based on matched asymptotic expansions in the small capillary number limit, $\mathrm{Ca_b} \lesssim 10^{-3}$, they derived the following leading-order relationship for the top and bottom liquid film thicknesses (h^+ and h^-, respectively) when $\mathrm{Bo} < 1$:

$$\frac{h^\pm}{b} = \frac{1.34\mathrm{Ca_b}^{2/3}}{1 \pm \mathrm{Bo}} \tag{2.27}$$

where b is half the thickness of the Hele-Shaw cell, which corresponds to a tube radius r. For vanishing values of the Bond number, Eq. (2.27) simplifies to Eq. (2.24) and as Bo increases, the top film thickness (h^+) decreases and the bottom one (h^-) increases. Note that Eq. (2.27) is not applicable to estimate h^- when $\mathrm{Bo} \to 1^-$, as predictions diverge to $+\infty$. When $\mathrm{Bo} > 1$, Jensen et al. [168] observed that the hydrostatic pressure in the bottom film becomes larger than the pressure induced by viscous forces. In this regime,

the bubble detaches from the bottom wall, so that a wetting film is present only at the top, while the bubble thickness becomes independent of the height of the channel. Using their leading-order relationships for the thicknesses of the bubble and the top film, the following expressions can be written:

$$\frac{h^+}{b} = \frac{1.34\mathrm{Ca_b}^{2/3}}{2\sqrt{\mathrm{Bo}}} \tag{2.28a}$$

$$\frac{h^-}{b} = 2\frac{\sqrt{\mathrm{Bo}}-1}{\sqrt{\mathrm{Bo}}} \tag{2.28b}$$

which suggest that $h^+ \to 0$ and $h^- \to 2b$ as $\mathrm{Bo} \to \infty$, i.e. the top film vanishes and the bottom film thickness converges to the Hele-Shaw cell thickness. Note that, as $\mathrm{Bo} \to 1^+$, Eq. (2.28a) converges smoothly to Eq. (2.27), whereas $h^- \to 0$. Therefore, while Eqs. (2.27) and (2.28a) yield continuous predictions of the top film thickness as Bo approaches 1 from both left and right, predictions of the bottom film thickness from Eqs. (2.27) and (2.28b) diverge at $\mathrm{Bo} = 1$. In deriving the equations above, Jensen et al. [168] assumed that $h \ll b$, such that the radius of the bubble front cap could be approximated as b, which is an acceptable assumption as long as $\mathrm{Ca_b} \lesssim 10^{-3}$ [161]. Atasi et al. [169] accounted for the presence of thick top and bottom films to derive better matching conditions for the film profile at the bubble nose, and thus extend the applicability of the model of Jensen et al. [168] to larger $\mathrm{Ca_b}$. The resulting predictive method was a four-equation model, valid for $\mathrm{Bo} < 1$, requiring an iterative solution, which they compared against experimental data for long bubbles travelling in a very viscous liquid ($\mathrm{Re_b} \ll 1$) in horizontal tubes with $0.05 < \mathrm{Bo} < 0.4$ and $10^{-3} < \mathrm{Ca_b} < 10^{-1}$. The comparison was satisfactory at low Bo, but increasing deviations at larger Bo were attributed to the ovalisation of the cross-sectional shape of the bubble, which could not be accounted for in their two-dimensional flow model.

Leung et al. [170] measured top and bottom film thicknesses and liquid flow fields for long gas bubbles travelling in horizontal channels in the range $\mathrm{Bo} \leq 0.25$, $0.05 \leq \mathrm{Ca_b} \leq 0.2$ with weak inertia effects ($\mathrm{Re_b} \leq 50$). Besides the asymmetry in the top and bottom liquid film heights, they observed that the bubble was inclined with respect to the tube axis, and related it to the drainage of the top film as liquid flows downward under the action of gravity. Assuming negligible deformation of the bubble from a circular shape in the cross-section, they applied a mass balance to the draining film flow and derived an expression

for the bubble inclination, which Atasi et al. [169] rearranged in the following form:

$$\tan\alpha = \frac{\left(H^{\mathrm{h}}\right)^3}{3\mathrm{Ca_b}}\mathrm{Bo} \tag{2.29}$$

where α is the inclination angle and H^{h} is the dimensionless film thickness extracted at the horizontal centre-plane of the channel. It should be noted that the original theory and Eq. (2.29) do not distinguish between top and bottom inclination angles. However, Atasi et al. [169] observed experimentally that the inclination angle at the top of bubble was smaller than that at the bottom, and compared the predictions of Eq. (2.29) to an average experimental inclination angle with good agreement between the two.

Rek and Zun [171] performed 3D numerical simulations of elongated bubbles with finite Bo, i.e. with gravitational effects, but used a very empirical approach and did not provide any systematic data regarding film thickness asymmetry or bubble inclination. Kreutzer et al. [162] performed a numerical study on the effect of inertia on the adiabatic flow of elongated bubbles, solving the Navier-Stokes equations in an axisymmetrical domain for the liquid phase only. The gas-liquid interface was treated as a free surface. Similar simulations were performed by Gupta et al. [172], but using volume of fluid (VOF) interface capturing with the Fluent solver. The predicted film thickness was found to be in excellent agreement with the Han and Shikazono correlation [164]. A grid convergence study was also performed, with the important result that 5 computational cells were necessary in the discretisation of the liquid film in order to obtain convergence in the bubble dynamics. Also, it was recommended to discretise the interface using uniform cells for a better estimate of the surface tension force.

2.3.1.2 Bubble flow with heat transfer and phase change

Heat transfer was introduced to a 2-D simulation of elongated bubble flow by Fukagata et al. [173] by imposing a constant heat flux at the wall and tracking the interface using a Level-Set algorithm. The wall temperature distribution obtained from the simulations was compared to that observed experimentally in mini-channels and the two were found to be qualitatively similar. Lakehal et al. [174] used the commercial software TransAT to perform a similar study, but with a constant temperature condition at the wall and

the gas and liquid phases injected as co-currently flowing streams. A domain length of 40 diameters proved to be sufficient for the flow to reach a state of full thermal development, identified by a periodic profile of the wall Nusselt number after 15-20 diameters of heated length. A gas-liquid co-flow inlet was also simulated by Gupta et al. [175] using TransAT, with the Level-Set method, and Fluent, with the VOF method. They studied both constant heat flux and temperature conditions. He et al. [176] used periodic boundary conditions for the velocity and temperature fields and performed a grid convergence analysis that suggested discretisation of the liquid film with a uniform mesh of 6 cells was appropriate. All of the studies mentioned in this paragraph reported a local Nusselt number around the bubble that was larger than the single-phase value by a factor of 2-4.

To extend the diabatic models described in the previous paragraph to flow boiling, phase change must be included. Simulations were performed across various studies by Mukherjee et al. [152, 177, 178] of the evaporation of a water bubble in a square micro-channel using the Level-Set method to track the interface. The flow was seeded with a small spherical vapour bubble initialised either in the channel centreline or at the wall. They found negligible gravitational effects and enhanced heat transfer in the liquid film region. Cases with Reynolds numbers in the range 50-200 were simulated, and it was found that Reynolds number had very little effect on the flow in this range. The heat transfer trends calculated by the simulations reflected those observed by various experimental studies on micro-channels.

Magnini [179] developed a solver using a VOF interface advection method in the commercial software Ansys Fluent to model micro-scale flow boiling in the slug flow regime in an axisymmetrical domain. This solver was later employed to give detailed insights into bubble dynamics and the effect of local flow patterns on heat transfer [180], and simulations showed thin-film evaporation to be the dominant heat transfer mechanism in the liquid film region, which was also observed in the works of Mukherjee et al. [152, 177, 178]. User-defined functions were added to generate a constant stream of bubbles [154], with the resulting simulations differing from those with a single bubble, showing that bubble-bubble interactions are significant.

Simulations of slug flow boiling in square micro-channels were performed by Ferrari et al. [155] using the built-in VOF method of OpenFOAM with phase change introduced using external subroutines. The phase change model was based on that of Hardt and

Wondra [181] and the authors validated its implementation against analytical models [182] and numerical investigations using ANSYS Fluent [180]. Drainage flows transversal to the main flow direction were observed to thin the liquid film toward the rear of the bubble, causing the the liquid film to dry out when the bubble becomes sufficiently long. Magnini and Matar [183] employed the same phase change model and solution procedure to assess the impact of channel shape on flow boiling in rectangular micro-channels.

2.4 Summary

A study of the literature surrounding flow boiling in horizontal pipes has been carried out. Theoretical, empirical and semi-empirical predictive methods for flow pattern, heat transfer and pressure drop in boiling flows have been considered. For the latter two, flow-pattern specific models with a firm theoretical basis are generally most accurate, but are also significantly more complicated to implement than other correlations. No single method applies to all flow geometries or test fluids, and numerous modifications have been made to early correlations for specific experimental conditions.

A large body of experimental work exists for refrigerant flow boiling in horizontal macro-scale pipes, with most studies employing similar measurement techniques for pressure drop and temperature and using sight glasses to observe flow patterns. The number of studies utilising R245fa as a test fluid has increased in recent years, but the majority of the existing literature focuses on condensation or boiling in micro-channels. A small number of studies have employed more advanced optical measurement techniques to study phase distribution, but detailed spatio-temporally resolved information in horizontal boiling flows is lacking in general. Laser-based optical diagnostic methods and infrared thermography have been used to investigate velocity and temperature fields in boiling flows in vertical channels with a rectangular cross-section and in pool boiling experiments. Particle image velocimetry and laser-induced fluorescence methods have been successfully employed to study isothermal liquid-liquid flows, gas-liquid annular flow and liquid films, and could provide new insights into boiling flows by facilitating detailed spatio-temporally resolved measurements of velocity and temperature fields. In the research space of numerical studies, there is a lack of interface-resolved models for flow boiling in macro-scale channels, although much has been done for micro-scale channels.

When moving from the micro- to the macro-scale the effects of turbulence, buoyancy and inertia must be considered. Evaporation of elongated bubbles in micro-channels has been studied, but requires extension to annular flows. It is clear that there is scope to develop a model of elongated bubbles in macro-channels with significant buoyancy and inertia effects that is validated by experimental data. From such a model, heat transfer and phase change could be added following numerical methods in the literature developed for flow boiling in micro-channels.

Chapter 3

Experimental Methods

A bespoke experimental Flow Boiling Facility (FLOBOF) was designed, commissioned and operated by the author for the investigation of boiling flows in horizontal tubes. The facility comprises a closed flow loop incorporating an electrically heated test section and a visualisation section providing optical access to the flow and enabling the application of advanced optical measurement techniques.

In this section FLOBOF and its constituent parts are described in detail, along with the measurement techniques applied and the methods used to analyse the collected data. Uncertainties in measured and derived values are also reported, along with validation of the facility and *in-situ* fluid properties.

3.1 Experimental design

Design of the facility was undertaken to ensure the resulting data provides a useful contribution to the flow boiling literature, whilst the findings are relevant to direct steam generation (DSG) solar collectors, amongst other applications. The flow patterns of interest to DSG helped to determine the experimental design and operating conditions for this work. Odeh et al. [12] generated flow pattern maps for two different horizontal collector tube diameters which showed that mainly stratified, intermittent and annular flow patterns are observed in DSG collectors; dispersed bubble flow only occurs at very high superficial liquid velocities which are not achieved in normal DSG collector operation. They also calculated that for a typical tube of 54 mm inside diameter with beam radiation of $1\,\mathrm{kW/m^2}$, annular flow accounted for 85 % of the two phase region. Stratified flow was

only observed at low radiation levels and low superficial gas velocities in larger absorber tubes, but is important to understand as it can induce large circumferential temperature gradients in the absorber walls, leading to damage to the tube and assembly. Intermittent flow is considerably less dominant, and significantly more difficult to measure optically due to the large number of interfaces. Stratified is the simplest two-phase flow pattern to measure optically so provides a good starting point for experimental measurements, whilst slug flow has some of the characteristics of intermittent flow but is more suited to optical measurement techniques so is also investigated in this work. Annular flow in horizontal pipes presents challenges in terms of optical measurement, so this work also developed laser diagnostic techniques for such flows.

The values for mass flux ($G = 350$ kg/m^2.s) and beam irradiation (up to 1 kW/m^2) reported by Odeh et al. [12] are typical of horizontal DSG collectors, and similar to those in other studies [184, 185]. In parabolic trough collectors (PTCs) the solar radiation is concentrated onto the absorber tube, and the ratio of the local heat flux on the tube to the beam irradiation is described by a local concentration ratio. This concentration ratio is around 30 for the largest commercial PTCs [11, 186], resulting in a local heat flux on the absorber tube of around 30 kW/m^2 at a maximum beam irradiation of 1 kW/m^2. Thus, similar heat and mass fluxes were targeted in this work.

3.2 Description of the experimental facility

A simplified flow diagram of FLOBOF is shown in Fig. 3.1, whilst a full detailed piping and instrumentation diagram (P&ID) is given in Fig. 3.2.

3.2.1 Flow loop

In the refrigerant flow loop, subcooled liquid is pumped from the bottom of a 20 l liquid receiver using a Crest AM50 TGARV centrifugal pump and passed to an Omega CHF081863 6 kW circulation heater used to preheat the liquid to the desired degree of subcooling at the test section inlet using a PID control loop. The liquid is then passed through a 90 µm filter, operated on a bypass loop, to protect the subsequent turbine flowmeter, the output of which is used to control the pump speed via an AC-10 Parker inverter and thus regulate the flow rate into the test section. The 12.6 mm-inside diameter, 2 m-long stainless steel

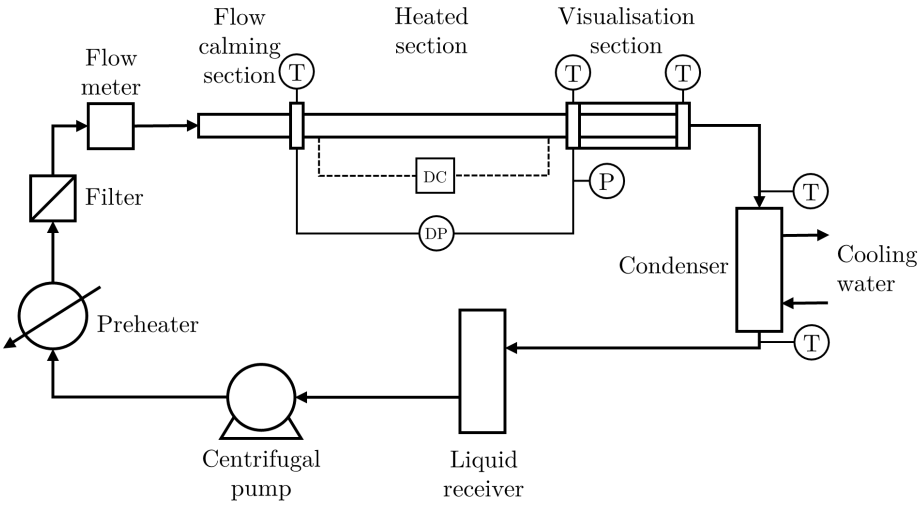


Figure 3.1: Simplified flow diagram of FLOBOF. Measurement locations for temperature, pressure and differential pressure are indicated by T, P and DP respectively.

heated test section is preceded by a 0.6 m-long flow calming section of the same material and inside diameter to eliminate entrance effects.

Fluid temperature is measured at the entrance to the heated section to determine the inlet conditions and again at the outlet along with system pressure. The liquid boils as it flows along the heated section, resulting in a two-phase vapour-liquid flow which enters the visualisation section. This section consists of a fluorinated ethylene propylene (FEP) pipe, of equal inside diameter to the stainless-steel heated section, encased in a perspex correction box filled with water. The fluid then flows through a water-cooled plate heat exchanger, in which the vapour condenses and the liquid is subcooled before being returned to the top of the liquid receiver.

The output signals from the facility instrumentation were processed by three data acquisition devices (DAQs) and recorded through a LabView interface, which was also used for monitoring and control of the system. For a given set of experimental conditions, a steady-state was considered to be achieved when the instrument data remained within a 5 % range for at least 300 s, after which data was recorded for a period of 120 s. This range was applied to the thermocouple readings reported in °C, as shown in the LabView interface.

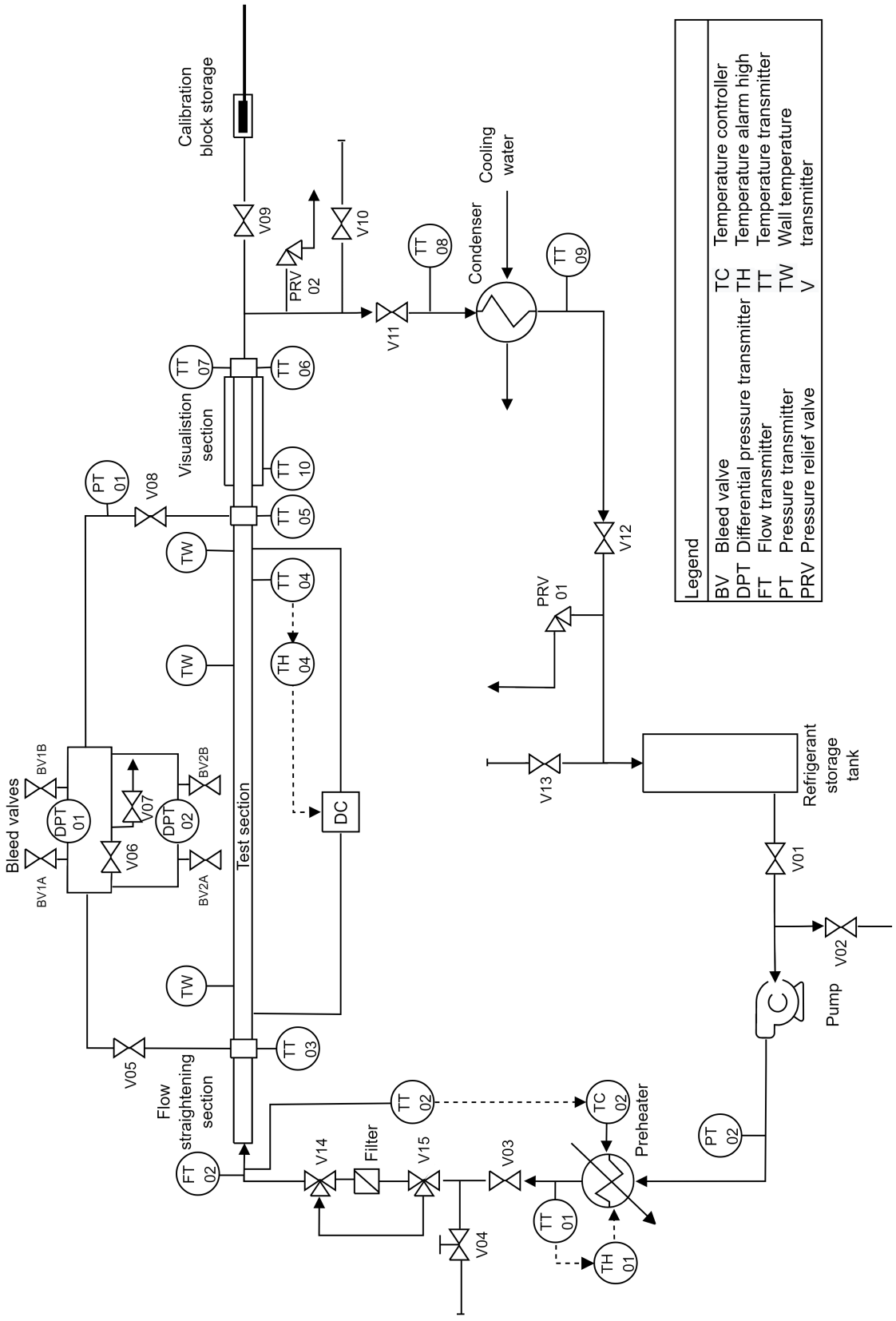


Figure 3.2: Detailed P&ID of FLOBOF.

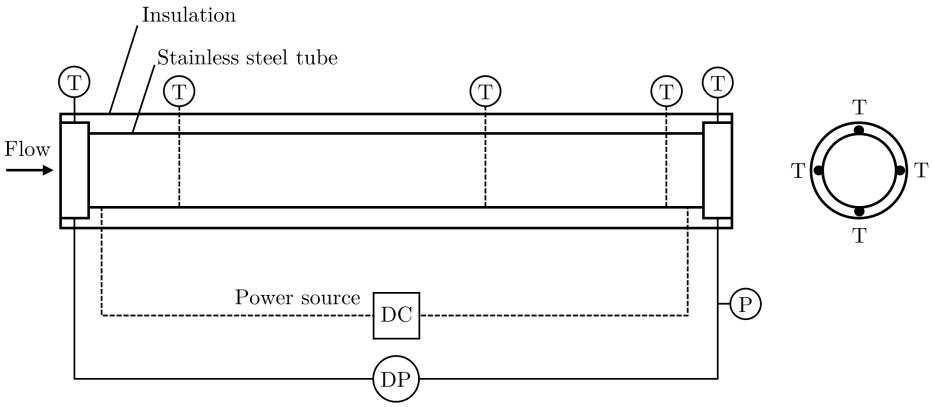


Figure 3.3: Schematic of the heated test section. Measurement locations for temperature, pressure and differential pressure are indicated by T, P and DP respectively.

3.2.2 Heated test section

The heated test section (see Fig. 3.3) comprises a stainless steel pipe with direct current (DC) heating, thermal insulation and measurement instrumentation. The pipe has an inside diameter, d_{i}, of 12.6 mm, outside diameter, d_{o}, of 15.9 mm and length, L_{ht}, of 2 m. These characteristics give a pipe of the same material and same scale of diameter as typical DSG applications, whilst still being practical at lab-scale.

The pipe is connected to a Glassman Europe BPI 20 V, 750 A DC power supply via copper rods and braids to uniformly heat its surface by application of direct current. The Ohmic losses in the rods and braids were checked and found to result in a 2 % loss of input power delivered to the pipe. The whole section is insulated with black nitrile rubber pipe insulation to a minimum thickness of 19 mm, with maximum heat losses of $< 1\,\%$ of input power calculated across all experimental conditions. Fluid enters the heated section as a subcooled liquid, is heated to saturation point, boils, and exits as a two-phase vapour-liquid flow with vapour quality x.

3.2.3 Visualisation section

To allow optical access, a visualisation section, shown in Fig. 3.4, was constructed at the outlet of the heated test section. An effective visualisation section for application of any optical diagnostic technique to two-phase pipe flows should be designed to minimise optical distortions due to the refraction of light at all fluid-fluid and fluid-solid interfaces, and this is ideally achieved with a fully refractive index (RI) matched system [187]. However,

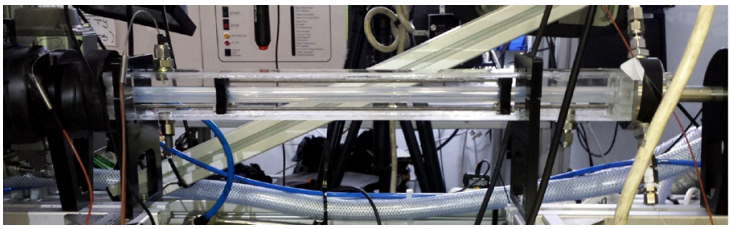


Figure 3.4: Photograph of the visualisation section.

this is highly challenging in a boiling flow since the two fluid phases have very different RIs, and additionally liquid R245fa has a low RI (1.25 at 20 °C) so RI-matching to solids is also difficult. As such, an FEP pipe, of equal inside diameter to the heated test section, was used for the visualisation section. FEP has a low RI compared to other compatible optically accessible pipe materials and is translucent, and therefore optically accessible. The FEP pipe is encased in a correction box constructed from acrylic and filled with distilled water (the RI of which closely matches that of the FEP pipe within the experimental temperature range). This box reduces optical distortion due to the curvature of the pipe and relative position of the camera.

Optical distortion can be further accounted for by placing and imaging a predefined graticule target of known dimensions in the measurement section. An example of this correction method in two-phase pipe flows is described by Morgan et al. [149, 188]. Typically, the visualisation section is drained and disconnected to allow placement of the graticule, then blocked at the outlet and refilled with the test fluid. Since FLOBOF operates under pressure, placement of the graticule is more challenging, so a mechanical device was developed to facilitate its movement within the pipe without opening or draining the system. During use a seal is maintained using o-rings, but during standard operation of the facility the graticule is retracted and stored behind a valve (V09 in Fig. 3.2). A photograph of the graticule positioned in the the visualisation section is shown in Fig. 3.5. The centres of the holes in the target are 1 mm apart and the target is of known dimensions, so once it is positioned in the centre of the pipe, i.e. in the laser plane, the image can be spatially calibrated to account for the inclination of the camera and other constant optical distortions.

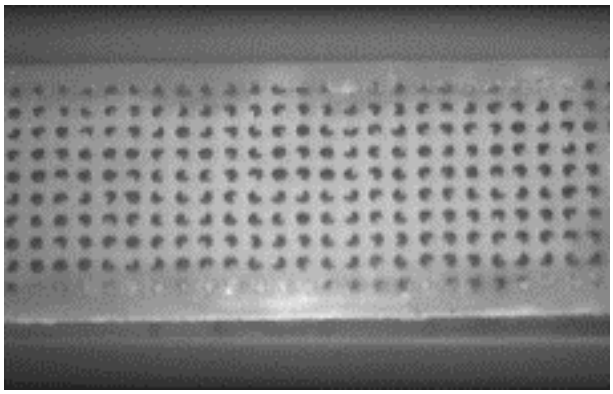


Figure 3.5: Photograph of graticule target inside the visualisation section.

3.2.4 Safety considerations

A number of safety aspects were taken into consideration in the design of the facility to ensure inherently safe operation. These included:

1. *Pressure.* The facility is designed to operate at approximately 2 bar and is protected against overpressure by two pressure relief valves (PRV01/02 in Fig. 3.2) rated to 3.5 bar. All the equipment is rated to at least this pressure.

2. *Temperature.* To prevent overheating of the system, high temperature safety switches are located in-flow at the test section entrance (TH02 in Fig. 3.2) and on the pipe wall (TH04). Insulation prevents accidental contact with the heated section and the failsafe mode for the system is with the preheater and power supply turned off.

3. *Electricity.* A power supply was selected of sufficiently low voltage (20 V) to pose an acceptably low risk of electrocution on incidental contact.

3.3 Description of integral measurement techniques

In this section, instrument-based measurement techniques are described for flow properties such as temperature, pressure and flow rate. The outputs signals of all such instruments were processed by three DAQs connected to a computer. A LabView interface was developed to read the instrument signals, display the data in real-time and store the results in a text file for further processing which will be described in Section 3.4. For each set of experimental conditions investigated the control variables were set and the system allowed to reach a steady state before data was recorded. A steady-state was considered to be

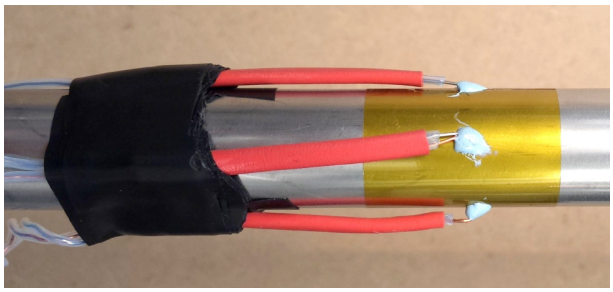


Figure 3.6: Photograph showing attachment of unsheathed thermocouples to the wall.

achieved when the instrument data remained within a 5 % range for at least 300 s, after which data was recorded for a period of 120 s.

3.3.1 Temperature

In-flow temperature measurements (indicated by TT in Fig. 3.2) were made using mineral insulated T-type thermocouples of 0.5 mm diameter. The stainless steel sheaths of these thermocouples provide robustness and durability, but they are sufficiently fine to give fast, accurate temperature measurements with little disturbance to the flow field. The wall temperature was measured using 0.38 mm diameter bead-welded T-type thermocouples, the fine junctions of which allow for fast, accurate temperature readings at a precisely known location. Response times for both thermocouple types are calculated in Appendix A.1. The wall thermocouples are electrically insulated from the live pipe wall by a thin layer of polyimide film to which the thermocouples are attached with thermally conductive epoxy glue, as shown in Fig. 3.6. The thermocouple wires are encased in electrically insulating sheaths then passed along the pipe wall inside the insulation to minimise conduction errors, an estimation of which is given in Appendix A.2. Wall thermocouples are placed at three measurement junctions 0.125 m, 1.575 m and 1.875 m from the inlet, with thermocouples placed at 90° intervals around the pipe circumference, as shown in Fig. 3.3.

All of the thermocouples in the facility were calibrated to an accuracy of ± 0.25 K in a thermal bath against a digital reference thermometer certified with a 5-point UKAS calibration. A detailed description of the calibration procedure is given in Appendix A.3.

3.3.2 Pressure

The absolute pressure at the outlet of the heated section was measured using an Omega PXM309 pressure transducer, indicated by PT01 in Fig. 3.2. This pressure transducer uses a silicon sensor protected by a stainless steel membrane and was supplied with a manufacturer calibration in the range 0–3.5 bar with an uncertainty of ± 1 % of the measured value. The instrument was installed below the test section so a hydrostatic pressure compensation was applied such that:

$$p = p_{\text{raw}} - \rho_{\text{l}} g \Delta y \tag{3.1}$$

where $\Delta y = 0.082\,\text{m}$.

Pressure is also measured at the pump outlet by a Gems3100 gauge pressure transmitter, indicated by PT02 in Fig. 3.2. This was used for system monitoring and control only.

3.3.3 Pressure drop

The pressure drop across the heated test section was measured using two Rosemount differential pressure transmitters, indicated by DPT01/02 in Fig. 3.2. The two instruments were calibrated over different ranges to provide accurate measurements across the full range of experimental pressure drop values and have a manufacturer-specified uncertainty of ± 0.1 % of the calibrated span. The transmitters were mounted below the heated test section, with the impulse piping connected at the bottom of the pipe, to ensure a liquid filled impulse line and thus maintain a constant density of fluid in the line. This positioning also ensured sloping of the impulse line to allow any bubbles to travel away from the transmitter and prevent vapour pockets.

The differential pressure transmitters were calibrated *in situ* using a Fluke709H HART-meter in the ranges 0–20 000 Pa and 0–5000 Pa for DPT01 and DPT02 respectively.

3.3.4 Flow rate

Volumetric flowrate was measured at the entry to the flow straightening section, as indicated by FT02 in Fig. 3.2, using a Titan 1065-EOS-O pulse output turbine flowmeter.

The device was purchased with a manufacturer calibration curve with an uncertainty of $\pm$ 0.75 % of the measured value.

3.4 Data reduction for integral measurements

The raw data obtained from the heated test section described in Section 3.2.2 required some treatment to provide the set of integral measurements common to the flow boiling literature. The data reduction process applied to the raw data is described in this section. All reduced quantities were calculated from the raw data then time-averaged for each investigated condition for further analysis as presented in Chapter 5. All data processing was undertaken using MATLAB with all thermophysical fluid properties calculated at the relevant conditions using CoolProp [189].

3.4.1 Mass flux

Mass flux, G, was calculated from the measured volumetric flowrate, $\dot{V}$ as follows:

$$G = \frac{\dot{V}\rho_{\mathrm{l}}}{\pi r_{\mathrm{i}}^2} \tag{3.2}$$

where r_{i} is the inside radius of the pipe and ρ_{l} is the liquid density evaluated at the inlet conditions.

3.4.2 Heat flux

The reported experimental heat flux was calculated as

$$q = \frac{Q_{\mathrm{in}}}{\pi d_{\mathrm{i}} L_{\mathrm{ht}}} \tag{3.3}$$

where L_{ht} is the heated length of pipe and Q_{in} is the heat input rate accounting for Ohmic losses due to the resistance of the copper rods and braids connecting the power supply to the test section, and thermal losses to the ambient such that $Q_{\mathrm{in}} = P_{\mathrm{in}} - Q_{\mathrm{out}}$. Then, the power delivered to the pipe is $P_{\mathrm{in}} = VI \times C$ where V and I are the voltage and current of the power supply and C is a constant that corrects for the Ohmic losses. The values of V and I were set as inputs to the control panel of the power supply, whilst the Ohmic corrective constant C was determined by measuring the voltage drop across the system

components using a multimeter and calculating the corresponding resistance, $R = V/I$. Then, the proportion of the total power delivered to the stainless steel pipe was found to be $C = R_{\text{pipe}}/R_{\text{total}} = 0.98$.

The heat losses to the ambient were estimated by considering one-dimensional heat transfer from the wall:

$$Q_{\text{out}} = h_{\text{ext}}(T_{\text{w}} - T_{\text{amb}}) \tag{3.4}$$

where the overall external heat transfer coefficient h_{ext} includes the contributions of the heat transfer coefficient in the insulation, h_{ins}, and of the convective heat transfer to the air, h_{ins}, according to the relation

$$\frac{1}{h_{\text{ext}}} = \frac{1}{h_{\text{ins}}} + \frac{1}{h_{\text{air}}} \tag{3.5}$$

$$h_{\text{ext}} = \frac{2\pi k_{\text{ins}}}{\ln d_{\text{ins}}/d_{\text{o}}} \quad ; \quad h_{\text{air}} = \pi r_{\text{ins}} \text{Nu}_{\text{air}} \frac{k_{\text{air}}}{d_{\text{ins}}} \tag{3.6}$$

$$\text{Nu}_{\text{air}} = 0.41 \left(\frac{g\beta(T_{\text{ins}} - T_{\text{amb}}) d_{\text{o}}^3}{\nu_{\text{air}}^2} \frac{c_{p,\text{air}}\mu_{\text{air}}}{k_{\text{air}}} \right)^{0.25} \tag{3.7}$$

where β is the thermal expansion coefficient.

The heat losses calculated using this method were found to be less than 1 % for most experimental conditions, and this was verified by single phase tests to assess the validity of the energy conservation equation

$$P_{\text{in}} = \dot{m} c_p (T_{\text{out}} - T_{\text{in}}) \tag{3.8}$$

in which the resulting heat losses were found to be approximately 1 % across a range of mass flux and heat flux conditions.

3.4.3 Heat transfer coefficient

The experimental heat transfer coefficient h was calculated as follows:

$$h = \frac{Q_{\text{in}}}{A_{\text{ht}}(T_{\text{w,i}} - T_{\text{sat}})} \tag{3.9}$$

where A_{ht} is the heat transfer surface area to the fluid, $A_{\text{ht}} = \pi d_{\text{i}} L_{\text{ht}}$. $T_{\text{w,i}}$ is the inside wall temperature and T_{sat} is the saturation temperature of the fluid evaluated at the measured saturation pressure.

The inside wall temperature, $T_{\mathrm{w,i}}$, was calculated from the outside wall temperature, $T_{\mathrm{w,o}}$, by solving a one-dimensional conduction equation across the pipe wall, assuming uniform heat generation in an isotropic and homogeneous material:

$$T_{\mathrm{w,i}} = T_{\mathrm{w,o}} + \frac{Q_{\mathrm{in}}}{2\pi k_{\mathrm{pipe}} L_{\mathrm{ht}} (r_{\mathrm{o}}^2 - r_{\mathrm{i}}^2)} \left(\frac{r_{\mathrm{o}}^2 - r_{\mathrm{i}}^2}{2} + r_{\mathrm{o}}^2 \ln \frac{r_{\mathrm{i}}}{r_{\mathrm{o}}} \right) \tag{3.10}$$

where $k_{\mathrm{pipe}} = 16.3$ W/m.K is the thermal conductivity of the stainless steel pipe and r_{i} and r_{o} are its inner and outer radii respectively. This approach has been used in the literature to solve similar heat transfer problems [136], and a more complete derivation of Eq. (3.10) is provided in Appendix A.

The inside wall temperature and corresponding heat transfer coefficient were calculated at each wall thermocouple location, then a spatially averaged h was calculated at each thermocouple junction from the four local h values.

3.4.4 Vapour quality

The vapour quality, x, was calculated by performing a heat balance across the heated test section:

$$x = \frac{Q_{\mathrm{in}} - \dot{m} c_p \Delta T_{\mathrm{sc}}}{\dot{m} h_{\mathrm{lv}}} \tag{3.11}$$

where m is the mass flow rate in kg/s, c_p is the liquid heat capacity at inlet conditions, ΔT_{sc} is the degree of subcooling at the pipe inlet, i.e. $\Delta T_{\mathrm{sc}} = T_{\mathrm{sat,in}} - T_{\mathrm{in}}$, and h_{lv} is the latent heat of vaporisation of the liquid. x was calculated at the outlet of the heated test section, and at the location of each thermocouple junction with Q_{in} scaled according to the corresponding heated length.

3.4.5 Pressure drop

The pressure drop measured experimentally, Δp_{exp}, was the total pressure drop and therefore the sum of the gravitational, frictional, and spatial acceleration contributions as follows:

$$\Delta p_{\mathrm{exp}} = \Delta p_{\mathrm{grav}} + \Delta p_{\mathrm{fric}} + \Delta p_{\mathrm{sa}} \tag{3.12}$$

Since the flow was horizontal, $\Delta p_{\mathrm{grav}} = 0$. Two-phase pressure drop predictive methods in the literature calculate the frictional pressure drop, so the spatial acceleration pressure

Table 3.1: Fixed errors in measured quantities.

Parameter	Unit	Uncertainty
I	A	$\pm$ 0.4 % of scale (0–750 A)
V	V	$\pm$ 0.1 % of scale (0–20 V)
d_i	mm	$\pm$ 2.3 % of measured value
L	m	$\pm$ 1 mm
p	Pa	$\pm$ 1 % of measured value
Δp	Pa	$\pm$ 0.1 % of span (0–20 000 Pa or 0–50 000 Pa)
$\dot{m}$	kg/s	$\pm$ 3 % of measured value
T_fluid	$\pm$ K	0.25 K
T_w	$\pm$ K	0.25 K

drop was calculated according to the method of Collier and Thome [18] as follows:

$$\Delta p_\mathrm{sa} = G^2 \left\{ \left[\frac{(1-x)^2}{(1-\varepsilon)\rho_\mathrm{l}} + \frac{x^2}{\varepsilon \rho_\mathrm{v}} \right]_\mathrm{out} - \left[\frac{(1-x)^2}{(1-\varepsilon)\rho_\mathrm{l}} + \frac{x^2}{\varepsilon \rho_\mathrm{v}} \right]_\mathrm{in} \right\} \tag{3.13}$$

where G is the mass flux, ρ_l and ρ_V denote the densities of the liquid and vapour phases respectively, and ε is the void fraction calculated using the Steiner [44] formulation of the Rouhani and Axelsson [45] drift flux void fraction correlation:

$$\varepsilon = \frac{x}{\rho_\mathrm{v}} \left[(1 + 0.12(1-x)) \left(\frac{x}{\rho_\mathrm{v}} + \frac{1-x}{\rho_\mathrm{l}} \right) + \frac{1.18(1-x)[g\gamma(\rho_\mathrm{l} - \rho_\mathrm{v})]^{0.25}}{G\rho_\mathrm{l}^{0.5}} \right]^{-1} \tag{3.14}$$

3.4.6 Uncertainty analysis

The overall experimental uncertainty was evaluated using the method proposed by Moffat [190] for multi-sample data-sets. This analysis considers the two main types of errors arising in experimentally measured quantities: fixed errors and random errors. Fixed errors can typically be attributed to the precision or calibration limits of the instrumentation and will be constant throughout the experiment. For a measured quantity X_j, the magnitude of the fixed error is determined by the bias limit

$$B_{X_j} = \frac{b_X}{100} \times X_j \tag{3.15}$$

where b_X is the percentage uncertainty due to instrument precision or calibration limitations. The fixed errors for the instrumentation in FLOBOF are reported in Table 3.1

Table 3.2: Experimental uncertainties. Percentage uncertainties pertain to the measured value.

Parameter	Unit	Uncertainty
$T_{\mathrm{w,o}}$	K	0.3 K
T_{fluid}	K	0.3 K
G	kg/m^2.s	8.8 %
q	W/m^2	1.7–6.6 %
h	W/m^2.K	6.0–23 %
x		0.0085
p	Pa	2.2 %
Δp	Pa	0.1–6.1 %

Random errors cannot be quantified in the same way as fixed errors as they are caused by unexpected variations in the experimental environment that result in variance in the measured values. They can be evaluated by considering the precision index

$$S_{X_j} = \sigma_{X_j} \tag{3.16}$$

where σ_{X_j} is the standard deivation of the measured value X_j. Then the total uncertainty, U_{X_j}, in a measured quantity is calculated as a combination of both the bias index and precision index commonly evaluated at the 95 % confidence interval:

$$U_{X_j} = \sqrt{(B_{X_j}^2) + (t_{0.95} S_{X_j})^2} \tag{3.17}$$

where $t_{0.95}$ is the t-value of the student distribution at a 95 % confidence interval for $N-1$ degrees of freedom, where N is the number of samples using in the calculation of S_{X_j}.

If n measured quantities were used to calculate a result, the root sum square method was used to determine the total uncertainty U_R in the resulting calculated value R:

$$U_R = \sqrt{\left\{ \sum_{j=1}^{n} \left(\frac{\partial R}{\partial X_j} U_{X_j} \right)^2 \right\}} \tag{3.18}$$

The resulting total experimental uncertainties are reported in Table 3.2.

When assessing the accuracy of predictive methods for pressure drop and heat transfer coefficient, the mean relative deviation (MRD) and mean absolute relative deviation

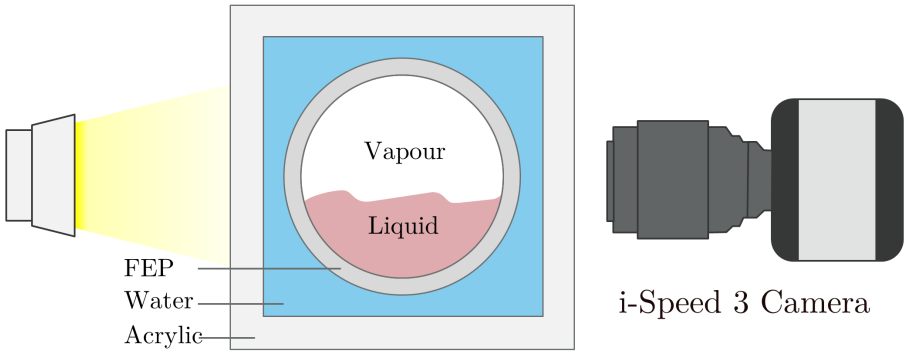


Figure 3.7: Camera arrangement for qualitative flow visualisation.

(MARD) of a variable X were calculated as:

$$\text{MRD} = \frac{1}{n}\sum_{i=1}^{n}\frac{X_{\text{pred}} - X_{\text{exp}}}{X_{\text{exp}}} \tag{3.19}$$

$$\text{MARD} = \frac{1}{n}\sum_{i=1}^{n}\left|\frac{X_{\text{pred}} - X_{\text{exp}}}{X_{\text{exp}}}\right| \tag{3.20}$$

3.5 Description of optical measurement techniques

3.5.1 High-speed imaging for flow pattern identification

For simple visualisation of the flow through high-speed imaging, and for flow pattern identification, a backlight and camera were positioned as shown in Fig. 3.7. The camera used was an Olympus i-Speed 3 with a maximum resolution of 1280 by 1024 pixels at a maximum frame rate of 2 kHz, equipped with a Sigma 105 mm lens and installed in a horizontal orientation perpendicular to the correction box.

3.5.2 Combined PLIF and PIV technique

The experimental set-up for combined planar laser-induced fluorescence (PLIF) and particle image velocimetry (PIV) is shown in Fig. 3.8. The flow was illuminated by a laser sheet generated by a copper-vapour laser that emits two narrow band laser beams at 510.6 nm

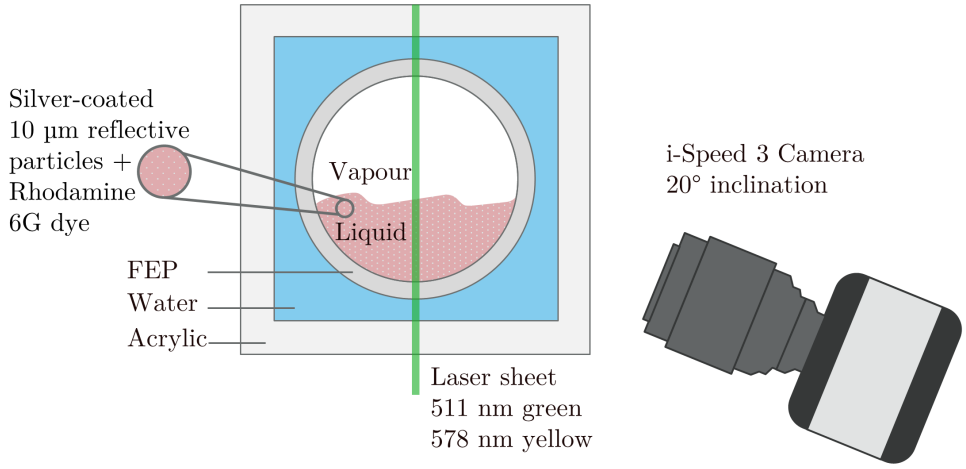


Figure 3.8: Camera arrangement for combined PLIF and PIV.

(green light) and 578.2 nm (yellow light) at a nominal output power of 20 W, frequency of 2 kHz, pulse-duration of 2 ns, and pulse energy of 2 mJ. The beams were directed to a sheet generator via a fibre-optic cable, with the sheet expanded in the streamwise direction and illuminating the flow in a plane through the (axial) centreline of the pipe from the bottom of the correction box. The same i-Speed 3 high-speed camera was used to capture instantaneous images of the flow. In this application, the camera was mounted at an angle of approximately 20° from the horizontal and fitted with a corrective Scheimpflug filter. Images were captured at a frame rate of 1500–2000 fps, depending on the flow velocity, and the shutter speed was set to 100 µs to allow sufficient light to reach the sensor whilst avoiding blurring of the particles due to displacement whilst the shutter is open.

The liquid phase of the flow was seeded with 10 µm silver-coated reflective particles to enable PIV measurements. These particles have a density comparable to that of the liquid phase and are sufficiently small to ensure they follow the streamlines of the flow with minimal interference, as determined by consideration of the Stokes number:

$$\mathrm{Stk} = \frac{\rho_\mathrm{p} d_\mathrm{p}^2}{18\mu_\mathrm{l}} \frac{u_\mathrm{l}}{d_\mathrm{pipe}} \tag{3.21}$$

where the subscript ‘p’ denotes properties of the particles. Tropea et al. [191] reported that for $\mathrm{Stk} \ll 0.1$ any tracing errors associated with the particles are $< 1\,\%$, and evaluating Eq. (3.21) gives a Stokes number of the order of 10^{-4}, which meets this condition. To produce laser-induced fluorescence, the fluorescent dye Rhodamine 6G was added to the

liquid R245fa at a concentration of 1 ppm. This concentration was small enough that it caused no considerable change to the fluid properties, as discussed in Section 3.7.1. The camera captured both the scattered light from the particles (for PIV) and the fluorescent emission from the dye (for PLIF) in the liquid phase. This experimental set-up was used to investigate to stratified, stratified-wavy and slug flows.

3.5.3 Combined BBLIF and PLIF technique

To evaluate film thickness in annular boiling flows, a combined brightness-based laser-induced fluorescence (BBLIF) and PLIF technique was developed. This facilitates the measurement of film thickness using two different methods for comparison. The experimental set-up for this approach is shown in Fig. 3.9. The flow was illuminated by a laser-sheet generated by a dual cavity neodymium-doped yttrium lithium fluoride (Nd:YLF) laser (Litron Lasers LDY 304), producing a roughly circular laser beam at 527 nm that was expanded into a 1–2 mm thick sheet that enters through the bottom of a pipe in a plane through the centreline. The laser produces up to 30 mJ per pulse at 527 nm with a maximum repetition rate of 20 kHz. The laser-sheet was inclined downwards at an angle of approximately 30° from the vertical to limit the occurrence of reflections along the waves, similarly to Cherdantsev et al. [17]. The i-Speed 3 camera was fitted with additional extension rings and a low-pass (< 540 nm) filter, and positioned underneath the pipe at an angle of 9° to the vertical for BBLIF measurements. This offset angle helps to avoid overlapping the fluorescence signals from the excited region of the flow and the opposite side of the pipe. For simultaneous PLIF measurements an i-Speed TR camera was fitted with a Sigma 105 mm lens, extension rings and a Scheimpflug filter and installed at an angle of 30° to the horizontal (60° to the vertical) to capture the underneath of the interface whilst minimising reflections. The two cameras were synchronised and operated at a frame rate of 2008 fps, with a shutter speed of 15 µs.

The same refrigerant was used for these experiments as in the PLIF+PIV set-up, so the refrigerant was seeded with dye and particles in the same manner, although additional rhodamine 6G was added to increase the fluorescent dye concentration to 2.5 ppm.

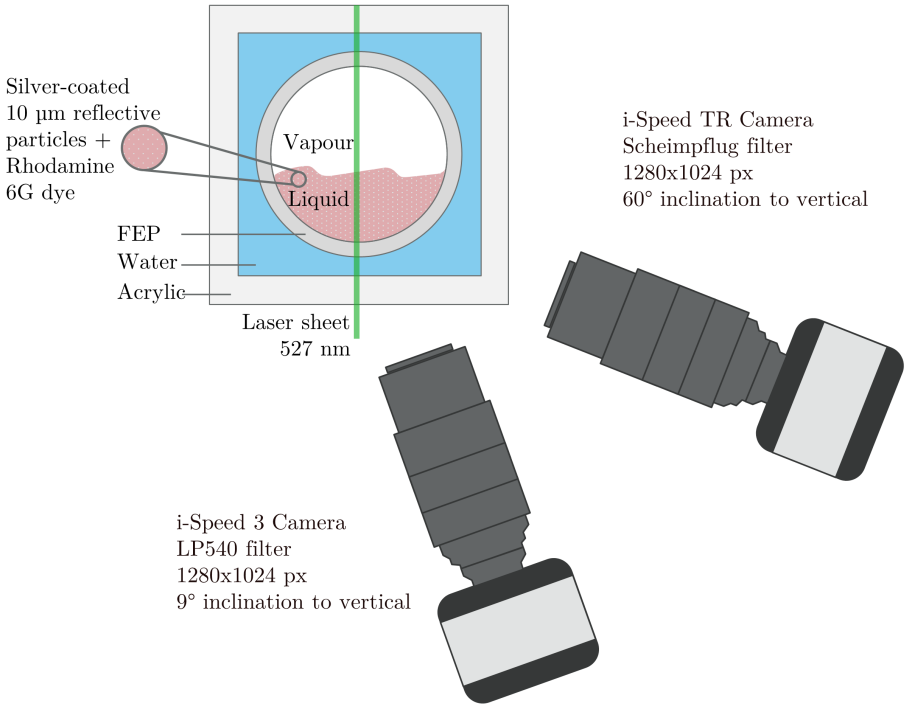


Figure 3.9: Camera arrangement for combined BBLIF and PLIF.

3.6 Image processing

3.6.1 High-speed imaging for flow pattern identification

In the horizontal flow boiling literature, flow patterns are often identified through inspection of high-speed images [43, 65, 97, 111]. This method is perfectly adequate for easily-identifiable flow patterns well within the corresponding region on a flow pattern map, but for data points closer to the transition boundaries the classification becomes somewhat more subjective, particularly given that detailed descriptions of visual flow pattern characteristics are difficult to come by. This was particularly true for the intermittent to annular transition. Therefore, a more quantitative approach was sought to reduce the uncertainty introduced by the observer's judgement.

Charnay et al. [115] developed an image analysis technique based on grayscale intensity of high-speed images for characterisation of flow patterns of R245fa boiling in minichannels. They used this technique to determine the frequency and velocity of small bubbles in bubbly flows. Hudaya et al. [192] utilised a similar technique to characterise different wave patterns in stratified flows. In this work, such an approach was further developed to identify additional flow patterns as an aid to visual observation.

The high-speed images were cropped to the pipe size and a vertical profile line of 10 px

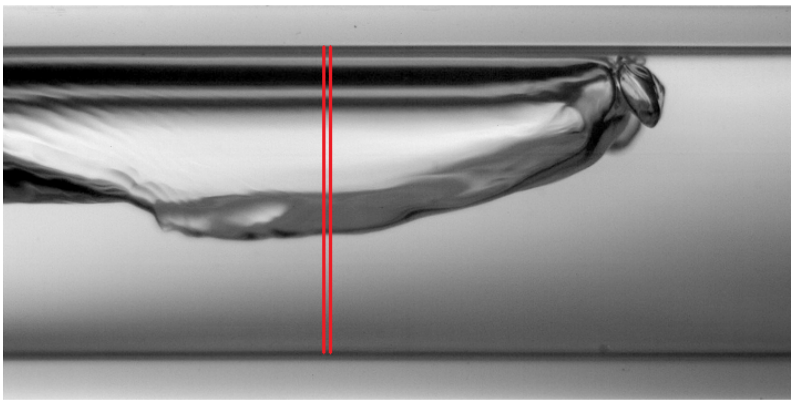


Figure 3.10: Example high-speed image used for flow pattern identification, with selection area for grayscale intensity analysis illustrated between the red lines (not to scale).

width selected in the mid-section of the image along which the grayscale intensity values were extracted, as illustrated in Fig. 3.10. A width of 10 px reduced any effect on results due to abnormally light or dark pixels or pixel-to-pixel variation caused by, e.g., dust or impurities on the lens. The position of the profile line in the direction of flow was found to have no significant impact on the results, since the images are consistently illuminated and focussed along the length of the pipe. Therefore a location away from the edges of the image was arbitrarily chosen and subsequently used for all image sets. The mean grayscale intensity (MGI) values within the selection area for each image in a set were calculated and plotted as a function of time. The resulting profiles had high temporal resolution since images were captured at 1500 fps but had high levels of noise. Fast Fourier transform analysis revealed a peak at approximately 150 Hz caused by flickering of the back-light. This peak was removed from each signal using a band stop filter, and a Savitzky-Golay filter applied to remove noise from the remaining signal. The filter was tuned based on the root mean square error (RMSE) for which a value of 0 indicates a perfect fit to the data. In this case, a RMSE value of approximately 1 was judged suitably low to preserve the signal characteristics whilst providing sufficient smoothing to aid interpretation of the profiles. This resulted in a Savitzky-Golay filter of polynomial order 4 and frame length 9.

Example MGI signals for the different flow patterns observed in FLOBOF are provided in Fig. 3.11. The time-dependent variations in the signals are caused by the appearance of different flow structures: vapour-liquid interfaces, and unstable, wavy or rippled flow, tend to present as darker in images than single phase regions (see Fig. 3.10). Since the high-speed images came from multiple experimental runs, sometimes with different

lighting conditions, the base value of grayscale intensity can differ between image sets. However, it is the temporal variation of the MGI signals that is of interest in this analysis, rather than the absolute value.

In stratified flow (Fig. 3.11a), the signal is typically very stable reflecting the low flow velocities and correspondingly smooth interfaces of this flow pattern. As flow velocities increase the smooth interface is disturbed by waves resulting in a stratified-wavy flow with more deviation in the MGI signal. The signal is still relatively stable since the wavy interface occupies a small proportion of the image compared to the separate single-phase regions. Slugs flows (Fig. 3.11c) are characterised by large cyclical variations in MGI. As the vapour-liquid interface of the slug front passes through the MGI selection area the MGI decreases sharply since the slug nose consists of a dark interface spanning a large proportion of the pipe diameter. Behind the nose there is typically a large undisturbed vapour region resulting in a sharp peak in the MGI signal. This is followed by the two-phase region behind the vapour slug which typically contains bubbles and disturbances and is thus darker than the vapour region. The peaks are not present in MGI profiles for slug + stratified-wavy flows (e.g. Fig. 3.11d) since there tends to be more disturbance (i.e. bubbles and waviness) around the vapour-liquid interface throughout the slugging cycle.

Similarly to stratified flow, the MGI signal for annular flow (Fig. 3.11e) does not display large deviations with time. The flow consists of a thin liquid film at the wall with a high-velocity vapour core. The difference in velocity between these two phases results in ripples in the liquid film but the flow structure is otherwise consistent in time. It can often be difficult to determine the difference between intermittent and annular flows through visual inspection, but the MGI analysis reveals clear differences between the flow patterns. Figure 3.11f shows repeating fluctuations of the MGI, although with smaller, less sharp deviations than for slug or slug + stratified-wavy flows. These deviations are caused by disruptions to the liquid annulus by regions of vapours bubbles in the liquid phase or large liquid droplets in the high-velocity vapour core. On visual inspection these disruptions appear random, but the MGI analysis reveals a periodic collapse of the annular flow structure. It is thus possible to determine between annular and intermittent flow patterns through further statistical analysis of the MGI signals.

The times-series of the MGI signals were characterised by their corresponding statis-

tical moments including the mean, standard deviation and variance ($\overline{MGI}$, σ and Var). The normalised variance (Var/$\overline{MGI}$) represents the relative deviation of the MGI signal about its mean and has markedly different values for annular and intermittent flows, as illustrated by Fig. 3.12. The following criteria were thus used to aid classification of annular and intermittent flow patterns:

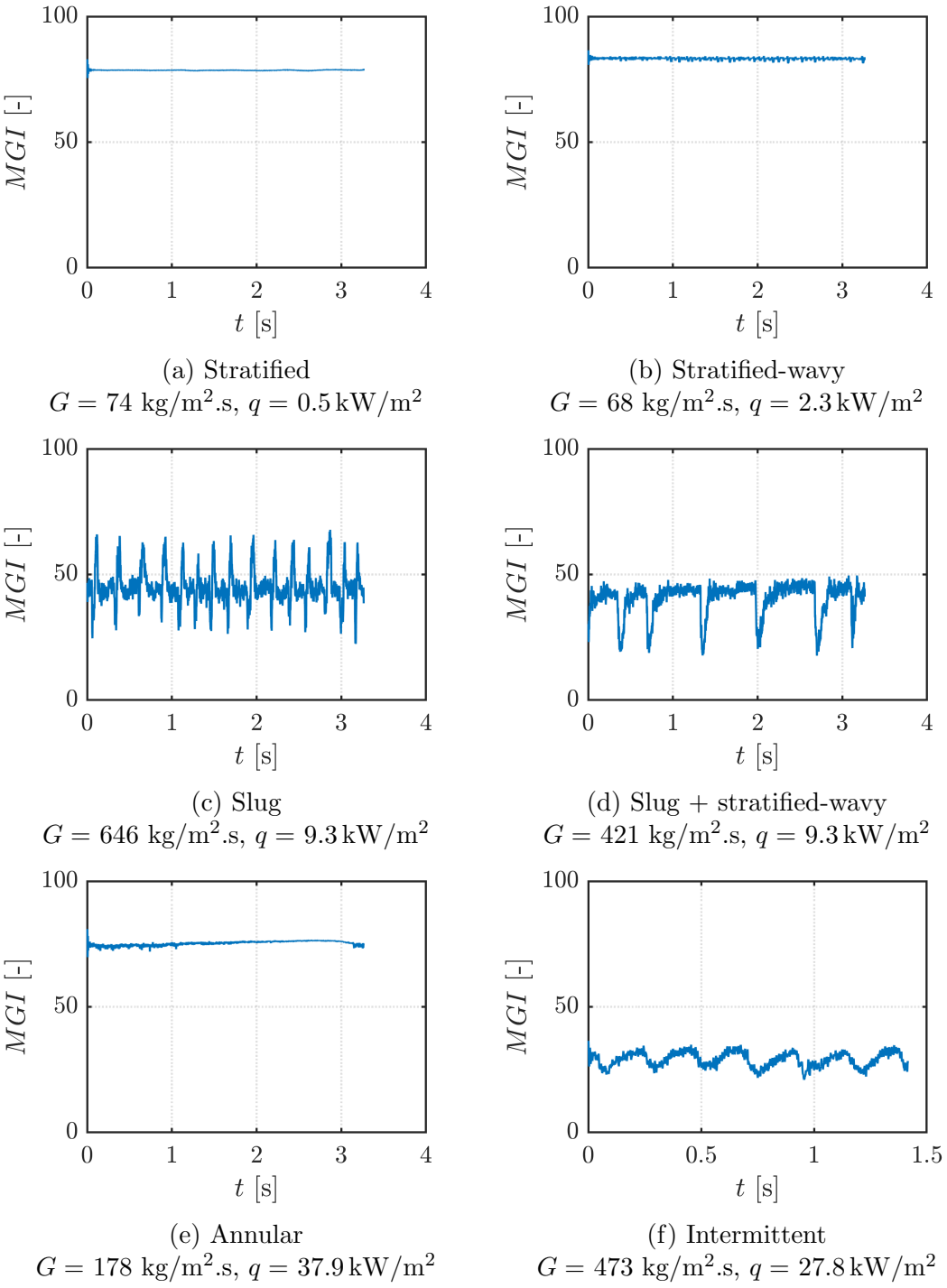
- If Var/$\overline{MGI} > 0.25 \Rightarrow$ intermittent flow;
- If Var/$\overline{MGI} < 0.25 \Rightarrow$ annular flow.

3.6.2 PLIF and PIV for stratified, stratified-wavy and slug flows

To obtain meaningful quantitative information from high-speed imaging of the laser-sheet-illuminated flows, extensive image processing was required. Images were recorded at a frame rate of 1500–2000 fps, with images recorded for a duration of at least 6.5 s for each flow condition to ensure statistical significance of the results. The image processing was undertaken using a combination of the *DaVis* software by LaVision and MATLAB algorithms developed in-house. After a preprocessing step in *DaVis*, two strands of image analysis were undertaken; interface detection and velocity field identification. The detailed steps in these processes are illustrated in Fig. 3.13 and were as follows:

1. First, the images were loaded into the *DaVis* software and a spatial correction was applied based on calibration images obtained of a grid of known dimensions inserted into the liquid-filled pipe. A raw image of the calibration target is shown in Fig. 3.14a. The calibration target was aligned with the laser plane and contained a grid of circular holes exactly 1 mm apart centre-to-centre. The raw image was binarised and the circles identified to facilitate accurate identification in *DaVis* (Fig. 3.14b). The spatial calibration procedure corrected for the distortion induced by the angle of the camera (see Fig. 3.8), and facilitated scaling of the images. The images were also rotated slightly to ensure alignment to the horizontal and mirrored around the vertical to give a flow direction of left-to-right.

2. The images obtained in *DaVis* were then loaded into MATLAB using LaVision's *Readimx* add-on. An algorithm was developed to identify the vapour-liquid interface comprising the following steps for each image:



(a) Stratified
$G = 74$ kg/m^2.s, $q = 0.5$ kW/m^2

(b) Stratified-wavy
$G = 68$ kg/m^2.s, $q = 2.3$ kW/m^2

(c) Slug
$G = 646$ kg/m^2.s, $q = 9.3$ kW/m^2

(d) Slug + stratified-wavy
$G = 421$ kg/m^2.s, $q = 9.3$ kW/m^2

(e) Annular
$G = 178$ kg/m^2.s, $q = 37.9$ kW/m^2

(f) Intermittent
$G = 473$ kg/m^2.s, $q = 27.8$ kW/m^2

Figure 3.11: Example mean grayscale intensity (MGI) signals plotted against acquisition time t for different flow patterns.

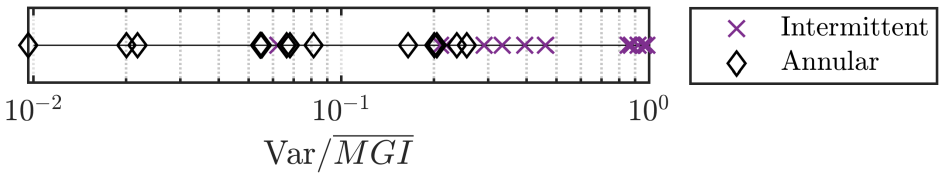


Figure 3.12: Values of $\mathrm{Var}/\overline{MGI}$ for intermittent and annular flow patterns.

(a) First, the image was cropped to the region of interest to remove the area outside of the pipe walls and any dead space introduced from the calibration. The remaining image had a height equal to the pipe inside diameter, d_i, and a width of approximately $2d_\mathrm{i}$ in the direction of flow. The resolution was 20.3 µm/px.

(b) An adaptive threshold was applied to the cropped image based on the local median at each pixel with a window size of 7 px. This removed the intensity hotspots of the particles and increased the intensity difference between the vapour and liquid phases.

(c) The image was binarised using the *imbinarize* function with an adaptive thresholding approach, a sensitivity of 0.5 and the classification of a bright foreground. An area filter was then applied to the resulting black and white image to extract only the largest structures thereby removing any residual light areas due to particles.

(d) The interface was identified by locating the point in the black and white image matrix at which a step change occurred. Any unphysical spikes in the interface were removed and the interface was smoothed using a Savitzky-Golay filter.

(e) A mask was created based on the interface location, with areas under the vapour-liquid interface (i.e. the liquid phase) assigned a value of 1 and any other areas assigned a NaN value.

3. Velocity fields were extracted from the spatially corrected images obtained in step 1 using the following method:

(a) In *DaVis*, the 'Subtract sliding average' processing step was applied to subtract a 2-D sliding average with a 5 px filter length based on a Gaussian profile. This enhanced the intensity difference between the particles and the liquid making them easier to identify in the following step.

(b) PIV vectors were calculated using the functionality in *DaVis* taking a multipass approach with a decreasing window size from 96 by 96 to 32 by 32. The particle patterns were tracked between temporally adjacent images and the velocity field inferred with a spatial resolution of 8 px, or 0.16 mm.

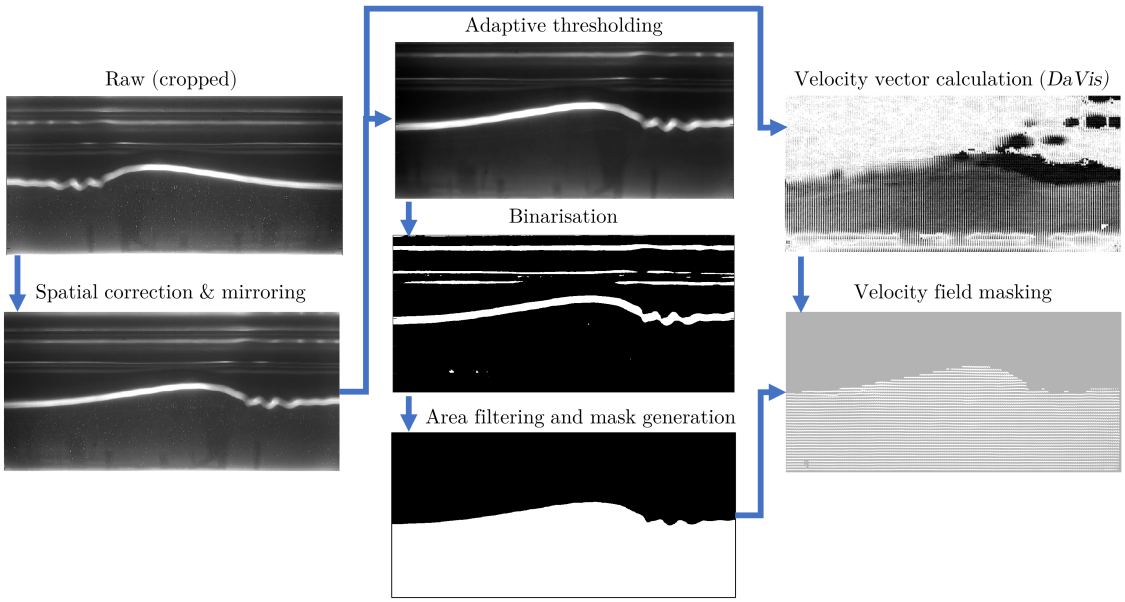
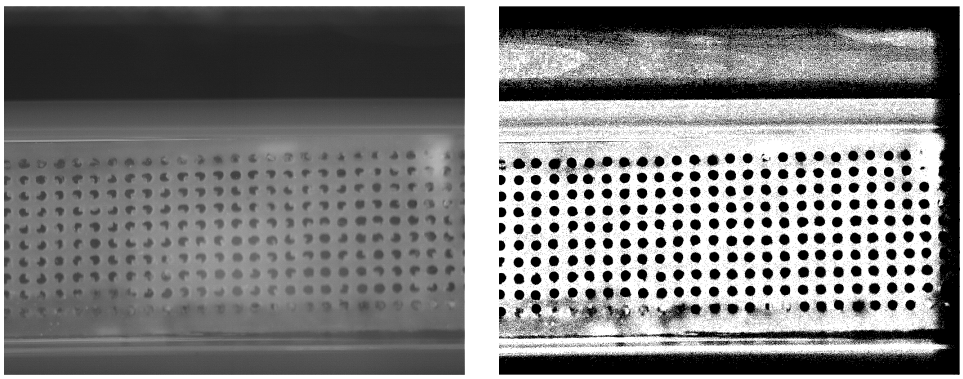


Figure 3.13: Example images at each stage of the image processing procedure.

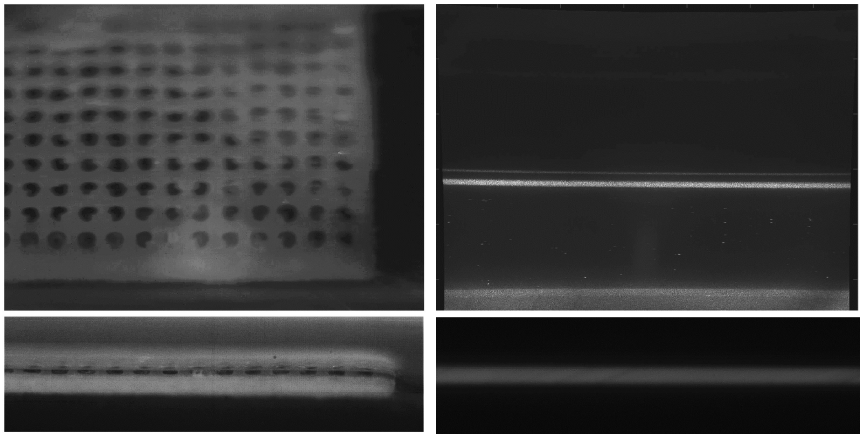


(a) (b)

Figure 3.14: Example images of calibration target inserted into the liquid flooded pipe in (a) raw and (b) binarised form. The centres of the circles on the target are exactly 1 mm apart.

(c) The resulting vector field was loaded into MATLAB using the *pivmat* toolbox and multiplied by the mask generated in step 2(e). This masking was applied after generating the velocity fields to ensure that the velocity field close to the interface was adequately captured.

The mean absolute uncertainty in the interface locations detected using the PLIF methods described in this chapter was evaluated based on the standard deviation of the measured interface height for flat liquid interfaces and found to be ± 0.16 mm, which is equal to approximately ± 8 px. The uncertainty in instantaneous velocity measurements was determined based on single phase validation of the PIV results, discussed further in



(a) (b)

Figure 3.15: Image calibration for BBLIF and PLIF with (a) example images of calibration target in the liquid-flooded pipe captured by the PLIF camera (top) and BBLIF camera (bottom) - see Fig. 3.9 for arrangement. (b) Brightness calibration with stable liquid film captured by PLIF camera (top) and BBLIF camera (bottom).

Section 3.8.2 and found to be approximately 6 %. Uncertainties in velocity profiles are reported as the standard deviation along the axial direction of the velocity at a given vertical (y) coordinate. This results in an average error of approximately $\pm$ 30 % of the measured value, although this is typically larger towards the interface and pipe wall.

3.6.3 BBLIF and PLIF for annular flows

Two sets of images were obtained from the BBLIF and PLIF cameras shown in Fig. 3.9. For both, the first processing step was a spatial correction based on insertion of a calibration target into the flooded pipe as shown in Fig. 3.15a. The calibration target was aligned with the laser plane and contained a grid of circular holes exactly 1 mm apart centre-to-centre. The end of the target and the horizontal line within the circular pattern were used to identify the relative location of the fields of view of the two cameras. The field of view of the PLIF camera was completely contained within that of the BBLIF camera, corresponding to 93 % of the width of the image. The resulting resolutions of the PLIF and BBLIF cameras were 11.6 µm/px and 11.8 µm/px respectively.

The PLIF images were then treated as described in Section 3.6.2, whilst a different approach based on that described by Cherdantsev et al. [17] was required to obtain the film thickness signal from the brightness recorded in the BBLIF images. The first step in this approach involved identifying the centreline of the illuminated flow area (i.e. the light area in the bottom image of Fig. 3.15b) and forming a matrix of local, instantaneous

raw brightness values with space and time (i.e. number of frames) dimensions. These brightness values were then converted into film thickness estimates using the Beer-Lambert law which, following the procedure used by Alekseenko et al. [193], leads to the expression:

$$J(z) = C(z)\left(1 - e^{-\alpha h(z)}\right)\left(1 + Ke^{-\alpha h(z)}\right) + D(z) \tag{3.22}$$

where $J(z)$ is the fluorescence brightness registered by a single camera pixel, $C(z)$ is a compensation matrix, α is the absorption coefficient of the rhodamine 6G fluorescent dye, K is the reflection coefficient at the vapour-liquid interface, $D(z)$ is the dark level of the camera and $h(z)$ is the film thickness at the axial position z. This equation accounts for the fraction of the light that is reflected back at the vapour-liquid interface and re-excites the dye, leading to a secondary fluorescence emission in addition to that from the initial excitation, by assuming that both the primary and secondary light rays are collinear and fully-overlapping. This is not the case in practice, and off-axis reflections can result in an overestimation of the corresponding film thickness by up to 50 % [17], depending on the interface angle.

From Eq. (3.22), K was set to a constant value of 0.02, but α is dependent on the dye concentration. A base estimate for α was obtained by creating two static liquid films of known thicknesses in the visualisation section and collecting images to measure the corresponding brightness, as shown in Fig. 3.15b. These two sets of values were inserted into Eq. (3.22) and solved numerically to give an estimate for α. The resulting form of Eq. (3.22) is plotted as the solid black line in Fig. 3.16, with the experimental data points shown as blue circles. Since the flow boils, the dye concentration in the liquid phase increases above the base value during the experiments, resulting in higher fluorescence intensities. This was accounted for based on the measured vapour quality and an example for $x = 0.15$ is plotted as a dashed black line in Fig. 3.16. It can be seen from Fig. 3.16 that as the film becomes thicker the intensity signal becomes saturated, limiting the film or wave height that can be measured. These measurements at a known liquid layer height can also be used as a reference signal, with time-averaged brightness $\langle J_0(z)\rangle$ and thickness h_0, for obtaining the compensation matrix $C(z)$ as follows:

$$C(z) = \frac{\langle J_0(z)\rangle - D(z)}{(1 - e^{-\alpha h(z)})(1 + Ke^{-\alpha h(z)})} \tag{3.23}$$

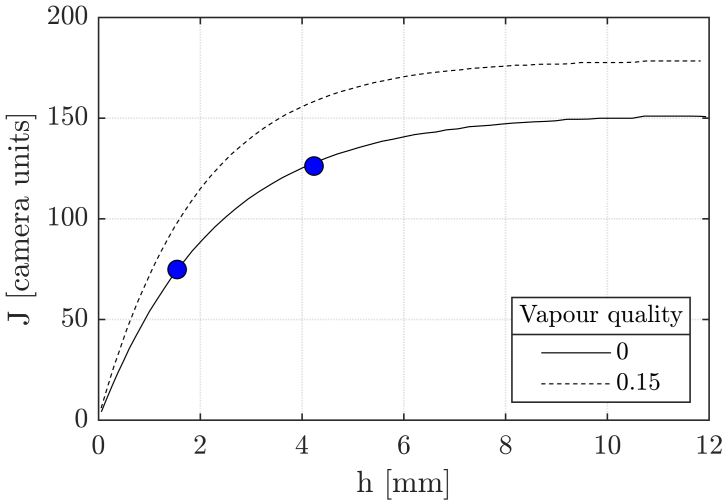


Figure 3.16: Image intensity as a function of film height with calibration data points (blue circles) and Eq. (3.22) fitted to the data (solid line) and adjusted for evaporation to a vapour quality of 0.15 (dashed line) as an example.

This compensation matrix converts the measured brightness to a film thickness estimate, and accounts for both non-uniform energy distribution along the laser sheet and the spatially non-uniform response of the camera sensor. A similar reference signal was used by Alekseenko et al. [194] and Alekseenko et al. [193]. Although the refrigerant temperature varies by up to approximately 20 K, the emission from Rhodamine 6G is not significantly affected by temperature so this effect does not need to be included in Eq. (3.23). Also, the system pressure was held constant (with a variation of < 0.06 bar) across the annular flow experiments so that the vapour-liquid equilibrium in the system did not change, as this would alter the base dye concentration in the liquid. In addition to the considerations described so far, it is important to correct for the dark level of the camera, $D(z)$. This increases over time, so dark-level measurements were taken periodically throughout the experimental campaign.

The final aspect to consider for BBLIF measurements is that of the measurement limitations due to the geometrical placement of the laser sheet and high-speed cameras. When the BBLIF camera is inclined at 9° to the excitation plane, the field of view traverses the thickness of the laser sheet (approximately 1 mm) diagonally, limiting the maximum measurable film thickness to approximately 4 mm. Any liquid film above this height will not contribute to the brightness detected by the camera, so the measured intensity will seem to saturate and the film thickness will be underestimated. A thicker laser sheet would decrease this error but will exacerbate other errors due to interfacial reflections,

and will require increased spatial averaging. Alternatively, a 3-D BBLIF technique could be employed, such as that of Alekseenko et al. [195] and Cherdantsev et al. [196].

The experimental error in BBLIF film thickness measurements will be mainly determined by the camera noise, non-uniformity in the camera sensitivity and pulse-to-pulse variation in the laser and is typically around 10 % [17]. However, internal reflections at the interface due to the presence of bubbles will contribute to significantly higher local errors. This could be overcome by using multiple PLIF cameras positioned at different locations around the illumination plane to identify bubble both in and out of the laser plane.

3.7 Test fluid

3.7.0.1 Test section design and fluid selection

In DSG solar collectors, one of the key applications for this work, water boils at pressures of up to 100 bar, at which the saturation temperature of water is approximately 300 °C. The collector tubes typically have inside diameters of 38 mm, 54 mm and 97 mm. The lengths and heat input required to investigate flow boiling in pipes of these sizes are prohibitively large for lab-scale experiments, as are the pressures and temperatures required to boil water. Therefore, alternative test fluids and geometries were considered. Hydrocarbon test fluids such as pentane and cyclopentane were considered, but were dismissed due to safety concerns over the explosive and/or flammable natures of the fluids. Refrigerants, which generally boil at much lower temperatures than water, were good test fluid candidates, particularly with the large amount of literature available on refrigerant flow boiling.

It was important to ensure that the experimental pipe diameter of the test section was of a similar order to that of the DSG application, since heat transfer and multiphase flow in smaller pipes is dominated by different forces and mechanisms. Also, for boiling in the experiment to be comparable to that in the application, the ratio of bubble departure diameter, d_b to pipe inside diameter should remain constant. The bubble departure diameter is the diameter of a bubble at the moment it detaches from the heated tube wall. An analysis by Fritz [197] taking into account buoyancy and surface tension effects yields the following proportional relationship between d_b, the capillary length, L_cap, and

Table 3.3: Experimental parameters of considered refrigerants. Fluid property data from various sources [199–202].

		R123	R150a	R22	R245fa
$T_{\mathrm{sat}}(p = 1\,\mathrm{atm})$	K	301	330	232	288
n_{l}		1.33	1.42	1.26	1.25
d_{pipe}	mm	4–49	5–62	3–42	4–47

the fluid properties:

$$d_{\mathrm{b}} \propto L_{\mathrm{cap}} = \sqrt{\frac{\sigma}{g(\rho_{\mathrm{l}} - \rho_{\mathrm{v}})}}. \tag{3.24}$$

However, this is a highly simplified model with large inaccuracies, particularly at high heat fluxes. Hamzekhani et al. [198] reported that the oversimplifications in the model can result in an error of over 60 %. When calculating the required experimental pipe diameter, the use of the ratio of the two bubble diameters then results in compound errors of more than 85 %. The corresponding ranges of d_{pipe} for four different refrigerants are reported in Table 3.3 along with the saturation temperature at atmospheric pressure and the liquid refractive index, n_{l}.

All the refrigerants in Table 3.3 had similar ranges for the required experimental pipe diameter based on d_{b}. However, it was also desirable for the test fluid to have a saturation temperature such that boiling could easily be achieved in the laboratory, and a refractive index as low as possible to enable optical measurements. As such, R245fa was selected. It is also readily available, not classified as hazardous to health and is non-reactive and non-corrosive towards all commonly used metals and most plastics. Additionally, despite it currently being one of the most common working fluids in organic Rankine cycle (ORC) systems there is a relative scarcity of data in the literature for boiling in pipe diameters above the 'mini' scale (i.e. $d > 3\,\mathrm{mm}$ [14]), so there is a real opportunity for this work to fill a literature gap.

3.7.1 Property analysis

Since fluorescent dye was added to the test fluid, it was necessary to determine the effect of this on fluid properties to ensure correct interpretation of the results. The surface tension and density of R245fa samples with different dye concentrations up to 10 ppm were measured using the maximum bubble pressure method, in which a fine-tipped quartz

capillary is gradually lowered into the R245fa samples under a low flowrate of argon ($< 0.5\,\mathrm{ml/min}$). When the capillary tip is below the liquid surface, a bubble forms, as illustrated in Fig. 3.17a. As the pressure increases, the bubble grows to the size of the capillary tip at which point a maximum pressure, p_{max}, is reached and the bubble detaches, causing a decrease in pressure. An example of this cyclic pressure behaviour is shown in Fig. 3.17c. A reference pressure, p_{ref}, was obtained by lowering the capillary tip to the surface of the liquid and recording the pressure just before it increased, i.e. just above the surface of the liquid. The pressure throughout the experiment was recorded using an Omega PX-409 pressure transmitter, and the fine capillary was characterised using a Labsun 14.0 MP HDMI optical microscope to measure its radius, r_{cap}. To keep the R245fa samples in liquid form, the experiments were conducted in an ice bath which maintained a temperature of approximately 3 °C. The temperature of the liquid sample was measured using an ETI digital reference thermometer.

Three sets of measurements were recorded for each sample, with five measurement depths recorded in each set to obtain profiles as a function of liquid depth, examples of which are given in Fig. 3.18. The gradient of the plot of p_{max} vs. depth is equal to ρg, where ρ is the liquid density and g gravitational acceleration. The surface tension, γ was calculated based on the Young-Laplace equation:

$$\gamma = \frac{\Delta p r_{\mathrm{cap}}}{2} = \frac{(p_{\mathrm{max}} - p_{\mathrm{min}}) r_{\mathrm{cap}}}{2} \tag{3.25}$$

where the minimum pressure, p_{min}, was calculated using p_{ref} and accounting for the rise in liquid level due to displacement by the capillary tube and thermometer.

Before using this method for analysis of R245fa samples, it was validated using deionised water. The average deviations in density and surface tension from the literature values were $-0.3\,\%$ and $+4.6\,\%$ respectively.

A representative set of results for R245fa with 7.5 ppm of Rhodamine-6G are displayed in Fig. 3.18. The gradient of the line in Fig. 3.18a gives $\rho = 1386\,\mathrm{kg/m^3}$, $0.5\,\%$ lower than the literature value for pure refrigerant at the same conditions. The mean absolute deviation of the density from the literature value over the sample set was $5.0\,\%$, and was not a function of dye concentration. The measured surface tension, corrected for temperature variations, is show in Fig. 3.18b as a function of depth for the same sample described previously in this paragraph. The mean absolute deviation of the surface tension

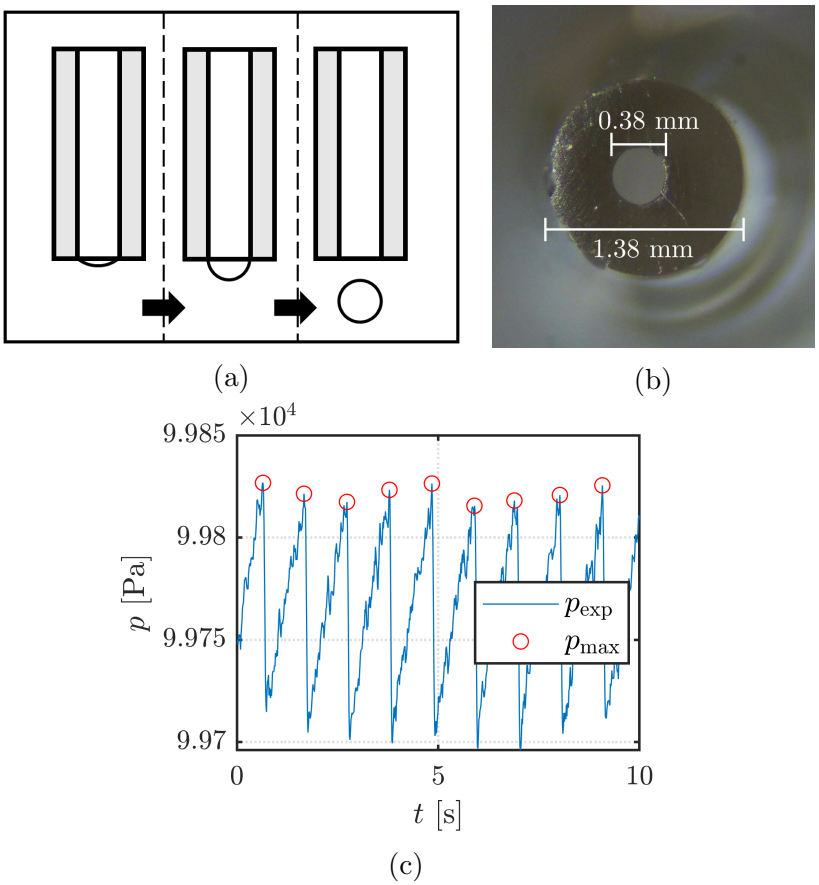


Figure 3.17: Illustrations of the maximum bubble pressure method: (a) describes the formation, growth and detachment of a gas bubble at the capillary tip; (b) shows an optical microscope image used to characterise the capillary tip; (c) shows a sample pressure trace against time t, where the peaks of $p_{\max}$ have been identified and correspond to the point of maximum bubble size and subsequent detachment.

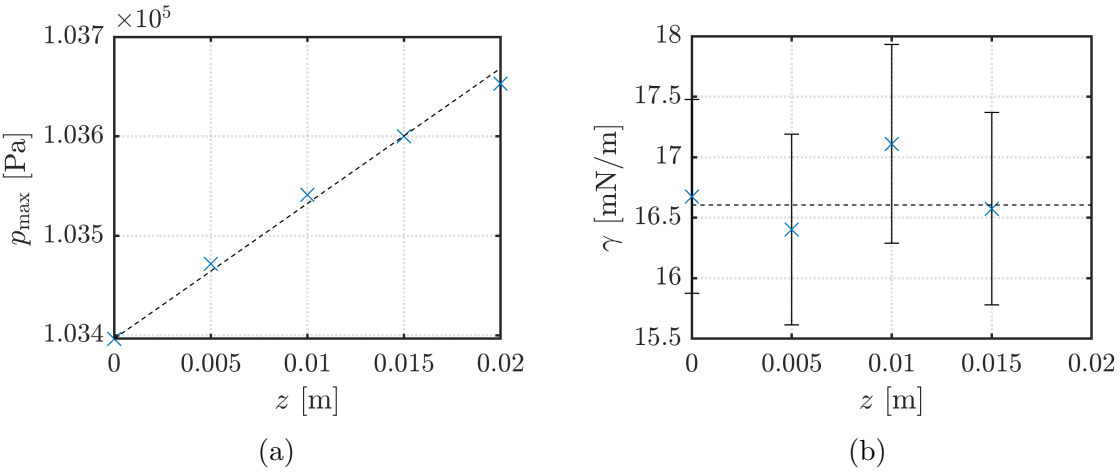


Figure 3.18: Representative data collected using the maximum bubble pressure method for R245fa with a dye concentration of 7.5 ppm. The gradient of the line in (a) is equal to ρg, and gives $\rho = 1386\,\mathrm{kg/m^3}$, 0.5 % lower than the theoretical density of pure refrigerant at the same conditions. In (b) the temperature-corrected surface tension values are plotted against immersion depth z, with the literature value indicated by the dashed line.

from the literature value was 5.1 % and was also not a clear function of dye concentration at the values measured.

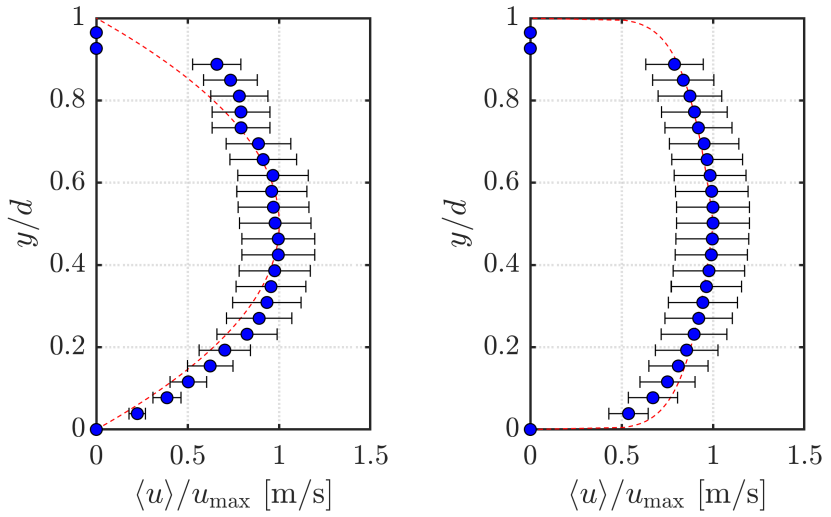
3.8 Facility commissioning and validation

3.8.1 Single phase validation of integral measurements

To validate the performance of the FLOBOF system and measurement instruments, experiments were performed with single phase liquid R245fa flow under both adiabatic and heated conditions, with care taken to monitor the visualisation section for the appearance of bubbles that would indicate the onset of boiling and invalidate the single phase tests. The resulting Nusselt numbers were compared to those calculated using the Meyer et al. [203] correlations to within an average deviation of 7 %. The pressure drop data were compared to the Fang et al. [74] correlation with an average deviation of 8 %. The mean deviations for both values are well within 10 % and the facility can be considered validated.

3.8.2 Single phase validation of PIV measurements

The PIV method described in Section 3.6.2 was validated by assessing the single phase flow rate velocity profiles for a range of conditions and comparing them to the parabolic



(a) Laminar (b) Turbulent

Figure 3.19: Single phase liquid flow velocity profiles from PIV measurements normalised by maximum velocity and pipe diameter (blue crosses) and theoretical predictions (red dashed line) for (a) laminar and (b) turbulent flows.

velocity profile for laminar flow, and the power law velocity profile for turbulent flow with $n = 7$. Figure 3.19 shows these velocity profiles, normalised by $u_{\max}$ and averaged across all relevant single phase cases to give a representative liquid phase streamwise velocity profile for both laminar and turbulent flows. The resulting profiles match the theoretical predictions of Eqs. (3.26) and (3.27) very closely, particularly in the centre of the pipe. Towards the pipe walls the glow of the translucent FEP pipe as it is illuminated by the laser sheet can distort the light scattered by the PIV particles, causing large uncertainties in the measurements and poor agreement with theory.

$$\text{Laminar:} \quad u/u_{\max} = 1 - \left(\frac{r}{r_{\text{pipe}}}\right)^2 \tag{3.26}$$

$$\text{Turbulent:} \quad u/u_{\max} = \left(1 - \left(\frac{r}{r_{\text{pipe}}}\right)\right)^{1/n} \tag{3.27}$$

To validate the absolute values of the streamwise velocity obtained with PIV, a flowrate and subsequently mass flux were calculated based on these measurements and compared to that measured using the flowmeter. For each validation case, the velocity profile was integrated across the pipe assuming a parabolic decay of the velocity towards the pipe wall from its maximum value at the centreline. The resulting mass flux values are plotted against the corresponding mass flux based on the flowmeter measurement in Fig. 3.20.

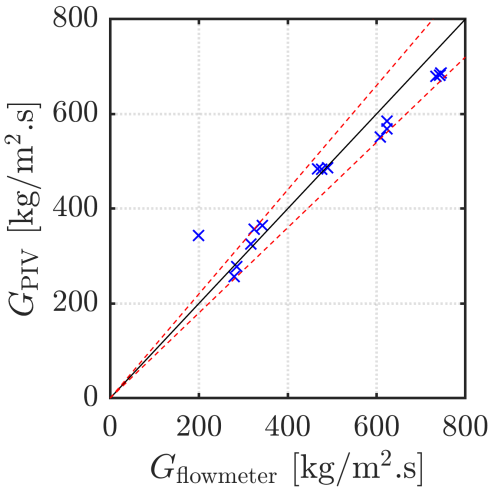


Figure 3.20: Mass flux G calculated based on PIV measurements versus flowmeter measurements for single phase liquid flow. The solid black line represents $G_{\mathrm{PIV}} = G_{\mathrm{flowmeter}}$, whilst the red dashed line represents $G_{\mathrm{PIV}} = G_{\mathrm{flowmeter}} \pm 10\%$.

The majority of points are within 10 % of the flowmeter value, with an average absolute deviation of 6 %. There is one outlier at $G_{\mathrm{flowmeter}} \approx 200$ kg/m^2.s, where some vapour may have been present in the flow, impacting the flowmeter reading.

Chapter 4

Computational Methods

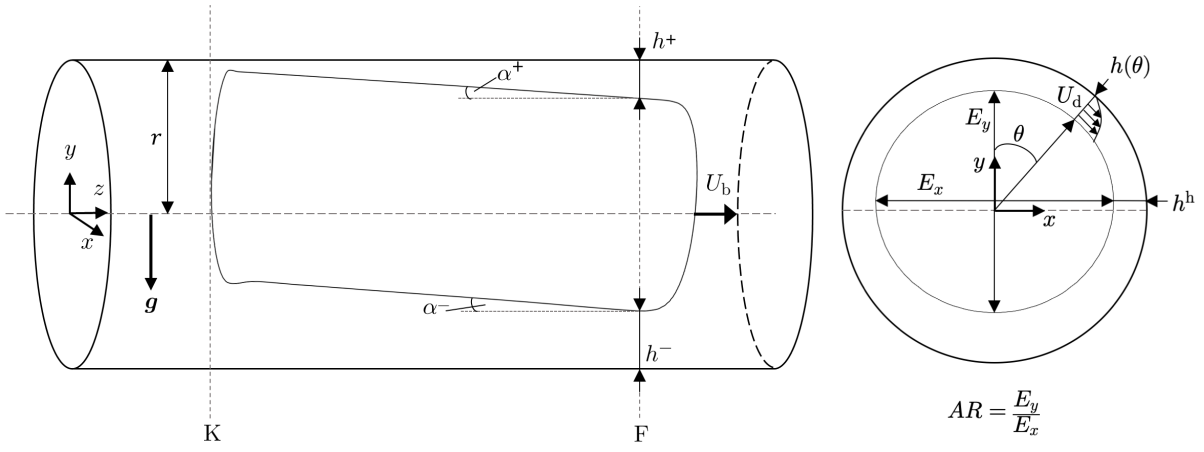
In this work, simulations have been performed for adiabatic multiphase flows and for heated multiphase flows with evaporation. This chapter is therefore divided into two parts with descriptions of the numerical models applied to the different flow conditions.

4.1 Numerical model for multiphase flow

4.1.1 Problem description

The adiabatic multiphase flow problem considered in this work is an elongated bubble travelling at a velocity U_b along a horizontal channel of circular cross-section with radius r (diameter d), through which liquid flows at an average velocity U_l. A representative sketch of the flow problem is shown in Fig. 4.1. The coordinate z is directed downstream, whilst the coordinates x and y represent the horizontal and vertical axes, respectively, with the origin located at the centre of the channel. The flow is subject to a gravitational acceleration, $\mathbf{g}$, acting in the negative y-direction.

In the absence of buoyancy effects, a region of constant film thickness between the bubble nose and tail exists. However, this does not happen in the case of non-negligible buoyancy effects, because the bubble is inclined in the channel [169, 170]. Therefore, the film thicknesses reported in this paper are extracted not at the very front of the bubble, but behind the bubble nose to ensure film development. This location is given the signifier 'F' and is defined as the z-value at which the minimum film thickness around the lower half of the bubble, h^-, occurs, with a corresponding film thickness at the top of the bubble h^+; see Fig. 4.1. The film thickness is non-dimensionalised with the channel



(a) (b)

Figure 4.1: Sketches of an elongated gas bubble flowing in a horizontal tube filled with liquid, and notation used in this work. (a) Two-dimensional bubble profile extracted on a vertical centreline plane, where $x = 0$. (b) Bubble cross-sectional profile extracted on an arbitrary x-y plane. In (a), position 'K' indicates the most upstream point of the bubble interface; position 'F' identifies the location of the lowest point of the bubble interface, which in this work is selected as the location where the film thicknesses are measured.

radius r, such that $H = h/r$, and all subsequent film thicknesses in this work are reported as dimensionless values (H^+ and H^-) at location F. The inclination angles at the top and bottom of the bubble, α^+ and α^- are calculated by considering the slopes of the developed middle regions of the bubble profile upstream of the nose but downstream of the tail, quantified as the region $2d$ up- and downstream of the centre of the bubble lengthwise.

The back of the bubble, location K, is defined as the minimum z-value in the bubble profile. From this point, the z-dimension will be non-dimensionalised in the manner $(z - z_\mathrm{K})/r$, thus always referring to coordinates relative to the back of the bubble tail. The bubble aspect-ratio in the cross-section, AR, describes the ovalisation of the bubble on the $x - y$ plane and is defined as $AR = E_y/E_x$. E_y is the maximum extension of the bubble along the vertical direction, which always occurs along the $y-$axis, and E_x is the maximum extension of the bubble along the horizontal direction, the location of which shifts above the $x-$axis as buoyancy effects become important (see Fig. 4.1b) and the whole bubble elevates above the channel axis. Note that $AR = 1$ corresponds to an exactly axisymmetric bubble (i.e. negligible gravity effects), whereas buoyancy tends to reduce the vertical extension of the bubble, leading to $AR < 1$.

Besides the top and bottom film thicknesses (both evaluated along the vertical $x = 0$

axis), a horizontal film thickness h^h is defined as the horizontal distance between the bubble interface and the tube wall, calculated along the same line as the maximum bubble extension E_x (see Fig. 4.1b). Figure 4.1b also includes a schematic representing the velocity profile in the liquid film region, on the cross-section of the channel. Along a radial line extending from the liquid-gas interface to the pipe wall, where the film has thickness $h(\theta)$, the velocity profile is parabolic due to the no-slip condition at the wall and the negligible tangential stress exerted by the gas phase at the interface. The average drainage velocity of the liquid in the film, obtained by integrating this velocity profile, is denoted as U_d and is a function of the circumferential angle, $U_\mathrm{d}(\theta)$. In this work, h^h, AR and U_d are always extracted on a cross-section located at position F.

The flow is assumed to be laminar and incompressible, and the two phases Newtonian and immiscible. The Reynolds number is defined as $\mathrm{Re} = \rho U d/\mu$ where the density ρ and the dynamic viscosity μ are those of the liquid, but the velocity U can be that of the bubble (U_b) or liquid (U_l). The capillary number is similarly defined as $\mathrm{Ca} = \mu U/\gamma$, where γ is the interfacial tension. The Weber number is then defined as $\mathrm{We} = \mathrm{Re}\,\mathrm{Ca} = \rho U^2 d/\gamma$. The results in this study are mostly reported as functions of the liquid dimensionless numbers, since simulations can be easily initialised for fixed values of these and in experimental studies of isolated bubble flow the liquid flow rate is usually the controlled parameter. The buoyancy effects are characterised by the Bond number, $\mathrm{Bo} = (\rho_\mathrm{l} - \rho_\mathrm{g}) g r^2/\gamma \backsimeq \rho_\mathrm{l} g r^2/\gamma$, where the gas density is assumed to be negligible compared to that of the liquid.

4.1.2 Numerical method

The numerical framework is based on OpenFoam's built-in VOF solver *interFoam* [204]. This solves the single-fluid continuity and momentum conservation equations for a Newtonian fluid in incompressible flow in the following form:

$$\nabla \cdot \mathbf{u} = 0 \tag{4.1}$$

$$\frac{\partial(\rho \mathbf{u})}{\partial t} + \nabla \cdot (\rho \mathbf{u}\mathbf{u}) = -\nabla p + \nabla \cdot \mu[(\nabla \mathbf{u}) + (\nabla \mathbf{u}^T)] + \rho \mathbf{g} + \mathbf{F}_\gamma \tag{4.2}$$

where $\mathbf{u}$ is the fluid velocity vector, $\mathbf{g}$ is the gravitational acceleration vector, and $\mathbf{F}_\gamma$ is the surface tension force. The fluid properties ρ and μ are defined as average properties

weighted by the volume fraction α as follows:

$$\rho = \rho_1\alpha + \rho_2(1-\alpha) \tag{4.3}$$

$$\mu = \mu_1\alpha + \mu_2(1-\alpha) \tag{4.4}$$

where the subscripts 1 and 2 denote the primary and secondary phases, respectively. α is defined as the ratio of the cell volume occupied by the primary phase, so is equal to 1 in a cell filled with the primary phase and 0 in a cell filled with the secondary phase, and is in the range $0 < \alpha < 1$ for an interfacial cell containing both phases. The fluid properties ρ_1, μ_1, ρ_2 and μ_2 are considered constant in this work. The surface tension force $\mathbf{F}_\gamma$ in Eq. (4.2) is formulated as a body force according to the continuum surface force (CSF) method proposed by Brackbill et al. [205] as $\mathbf{F}_\gamma = \gamma\kappa\nabla\alpha$, where the surface tension coefficient γ is considered to be constant and κ is the local interface curvature. The latter is estimated by means of derivatives of the volume fraction field, $\kappa = -\nabla\cdot\mathbf{n}$, where $\mathbf{n}$ is the interface unit normal vector, $\mathbf{n} = \nabla\alpha/|\nabla\alpha|$.

InterFoam solves the volume fraction equation by including an artificial compressive term to counteract numerical diffusion at the interface:

$$\frac{\partial\alpha}{\partial t} + \nabla\cdot(\alpha\mathbf{u}) + \nabla\cdot(\alpha(1-\alpha)\mathbf{U_r}) = 0 \tag{4.5}$$

where the artificial compressive velocity $\mathbf{U_r}$ is given by:

$$\mathbf{U_r} = \min\left[C_\alpha\frac{|\phi|}{|\mathbf{S_f}|}, \left(\frac{|\phi|}{|\mathbf{S_f}|}\right)_{max}\right]\mathbf{n_f} \tag{4.6}$$

Here, ϕ is the volumetric flux through the control volume face, $\mathbf{S_f}$ is the surface area vector of the cell face, $\mathbf{n_f}$ is the unit normal vector to the interface evaluated at the control volume face, and C_α is a numerical multiplier used for tuning of the interface compression. For this study, the default value $C_\alpha = 1$ [165, 204, 206] has been used since it presents an appropriate compromise between interface sharpness and accuracy of the surface tension calculation.

The flow equations are discretised based on a finite-volume discretisation in a co-located grid arrangement. Eq. (4.5) is discretised based on the Multidimensional Uni-

versal Limiter with Explicit Solution (MULES) algorithm, a first-order time-explicit scheme. The temporal discretisation of the remaining equations follows a first-order implicit scheme. The divergence terms are discretised with second-order upwind schemes, whereas the Laplacian terms utilise second-order central finite-difference schemes. The pressure and velocities are iteratively updated within each time step using the Pressure Implicit Splitting of Operators (PISO) algorithm [207], with the number of correctors set to 3. The residual thresholds for the iterative solution of the flow equations were set to 10^{-6} for velocity, 10^{-8} for volume fraction, and 10^{-7} for pressure. A variable time-step was adopted for the progress of the solution, the value of which is calculated by the solver in accordance with an assigned maximum Courant number of $\mathrm{Co} = 0.4$.

4.1.3 Simulation set-up

The simulated geometry consists of a channel of circular cross-section with radius r, modelled with a 3-D mesh, through which liquid flows at an average velocity U_l. A channel length of $100r$ was simulated to allow for full development of the flow. At the inlet, a uniform liquid velocity profile was fixed, along with a zero-gradient pressure condition. At the outlet, the velocity was subject to a zero-gradient condition whilst the pressure was set to a uniform reference value. No-slip was imposed at the walls along with a zero-gradient pressure condition. A bubble was initiated close to the inlet at the centre of the channel with a radius of $0.9r$ and a length of $20r$ to ensure full development of the liquid film between the nose and tail across the whole parameter space [208]. The liquid to gas density and viscosity ratios were set to 1000 and 100, respectively.

The computational grid, the $x - y$ cross-section of which is depicted in Fig. 4.2, was a block-structured mesh. The core of the domain was discretised with a uniform cubic mesh. Outside of this central core, the mesh was refined radially towards the wall, allowing accurate capture of the liquid film dynamics without the computational expense of a universally fine mesh. For accurate simulations of liquid films, Gupta et al. [172] recommended that there should be at least 5 cells in the liquid film in the radial direction.

4.1.3.1 Mesh independence study

To determine the optimum mesh configuration, a preliminary grid convergence study was performed, starting with the conditions $\mathrm{Ca_l} = 0.024$, $\mathrm{Bo} = 0.42$, and $\mathrm{Re_l} = 1$. These

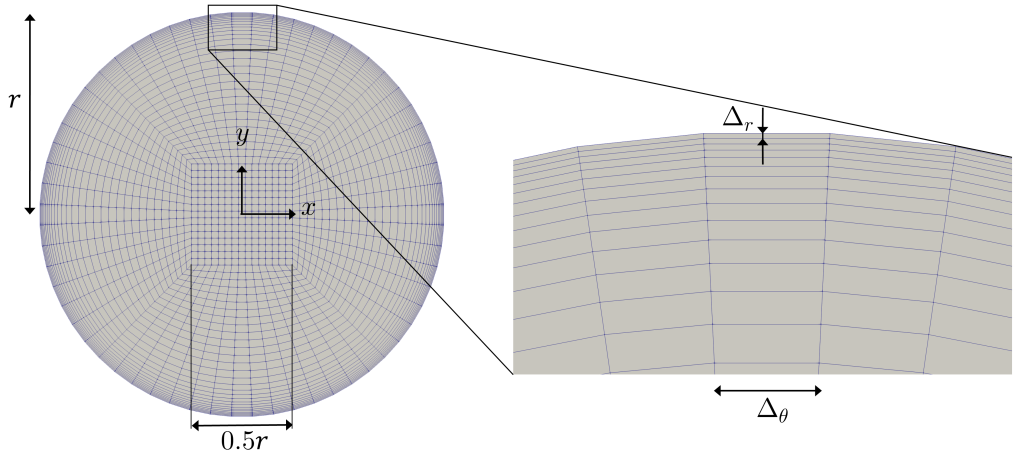
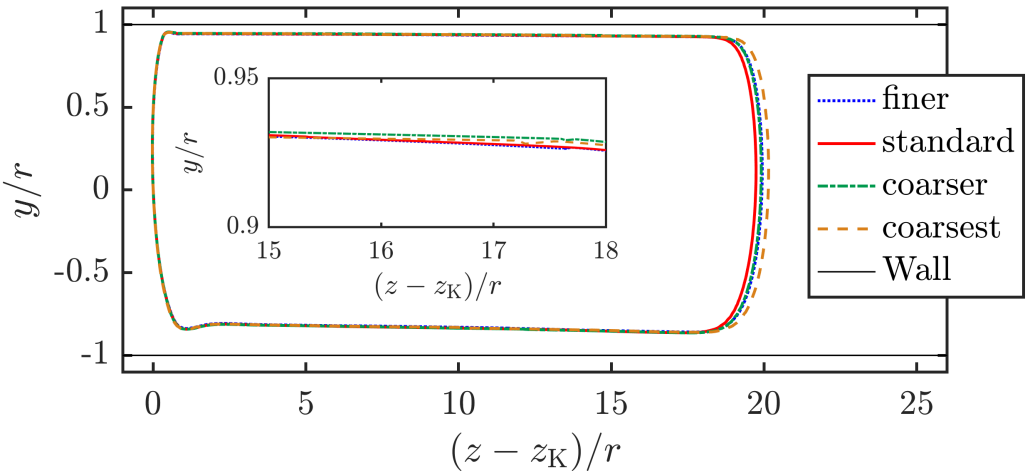


Figure 4.2: Illustration of the x-y cross-section of the computational mesh. The core consists of a square rod of size $0.5r \times 0.5r$ meshed with uniform cubes, outside of which the mesh is gradually refined radially towards the wall. At the wall, the size of the elements along the radial and circumferential directions are denoted as Δ_r and Δ_θ, respectively. For the mesh depicted here, $\Delta_r = 0.0041r$ and $\Delta_\theta = 0.105r$.

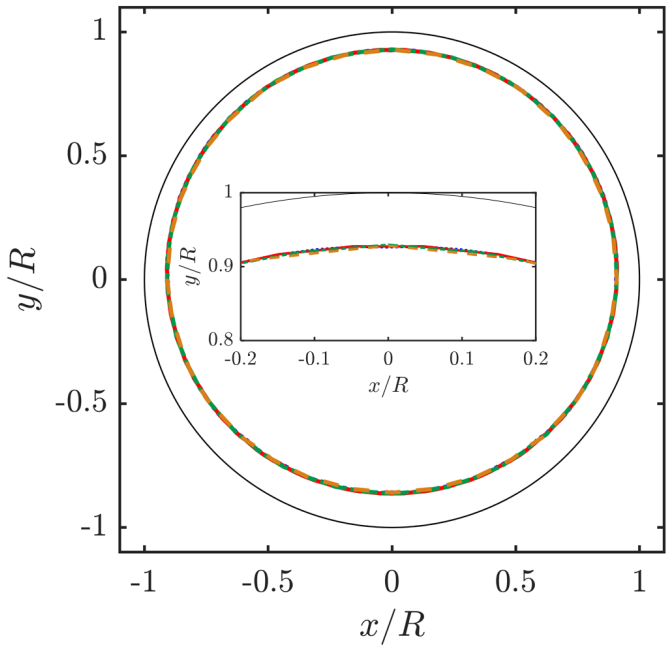
conditions were characterised by a minimum film thickness at the bubble top of $H^+ \approx 0.07$.

Four different meshes with different levels of refinement were considered and the geometrical parameters characterising each are reported in Tab. 4.1 and illustrated in Fig. 4.2. The first set of conditions tested was $\mathrm{Ca_l} = 0.024$, $\mathrm{Bo} = 0.42$, and $\mathrm{Re_l} = 1$, and the resulting bubble profiles are displayed in Fig. 4.3. The differences among the standard and finest meshes are imperceptible, and the change in the top film thickness is 1.5%. The second set of conditions tested was $\mathrm{Ca_l} = 0.024$, $\mathrm{Bo} = 0.42$, and $\mathrm{Re_l} = 750$, and the resulting bubble profiles are displayed in Fig. 4.4. Even for this case, the bubble profiles and top film thickness can be considered converged when using the standard mesh, proving the applicability of this mesh to larger values of $\mathrm{Re_l}$. Therefore, the standard mesh was used throughout most of this work, providing $H^+ \geq 0.04$ (at least 7 cells discretising the film). For conditions leading to thinner films, the finest mesh was used, ensuring an adequate number of cells within the thin liquid film even when Bo was large.

For model validation (see Section 7.1.2), the results of 2-D simulations, with the gravitational force vector acting transversal to the flow direction, are presented alongside the 3-D cases. The 2-D set-up and boundary conditions are analogous to the 3-D, and an orthogonal mesh with near-wall refined elements is employed to have a minimum of 10 cells resolving the flow in the thin liquid film.

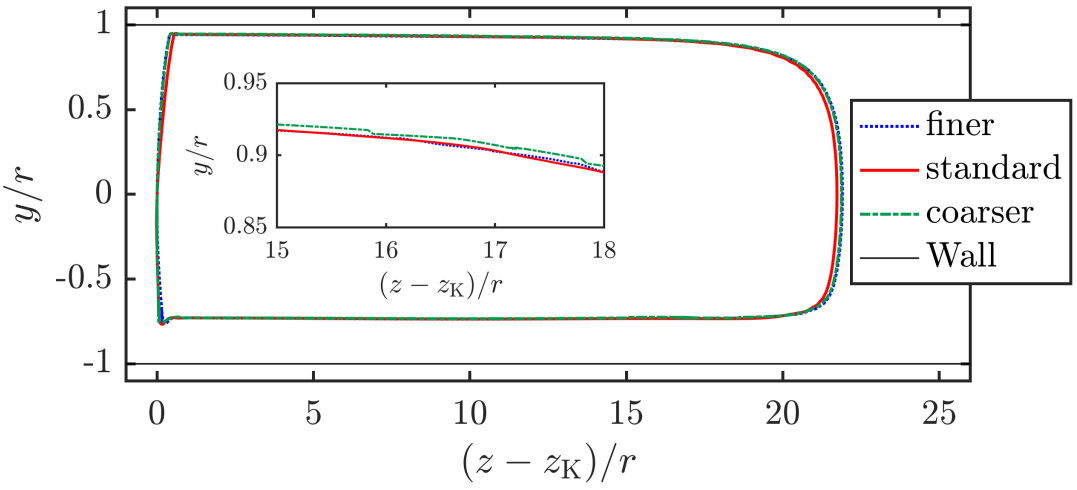


(a)

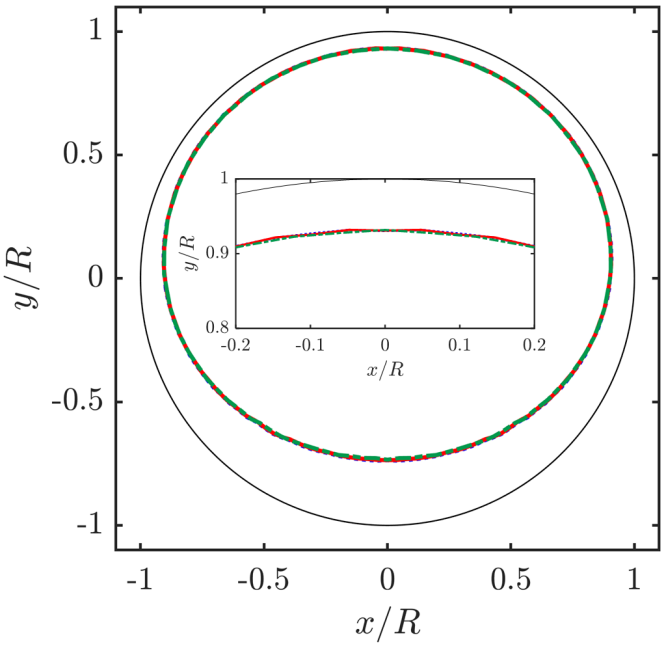


(b)

Figure 4.3: Mesh independence study for conditions $\mathrm{Ca_l} = 0.024$, $\mathrm{Bo} = 0.42$, and $\mathrm{Re_l} = 1$: (a) bubble profile on a vertical centreline plane ($x = 0$) and (b) bubble cross-sectional shape at the location F (see Fig. 4.1). The geometric details of the meshes and corresponding values of the top film thickness at F are reported in Tab. 4.1.



(a)



(b)

Figure 4.4: Mesh independence study for conditions $\mathrm{Ca_l} = 0.024$, $\mathrm{Bo} = 0.42$, and $\mathrm{Re_l} = 750$: (a) bubble profile on a vertical centreline plane ($x = 0$) and (b) bubble cross-sectional shape at the location F (see Fig. 1 in the article). The geometric details of the meshes and corresponding values of the top film thickness at F are reported in Tab. 4.1.

Table 4.1: Geometrical details of the meshes tested and corresponding values of the top film thickness evaluated at F, for the simulation cases illustrated in Fig. 4.3 and 4.4. Δ_r and Δ_θ denote the radial and circumferential size of the mesh elements at the wall (see Fig. 4.2), while Δ_z indicates the longitudinal extension of the cell, which is constant across each mesh. The top film thickness H^+ is evaluated at the location F (see Fig. 4.1).

Mesh	Δ_r/r	Δ_θ/r	Δ_z/r	H^+ ($\mathrm{Re_l} = 1$)	H^+ ($\mathrm{Re_l} = 750$)
Finer	0.0023	0.1040	0.0333	0.0737	0.0715
Standard	0.0041	0.1046	0.0333	0.0728	0.0706
Coarser	0.0067	0.1298	0.0423	0.0704	0.0690
Coarsest	0.0090	0.1947	0.0624	0.0718	

4.2 Numerical model for multiphase flow with phase change

4.2.1 Problem description

Two flow boiling problems have been simulated in this work: boiling of a single bubble in a square micro-channel, and stratified flow boiling in a geometry equivalent to that of the FLOBOF facility (see Section 3.2.2) at selected conditions from experiments performed. The characteristics of these two problems are described in this section.

4.2.1.1 Micro-channel validation

The micro-channel boiling problem considered in this work is that of a single bubble growing from the bottom wall of a horizontal micro-channel with a square cross-section of width $w = 229\,\mu\mathrm{m}$ to match the experimental validation performed by Mukherjee et al. [152]. A representative sketch of the flow is shown in Fig. 4.5. Liquid flows in the channel at a velocity U_l and bubble nucleation is emulated by initiating a bubble of 25 µm radius at an axial distance of $1w$ into the channel with a contact angle of 30°, as determined by the experiments of Mukherjee et al. [152]. The growth of the bubble with time can be tracked by considering the bubble equivalent diameter, d_equiv, which is the diameter of a sphere of equal volume to that of the bubble, V_b, such that

$$d_\mathrm{equiv} = \left(\frac{6V_\mathrm{b}}{\pi}\right)^{1/3} \tag{4.7}$$

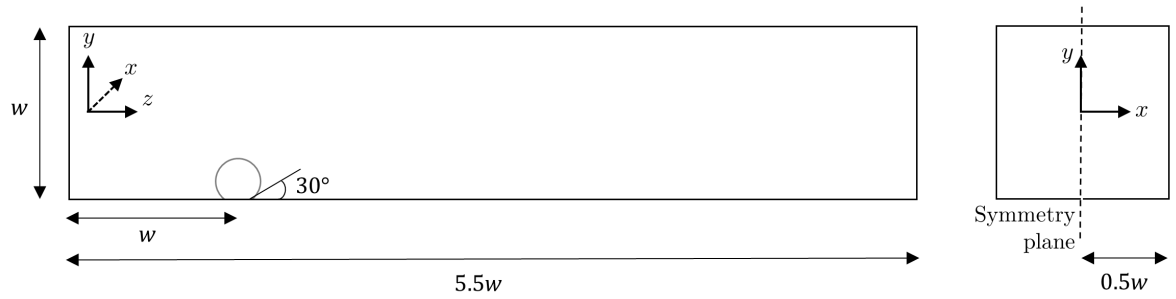


Figure 4.5: Sketch (not to scale) of the simulation set-up for flow boiling in a square micro-channel. The channel width is $w = 229\,\mu\text{m}$ and flow is from left to right.

The flow is assumed to be laminar and incompressible and the vapour and liquid phases Newtonian and immiscible. The Reynolds number of the liquid is defined as $\text{Re}_\text{l} = \rho_\text{l} U_\text{l} w/\mu_\text{l}$. The vapour and liquid phases have the specific heat capacities $c_{p,\text{v}}$ and $c_{p,\text{l}}$ respectively, and the liquid phase has the latent heat of vaporisation h_lv.

4.2.1.2 Experimental comparison case

For flow boiling at a larger scale, laminar flow in the geometry of the experimental facility FLOBOF (see Section 3.2) was simulated. A representative sketch of the pipe is shown in Fig. 4.6. The pipe has diameter d, and the liquid phase occupies the bottom of the pipe up to an interface height y_int. The liquid phase moves at an average velocity U_l, whilst the vapour phase moves at U_v. These values are determined by the experimental mass flux G, vapour quality x and void fraction ε such that

$$U_\text{l} = \frac{G(1-x)}{\rho_\text{l}(1-\varepsilon)} \qquad \text{and} \qquad U_\text{v} = \frac{Gx}{\rho_\text{v}\varepsilon} \tag{4.8}$$

The flow is assumed to be laminar and incompressible and the vapour and liquid phases Newtonian and immiscible. The vapour and liquid Reynolds numbers are defined as $\text{Re}_\text{v} = \rho_\text{v} U_\text{v} d/\mu_\text{v}$ and $\text{Re}_\text{l} = \rho_\text{l} U_\text{l} d/\mu_\text{l}$ respectively, whilst superficial Reynolds numbers can also be defined such that $\text{Re}_{\text{s,v}} = Gxd/\mu_\text{v}$ and $\text{Re}_{\text{s,l}} = G(1-x)d/\mu_\text{l}$. The vapour and liquid phases have the specific heat capacities $c_{p,\text{v}}$ and $c_{p,\text{l}}$ respectively, and the liquid phase has the latent heat of vaporisation h_lv.

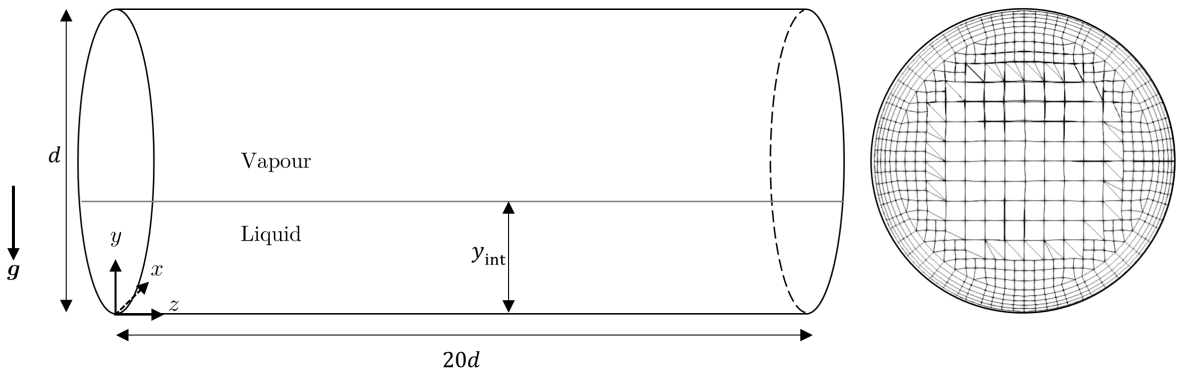


Figure 4.6: Sketch (not to scale) of the simulation set-up for flow boiling in geometry based on FLOBOF. The pipe diameter is $d = 12.6\,\text{mm}$ and flow is from left to right. The cross-section on the right shows the computational mesh.

4.2.2 Numerical method

4.2.2.1 Governing equations

For a heated flow with phase change, some changes and additions are required to Eqs.(4.1), (4.2) and (4.5), which form the governing set of equations for the adiabatic multiphase flow problem. The continuity equation (Eq. (4.1)) must also be written to include a mass source term due to evaporation, $\dot{\rho}$:

$$\nabla \cdot \mathbf{u} = \frac{\dot{\rho}}{\rho} \tag{4.9}$$

Then, an energy balance is also required and can be written as:

$$\frac{\partial(\rho c_p T)}{\partial t} + \nabla(\rho c_p \mathbf{u} T) - \nabla \cdot (k \nabla T) = \dot{h} \tag{4.10}$$

where the density ρ, viscosity μ and thermal conductivity k are properties of the mixture, and the volumetric heat capacity of the mixture is calculated as $\rho c_p = \alpha \rho_\text{l} c_{p,\text{l}} + (1-\alpha)\rho_\text{v} c_{p,\text{v}}$. The calculation of the energy source term $\dot{h}$ is explained in Section 4.2.2.2. The derivation of Eq. 4.10 assumes that the specific internal energy e for a fluid with constant heat capacity c_p can be written as a linear function of temperature:

$$e = e_0 + c_p(T - T_0) \tag{4.11}$$

where for simplicity the reference value for the specific energy is taken to be $e_0 = 0\,\text{J/kg}$ and the reference temperature is $T_0 = 0\,\text{K}$, such that Eq. (4.10) reduces to $e = c_p T$. Viscous heating is neglected and the fluid properties are considered constant throughout the

domain since the liquid superheat measured experimentally at the conditions simulated did not exceed 4 K.

4.2.2.2 Phase change model

An evaporation model is required to estimate the local evaporation rate at the liquid-vapour interface, which will be a function of the local temperature field. The model employed is that described by Ferrari et al. [155], who adapted the *interFoam* VOF method in OpenFOAM 2.3.1 to model phase change.

Many of the evaporation models used in simulation of boiling flows make the assumption of thermodynamic equilibrium at the interface such that the temperature of the two phases is the same, i.e. $T_\mathrm{l} = T_\mathrm{v}$, and equal to the interface temperature T_int [177, 178, 205]. The equilibrium condition requires that the vapour and liquid temperatures at the interface are equal to the saturation temperature at the reference system pressure p_∞, and therefore $T_\mathrm{int} = T_\mathrm{l} = T_\mathrm{v} = T_\mathrm{sat}(p_\infty)$. This assumption is acceptable for most macro-scale boiling problems, but may not apply at the micro-scale, where significant departures from equilibrium may occur due to interfacial superheating induced by interfacial resistance and capillary pressures. It can instead be assumed that both the liquid and vapour exist at the saturation temperatures associated with their local pressures which are not the same, so a temperature jump occurs at the interface, i.e. $T_\mathrm{sat}(p_\mathrm{l}) = T_\mathrm{l} \neq T_\mathrm{v} = T_\mathrm{sat}(p_\mathrm{v})$ [209]. Tanasawa [210] assumed that when interface superheating is low compared to the local vapour equilibrium saturation temperature, the local mass flux across the interface is linear dependent on the local interfacial temperature jump. This resulted in the equation for the interphase mass flux per interfacial area:

$$\dot{m} = \frac{2C}{2-C}\left(\frac{M}{2\pi R_\mathrm{g}}\right)^{1/2}\frac{\rho_\mathrm{v} h_\mathrm{lv}}{T_\mathrm{v}^{2/3}}(T_\mathrm{int} - T_\mathrm{v}) \tag{4.12}$$

where C is the fraction of molecules crossing the interface during evaporation, known as the accommodation coefficient, M is the molecular weight and R_g is the universal gas constant. If the capillary pressure jump across the interface is sufficiently small, the vapour temperature can be assumed to be at the saturation value associated with the system pressure, i.e. $T_\mathrm{v} \simeq T_\mathrm{sat}(p_\infty)$. In channels of the size investigated in this work this

assumption is valid and

$$\dot{m} = \phi \left(T - T_{\text{sat}}(p_\infty) \right) \tag{4.13}$$

where ϕ is known as the kinetic mobility, with $1/\phi$ representing the interfacial resistance to evaporation, and is defined as:

$$\phi = \frac{2C}{2 - C} \left(\frac{M}{2\pi R_{\text{g}}} \right)^{1/2} \frac{\rho_{\text{v}} h_{\text{lv}}}{T_{\text{v}}^{2/3}} \tag{4.14}$$

The accommodation coefficient C in Eq. 4.14 was set to $C = 1$, making the kinetic mobility constant across the whole computational domain. The evaporative mass transfer is thus directly proportional to the local interface superheating. If in each cell an amount of vapour $\dot{m}\delta_{\text{int}}$ is created, and the corresponding amount of liquid thus disappears, then the local evaporation rate can be given by:

$$\dot{\rho} = \dot{m}\delta_{\text{int}} = \phi \left(T - T_{\text{sat}}(p_\infty) \right) |\nabla \alpha| \tag{4.15}$$

This evaporation removes the corresponding latent heat of vaporisation from the energy in the interfacial cell such that the source term in the energy balance can be formulated

$$\dot{h} = -\dot{\rho} h_{\text{lv}} \tag{4.16}$$

which results in a local temperature drop to a value close to the saturation point. This ensures that the interface temperature does not rise significantly above the saturation temperature.

Implementing these mass and energy source terms directly as shown in Eqs. (4.15) and (4.16) would result in their localisation in a small number of cells across the interface. Such a concentration of the source terms could result in numerical instabilities at high evaporation rates [181]. The procedure developed by Hardt and Wondra [181] and Kunkelmann [211] is thus used instead. In this procedure the mass source term is smoothed using a diffusion equation before being redistributed across the interface. The main steps of this approach are described below:

1. An initial sharp source term on the liquid side of the interface is calculated, since

evaporation occurs only in the liquid phase:

$$\dot{\rho} = N\alpha\dot{m}\delta_{\text{int}}|\nabla\alpha| \tag{4.17}$$

where N is a normalisation factor used to preserve the global evaporation rate such that:

$$N = \frac{\int_V |\nabla\alpha| dV}{\int_V \alpha|\nabla\alpha| dV} \tag{4.18}$$

2. A diffusion equation is formulated to smear the source term:

$$\Gamma\nabla^2\dot{\rho}_1 = (\dot{\rho}_1 - \dot{\rho}_0) \tag{4.19}$$

where Γ is a diffusion constant that is adjusted according to the mesh resolution to smear the source term over several cells on either side of the interface. The diffusion equation is solved using Neumann boundary conditions at all boundaries to ensure equality of the volume integrals of $\dot{\rho}_0$ and $\dot{\rho}_1$.

3. In cells where both liquid and vapour are present and $\alpha_{\text{cut}} < \alpha < 1-\alpha_{\text{cut}}$, the source term is set to zero to prevent appearance of the source term in the interface region, as this can cause issues when the advection equation is solved [211]. Outside of these cells the source term is redistributed across the interface such that the global rates of vapour production and liquid disappearance are equal. Then, the mass source term is:

$$\dot{\rho} = \begin{cases} N_{\text{v}}(1-\alpha)\dot{\rho}_1 & \text{if } \alpha < \alpha_{\text{cut}} \\ N_{\text{l}}\alpha\dot{\rho}_1 & \text{if } \alpha > 1-\alpha_{\text{cut}} \\ 0 & \text{if } \alpha_{\text{cut}} < \alpha < 1-\alpha_{\text{cut}} \end{cases} \tag{4.20}$$

where the normalisation factors are defined as

$$N_{\text{v}} = \frac{\int_{\Omega_{\text{v}}} \dot{\rho}_0 d\Omega_{\text{v}}}{\int_{\Omega_{\text{v}}} (1-\alpha)\dot{\rho}_1 d\Omega_{\text{v}}} \qquad \text{and} \qquad N_{\text{l}} = \frac{\int_{\Omega_{\text{l}}} \dot{\rho}_0 d\Omega_{\text{l}}}{\int_{\Omega_{\text{l}}} \alpha\dot{\rho}_1 d\Omega_{\text{l}}} \tag{4.21}$$

where Ω_{v} indicates the vapour domain where $\alpha < \alpha_{\text{cut}}$ and Ω_{l} the liquid domain where $\alpha > 1-\alpha_{\text{cut}}$, in which regions the phase is considered pure. The volume cut-off fraction has been set to a value of $\alpha_{\text{cut}} = 10^{-3}$.

4. The final form of the enthalpy source term accounts for contributions from the enthalpy of evaporation that causes local cooling on the liquid side of the interface, and a correction assocaited with the structure of the mass source term [181]:

$$\dot{h} = -\dot{\rho}_0 h_{\mathrm{lv}} - \dot{\rho} c_p T \tag{4.22}$$

4.2.2.3 Solution procedure

Flow boiling simulations were performed using the open-source CFD software OpenFOAM 2.3.1 with the *interFoam* solver modified to include the evaporation model described in Section 4.2.2.2. The discretisation schemes and solvers follow the same structure as those used for the adiabatic multiphase case (see Section 4.1.2). The residual thresholds for the iterative solution of the governing equations were set to 10^{-7} for velocity, 10^{-8} for volume fraction, 10^{-7} for pressure, 10^{-10} for temperature and 10^{-10} for evaporation rate. A variable time step was adopted for the progress of the solution with an assigned maximum Courant number of $\mathrm{Co} = 0.1$.

4.2.3 Simulation set-up

4.2.3.1 Micro-channel validation

The simulated geometry, shown in Fig. 4.5, was half of a square micro-channel with width $w = 229\,\mu\mathrm{m}$ through which liquid flows at an average velocity U_{l}. The fluid properties were those of air and water at a temperature of 373.15 K, the saturation temperature of water at a pressure of 1 atm. Bubble growth was assumed to be symmetrical about the central $x = 0$ plane, so only half of the channel was simulated to reduce the computational time with a symmetry plane condition imposed along the $x = 0$ plane. A channel length of $5.5w$ was sufficient to observe the period of bubble growth reported by Mukherjee and Kandlikar [177], whose experimental results were used for the model validation presented in Section 7.2.1. The domain was modelled with a 3-D cubic mesh with 100 cells per channel width w. At the inlet, a uniform liquid velocity U_{l} was set corresponding to a Reynolds number of $\mathrm{Re}_{\mathrm{l}} = 100$ along with a zero-gradient pressure condition. The inlet temperature was fixed to the saturation temperature with zero-gradient conditions for the volume fraction and evaporation rate. At the outlet the pressure was set to a uniform

reference value whilst all other variables were subject to a zero-gradient condition. No-slip was imposed at the walls along with zero gradient pressure and evaporation rate conditions, and a constant contact angle (set to 30° [178]) for the volume fraction. The temperature at the bottom and side walls was set to 375.25 K, whilst a zero-gradient temperature condition was imposed at the top to emulate an adiabatic boundary.

A vapour bubble of radius 25 um was initiated at a distance of $1w$ into the channel, positioned to give a contact angle of 30° to the wall. The temperature inside the bubble was always set to the saturation temperature. The effect of different initial liquid temperature conditions on the bubble growth was investigated, with the initial temperature fields taking the following forms:

1. Uniform temperature of $T = T_{\text{sat}} = 373.15\,\text{K}$ across the whole domain.

2. Temperature field decaying linearly with height from $T = T_{\text{wall}} = 375.25\,\text{K}$ at the bottom wall to $T = T_{\text{sat}} = 373.15\,\text{K}$ at the top wall. This condition was set using the *funkySetFields* function of OpenFOAM. A thermal boundary layer in which $T = T_{\text{sat}}$ was initiated around the bubble with two thicknesses investigated; a small layer of 3 cells (7 µm) and an arbitrarily large layer of 50 µm.

3. Thermally developed temperature field, obtained by running a liquid-phase only simulation of the flow using the OpenFOAM solver *icoTempFoam*. The boundary conditions, divergence schemes and solvers for pressure, velocity and temperature were the same as those used in the phase change simulations, with the residual thresholds set to 10^{-5}, 10^{-6} and 10^{-7} for velocity, pressure and temperature respectively. The simulation was run for 15 ms until a thermal steady state was reached, at which point the temperature field was extracted and used as an initial condition for the phase change simulations. A thermal boundary layer of 3 cells was initiated around the vapour bubble.

The initial fields for pressure and evaporation rate were set to 0, whilst the initial temperature field was set to a uniform value of U_{l}.

4.2.3.2 Experimental comparison case

The simulated geometry for direct comparison to experimental data consisted of a pipe of diameter $d = 12.6\,\text{mm}$ through which liquid and vapour flow in two layers at average

velocities U_l and U_v respectively. These velocities were calculated based on the experimental mass flux G and vapour quality x at the visualisation section of the experimental facility FLOBOF as:

$$U_\mathrm{l} = \frac{G(1-x)}{\rho_\mathrm{l}(1-\varepsilon)}; \qquad U_\mathrm{v} = \frac{Gx}{\rho_\mathrm{l}\varepsilon} \tag{4.23}$$

where ε is the void fraction estimated using Eq. (3.14). The fluids properties used were those of R245fa at a saturation temperature of $T_\mathrm{sat} = 299.9\,\mathrm{K}$, calculated using the CoolProp package [189]. The computational domain had a length of $20d$, which was deemed sufficiently long to make a meaningful comparison to experimental data without the computational expense of modelling the entire pipe length. A block-structured mesh was used for the computational grid, the $x-y$ cross-section of which is shown in Fig. 4.6. The core was discretised with a uniform cubic mesh with one level of refinement away from the centre, surrounded by a layer of radially oriented cells with refinement towards the wall.

The liquid height was initially set to a value of y_int, determined based on the experimental void fraction ε. At the inlet, and in the initial velocity field, the velocity was set to U_l below y_int and U_v above y_int. The inlet and initial temperatures were set to the saturation temperature $T_\mathrm{sat} = 299.9\,\mathrm{K}$, whilst zero-gradient conditions at the inlet and zero-value initial conditions were used for pressure and evaporation rate. No-slip was imposed at the pipe wall along with zero-gradient conditions for pressure and evaporation rate. The contact angle of R245fa on FEP is not well characterised in the literature, so an arbitrary constant contact angle of 40° was imposed at the wall for the volume fraction. A fixed gradient temperature condition was used at the pipe wall to emulate constant heat flux, with the value of the gradient set to q/k_l.

Chapter 5

Integral Measurements

In this chapter, results from integral measurements of pressure drop and heat transfer coefficient in boiling flows of R245fa are presented and are compared to predictive methods in the literature. Flow pattern maps are also constructed and the locations of transition boundaries are compared to literature correlations. Parts of this chapter are based on work presented in Moran et al. [212].

5.1 Experimental parameter ranges

Experiments were conducted using the facility and methods described in Chapter 3 and data were collected for 142 data points over a range of conditions. The ranges of the experimental variables governing these conditions are given in Table 5.1. The saturation pressure was maintained with as little variation across data points as possible to ensure comparability across the set, and 60 % of points had the condition $p_{\text{sat}} = 1.7 \pm 0.1$ bar. The wider variations in p_{sat} correspond to the points with values of G and q at the extremes of their respective ranges where it was not possible to stabilise the facility at 1.7 bar. Changes in p_{sat}, and correspondingly T_{sat}, result in changes in the fluid properties at the saturation point, which can impact the boiling mechanism. For example, for R245fa, as T_{sat} increases vapour density increases whilst liquid density and surface tension decrease resulting in an enhanced contribution of nucleate boiling to the total flow boiling heat transfer mechanism as the bubble detachment radius decreases and there are more nucleation sites. However, Billiet et al. [213] observed this not to be the case for conditions with high mass flux and vapour quality x, where the latter has the effect of thinning the

Table 5.1: Experimental parameter ranges.

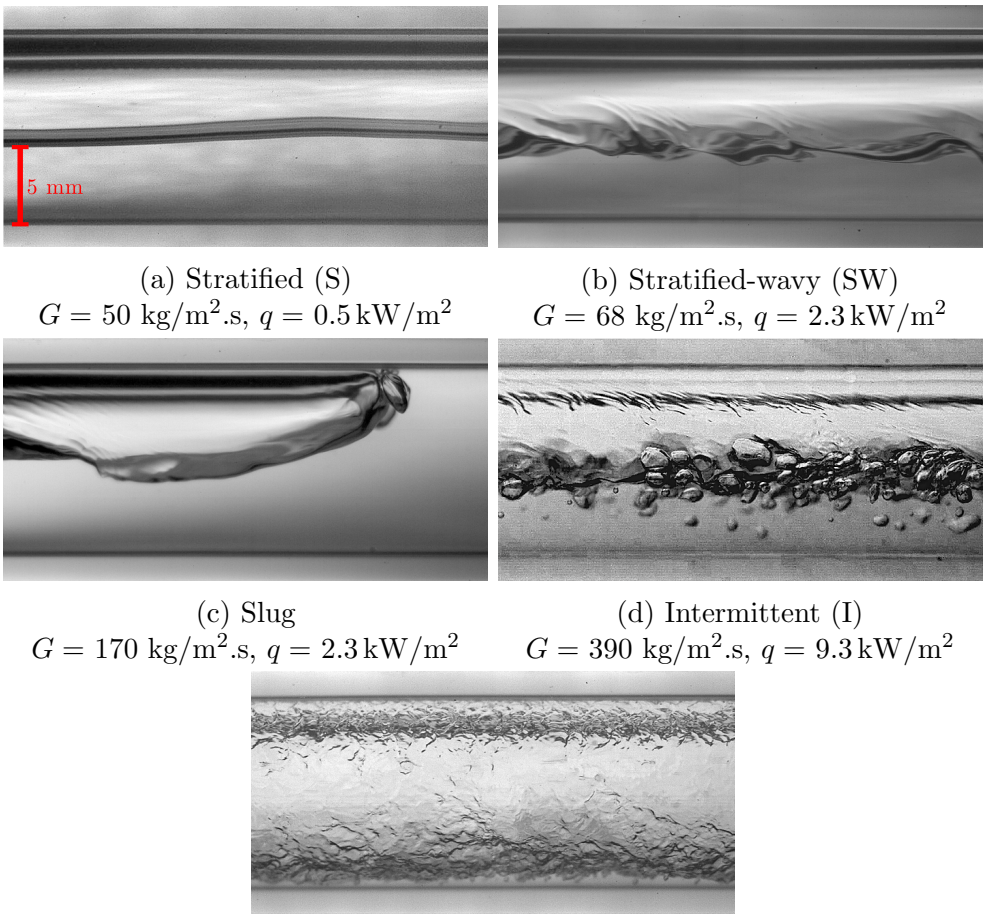
Parameter	Unit	Range
p_{sat}	bar	1.4–2.1
T_{sat}	K	297.1–307.7
$\Delta T_{\text{sc,in}}$	K	2.1–12.0
G	kg/m^2.s	32–720
q	W/m^2	0.5–38

liquid film thereby decreasing the wall super-heat and reducing the number of nucleation sites. They considered the heat transfer behaviour of R245fa at saturation temperatures of 313 K and 343 K and found similar trends of the heat transfer coefficient h as a function of x across these conditions, with deviations in absolute value of up to 20 %. Guo et al. [103] investigated heat transfer behaviour of R245fa for p_{sat} = 2.0–3.6 bar and reported very little variation in h across this range. Yang et al. [131] performed a similar analysis for R1234ze(E) with p_{sat} = 2.15–4.15 bar and found there to be little influence of p_{sat} on h at low heat flux, and a maximum variation of 40 % at q = 43.4 kW/m^2. Given the comparatively small p_{sat} range in this study, comparison of data points across that range was deemed valid, with any resulting deviations likely to fall within the experimental uncertainty. The results presented in this thesis are subsequently reported for a mean p_{sat} of 1.7 bar, which corresponds to T_{sat} = 301.5 K.

For the purposes of comparison and analysis in the rest of this chapter, experimental conditions are characterised by G and q, with data points grouped to within 10 % of a given value. This is common practice within the flow boiling literature and provides sufficient similarity of behaviour within groupings to draw meaningful conclusions.

5.2 Flow patterns

High-speed images were recorded for various flow patterns, and some representative examples are shown in Fig. 5.1. The selected images demonstrate the characteristic features of the various flow regimes: a smooth, flat interface in stratified (S) flow with two continuous phases; the same two phases present in stratified-wavy (SW) flow but with a perturbed interface; a continuous liquid phase interrupted by elongated vapour bubbles in slug flow, with the liquid film maintained at the top of the vapour bubble; a liquid film on the pipe



(a) Stratified (S)
$G = 50$ kg/m^2.s, $q = 0.5$ kW/m^2

(b) Stratified-wavy (SW)
$G = 68$ kg/m^2.s, $q = 2.3$ kW/m^2

(c) Slug
$G = 170$ kg/m^2.s, $q = 2.3$ kW/m^2

(d) Intermittent (I)
$G = 390$ kg/m^2.s, $q = 9.3$ kW/m^2

(e) Annular (A)
$G = 420$ kg/m^2.s, $q = 38$ kW/m^2

Figure 5.1: Flow patterns captured in FLOBOF using high-speed imaging.

walls in annular (A) flow with ripples at the vapour/liquid interface; and a combination of a number of these characteristics in intermittent (I) flow. Mist (M) and dryout (D) flows were not captured in FLOBOF due to the high heat and mass fluxes required, and the unstable behaviour of the facility at high x due to the large vapour volumes present in the system. High-speed images were captured at 1500 fps and used to identify flow patterns according to the classifications put forward by Wojtan et al. [36] using a combination of visual inspection and the mean grayscale intensity-based method described in Section 3.6.1.

In this section, the experimental data collected over the full range of conditions are plotted on single flow maps to facilitate visualisation. However, flow map transition lines, such as those proposed by Wojtan et al. [36], should strictly be plotted for each data point if one wishes to accurately determine the flow pattern, since their position can be dependent on the unique experimental parameters (x, G, q, T_{sat}). The transition lines

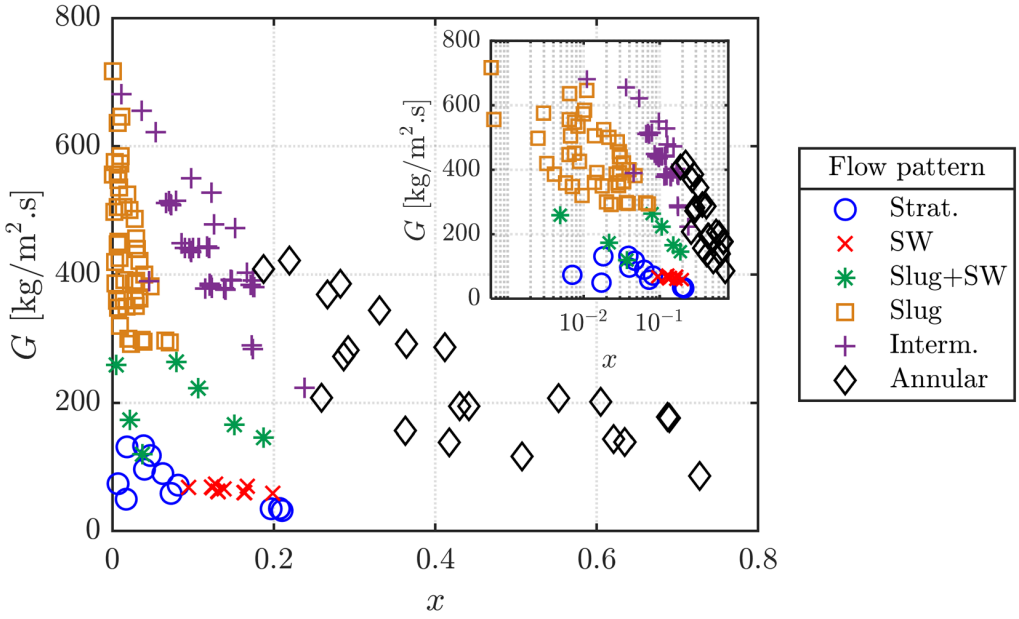


Figure 5.2: Flow pattern map with G vs. x axes summarising all experimental data points for $p_{\text{sat}} = 1.7\,\text{bar}$, with the inset showing a logarithmic x-axis for better visualisation of the data at low x.

most affected by these parameters are the A/SW-to-D, and D-to-M transitions, which were irrelevant for this data set. For the range of experimental conditions studied, the other transitions lines vary by a maximum of approximately 20 %.

The most common flow map configuration in the modern flow boiling literature is that of mass flux G versus vapour quality x. The data points collected in FLOBOF are presented on these axes in Fig. 5.2, where an alternative presentation with a logarithmic x is provided as an inset to show the region $x < 0.1$ in more detail. The resulting map shows clearly the limitations of the facility, with data points at both high x and G not possible to obtain, making the dryout and mist regimes inaccessible. The facility also does not allow for data collection at high x and low G, since the resulting vapour volumes destabilise its operation by inducing slugging within the system. Figure 5.2 shows clear regions for Slug, I, and A flows, with some overlap of the S, SW, and Slug+SW regimes. Stratified flow occurs at low G and low x, but as x increases the interface becomes less stable and a stratified wavy flow is observed. As G increases, the vapour phase is no longer continuous and the flow moves into the Slug+SW and Slug regimes. As x increases further, the mass flow rate of vapour increases and intermittent, then annular flows, can be observed.

In Fig. 5.3, the experimental data points are plotted along with the Wojtan et al. [36]

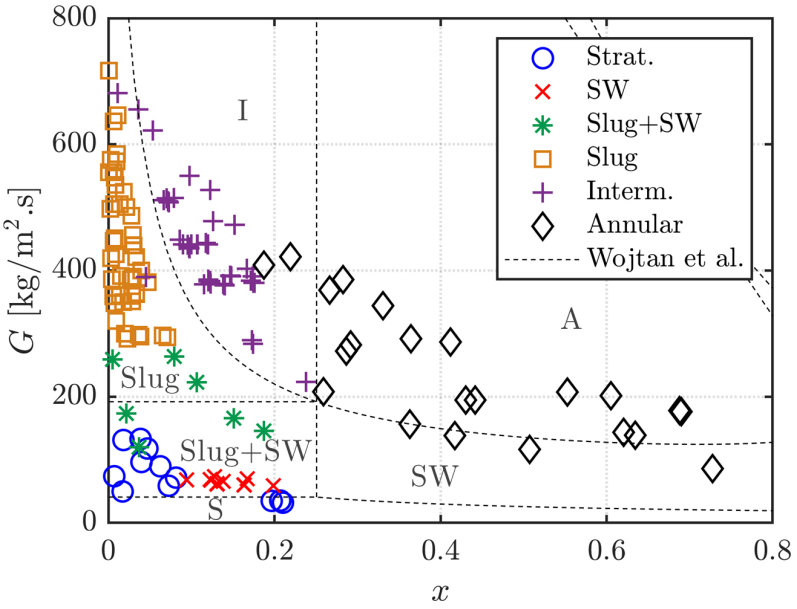


Figure 5.3: Flow pattern map summarising all experimental data points, $p_{\text{sat}} = 1.7\,\text{bar}$, with transition lines and flow pattern regions according to method of Wojtan et al. [36] for the conditions $q = 14\,\text{kW/m}^2$, $G = 330\ \text{kg/m}^2\text{.s}$.

transition lines calculated for the conditions $q = 14\,\text{kW/m}^2$, $G = 330\ \text{kg/m}^2\text{.s}$, $p_{\text{sat}} = 1.7\,\text{bar}$, which are representative of the data set as a mean. The Wojtan et al. [36] transition lines describe the data reasonably well with the flow pattern prediction aligning with the experimental observation for 79 % of data points. The majority of the incorrectly predicted flow patterns occurred in the Slug+SW, SW, and S regimes below the transition curve to the I and A regimes (G_{wavy}), with some more around the I-to-A transition line (x_{IA}). Wojtan et al. [36] divided the region between the G_{strat} and G_{wavy} curves into Slug, Slug+SW, and SW, a modification to the earlier version of this map by Kattan et al. [31]. These three different flow patterns were clearly observed experimentally, but alternative transition boundaries to those of Wojtan et al. [36] may be more appropriate for R245fa based on the lack of alignment with experimental data points in Fig. 5.3. Wojtan et al. [36] also modified the Kattan et al. [31] S-to-SW/Slug+SW transition curve (G_{strat}), assigning a constant value to G_{strat} at $x < x_{\text{IA}}$. This does not fit the experimental data well, and it should be noted that Wojtan et al. [36] did not observe any stratified flow in their experiments so the transition curve bounding the stratified region is not validated. For R245fa boiling at these conditions ($d = 12.6\,\text{mm}$, $p_{\text{sat}} = 1.7\,\text{bar}$), it may also be appropriate to shift the I-to-A transition line to a smaller value of x_{IA}, although more data are required to validate this. Detailed laser-based measurements of the interface location could be used to improve the predictions of A_{LD}, θ_{strat} and P_{iD} in the Wojtan

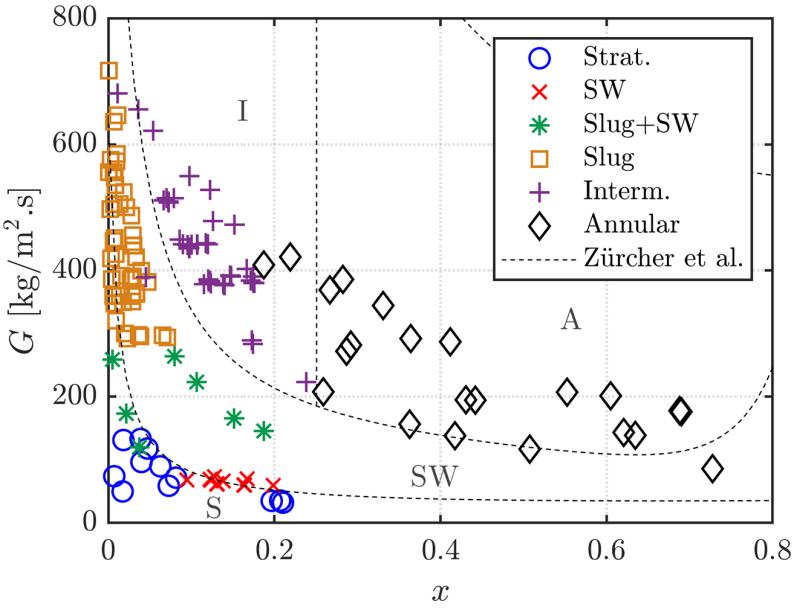


Figure 5.4: Flow pattern map summarising all experimental data points, $p_{sat} = 1.7$ bar, with transition lines and flow pattern regions according to the method of Zürcher et al. [49] calculated for the conditions $q = 14\,\text{kW/m}^2$, $G = 330$ kg/m^2.s.

et al. [36] method for the stratified family of flow patterns.

Zürcher et al. [49] modified the G_{strat} and G_{wavy} transition curves of the Kattan et al. [31] flow map. The Zürcher et al. [49] G_{strat} line, as plotted in Fig. 5.4, does appear to give a better match to the experimental data. Note that the q dependence is mostly expressed in the part of the curve at high x, i.e. the dryout region, but this is irrelevant to this analysis since such conditions cannot be reached with the current experimental setup. The G_{wavy} line also fits the data slightly more accurately than that of the Wojtan et al. [36] map since it returns a lower value of G_{wavy} at intermediate values of x.

It is also interesting to consider specifically the transition from slug/bubble based flow to annular/intermittent type flows, i.e. the G_{wavy} transition line. Figure 5.5 shows three such transition lines (those of Wojtan et al. [36], Ong and Thome [50], and Costa-Patry and Thome [51]) plotted for the experimental conditions. More of the I/A data points are correctly situated on the flow map for both the Ong and Thome [50] and Costa-Patry and Thome [51] transition lines, the calculation of both of which involves the confinement number $\text{Co} = (1/d_i) \cdot \sqrt{\sigma/(g(\rho_L - \rho_V))}$ [214]. This dimensionless number introduces a ratio of geometrical to capillary length scales (the latter set by consideration of the interfacial tension and buoyancy effects) to the transition line equations.

The Barbieri et al. [52] transition line in Fig. 5.5 presents an alternative I-to-A transition to the fixed value of x_{IA} used by Wojtan et al. [36]. The position of the experimental

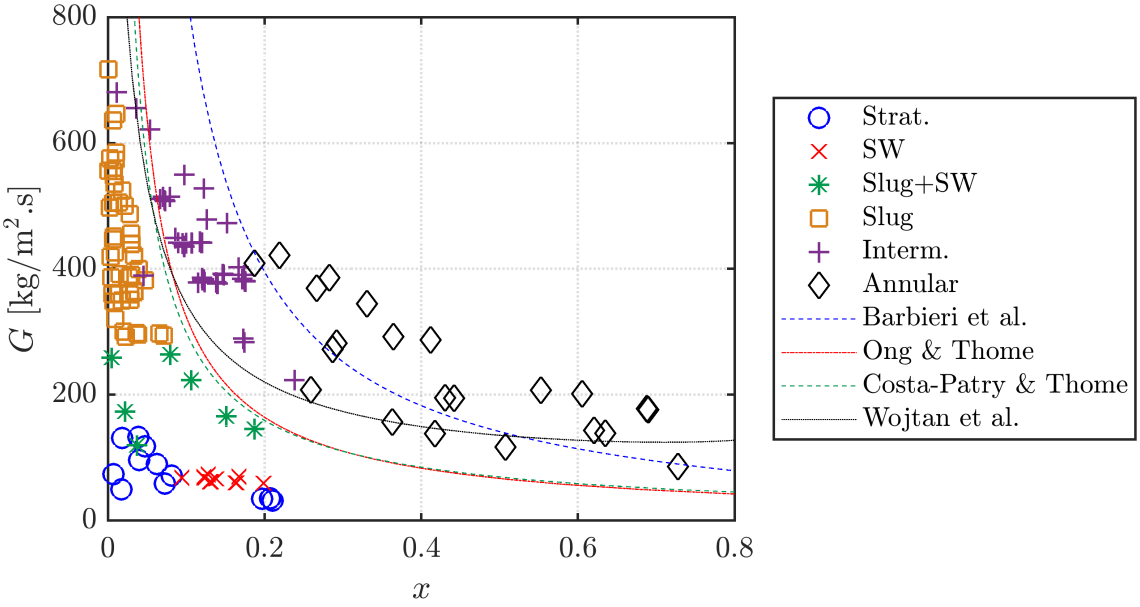


Figure 5.5: Flow pattern map summarising all experimental data points and a range of transition curves, $p_{\text{sat}} = 1.7\,\text{bar}$. The Costa-Patry and Thome [51] curve was generated for $q = 14\,\text{kW/m}^2$.

data points on the flow pattern map suggests that a transition curve of this type may be more appropriate, but the Barbieri et al. [52] curve does not fit the data well. The calculation is independent of q, so the differing q-conditions of the data points cannot account for this deviation. Instead, tuning of the empirical coefficients is required to account for surface wettability effects since the Barbieri et al. [52] transition curve was developed for R-134a in a brass tube and may not apply to different fluids and pipe materials.

5.3 Pressure drop

In this section, experimental pressure drop data and comparisons to relevant predictive methods are presented. The experimental frictional pressure drops reported in this section were calculated from the raw experimental data using Eqs. (3.12) and (3.13).

5.3.1 Experimental data

The effects of vapour quality and mass flux on pressure drop in R245fa boiling flows are illustrated in Fig. 5.6, where $\Delta p_{\text{fric,exp}}$ is plotted as a function of x for groupings of $G \pm 10\,\%$. Figure 5.6 shows explicitly that for a given vapour quality the frictional pressure drop increases with mass flux, a result also shown by similar plots in the work of

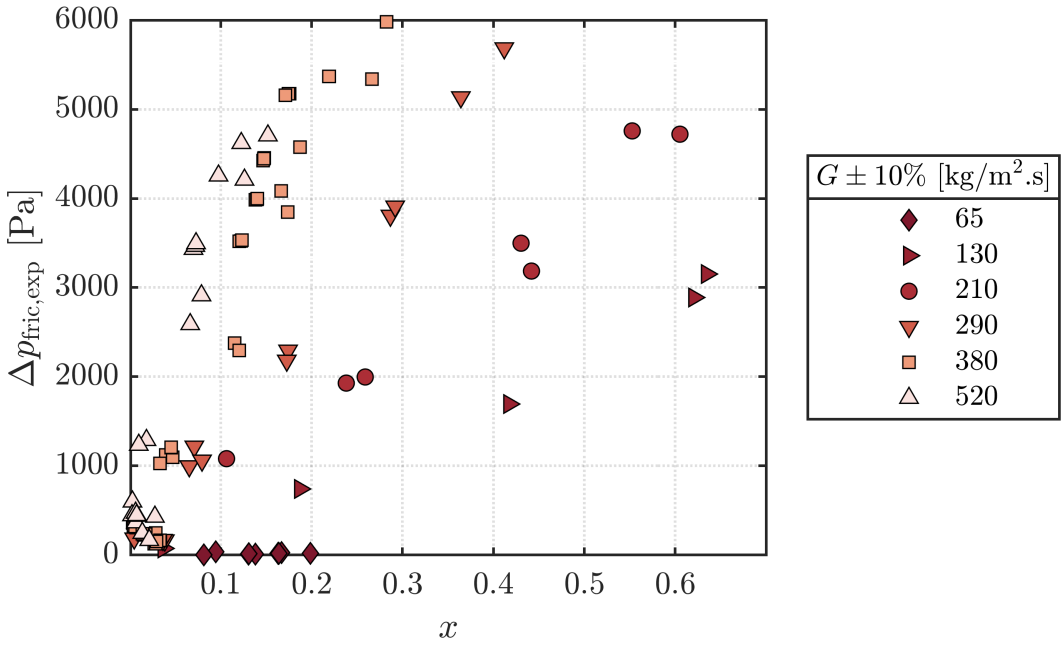


Figure 5.6: Frictional pressure drop as a function of vapour quality for a range of mass flux conditions.

Hardik and Prabhu [73] and Garcia Pabon et al. [134]. An increase in mass flux results in higher velocities leading to increased frictional pressure losses.

Across the vapour quality range of Fig. 5.6, $\Delta p_{\mathrm{fric,exp}}$ increases with x for all values of G. For an increase in x at constant G, the mixture density decreases and the flow velocity increases, which in turn increases the turbulence intensity and therefore the frictional pressure drop. The linear nature of this behaviour is reflected in the literature for similar geometries and vapour qualities [69, 73, 215]. Various authors report a peak in $\Delta p_{\mathrm{fric,exp}}$ at $x \cong 0.7$–0.8 after which $\Delta p_{\mathrm{fric,exp}}$ decreases with increasing x [39, 81, 134], but such high values of x were not reached in this work.

5.3.2 Comparisons with pressure drop predictions

Many correlations for the prediction of frictional two-phase pressure drop (Δp_{fric}) of boiling flows are available in the literature, but the application of these methods to R245fa boiling in macro-scale tubes (i.e. $d_{\mathrm{i}} > 3\,\mathrm{mm}$) is not well documented. A few methods that perform well for similar experimental set-ups were selected and are compared to experimental data in plots of predicted vs. experimental frictional pressure drop in Fig. 5.7. The Fang et al. [74] friction factor was used in the pressure drop calculations. Inspection

Table 5.2: Summary of the discrepancies between the predicted and experimental pressure drops in terms of the the mean relative deviation (MRD) and mean absolute relative deviation (MARD).

Correlation	MRD (all data) [%]	MARD (all data) [%]	MRD ($\Delta p_{\text{fric,exp}} > 600\,\text{Pa}$) [%]	MARD ($\Delta p_{\text{fric,exp}} > 600\,\text{Pa}$) [%]
Müller-Steinhagen and Heck [71]	+126	481	+6	15
Friedel [66]	+179	563	−13	20
Grönnerud [63]	+3	156	−50	51
Hardik and Prabhu [73]	−9	177	−67	68
Xu and Fang [72]	+134	500	+10	16
Quibén and Thome [81]	−27	130	−69	69

of Fig. 5.7 reveals that the predictions of a subset of these correlations are within ±30% of the experimental data for $\Delta p_{\text{fric}} > 2000$ Pa. The discrepancies between the predicted and measured pressure drops, however, deteriorate significantly at lower Δp_{fric} values. This is illustrated further in Fig. 5.8 which shows a semi-log plot of the ratio of predicted to experimental Δp_{fric} as a function of vapour quality.

The logarithmic scale used for x in Fig. 5.8 demonstrates clearly the discrepancy over a vapour quality range, approximately $x = 0.01$–0.05, in which none of the predictive methods perform well. This also corresponds approximately to $\Delta p_{\text{fric,exp}} > 600\,\text{Pa}$. Particularly towards the lower end of this x-range, the uncertainty in experimental x (± 0.0085 as shown in Table 3.2) becomes large compared to its absolute value. Also, at these low values of pressure drop the spatial acceleration pressure drop calculated by Eq. (3.13) accounts for a greater proportion of the total pressure drop, so the frictional contribution is more sensitive to uncertainties in that calculation. More interestingly though, the data points with the largest deviations compared to predictive methods correspond to stratified and slug-type flow patterns. The best-performing predictive method in this x-range is that of Quibén and Thome [81] which, unlike the other methods, is flow pattern-based. This suggests that a phenomenological approach is required for accurate predictions of pressure drop in stratified and slug flow patterns at low vapour quality. The prediction accuracy in these regimes could also be improved using detailed spatio-temporally resolved measurements of the interface location and velocity fields.

To summarise, the performance of the different predictive methods, the mean relative deviation (MRD) and mean absolute relative deviation (MARD) of each, as compared

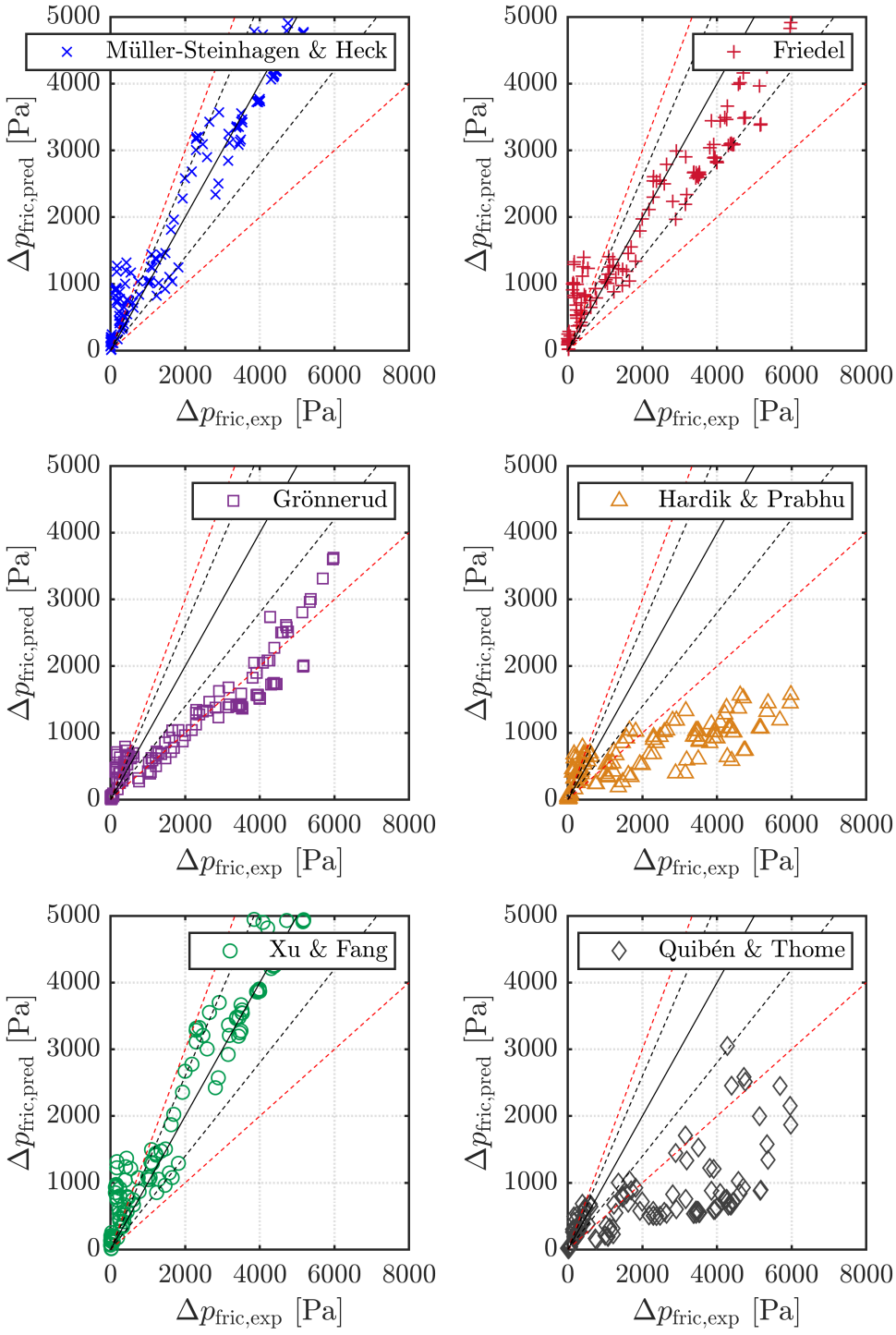


Figure 5.7: Comparison of predicted and experimental frictional pressure drops using a selection of predictive methods. The solid lines represent $\Delta p_{\text{pred}} = \Delta p_{\text{exp}}$, the black dashed lines $\Delta p_{\text{pred}} = \Delta p_{\text{exp}} \pm 30\%$, and the red dashed lines $\Delta p_{\text{pred}} = \Delta p_{\text{exp}} \pm 50\%$.

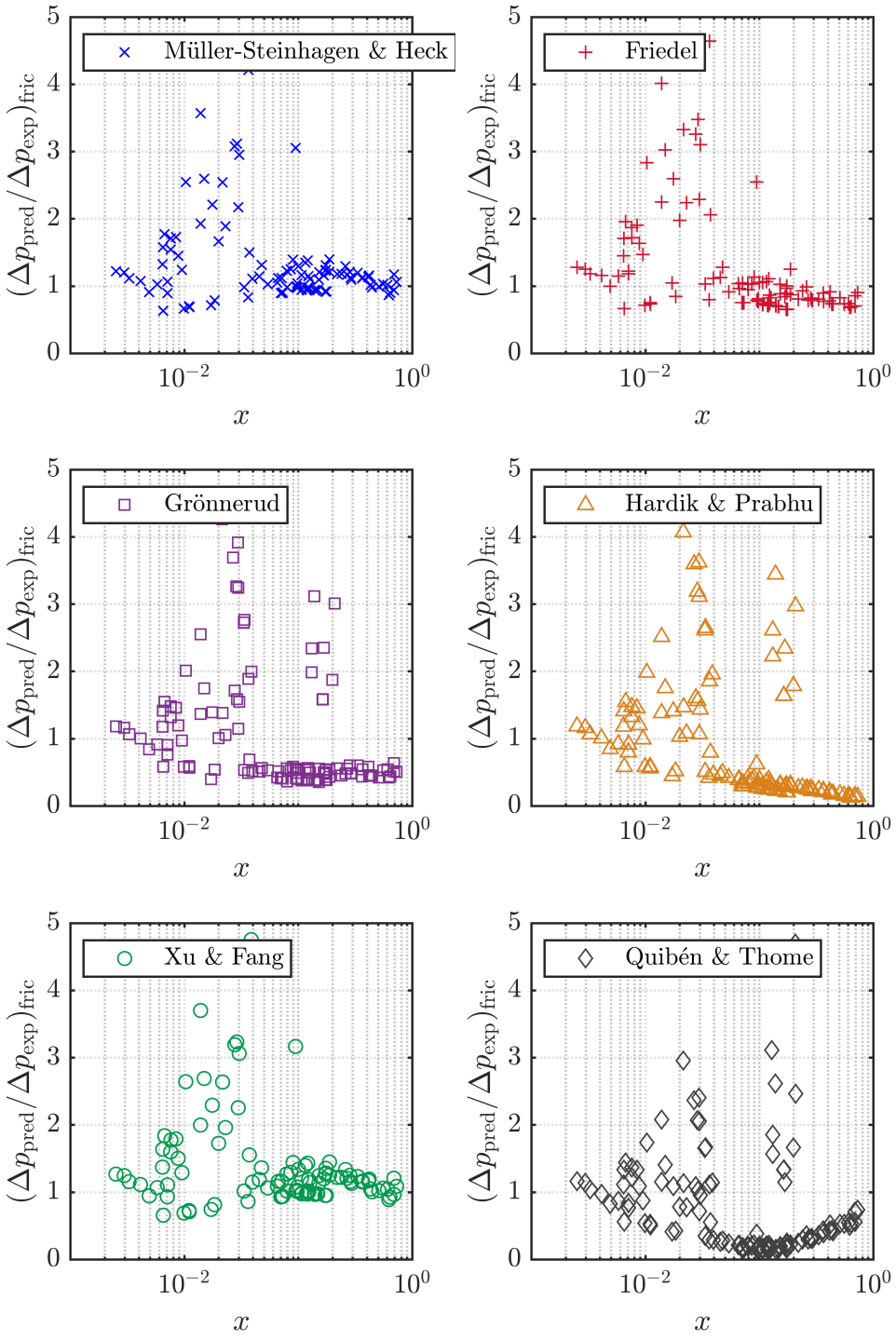


Figure 5.8: Comparison of predicted and experimental frictional pressure drops using a selection of predictive methods, presented as the ratio of predicted to experimental frictional pressure drop as a function of vapour quality.

to the experimental data, are presented in Table 5.2. Values are reported for the full data-set and for the subset $\Delta p_{\text{fric,exp}} > 600\,\text{Pa}$, which effectively removes the data points with a large uncertainty in x, allowing for a more effective assessment of the applicability of predictive methods to the rest of the data. Comparing the values reported in Table 5.2 with inspection of the plots in Fig. 5.7, the empirical Müller-Steinhagen and Heck [71] correlation most accurately predicts the pressure drop outside of the low-x, low-$\Delta p_{\text{fric,exp}}$ region. Other authors have found this to be the case over a range of fluids and experimental conditions [64, 68, 72, 216], although they also report deviations of up to 20 % [68]. The Xu and Fang [72] correlation performs similarly well, as Garcia Pabon et al. [134] also found to be true for boiling of R1234yf in 3.2–8.0 mm tubes. This correlation outperforms the other separated flow models of Grönnerud [63] and Friedel [66]. The Grönnerud [63] correlation was developed specifically for refrigerants, but Turgut et al. [64] found it to give accurate results for only a small subset of these fluids. For the experimental data presented here, it underpredicts the pressure drop by approximately 50 %. Whalley [67] compared the Friedel [66] correlation to over 25 000 data points and found it to give the best predictions for most fluids, whilst Xu et al. [68] grouped it amongst the best with Müller-Steinhagen and Heck [71], reporting deviations of up to 30 %, in agreement with the deviation reported in Table 5.2. Hardik and Prabhu [73] found literature correlations generally underpredicted the pressure drop in comparison to their experimental data for flow boiling of water in 5.5–12 mm tubes, but their resulting correlation does not perform well here for R245fa.

As expected, correlations developed for similar fluids or validated across a wide range of fluids tend to give more accurate predictions of experimental data. Despite performing well at low vapour qualities, the flow-pattern-based Quibén and Thome [81] correlation underpredicts larger pressure drops. These larger pressure drops mostly correspond to intermittent and annular flow patterns, suggesting that either the flow pattern classification or the corresponding pressure drop predictive method is not in fact suitable for these conditions. The correlation uses the flow pattern classification method of Wojtan et al. [36], which Fig. 5.3 shows to correctly classify most intermittent and annular data points. In the Quibén and Thome [81] method, the calculated pressure drop for annular flow depends heavily on the interfacial friction factor which was developed based on an experimental data set which did not include R245fa. The prediction of this interfacial

friction factor could be enhanced by measuring the velocity field close to the interface using e.g. PIV to understand the shear stresses in this region.

Figure 5.8 provides an insight into the performance of each predictive method with x. At $x > 0.05$, the Müller-Steinhagen and Heck [71] method, along with the separated flow models of Grönnerud [63], Friedel [66], and Xu and Fang [72], performs most consistently with little deviation in the average value of $(\Delta p_{\text{pred}}/\Delta p_{\text{exp}})_{\text{fric}}$ as x increases. However, the accuracy of the Hardik and Prabhu [73] method deteriorates as x increases whilst that of the Quibén and Thome [81] method improves. Even though there are relatively few data points in the region $x < 0.05$, the prediction accuracy for all six methods presented in Fig. 5.8 is almost identical. When x is very small, predictive methods generally collapse to a liquid-only pressure drop, suggesting that at such low vapour qualities the vapour phase does not have a significant impact on Δp_{fric}.

5.4 Heat transfer

In this section, experimental heat transfer coefficient data and comparisons to relevant predictive methods are predicted. The fluid always entered the measurement section as a subcooled liquid, and the vapour quality was calculated using Eqs. (3.10) and (3.11) at each temperature measurement junction according to the corresponding heated length. At the most upstream junction, the fluid was still in the liquid phase and $x = 0$, so measurements from this junction are not included in this section. The reported results are spatially-averaged around the circumference of the pipe by taking the mean of the calculated heat transfer coefficients corresponding to the four wall temperature readings at each junction, and time-averaged over the sampling time.

5.4.1 Experimental data

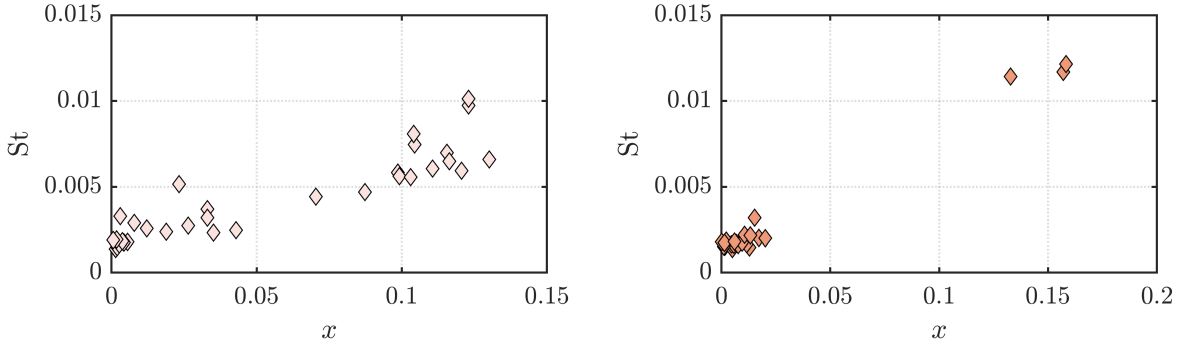
In the flow boiling literature, experimental heat transfer measurements are usually reported in terms of heat transfer coefficient, h, as a function of x for constant G and q. However, in this work boiling in the heated test section was always induced from the subcooled ($x = 0$) condition, and therefore to achieve the widest possible range of x at the outlet, G and q were manipulated. Thus, to examine heat transfer as a function of x, normalisation by one or both of these parameters is required. In Fig. 5.9 experimental

values of the Stanton number, $\mathrm{St} = h/Gc_p$, are plotted against x. St is the ratio of heat transferred to the liquid specific heat capacity, and plotting of St allows for normalisation by G and subsequently assessment of heat transfer as a function of x. Such plots have a very similar shape across the full experimental range of x to those of h vs. x for constant G in the literature (e.g. [37, 103, 217]). Figure 5.9 will therefore be discussed in comparison to literature plots of h vs. x for constant G.

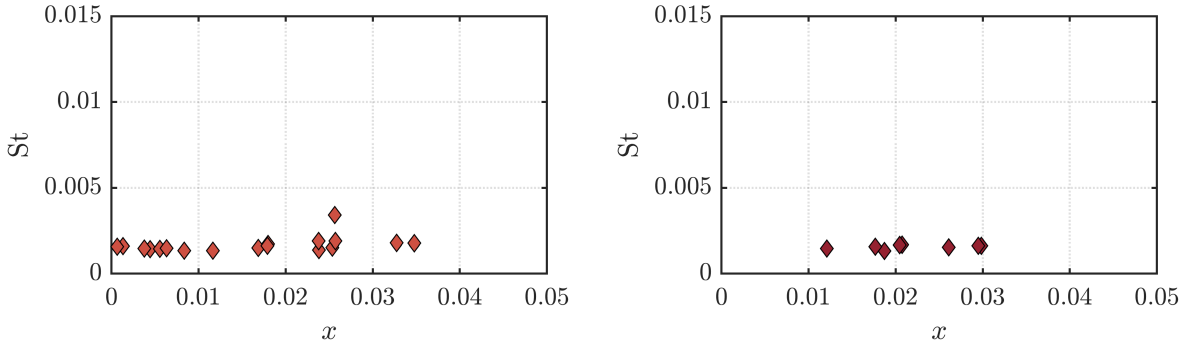
Figure 5.9 shows that in general, higher q results in increased heat transfer, as expected. However, for the three highest heat flux values (Fig. 5.9f-5.9h) St does not vary significantly with q, suggesting there is an upper limit to the amount of heat that can be transferred to the flow in this set-up. Across the full range of experimental x values, heat transfer increases with increasing x. The majority of the data points at low vapour quality ($x < 0.05$) fall into the slug flow regime, whilst the intermittent and annular regimes dominate at higher vapour qualities. These regimes are characterised by liquid films at the wall, the thickness of which decreases with increasing x. This reduces the thermal resistance and enhances heat transfer. Such behaviour has been observed previously in similar geometries [37, 39, 73], and for the same fluid in 3 mm tubes [103], up to $x \cong 0.7$–0.8 where a peak in the heat transfer coefficient occurs. This also corresponds to reported peaks in the pressure drop, but sufficiently high values of x to investigate this effect were not reached in this work.

At low heat flux (Fig. 5.9a-5.9e) and low vapour quality ($x < 0.05$), St is relatively constant with x. From the formulation of St, this suggests that h and G are linearly proportional which is indicative of a forced convection boiling mechanism. These data points correspond predominantly to slug flow.

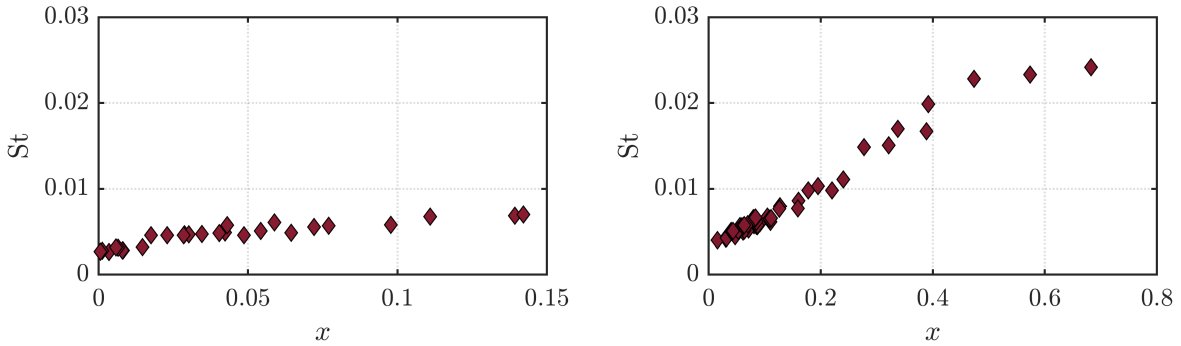
To provide insight into the effect of mass flux on heat transfer, Fig. 5.10 shows the experimental heat transfer coefficient h_{exp} for two different G values, separated by the same q values used in Fig. 5.9. The two plots look very similar, but it is important to note that the x-range in Fig. 5.10b is half of that in Fig. 5.10a. Therefore, assuming the data would follow the trend in Fig. 5.9 of increasing heat transfer with increasing x at $x > 0.05$, an increase in G results in an increase in h for fixed q and x. This behaviour is widely reported in the literature [43, 69, 93, 136].



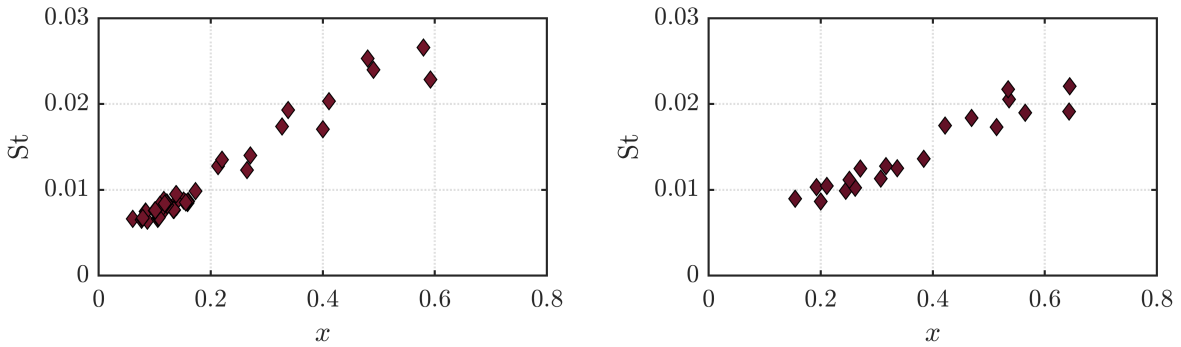
(a) $q = 2.6\,\mathrm{kW/m^2} \pm 10\%$ (b) $q = 3.7\,\mathrm{kW/m^2} \pm 10\%$



(c) $q = 5.3\,\mathrm{kW/m^2} \pm 10\%$ (d) $q = 6.5\,\mathrm{kW/m^2} \pm 10\%$

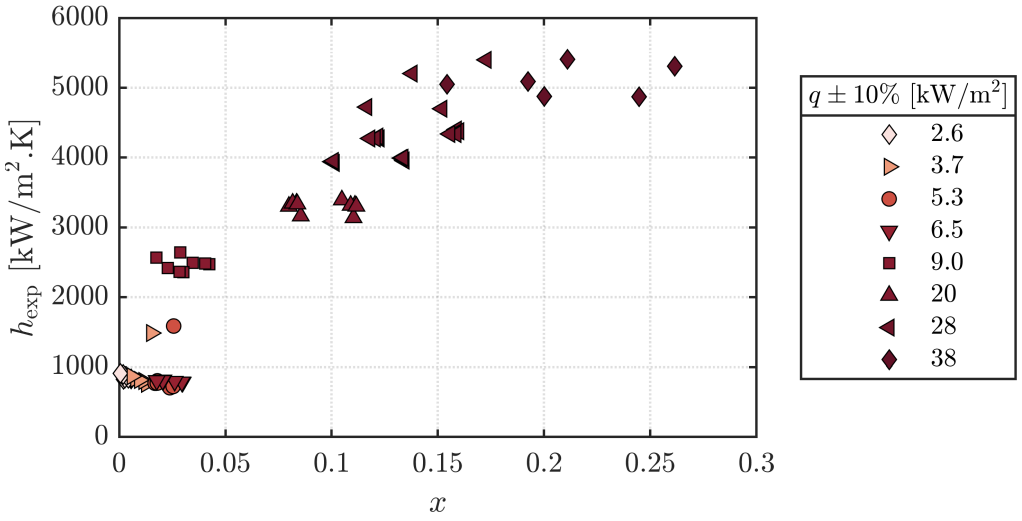


(e) $q = 9.0\,\mathrm{kW/m^2} \pm 10\%$ (f) $q = 20\,\mathrm{kW/m^2} \pm 10\%$

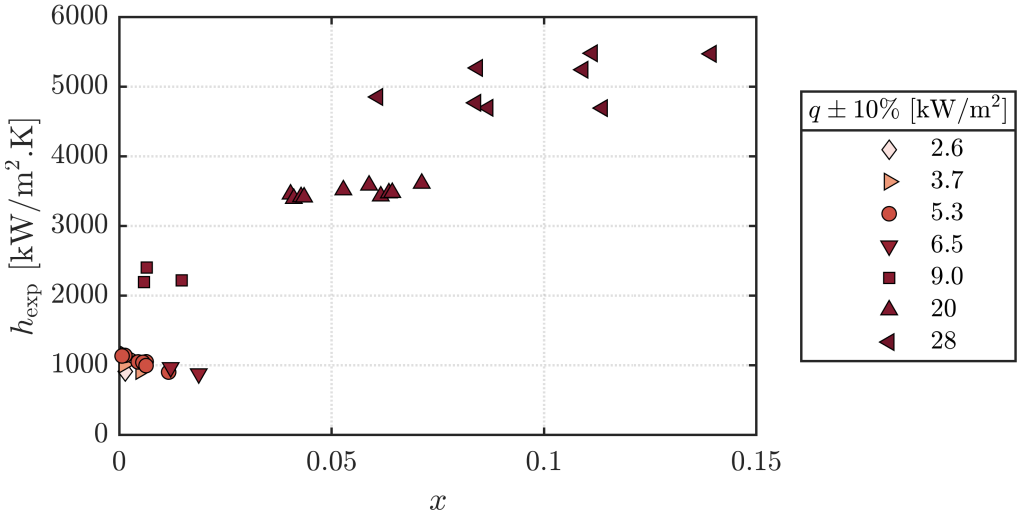


(g) $q = 28\,\mathrm{kW/m^2} \pm 10\%$ (h) $q = 38\,\mathrm{kW/m^2} \pm 10\%$

Figure 5.9: Stanton number as a function of vapour quality for a range of heat flux conditions.



(a) $G = 380$ kg/m^2.s $\pm$ 10 %



(b) $G = 520$ kg/m^2.s $\pm$ 10 %

Figure 5.10: Heat transfer coefficient vs. vapour quality for a range of heat flux conditions and two mass flux conditions.

5.4.2 Comparisons with heat transfer coefficient predictions

5.4.2.1 Flow boiling correlations

Similarly to pressure drops, many predictive methods are available in the literature for estimation of heat transfer coefficients in boiling flows but there is little validation of these methods for R245fa in macro-scale tubes. A selection of these methods is presented in terms of predicted versus experimental h in Fig. 5.11. Further insight into correlation performance as a function of x is provided by plots of $h_{\text{pred}}/h_{\text{exp}}$ vs. x in Fig. 5.12, and the mean relative deviations of each method compared to experimental data are detailed in Table 5.3.

The spread of the data points on the plots in Figs. 5.11 and 5.12 varies between methods. Prediction accuracy deviates significantly for several of the selected methods at approximately $h < 1000$ W/m^2.K and $x < 0.05$, with both underprediction and overprediction of h. For these lower values of h and x, the relative uncertainty is larger and can be amplified further by the calculation method. However, some of the methods perform consistently well at this lower end of the parameter ranges, with divergence at higher values. This is most noticeable for the Guo et al. [103] correlation, which is the second-best performing correlation for $x < 0.05$, but the worst for $x > 0.05$. It is also the only method for which $h_{\text{pred}}/h_{\text{exp}}$ increases with x at $x > 0.05$. The correlation was developed based on flow boiling experiments with R245fa and an R134a/R245fa mixture in 3 mm horizontal tubes, and this difference in scale may account for the observed behaviour. At the larger scale of the pipe diameter used in this work, gravitational effects become more significant with the most relevant effect being the asymmetry of the liquid film between the top and bottom of the tube for flow patterns in which the wall is completely wetted, i.e. slug and annular flows. Most of the data points with larger h or x correspond to slug, annular or intermittent flow. This highlights the importance of using predictive methods developed for similar scales.

The Guo et al. [103] correlation is a modified version of the Liu and Winterton [100] correlation and performs better overall due to the poor predictive capability of the latter at $x < 0.05$. Also, the extent of the underprediction of the Liu and Winterton [100] correlation for $x > 0.05$ increases as $x \to 1$. The Liu and Winterton [100] correlation was developed for tubes with $d > 3$ mm.

The most consistent correlation across the data set, and most accurate overall with

MARD = 23 %, is that of Shah [92] which despite being one of the earliest enhancement-factor correlations has been reported to give reasonable predictions for both boiling [93] and condensation [94] of R245fa in smaller tubes. The Kandlikar [95] correlation is a further development of that of Shah [92] and performs similarly well (MARD = 28 %) overall despite larger deviations at $x < 0.05$. Kandlikar [95] introduced a fluid-specific parameter, F_{fl}, to the calculation method and since no such parameter is reported for R245fa it was tuned to the experimental data to a value of $F_{\mathrm{fl}} = 1.3$. The tuning required a trade-off between prediction accuracy at low and high values of x and h, so better accuracy could be achieved by using different values for the two regions. The resulting value of $F_{\mathrm{fl}} = 1.3$ is the same as those of R11 and R113 as defined by Kandlikar [95]. These have different chemical structures to R245fa being chloro-fluoro-hydrocarbons of lower carbon number, but R11 particularly has a similar molar mass and boiling point to R245fa. Fang et al. [218] reported a similar accuracy of MARD = 30 % for the Kandlikar [95] correlation applied to R245fa boiling.

After the Shah [92] correlation the flow pattern-based correlation of Wojtan et al. [37] is the next most consistent across the data range despite also tending to underpredict h. This suggests that a flow pattern-based approach is effective for predicting heat transfer despite this not being the case for pressure drop across the full range of x (see the Quibén and Thome [81] correlation in Fig. 5.8).

It is clear from the assessment of these predictive methods that a single correlation is rarely effective for the whole data set, and that the applicability of any given correlation is generally restricted to the conditions of the experiment upon which it is based. In their review paper, Thome et al. [106] also found that no single method predicted their entire database well, highlighting the difficulty of finding a universal approach. Many correlations are not well-validated for the low vapour quality region due to high relative uncertainties in integral measurements at the necessary experimental conditions, so detailed spatially and temporally resolved measurements of these flow could provide much-needed insight into the associated flow structures and phenomena.

5.4.2.2 Pool boiling correlations

One of many ways to predict the dominant boiling mechanism in boiling flow is by evaluation of the convection number, $\mathrm{Cv} = \left(\frac{1-x}{x}\right)^{0.8}\left(\frac{\rho_{\mathrm{v}}}{\rho_{\mathrm{l}}}\right)^{0.5}$, with $\mathrm{Cv} < 0.65$ defining the

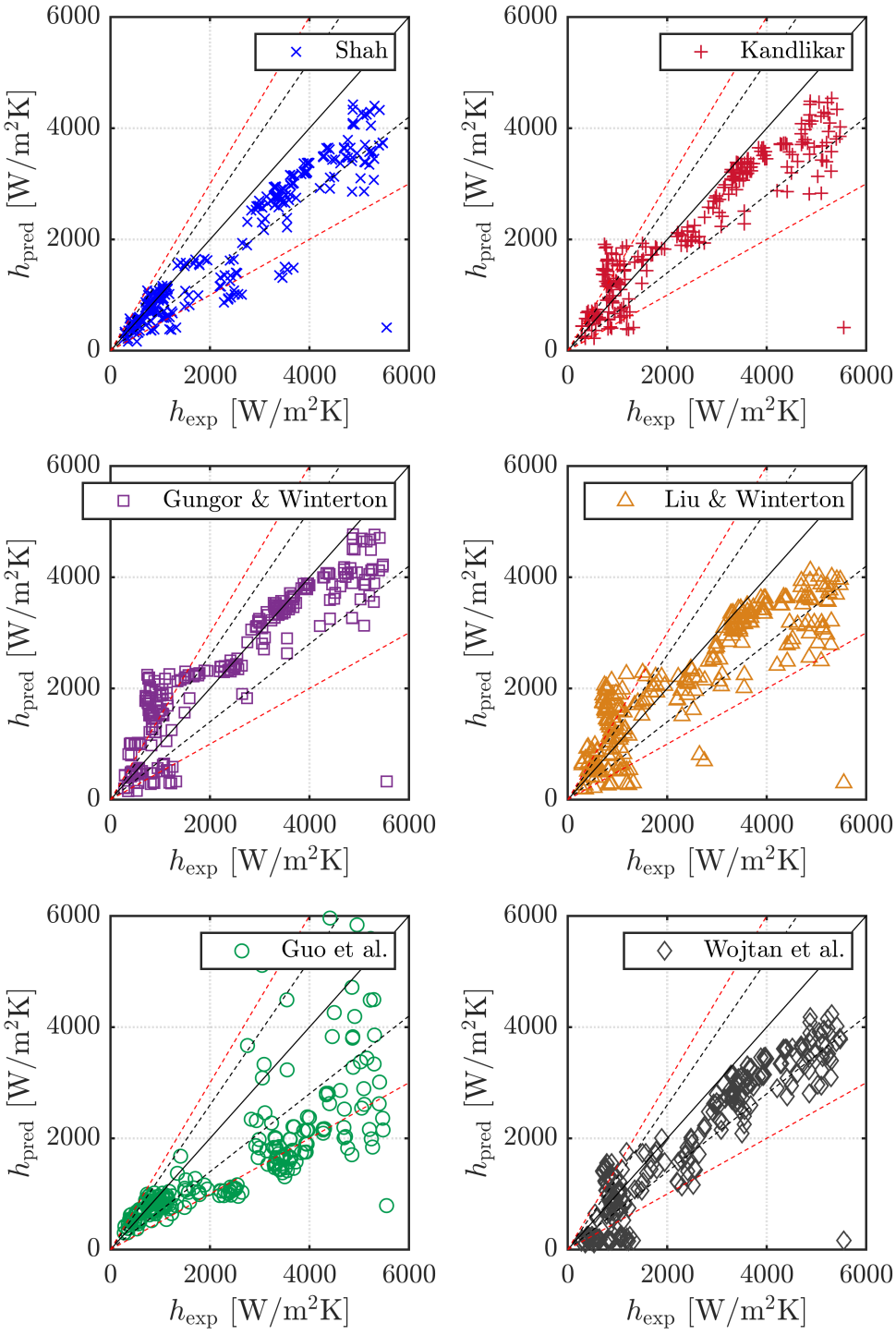


Figure 5.11: Comparison of predicted and experimental frictional heat transfer coefficients using a selection of predictive methods. The solid lines represent $h_{\text{pred}} = h_{\text{exp}}$, the black dashed lines $h_{\text{pred}} = h_{\text{exp}} \pm 30\%$, and the red dashed lines $h_{\text{pred}} = h_{\text{exp}} \pm 50\%$.

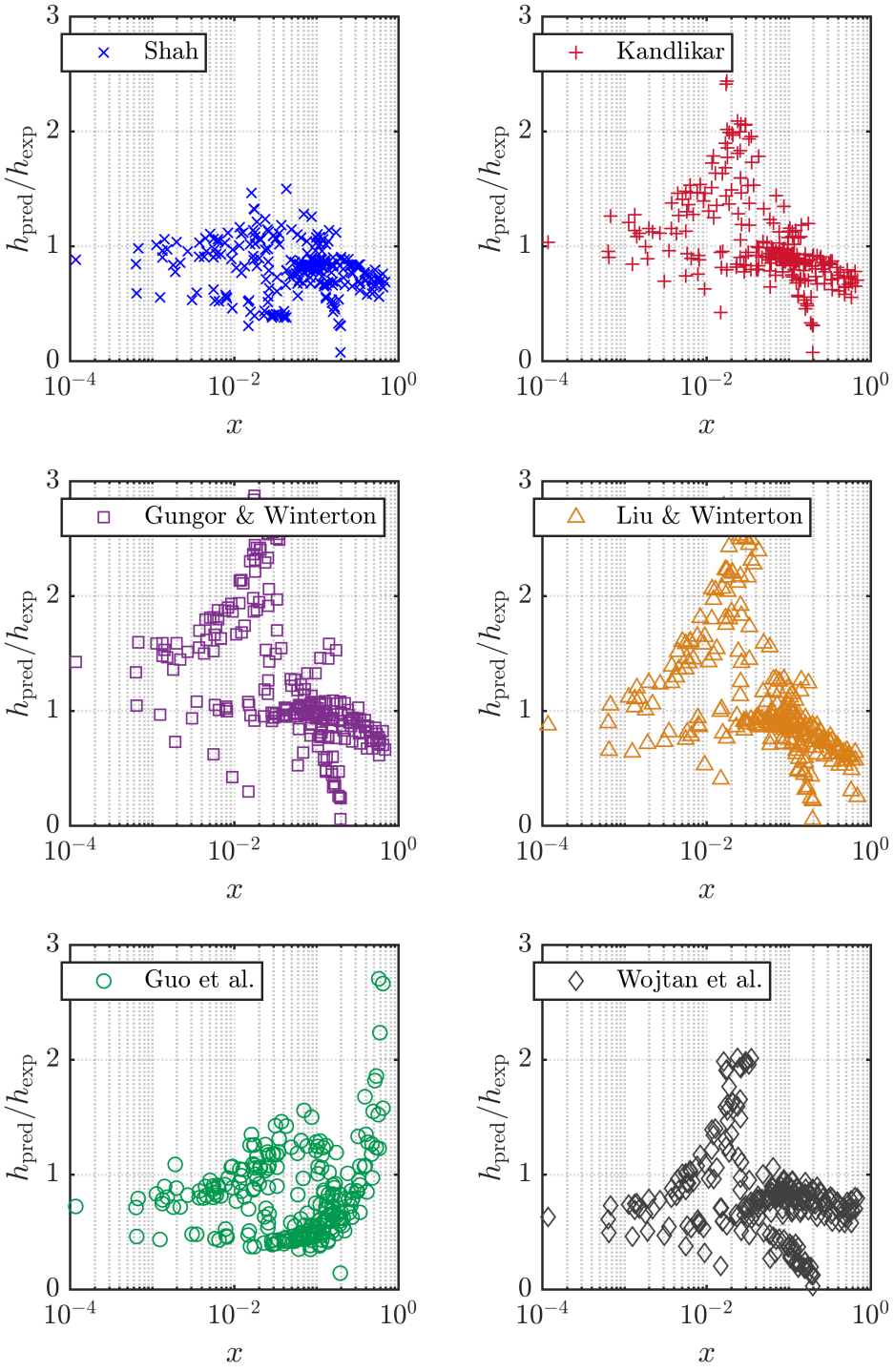


Figure 5.12: Ratio of predicted to experimental frictional heat transfer coefficients plotted against vapour quality using a selection of predictive methods.

Table 5.3: Summary of the discrepancies between the predicted and measured heat transfer coefficients in terms of the mean relative deviation (MRD) and mean absolute relative deviation (MARD).

Correlation	MRD (all data)	MARD (all data)	MARD ($x > 0.05$)	MARD ($x < 0.05$)
Shah [92]	−19	23	23	24
Kandlikar [95]	+3	28	19	41
Gungor and Winterton [99]	+18	37	17	67
Liu and Winterton [100]	+7	37	23	58
Guo et al. [93]	−20	36	41	28
Wojtan et al. [37]	−20	33	31	37

nucleate boiling dominant zone [95]. Vapour quality is perturbed the most, up to two orders of magnitude, of all experimental parameters investigated in this study, whilst other parameters affecting the establishment of nucleate boiling-dominated conditions, such as mass velocity and surface roughness, do not change as much, if at all, over the data set. This is reflected in the operation of real engineering systems utilising flow boiling, so Cv was selected as an appropriate characterisation parameter. Considering the experimental heat transfer coefficient data, 46 % of the points fall into the nucleate boiling dominant zone as defined by the condition Cv < 0.65. The heat transfer behaviour in this zone could be described by pool boiling correlations. These are not a function of vapour quality or mass flux, so should not be affected by the large proportional uncertainties discussed for flow boiling correlations, but are simply dependent on the fluid and pipe properties, and on empirical constants.

Six pool boiling correlations were selected and the ratios of the resulting heat transfer coefficient to the corresponding experimental h are plotted as a function of the measured h values in Fig. 5.13. The corresponding deviations are given in Table 5.4. With the exception of the Mostinski [89] correlation, the reduced pressure-based correlations (Gorenflo [85], Cooper [87], and Ribatski and Jabardo [88]) provide the most accurate predictions of the experimental data. Chen [91] also found the Cooper [87] correlation to give reasonable predictions of h for pool boiling of R245fa on a cylinder. The performance of the Gorenflo [85] correlation depends on the reference h, for which a tabulated value for R245fa is not provided. The appropriate value was thus determined by fitting of the experimental data, but interestingly this still does not provide the best fit according to Table 5.4. The Gorenflo and Kenning [86] correlation provided a modified and improved

Table 5.4: Summary of discrepancies between the predicted and measured pool boiling heat transfer coefficients in terms of mean relative deviation (MRD) and mean average relative deviation (MARD).

Correlation	MRD	MARD
Cooper [87]	−21	30
Gorenflo [85]	+12.7	27
Mostinski [89]	−49	49
Ribatski and Jabardo [88]	+3	26
Stephan and Abdelsalam [83]	−24	31
Jung et al. [90]	−27	32

version of the Gorenflo [85] correlation, but included several fluid specific correction factors as well as reference values which are not yet provided for R245fa. A more accurate prediction could be obtained by further investigation of the correct values of these factors for R245fa. Based on Table 5.4, the Ribatski and Jabardo [88] correlation is most accurate, and Fig. 5.13 shows that it underpredicts h at high values of h_{exp} to a lesser extent than most of the other correlations. The empirical constants in the Ribatski and Jabardo [88] correlation are pipe-specific rather than fluid-specific and are well-defined for stainless steel, unlike the fluid-specific quantities in other correlations for R245fa.

The Stephan and Abdelsalam [83] correlation underpredicts h significantly, despite claiming to be valid for the experimental conditions. This thermo-physical property-based correlation is a function of the bubble departure diameter, calculated based on the contact angle β to which the authors advise to assign the value of 35° for all refrigerants. Halon et al. [84] found this correlation to give a poor prediction of h for pool boiling of R245fa on a heated plate, finding deviations of up to 157 % and suggesting that it overestimates the effects of q and T_{sat} on h. The empirical correlation of Jung et al. [90] uses the same calculation of bubble departure diameter, but the term containing this value, q and T_{sat} is raised to a different value to that in the Stephan and Abdelsalam [83] equation. In the Jung et al. [90] equation this value is calculated based on fluid properties, the reduced pressure and empirical constants. These empirical constants could be better tuned for these experiments to improve the prediction accuracy.

Overall, the experimental heat transfer coefficient is not well-predicted by pool boiling correlations, particularly at low values of h_{exp}. This suggests that convective heat transfer cannot be neglected at these conditions and superposition approaches, such as that of Liu et al. [94] as investigated in Figs. 5.11 and 5.12 are more appropriate. This contribution of

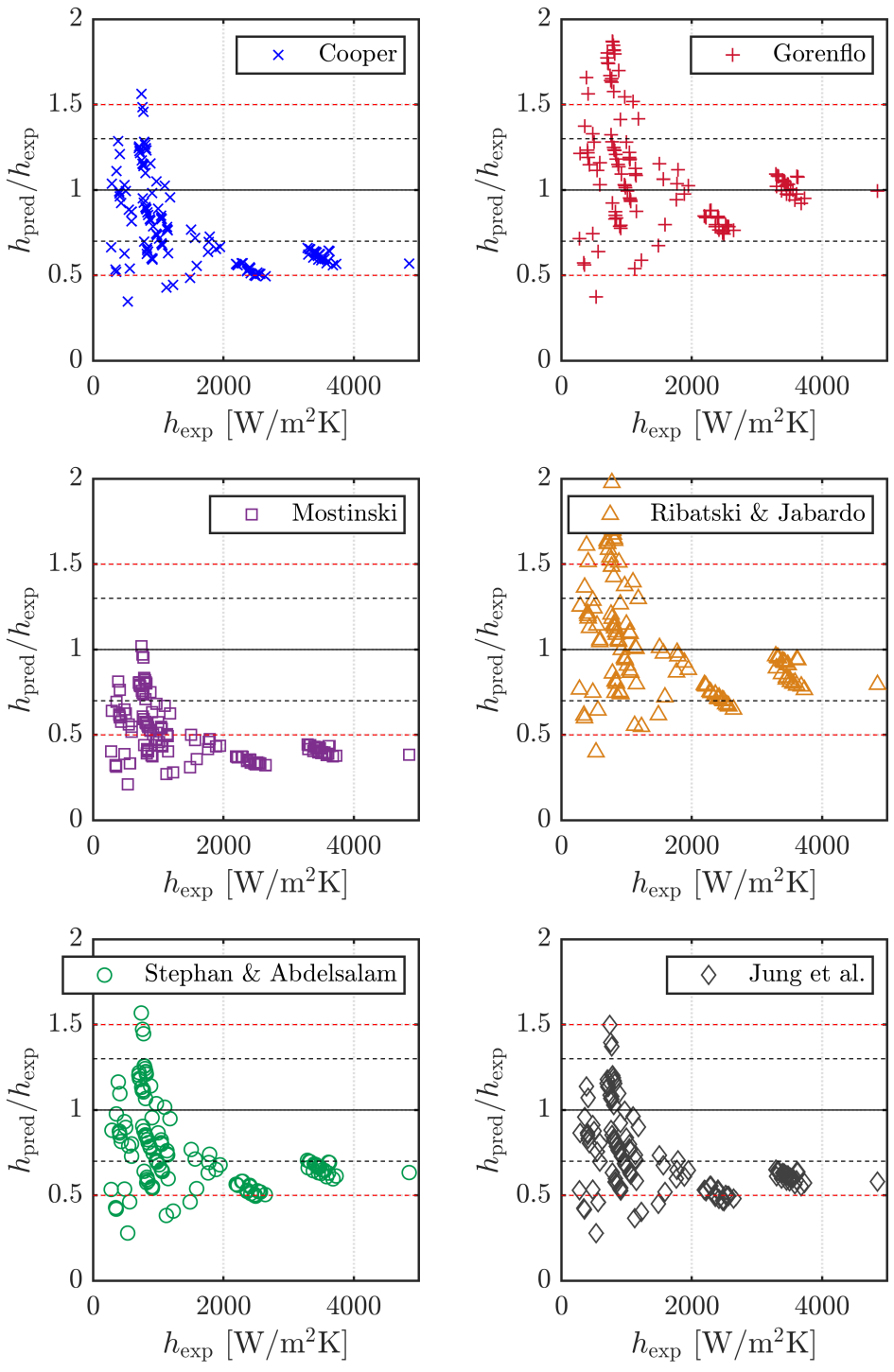


Figure 5.13: Ratio of predicted to experimental frictional heat transfer coefficients plotted against experimental heat transfer coefficient for data in the nucleate boiling dominant zone.

convective boiling effects is to be expected at the low heat fluxes associated with the low h_{exp} data points, and due to R245fa being a low pressure refrigerant with a correspondingly high vapour specific volume that results in high two-phase flow velocities.

5.5 Summary

A bespoke experimental flow boiling facility has been used to investigate flow boiling of R245fa in a 12.6 mm pipe. Flow patterns were identified using high-speed imaging, whilst integral measurements of pressure drop and heat transfer were made. For the experimental conditions investigated, the frictional pressure drop was found to increase with increasing mass flux and vapour quality, in line with results from previous comparable literature studies. Generally, heat transfer also increases with increasing mass flux and vapour quality.

Since the applicability of predictive methods in the literature to the combination of fluid, geometry and experimental conditions in this work is not widely reported, comparisons of experimental results to predictive methods for flow pattern maps, pressure drops, and heat transfer coefficients have been made. The classifications of flow patterns put forward by Wojtan et al. [36] were found to describe the range of observed flow patterns well, but it was not possible to observe mist and dryout flows in the experimental facility FLOBOF. However, the Wojtan et al. [36] map did not accurately describe the transitions between slug and stratified flow types, with the Zürcher et al. [49] formulation of this transition line better fitting the experimental data. The intermittent-annular transition lines also require some modification to fit the data set generated in this work.

The experimental frictional pressure drop was most accurately described at high vapour qualities by the Müller-Steinhagen and Heck [71] and Xu and Fang [72] methods, although accurate prediction at very low vapour qualities was not achieved by any of the tested methods. Correlations for heat transfer coefficient were more accurate across the dataset, with the Shah [92] method proving the most consistently accurate one, followed by the flow pattern-based model of Wojtan et al. [37]. This suggests that a flow pattern-based approach is appropriate for the prediction of heat transfer, despite this not being the case for pressure drop across the full vapour quality range. A significant proportion of the experimental data points fell into the nucleate boiling dominant zone so the

applicability of pool boiling correlations was also investigated. Many of these methods rely on empirical constants and fluid specific parameters which require further tuning for R245fa flow at the macro-scale (i.e. $d > 3\,\text{mm}$).

Chapter 6

Detailed Spatio-temporally Resolved Measurements

In this chapter, results obtained by applying the laser-based measurement methods described in Section 3.5 are presented and discussed. Boiling in the flows investigated in this work has not previously been investigated with such laser-based methods, which provide detailed spatio-temporally resolved information that can be linked to the integral thermohydraulic data on flow regimes, pressure drops and heat transfer presented in Chapter 5. The chapter is sub-divided by flow pattern since the experimental methods, post-processing techniques, and resulting information differ between them. Results are presented for stratified, stratified-wavy, slug, and annular flows. Parts of this chapter are based on work presented in Moran et al. [212].

6.1 Stratified flow

After liquid-phase validation (see Section 3.8.2), the first flow pattern to be investigated in FLOBOF using laser-diagnostic techniques was stratified flow. Of the two-phase flow patterns in horizontal flow boiling, stratified flow is the simplest to investigate optically due to the presence of two continuous phases separated by a single, mostly flat interface. A combined PIV and PLIF technique was applied, and the interface was detected using the method described in Section 3.6.2.

6.1.1 Velocity field and interface information

Figure 6.1 presents time-averaged velocity fields and the corresponding velocity profile averaged over the streamwise direction for two stratified flow conditions with $\mathrm{Re}_{\mathrm{l,in}} = Gd/\mu_{\mathrm{l}} = 1070$ and 3290 at the inlet for the top and bottom figure sets, respectively. Figs. 6.1a and 6.1c show that the velocity profile does not change significantly over the streamwise direction for either case. This is representative of all stratified flow conditions examined, i.e. $G = 35$–150 kg/m^2.s, and is expected in a stratified flow which is characterised by a stable interface with very little variation in flow structure along the streamwise direction. In the lower $\mathrm{Re}_{\mathrm{l,in}}$ case (Figs. 6.1a and 6.1b), the velocity increases in the wall-normal direction towards the interface, and the profile is well described by the Yiantsios and Higgins [219] method for laminar, adiabatic stratified flows except in the close proximity to the pipe wall. This is likely due to the glow of the translucent FEP pipe as it is illuminated by the laser, which has a masking effect on the scattered light detected by the camera in the immediate vicinity of the wall. For the higher $\mathrm{Re}_{\mathrm{l,in}}$ case (Figs. 6.1c and 6.1d), $u_{\max}$ is larger and the gradient of the increase in u is highest close to the pipe wall, but this gradient decays with subsequently very little change in u between $y \approx 2\,\mathrm{mm}$ and $y = y_{\mathrm{int}}$. This flattening of the profile corresponds to the flow becoming increasingly turbulent as Re increases. Consequently, the velocity profile is not well described by the Yiantsios and Higgins [219] model over the entire range of y/y_{max} values.

Although the PIV data presented in Figs. 6.1b and 6.1d show a decrease in u close to the interface for both Re_{l} investigated, it is important to note that the error in these measurements is high due to reflection by the interface of the scattered light from the particles, which is reflected in the corresponding error bars. In fact, one expects the peak in liquid velocity to occur at the interface at which there is continuity of velocity. In boiling flows, the vapour phase accelerates as it boils due to the decrease in density, and collection of velocity field data in the vapour phase in addition to the liquid phase would provide further insights into their relative magnitudes and profile shapes.

A selection of time- and space-averaged velocity profiles are presented in Fig. 6.2 for the heat flux condition $q = 1.7\,\mathrm{kW/m^2}$ and a range of mass flux conditions. The corresponding interface heights and other relevant data can be found in Table 6.1. On visual inspection, the velocity profiles behave as expected for the denser phase of a stratified flow [220], with

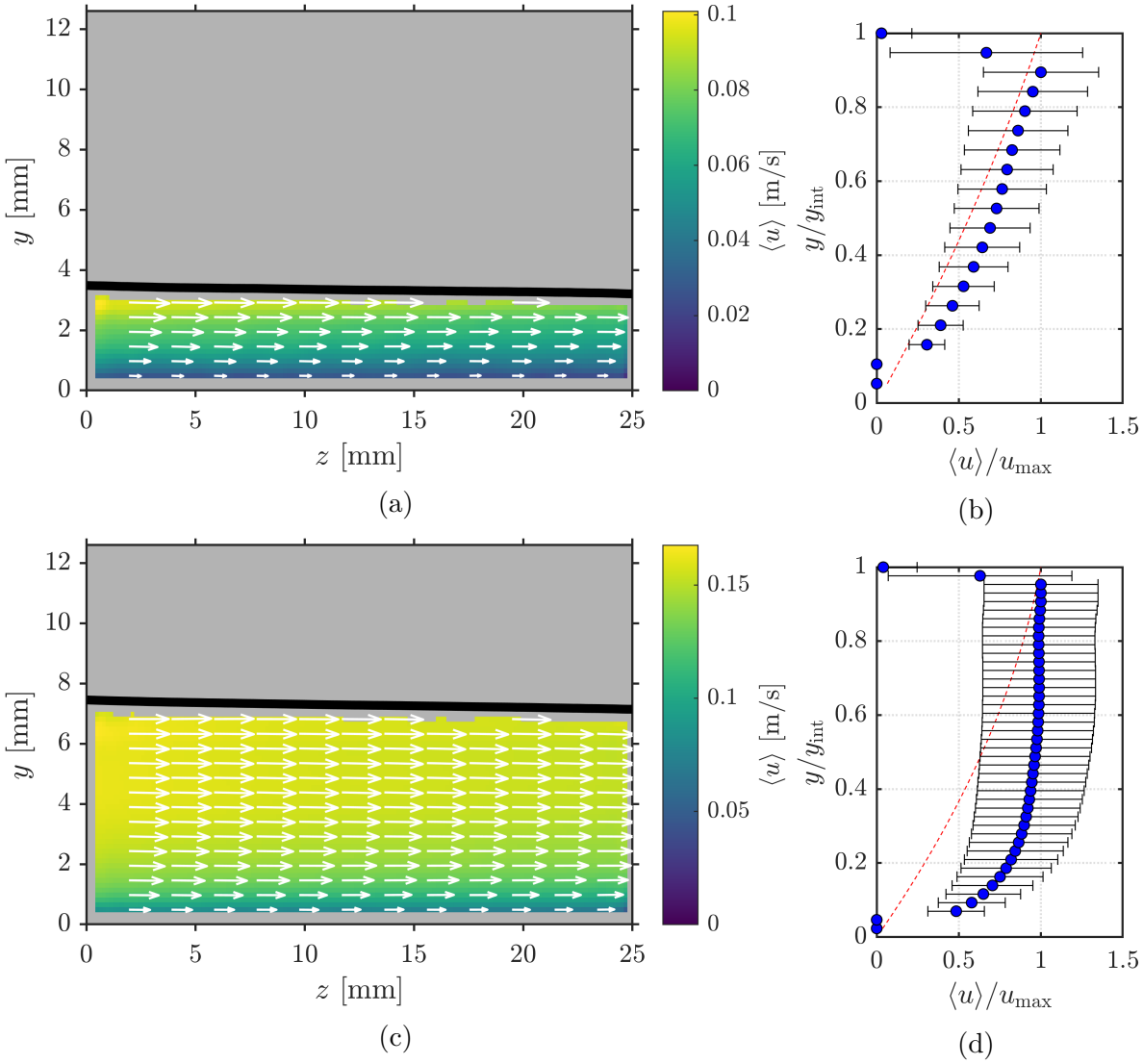


Figure 6.1: Time-averaged velocity information for two stratified flow conditions with the following experimental parameters: (a,b) $G = 32$ kg/m^2.s, $q = 1.9$ kW/m^2, $x = 0.21$; (c,d) $G = 97$ kg/m^2.s, $q = 1.1$ kW/m^2, $x = 0.04$. The velocity fields (a,c) have the colour scale $u = 0$–u_{max}. The velocity profiles (b,d) were spatially-averaged over the streamwise direction, with the red dashed line showing the velocity profile as predicted according to the Yiantsios and Higgins [219] method, and are presented with $\langle u \rangle$ normalised by $u_{\max}$ and y normalised by the interface height y_{int}.

Table 6.1: Stratified flow experimental parameters and results for the heat flux condition $q = 1.7\,\mathrm{kW/m^2}$, including the Reynolds numbers at the pipe inlet, and for the liquid phase at the measurement location, $\mathrm{Re_{l,in}} = \mathrm{Gd}/\mu_\mathrm{l}$ and $\mathrm{Re_l} = (\mathrm{G}(1-\mathrm{x})/(1-\varepsilon))\mathrm{d}/\mu_\mathrm{l}$ respectively.

G [kg/m^2.s]	$\mathrm{Re_{l,in}}$ [-]	$\mathrm{Re_l}$ [-]	x [-]	$u_{\max}$ [m/s]	y_{int} [mm]	h_{exp} [kW/m^2.K]
32	1070	4290	0.21	0.078	3.6	1.2
72	2361	8113	0.08	0.11	6.6	0.43
90	2940	9580	0.06	0.13	6.8	0.43
130	4211	13 200	0.02	0.16	9.0	0.36

the velocity going to 0 towards the wall ($y = 0\,\mathrm{mm}$) and rising with increasing proximity to the interface. As noted above, the error bars associated with the data close to the interface are rather large; consequently, the sudden reduction in velocity in this region should be interpreted with caution. At the lowest mass flux ($G = 32$ kg/m^2.s) examined, the spatiotemporally-averaged streamwise velocity component increases monotonically with wall-normal distance (with the exception of the near-interface region, as mentioned above), as shown in Fig. 6.1b. The liquid-only Reynolds number at the heated pipe inlet for this condition is $\mathrm{Re_{l,in}} = 1070$, so the flow enters the test section in the laminar regime. With increasing G, the interface height increases since a smaller proportion of the flow is evaporated at constant heat flux. Since it is proportional to the liquid layer thickness, the liquid phase Reynolds number at the measurement location $\mathrm{Re_l}$ therefore increases with G, and the flow regime in the liquid becomes transitional and then turbulent with increasing mass flux. As can be seen from Fig. 6.2, the velocity profiles become progressively flatter as a function of the wall-normal direction for $G = 72$ kg/m^2.s and $G = 90$ kg/m^2.s. For $G = 131$ kg/m^2.s, it appears that maximal velocity occurs at an intermediate wall-normal location, though it is important to note that the error bars associated with these data are large and this feature of the flow at the highest mass fluxes examined should also be interpreted with caution. A similar maximal velocity location was observed by Morgan [221] in the denser phase of a stratified liquid-liquid flow with a considerable difference in viscosity between the two phases, although the near-interface measurements would also have been subject to large errors due to internal reflection.

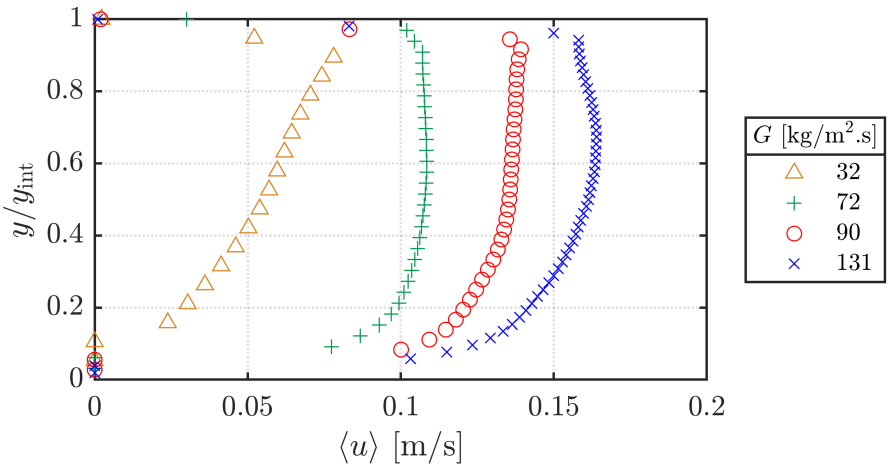


Figure 6.2: Streamwise velocity profiles, averaged over the streamwise direction and time, for stratified flow with $q = 1.7\,\text{kW/m}^2$ at a range of mass fluxes, with the vertical direction y scaled by the corresponding interface height y_{int} for each case.

6.1.2 Heat transfer effects

The average experimental heat transfer coefficient at the furthest downstream measurement junction (see Fig. 3.3) for each case in Fig. 6.2 is reported in Table 6.1. In boiling flows, h generally increases with increasing G, although this effect has been observed to become more prominent with increasing vapour quality such that at very low x, G has little impact on h [39, 69, 103]. However, Lillo et al. [136] observed the opposite effect at $x < 0.2$ with h decreasing with increasing G. This effect is also exhibited by the values in Table 6.1, where the highest value of h_{exp} corresponds to the lowest value of G and vice versa.

It is also evident that h_{exp} increases with decreasing interface height, and h_{exp} is considerably higher when the vapour liquid interface height is below the centreline ($y = 6.3\,\text{mm}$). In stratified flow, the heat transfer is dominated by the liquid phase travelling along the bottom of the pipe, which has a larger heat capacity than the vapour phase. When the film is thin, there is lower resistance to heat transfer and for the conditions presented here this film effect is greater than the effect of increased turbulence due to increasing G. Markides et al. [222] observed similar heat transfer enhancement in thin-film regions using PLIF and IR to investigate falling film flows over an inclined heated foil.

6.1.3 Heat transfer coefficient prediction

The flow-pattern based Wojtan et al. [37] predictive method for h relies on the prediction of the stratified angle, θ_{strat} (see Eq. (2.5)), and the liquid film thickness. However, the method tends to underpredict h, as shown in Fig. 5.12. Figure 6.3 shows a comparison of θ_{strat} calculated using Eq. (2.5) with θ_{strat} calculated based on the experimental interface height obtained using PLIF. In both cases the calculation assumes a flat interface. It is clear that Eq. (2.5) overpredicts the experimental θ_{strat}. The predicted two-phase heat transfer coefficient, h_{pred}, is calculated as

$$h_{\text{pred}} = \frac{\theta_{\text{strat}} h_{\text{v}} + (2\pi - \theta_{\text{strat}}) h_{\text{l}}}{2\pi} \tag{6.1}$$

and $h_{\text{l}} \gg h_{\text{v}}$, so overpredicting θ_{strat} decreases the contribution of the liquid phase heat transfer and results in an underprediction of h, as seen in Fig. 5.12. Therefore, an attempt was made to reduce the θ_{strat} prediction empirically to be in line with the experimental measurements and a relation was fitted such that:

$$\theta_{\text{strat,new}} = 0.23\theta_{\text{strat,pred}}^{1.9} \tag{6.2}$$

Inserting this relationship into the Wojtan et al. [37] method for prediction of h improved the MARD for stratified flow from 58 % to 42 %, for stratified-wavy flow from 71 % to 64 % and for all conditions from 33 % to 31 %.

To improve the prediction further, additional data points are required spanning a wider range of conditions. It would also be desirable to apply PLIF, or a similar technique, to the cross-section to determine the shape of the interface, θ_{strat} and the void fraction. Ursenbacher et al. [139] developed a technique of this type and found the Biberg [46] model (based on the Rouhani and Axelsson [45] void fraction model) to be reasonably accurate but with a tendency to overpredict the dry angle at very low or very high vapour qualities, and at high mass fluxes. Measurements of this type would provide a stronger basis for an improved θ_{strat}, and consequently h, predictive model.

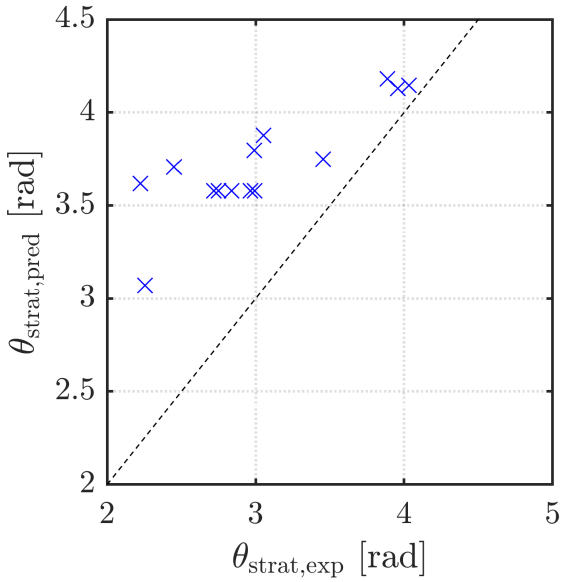


Figure 6.3: Stratified angle calculated using the Biberg [46] method, as utilised by Wojtan et al. [36], compared to that measured experimentally using PLIF. The dashed line represents $\theta_{\text{strat,pred}} = \theta_{\text{strat,exp}}$.

6.2 Stratified-wavy flow

From stratified flow, if G and/or q (and subsequently x) are increased, the characteristic flat, stable interface characteristic becomes disturbed and waves form, giving rise to stratified-wavy flow. The same PLIF and PIV methods and post-processing techniques used for stratified flow were applied to a number of stratified-wavy flow conditions. The results are presented in this section, along with some comparisons to stratified flows.

6.2.1 Velocity field information

Figure 6.4 shows instantaneous velocity fields from a stationary frame of reference in stratified-wavy flows with the parameters $G = 73$ kg/m^2.s, $q = 2.6\,$kW/m^2 (6.4a) and $G = 70$ kg/m^2.s, $q = 3.4\,$kW/m^2 (6.4b). The vapour-liquid interface is marked with a black line, and has an uncertainty of $\pm\, 0.16\,$mm. In both plots, the streamwise velocity increases from the bulk underneath the wave peak, with the highest velocity on the back slope of the wave. Figure 6.4b demonstrates higher velocities both in the bulk and in the wave crest than Fig. 6.4a despite the mass flux G being very similar. This is because Fig. 6.4b is subject to a higher heat flux q, resulting in evaporation of more of the liquid phase and therefore a higher vapour quality x and void fraction ε. This can be seen in the relative interface heights of the two plots, with Fig. 6.4b being lower. The wave height relative to

that between the waves is also higher in Fig. 6.4b, indicating enhanced waviness due to the higher heat flux. The liquid phase Reynolds numbers $\mathrm{Re_l} = (G(1-x)/(1-\varepsilon))d/\mu_\mathrm{l}$ for Figs. 6.4a and 6.4b respectively are 9430 and 11 000, indicating higher velocities and increased turbulence in the latter.

It can be seen from the changes in direction of the arrows that the wave induces secondary flows, particularly at the crest where the flow accelerates in both the streamwise and vertical directions. These secondary flows, particularly as waves become larger, can move liquid away from the heated wall as they disturb the layer of unidirectional streamwise flow close to the wall. The presence of non-zero y-components of the velocity is clearly demonstrated in both plots in Fig. 6.4, where the flow close to the interface accelerates upwards in the back of the wave (i.e. the left-hand side) then downwards out of the wave front. This downwards motion is carried into the bulk ahead of wave, with the y-component of the velocity decreasing in magnitude towards the wall. As a result, hot fluid close to the heated tube wall is moved away and replaced with cooler fluid. This increases the temperature gradient between the wall and the liquid and therefore increases the rate of heat transfer. For the stratified-wavy flow shown in Fig. 6.4a the average heat transfer coefficient at the furthest downstream measurement junction (see Fig. 3.3) is 26 % larger than that for a stratified flow of equal heat flux and 45 % larger mass flux. Since h generally decreases with decreasing mass flux in convective boiling [73, 93], this increase in h for the stratified-wavy flow is likely to be a result of the flow structures as described above. This effect was found to be consistent across all investigated conditions with comparable heat flux, suggesting a pronounced heat transfer enhancement due to interfacial waviness.

6.2.2 Interface statistics and heat transfer effects

The interface location data obtained using the image processing techniques described in Section 3.5 can be used to quantitatively characterise the interface by performing statistical analysis of the waves. Firstly, probability density functions were estimated using a minimum of 4897 frames per case. For stratified flows the interface heights were grouped into 20 bins, whilst 50 bins were used for stratified-wavy. Figure 6.5 shows the resulting probability functions, with stratified flows represented by lines in shades of red, and stratified-wavy flows in shades of blue. The colour grading is representative of the

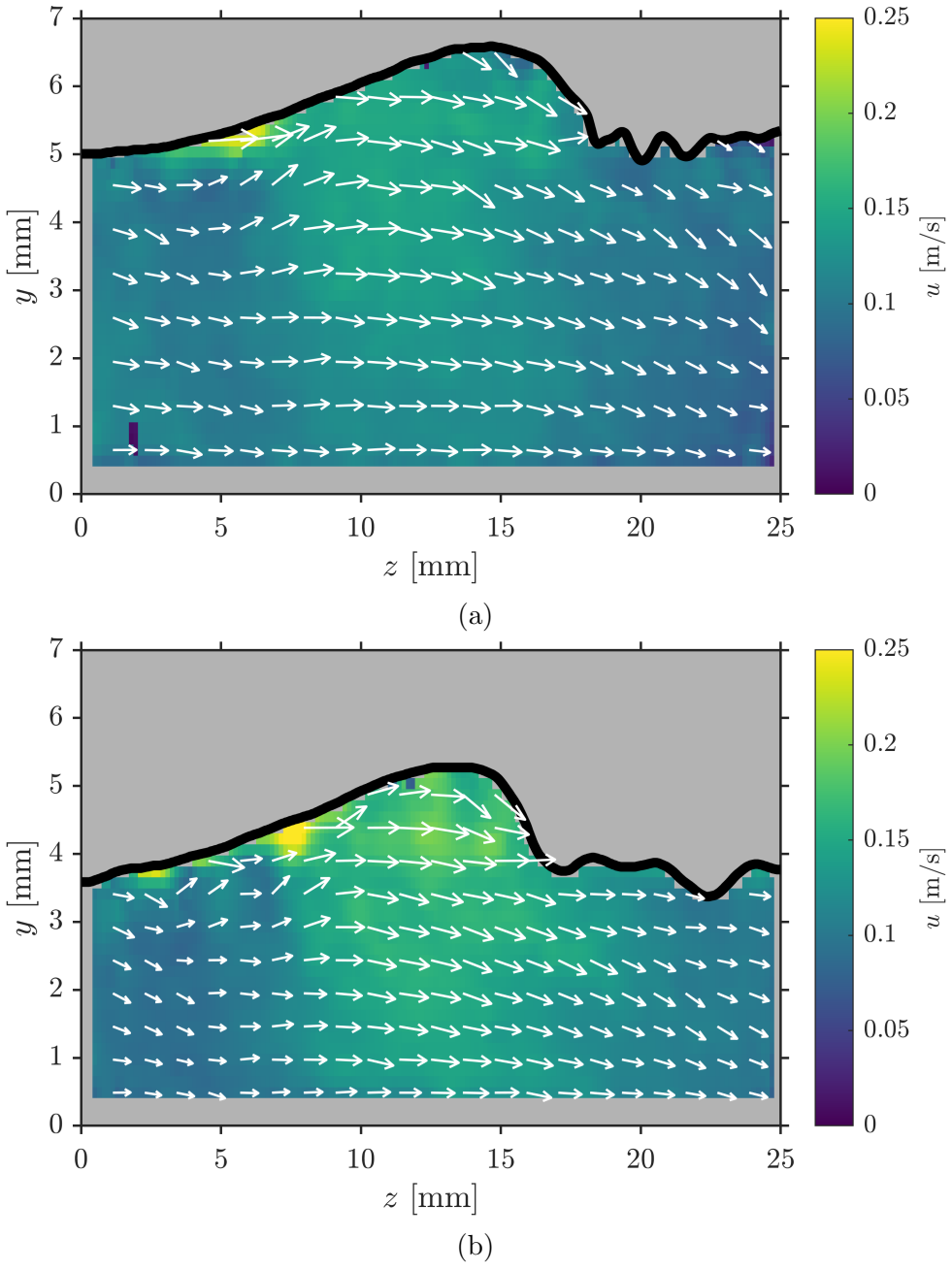


Figure 6.4: Instantaneous liquid-phase velocity fields from a stationary frame of reference in stratified wavy flows with the conditions (a) $G = 73$ kg/m^2.s, $q = 2.6$ kW/m^2, $x = 0.13$ and (b) $G = 70$ kg/m^2.s, $q = 3.4$ kW/m^2, $x = 0.17$. The pipe inside diameter is $d = 12.6$ mm. The interface is identified with the black line and the length of the arrows represents the magnitude of the velocity vector, whilst the colour map in the background represents the magnitude of the velocity in the streamwise direction, z.

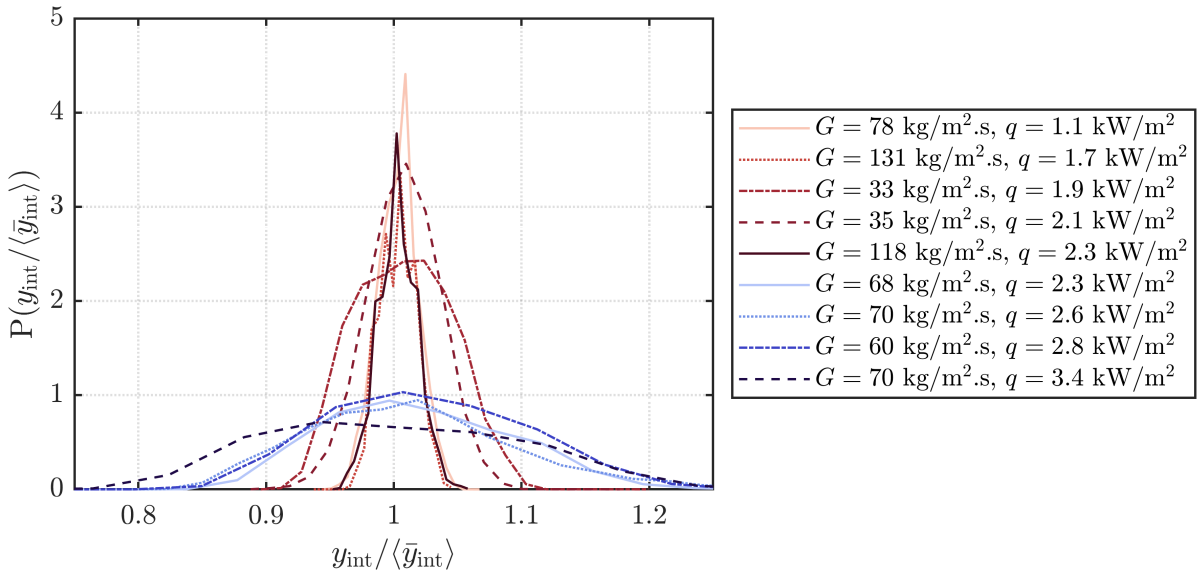


Figure 6.5: Probability density functions of film thickness normalised by the mean film thickness over all frames and pixels for each set of experimental conditions. Red lines represent stratified flow and blue lines represent stratified-wavy flow, with colour grading corresponding to heat flux.

value of the heat flux. To enable comparison, the interface height is normalised by the mean interface height $\langle\bar{y}_{\mathrm{int}}\rangle$, obtained by averaging the interface height across all pixels in all frames for each case.

The range of $y_{\mathrm{int}}/\langle\bar{y}_{\mathrm{int}}\rangle$ in Fig. 6.5 is approximately two to three times as large for stratified-wavy flows as for stratified, indicating more variation in interface height as expected in the presence of waves and interfacial disturbances. The mass flux is relatively constant across the stratified-wavy cases, but varies more across the stratified cases due to the limitations of the facility. For both flow types, at comparable values of G the distribution is wider for higher heat fluxes. At a constant mass flux, increasing the heat flux results in an increase in vapour quality. The larger volume of fast-moving vapour induces more disturbance at the interface and hence a wide interface height distribution.

Both stratified and stratified-wavy flows in Fig. 6.5 are characterised by distributions with a single peak. In similar analysis for liquid film flows, Charogiannis et al. [16] observed a double-peak distribution which they attributed to the presence of two types of waves: large disturbance (or primary) waves and small ripple (or secondary) waves. Zadrazil and Markides [15] reported the occurrence of disturbance waves with recirculation for wave peak to film height ratios above 3, but it can be seen from Fig. 6.5 that such high ratios were not reached in this work. Indeed, a normalised interface height of 3 will

not be achievable in pipe flow unless $\langle \bar{y}_{\text{int}} \rangle < d/3$, but even taking this limitation into account the ratios found in this work are much smaller than required for the formation of disturbance waves. Also, no recirculation flows were observed in this work, even for the largest waves. This is apparent in Fig. 6.4, in which variation in the flow direction under the waves is evident, but there is no flow reversal.

To assess the impact of the interfacial characteristics on heat transfer it was necessary to extract an integral measurement, since the corresponding heat transfer coefficient measurements for each case are also integral measurements. The mean interface height, $\langle \bar{y}_{\text{int}} \rangle$, was calculated by averaging the interface height across all pixels and frames for each case, whilst an interfacial roughness was calculated as the ratio of the root mean square of the interface heights across all pixels and frames for each case, normalised by the corresponding mean interface height. The dimensionless heat transfer, expressed in terms of the Stanton number, $\text{St} = h/Gc_{p,\text{l}}$, is plotted as a function of these two variables for both stratified and stratified-wavy flows in Fig. 6.6.

Figure 6.6a shows that in general the mean film thickness was greater in the stratified flows investigated than the stratified-wavy flows. To achieve stratified flows as opposed to stratified-wavy flows, lower heat flux conditions were mostly used, resulting in less evaporation of the liquid phase and a higher liquid-vapour interface. The two points at approximately 4 mm correspond to a stratified flow condition with low mass flux and relatively high heat flux. Figure 6.6b shows that interfacial roughness was higher for stratified-wavy flows than stratified flows, as expected based on Fig. 6.5. However, the magnitude of the interfacial roughness for stratified-wavy flows indicates that they are not dominated by large disturbance waves, or it would be much higher.

Considering Fig. 6.6a it is clear that heat transfer decreases with increasing interface height when $\langle \bar{y}_{\text{int}} \rangle \lesssim d/2$ (note that $d = 12.6\,\text{mm}$), particularly for stratified-wavy flows. Thin film heat transfer enhancement has been observed in heated falling films [222, 223], where a thinner film presents lower resistance to heat transfer and will be proportionally more affected by interfacial waves and disturbances resulting in more efficient replacement of warm fluid at the wall with colder fluid.

Aside from the two points in the top left of the plot, Fig. 6.6b suggests that increasing interfacial roughness enhances heat transfer, although the correlation is not definitive enough to completely isolate this effect. However, this behaviour is in line with observa-

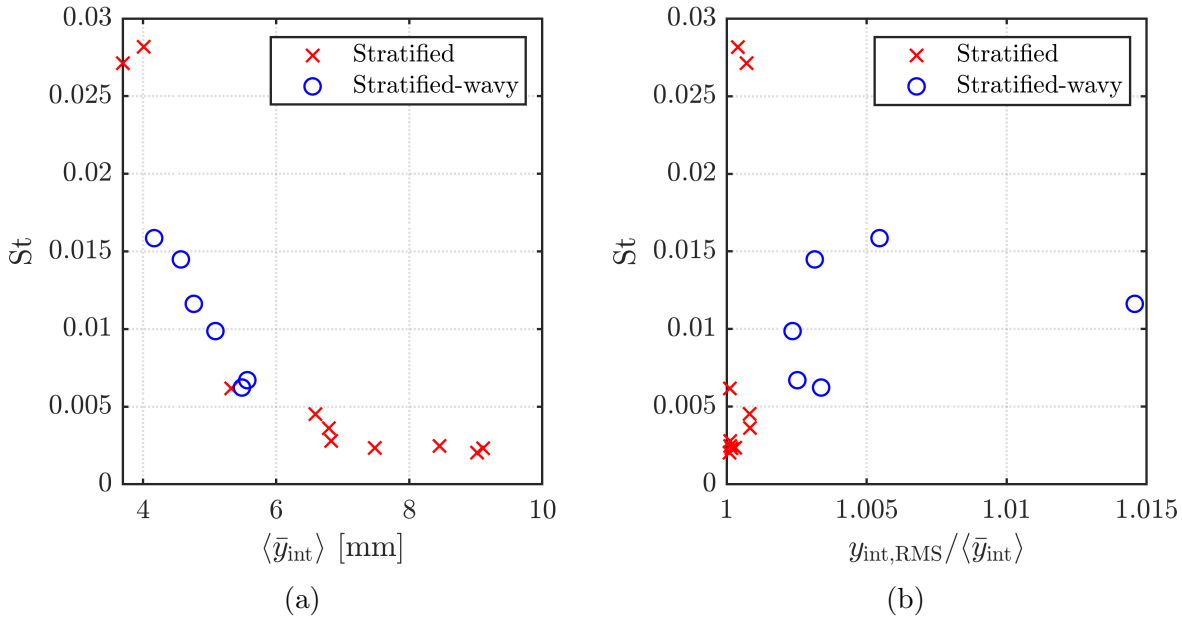


Figure 6.6: Stanton number ($\mathrm{St} = h/Gc_{p,\mathrm{l}}$) vs. (a) mean interface height $\langle \bar{y}_{\mathrm{int}} \rangle$ and (b) interfacial roughness $y_{\mathrm{int,RMS}}/\langle \bar{y}_{\mathrm{int}} \rangle$ for stratified and stratified-wavy flows.

tions of heat transfer enhancement due to film waviness reported for film flows [223–225] caused by increased mixing and turbulence. The two outlier points correspond to cases with very low mass flux, higher heat flux and consequently a very thin film, suggesting that the thin film heat transfer enhancement is dominant over the enhancement due to film waviness for these conditions.

6.2.3 Wave characteristics

To further investigate the interfacial disturbances, the waves were characterised by locating their peaks and troughs and fitting a radius of curvature to both. This was an effective way to gain insights into the size of waves across the data set, since the large peak heights of 2–3 times the mean interface height observed in film flows [15] were not present at the conditions investigated in this work. The resulting probability density distributions of radii of curvature from this analysis as applied to both peaks and troughs are presented in Fig. 6.7. Distributions for both stratified and stratified-wavy flow are included to assess the flatness of the stratified vapour-liquid interface. Clearly, any interfacial disturbances are smaller in magnitude for stratified flow, with the range of radius of curvature up to 20 times smaller than for stratified-wavy flow. The span of the distributions varies across the stratified flows presented, with the widest for a low mass flux, high heat flux condition,

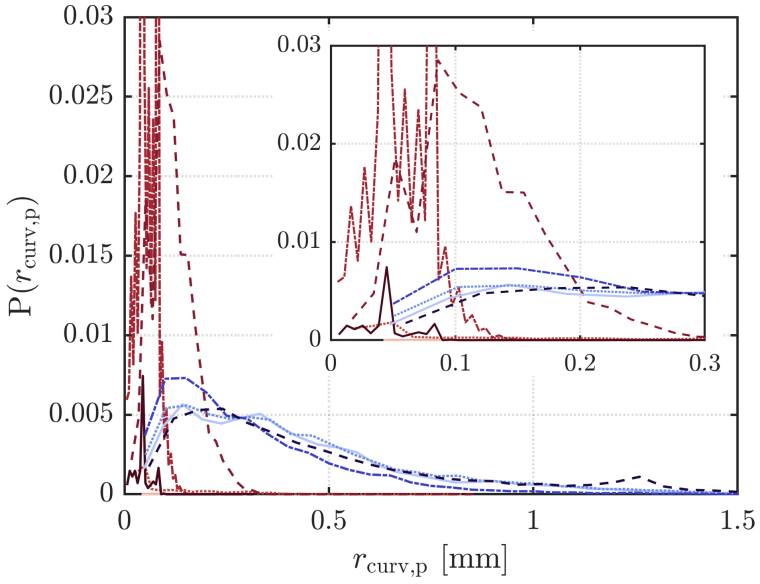
as would be expected. For all stratified distributions the peak is far towards the left of the plot, but is not at 0 mm, indicating the interface is not generally entirely flat.

For stratified-wavy flows in Fig. 6.7 the distributions are much wider but do not vary significantly between cases, as might be expected due to the similarity of the experimental conditions. The distributions have a single peak shifted towards the left, indicating dominance of small waves and confirming the lack of large disturbance waves. For both flow patterns, the radius of curvature distributions are very similar for both peaks and troughs, suggesting vertical mirroring of waves - i.e. every peak has a corresponding trough of a comparable size. The trough distributions tend to extend to slightly larger radii of curvature than the peaks, up to 0.5 mm larger but with low corresponding probability density estimates at these values.

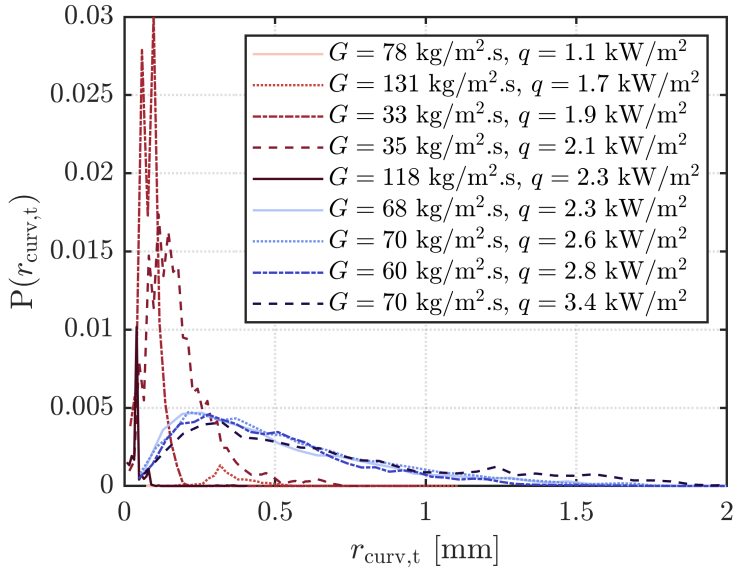
The distributions obtained in Fig. 6.7 were used to group the waves by their characteristic sizes and apply an ensemble averaging technique similar to that used by Charogiannis et al. [16] to examine the velocity fields underneath waves and troughs. For a given r_{curve} range, the relevant peaks and troughs were identified and the mean interface height of each, and across all peaks or troughs in the range, was calculated. The velocity fields of each individual peak or trough were scaled based on the ratio of the individual to overall mean interface height, then averaged across the set.

Relatively large radius of curvature limits were selected for Figs. 6.8 and 6.9 to illustrate the velocity fields under more significant waves and troughs, as the analysis up to this point has suggested that it is these interfacial disturbances that are responsible for heat transfer enhancement. Figures 6.8b and 6.9b show the ensemble averaged velocity profiles extracted under the central point of the waves and troughs respectively.

Underneath both peaks (Fig. 6.8) and troughs (Fig. 6.9), the velocity profile in the bulk has the flattened parabolic shape seen in transitional-turbulent stratified flows in Fig. 6.2. However the maximum velocity on this parabola occurs low down, close to the wall, above which there is a steady slight deceleration to a local minimum approximately 1.5 mm below the interface. Moving upwards from that point, the streamwise velocity increases towards the interface, suggesting the interface is moving faster than the bulk liquid. These effects are more pronounced under the peak than the trough. Similar mean streamwise velocity profile shapes were observed in stratified-wavy air-water flows in larger pipes ($d_{\text{i}} = 50$–100 mm) by Birvalski et al. [226] and Ayati et al. [227], and by Lee et al.



(a)



(b)

Figure 6.7: Probability density functions of the wave radii of curvature r_{curv} for (a) peaks and (b) troughs. Red lines represent stratified flow and blue lines represent stratified-wavy flow, with colour grading corresponding to heat flux. An inset is provided in (a) expanding the $r_{curv,p} = 0$–0.3 mm region.

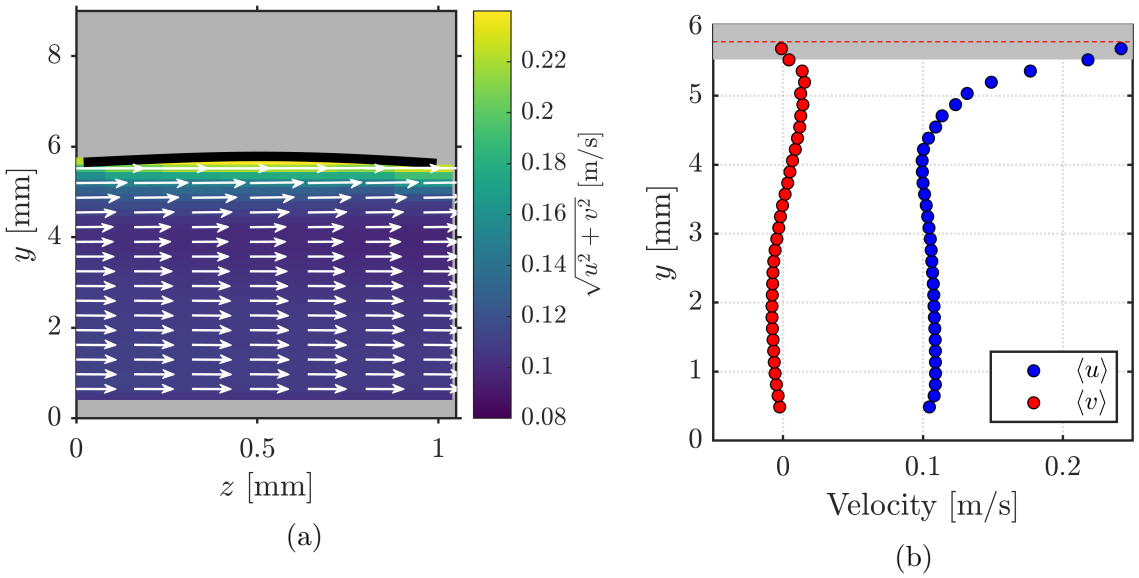
[228] for air-water and steam-water flows in a horizontal rectangular channel.

The behaviour of the vertical component of the velocity, v, is more obvious from the velocity profiles (Figs. 6.8b and 6.9b) than the fields (Figs. 6.8a and 6.9a). In the bulk, $v < 0\,\mathrm{m/s}$ and the liquid is moving downwards (i.e. towards the wall) with a velocity approximately 10 times smaller than that in the streamwise direction. However, close to the local minimum in u, v increases above $0\,\mathrm{m/s}$ and the liquid accelerates upwards to a maximum approximately 0.5 mm below the interface before decreasing back to $0\,\mathrm{m/s}$ at the interface. This description corresponds to the velocity vectors under the wave crests in the instantaneous velocity fields in Fig. 6.4. The negative v in the bulk has a larger maximum magnitude under the trough than the peak by approximately 30 %, although the maximum v close to the interface only differs by approximately 1 %.

It is also clear from Figs. 6.8 and 6.9 that there is no recirculation since it is always the case that $u > 0$. No recirculation flows were observed under any of the waves or troughs investigated either before or after ensemble averaging. This again points to the lack of large disturbance waves in these flows as such waves would typically experience flow recirculation in the main wave hump [229]. Yet, despite the lack of recirculation flows there is heat transfer enhancement due to interfacial waviness, as seen in Fig. 6.6. This could be attributed to the increased turbulence both in the bulk and at the interface, and the vertical movement of bulk fluid towards the wall. This movement results in cooler fluid temperatures close to the wall, increasing the local temperature difference and enhancing the driving force for heat transfer. Local temporally resolved measurements of wall and fluid temperatures would further aid the understanding of this mechanism and the interaction between the thermal and hydrodynamic behaviour.

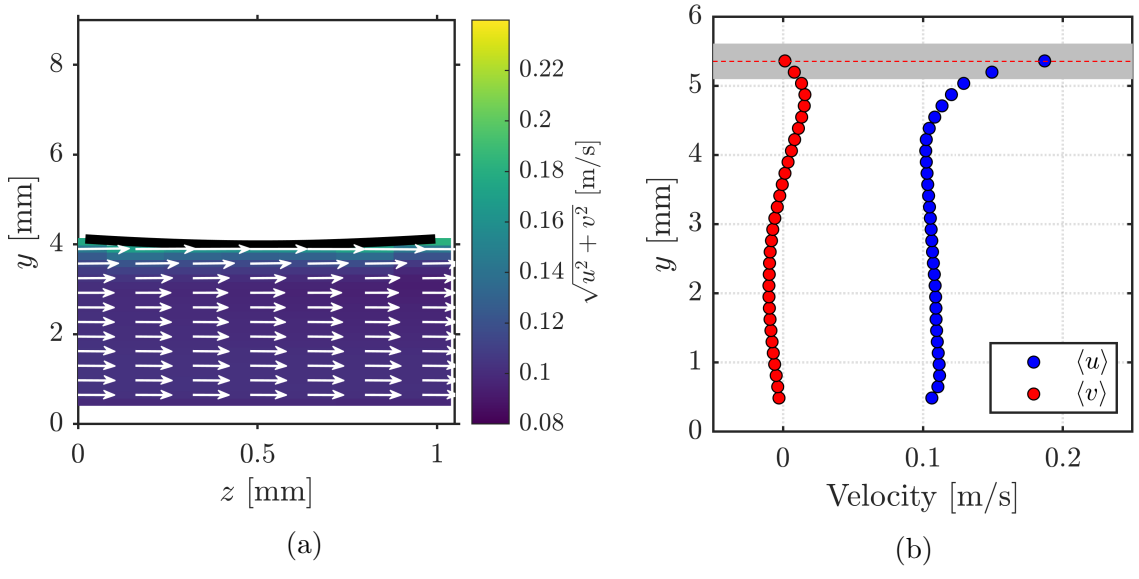
6.3 Slug flow

Slug flow occurs at low vapour qualities (see Fig. 5.3) as the mass flux is increased above that at which stratified flow occurs. It is characterised by alternating liquid slugs, in which the liquid phase occupies the entire cross-section of the pipe, and vapour bubbles around which a liquid film exists. This structure can result in effective heat transfer, but the intermittent nature of the flow pattern can cause large variations in pressure drop and momentum transfer. It is thus useful to understand the velocity fields in slug flow and



(a) (b)

Figure 6.8: (a) Ensemble averaged velocity field and (b) corresponding profiles under waves for $0.9 < r_{\text{curv}} < 1$ at the conditions $G = 68$ kg/m^2.s, $q = 2.3\,$kW/m^2. The velocity profiles were extracted at the centre of the wave for the streamwise and vertical velocities, u and v respectively.



(a) (b)

Figure 6.9: (a) Ensemble averaged velocity field and (b) corresponding profiles under troughs for $0.9 < r_{\text{curv}} < 1$ at the conditions $G = 68$ kg/m^2.s, $q = 2.3\,$kW/m^2. The velocity profiles were extracted at the centre of the trough for the streamwise and vertical velocities, u and v respectively.

characteristic parameters such as slug frequency.

The results presented in this section were obtained for slug flows at three heat flux conditions: $q = 5.3\,\mathrm{kW/m^2}$, $6.6\,\mathrm{kW/m^2}$ and $7.9\,\mathrm{kW/m^2}$. At each condition, three measurements were taken with $G = 300$ to $460\ \mathrm{kg/m^2.s}$. The film above the vapour bubble was not discernible at the camera magnification used (frame size 12.6 by 25 mm, resolution of 20 µm/px) and was in the region obscured by the glow from the top of the FEP pipe. Therefore, the same interface detection algorithm used for stratified and stratified-wavy flows, as described in Section 3.6.2, was applied to slug flow to identify the liquid phase underneath the vapour bubbles. The presence of smaller vapour bubbles, particularly around the nose and tail of the vapour slug, causes unphysical peaks in the detected interface, so the interface data was also smoothed along the time dimension on a pixel-by-pixel basis. A selection of high-speed images with the identified vapour-liquid interfaces and the corresponding velocity fields masked to show the liquid phase only are presented in Fig. 6.10.

6.3.1 Velocity fields

The bottom row of Fig. 6.10 shows velocity fields extracted along the centre plane of the pipe in a stationary frame of reference around a vapour bubble in slug flow at the conditions $G = 460\ \mathrm{kg/m^2.s}$, $q = 7.9\,\mathrm{kW/m^2}$, where the interface is marked by a black line. The colour map represents the magnitude of the velocity, whilst the arrows indicate both its magnitude and direction. In Fig. 6.10, (a) and (c) show the tail and nose, respectively, of a vapour bubble, whilst (b) corresponds to the middle of the vapour bubble and was extracted at a time stamp halfway between (a) and (c).

As the bubble enters the frame (Fig. 6.10c), the flow in the tail of the liquid slug is disturbed and there is movement in both the streamwise and vertical directions. The velocity magnitude decreases from the bulk, perhaps indicating some stagnation points as the flow direction changes in this region. The vertical movement is predominantly downwards, showing the liquid shedding as the liquid is pushed away by the advancing vapour phase. The flow field below the interface height corresponding to the body of the bubble (around 7 mm) is not significantly affected by the appearance of the bubble nose with flow predominantly in the streamwise directions with a maximum velocity in the centre of the pipe that decreases in magnitude towards the wall.

The flow behind the bubble (Fig. 6.10a), in the liquid slug nose, is similarly disturbed, although the vertical movement is mainly upwards as liquid fills the space previously occupied by the vapour bubble. However, the magnitude of the velocity in the liquid slug nose is up to 2 times higher than in the tail (Fig. 6.10c), an effect observed by various other authors both experimentally [230, 231] and computationally [231–233]. The bulk flow under the back of the vapour bubble also demonstrates a more significant upwards movement further towards the interface than the downwards movement under the front of the bubble in Fig. 6.10c. The velocity variations in the liquid slug nose are indicative of the formation of the mixing eddy proposed by Dukler and Hubbard [234], and it would be interesting to see how these relate to local variations in heat transfer coefficient. Such measurements could be obtained by, for example, infrared imaging of the pipe wall.

Underneath the central region of the vapour bubble (Fig. 6.10b) the velocity field is very similar to that in a turbulent stratified flow (see Fig. 6.1c). The streamwise velocity in most of the liquid is close to constant, with a decrease in magnitude towards the pipe wall. There are some variations close to the interface corresponding to interfacial waviness, similar to a stratified-wavy flow (see Fig. 6.4). Xu et al. [230] also observed similarly-shaped velocity profiles under the vapour bubble in an air-water slug flow in a 51 mm pipe.

Across the three regions in Fig. 6.10, the magnitude of the velocity in the near wall region, approximately $y = 0$–$2.5\,\text{mm}$ is very similar. Xu et al. [230] also noted this behaviour, and it shows how the impact of the vapour slug on the liquid phase velocity decays with distance from the interface. It might then be expected that the local heat transfer coefficient at the bottom of the pipe would not vary as much with time as that at the top of the pipe.

6.3.2 Slug frequency

The slug frequency was calculated for the slug flows investigated in FLOBOF through analysis of the time-dependent trace of the interface location. An example of such a trace, extracted at the $z = 12.5\,\text{mm}$ location (see Fig. 6.10) for slug flow at the conditions $G = 460\ \text{kg/m}^2\text{.s}$, $q = 7.9\,\text{kW/m}^2$ is shown in Fig. 6.11a. In this figure, the periods in which the interface height is equal to 12.6 mm, i.e. the pipe inside diameter, correspond to the liquids slugs since there is no vapour-liquid interface, and therefore no vapour,

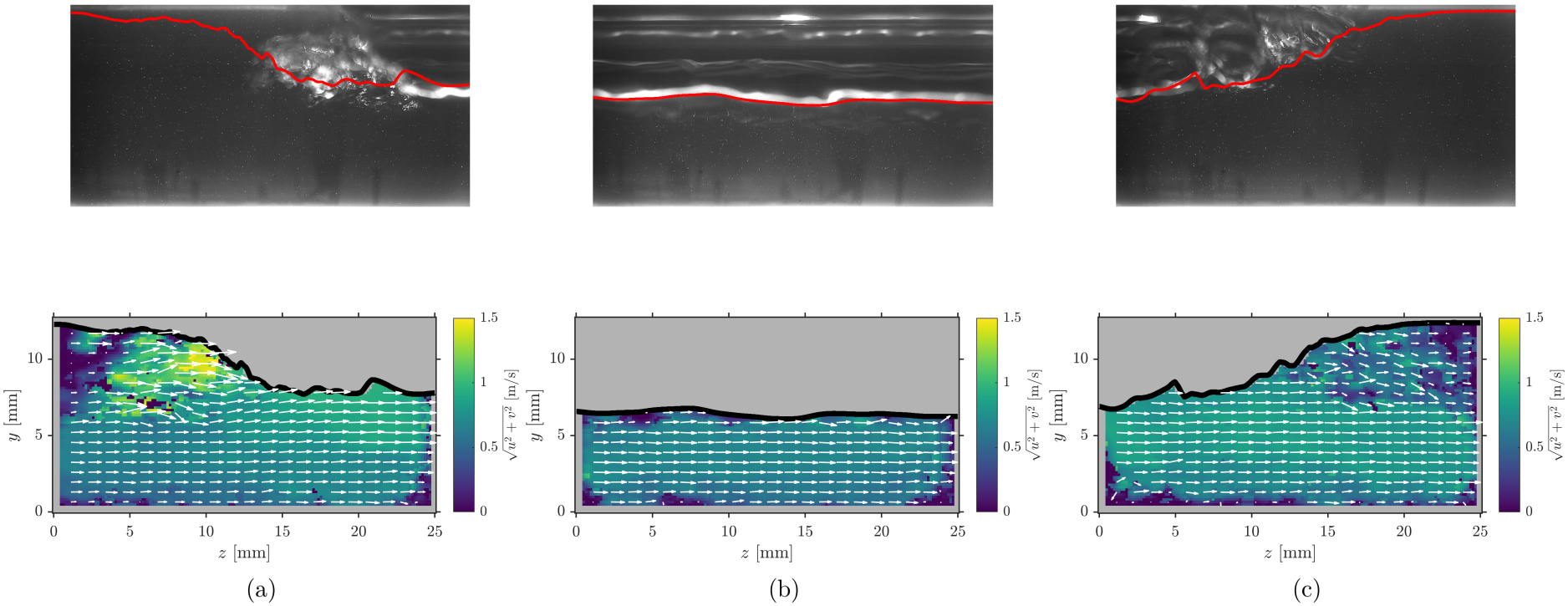


Figure 6.10: Representative high speed images (top row) with the detected interface marked with a red line and corresponding masked instantaneous velocity fields (bottom row) in a stationary frame of reference for slug flow at the conditions $G = 460\,\mathrm{kg/m^2.s}$, $q = 7.9\,\mathrm{kW/m^2}$. Images and velocity fields are shown at the (a) tail, (b) middle and (c) nose of a vapour bubble.

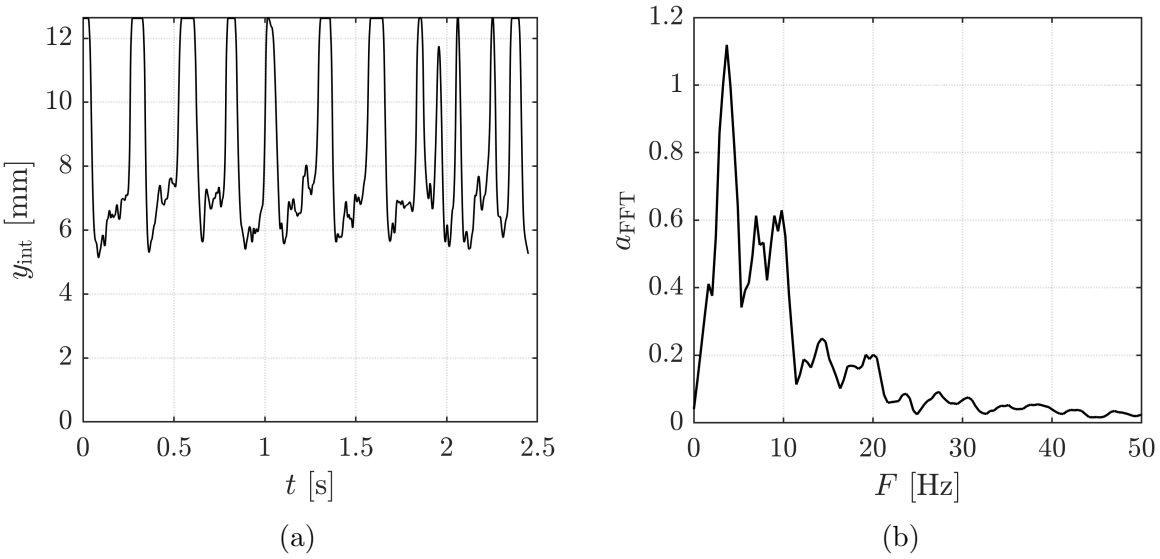


Figure 6.11: (a) Interface height versus time and (b) corresponding fast Fourier transform displayed as amplitude versus frequency at the $z = 12.5\,\mathrm{mm}$ location in the stationary frame of reference of the high-speed images, for slug flow at the conditions $G = 460\ \mathrm{kg/m^2.s}$, $q = 7.9\,\mathrm{kW/m^2}$.

present. After each of these periods the trace undergoes a sudden decrease in interface height indicating the appearance of a vapour bubble. The interface height appears to increase slightly as the bubble moves past the reference point before jumping back to 12.6 mm when the back of the bubble has passed. The shape of the peaks is somewhat different just before 2 s, where some small vapour bubbles remained at the top of the pipe in the liquid slug between consecutive long vapour bubbles.

It is clear from Fig. 6.11a that a characteristic slug frequency exists, so a fast Fourier transform was performed on the interface height trace in order to express the data in the frequency domain. The resulting frequency signal is shown in Fig. 6.11b. The significant peak at a frequency of 3.7 Hz indicates the slug frequency, and corresponds to Fig. 6.11a where the interface height reaches 12.6 mm around 4 times in each second.

The slug frequency for each set of conditions investigated was determined using the procedure described above. To assess the effect of slug frequency on heat transfer, it is plotted against the Stanton number St in Fig. 6.12 with data points separated by heat flux q conditions. Considering all of the points together, it might be concluded that St increases with slug frequency. A higher slug frequency would result in more frequent appearances of slug noses and tails in which the flow is disturbed as seen in Fig. 6.10 and mixing eddies form. These secondary flows enhance the heat transfer, as discussed

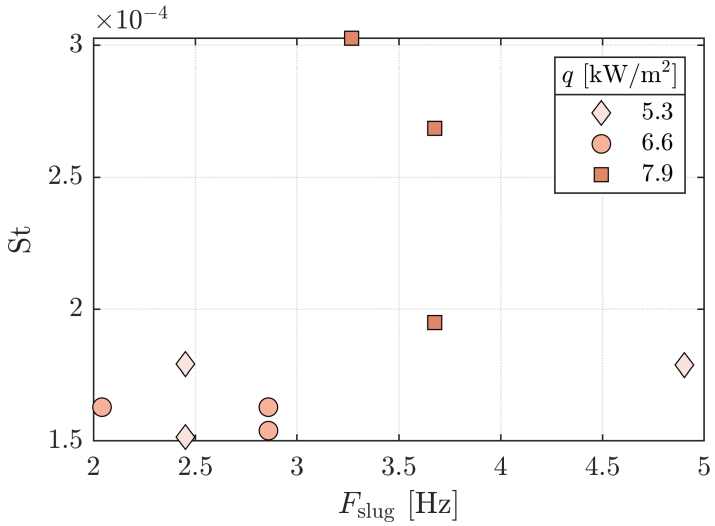


Figure 6.12: Effect of slug frequency F_{slug} on heat transfer, illustrated by plotting the Stanton number $\text{St} = h/Gc_{p,\text{l}}$, to normalise for the differing mass fluxes, against slug frequency. The different heat flux conditions are indicated by different marker symbols and colours.

for stratified-wavy as opposed to stratified flow in Section 6.2.2. However, the picture is less clear if the effects of the different heat flux conditions are taken into account, with St seemingly independent of slug frequency for $q = 5.3\,\text{kW/m}^2$ and $6.6\,\text{kW/m}^2$, yet varying by up to 25 % over a small range of frequencies for $q = 7.9\,\text{kW/m}^2$. More data is required across the range of heat flux conditions to draw any significant conclusion, and could be the focus of further work with the FLOBOF facility.

Various methods exist in the literature for predicting slug frequency in adiabatic vapour-liquid flows. A long-standing and widely used method is that of Gregory and Scott [235], which was developed from experiments with carbon dioxide and water in a 19 mm inside diameter (ID) pipe and has the form

$$F_{\text{slug}} = 0.0226 \left[\frac{u_{\text{s,l}}}{gd} \left(\frac{19.75}{u_{\text{m}}} + u_{\text{m}} \right) \right]^{1.2} \tag{6.3}$$

where $u_{\text{s,l}}$ is the superficial liquid velocity $u_{\text{s,l}} = G(1-x)/\rho_{\text{l}}$ and u_{m} is the superficial mixture velocity $u_{\text{m}} = u_{\text{s,l}} + u_{\text{s,v}} = G(1-x)/\rho_{\text{l}} + Gx/\rho_{\text{v}}$. However, Al-Safran [236] found this model to be insufficient since it does not account for the probability associated with the predicted slug frequency value, and instead proposed a probabilistic model of the form

$$F_{\text{slug}} = \exp(1.51 - 17.04d + 0.77 \ln u_{\text{s,l}} - 0.181 \ln S) \tag{6.4}$$

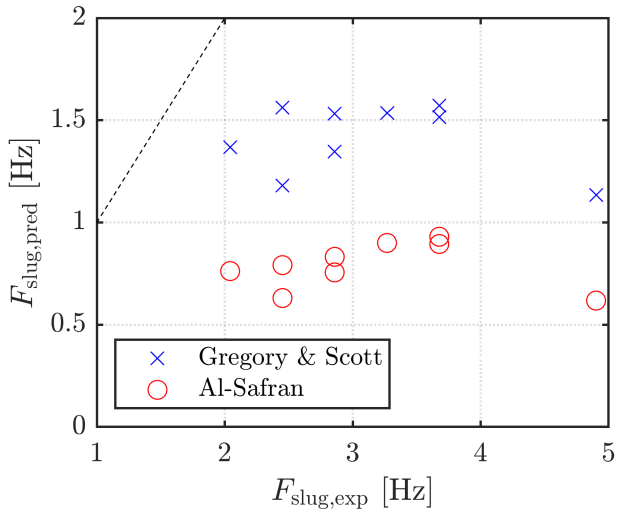


Figure 6.13: Predicted versus experimental slug frequency for predictive methods proposed by Gregory and Scott [235] and Al-Safran [236]. The black dashed line indicates equality of the predicted and experimental values.

where S is the slip ratio calculated according to Schmidt et al. [237] as

$$S = \frac{u_{\text{v}}}{u_{\text{l}}} = 1 + \alpha \left(\frac{\mu_{\text{l}}}{\mu_0} \right)^{\beta} \left(\frac{u_{\text{s,v}}}{u_{\text{s,l}}} \right)^{\gamma} \tag{6.5}$$

and μ_0 is a reference viscosity equal to 1 Pa s. α, β and γ are empirical parameters estimated by Al-Safran [236] as 1.95, 0.01 and 1.5 respectively as a best fit to their data.

Figure 6.13 shows the slug frequencies predicted using these methods against the experimentally-determined slug frequencies. Neither method predicts the experimental values well, with the Gregory and Scott [235] method underpredicting by a mean value of 52 % and the Al-Safran [236] method by 73 %. However, Al-Safran [238] showed the average error across several existing predictive methods to be 75 %, so the apparently large errors in comparison to this work are in line with performance of such correlations in the literature. Also, both the correlations were developed for adiabatic flow, so do not take heat transfer and boiling affects into account. The error in the Al-Safran [236] method could likely be reduced with tuning of the parameters α, β and γ in Eq. 6.5 for the experimental conditions.

6.3.3 Vapour bubble velocity

Another flow characteristic of note that can be extracted from the interface data is the vapour bubble velocity. Figure 6.14 shows the time-dependent traces of interface height

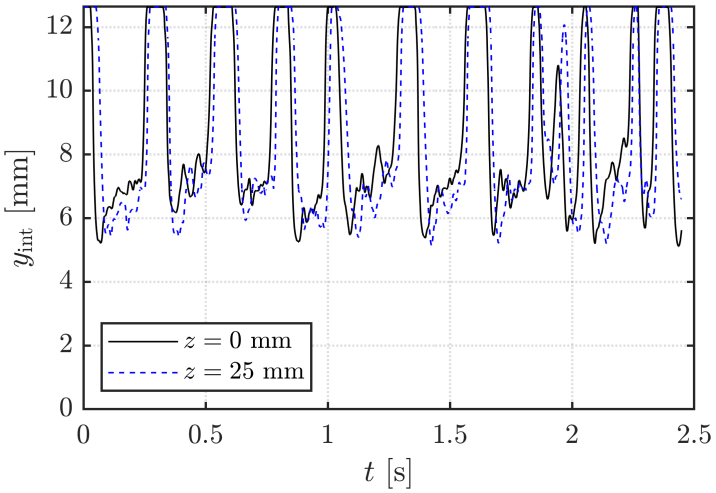


Figure 6.14: Interface height versus time at the $z = 0\,\mathrm{mm}$ (solid black line) and $z = 25\,\mathrm{mm}$ (dashed blue line) locations in the stationary frame of reference of the high-speed images, for slug flow at the conditions $G = 460\ \mathrm{kg/m^2.s}$, $q = 7.9\,\mathrm{kW/m^2}$.

extracted at the locations $z = 0\,\mathrm{mm}$ and $z = 25\,\mathrm{mm}$ (see Fig. 6.4) in a stationary frame of reference. It is clear that there is a time shift from one to the other as identical flow features pass the two points at different times. For example, the shift between the two lines at the points at which the interface height decreases from 12.6 mm is equal to the time taken for the front of the vapour bubble to travel from the left-hand side of the frame to the right-hand side, i.e. 25 mm. Based on this time shift and the known distance travelled, an average bubble velocity was determined for each set of slug flow conditions.

Figure 6.15 shows the calculated vapour bubble velocities plotted against the corresponding superficial mixture velocities, with points separated by heat flux. Overall, bubble velocity increases with mixture velocity, as would be expected. For the heat flux conditions $q = 5.3\,\mathrm{kW/m^2}$ and $7.9\,\mathrm{kW/m^2}$ the bubble velocity increases linearly with the mixture velocity, albeit with a larger gradient for the higher q conditions. This linear behaviour is in line with the relationship proposed by Nicklin et al. [239], where the bubble velocity is calculated as $u_{\mathrm{b}} = C_0 u_{\mathrm{m}} + C_1$, where C_0 and C_1 are constants with the latter interpreted as the drift velocity. From Fig. 6.15, it would appear that for boiling flow C_0 is dependent on heat flux.

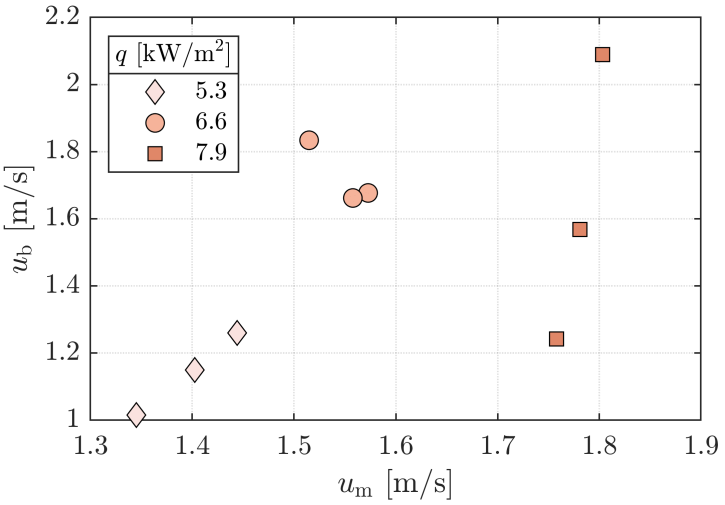
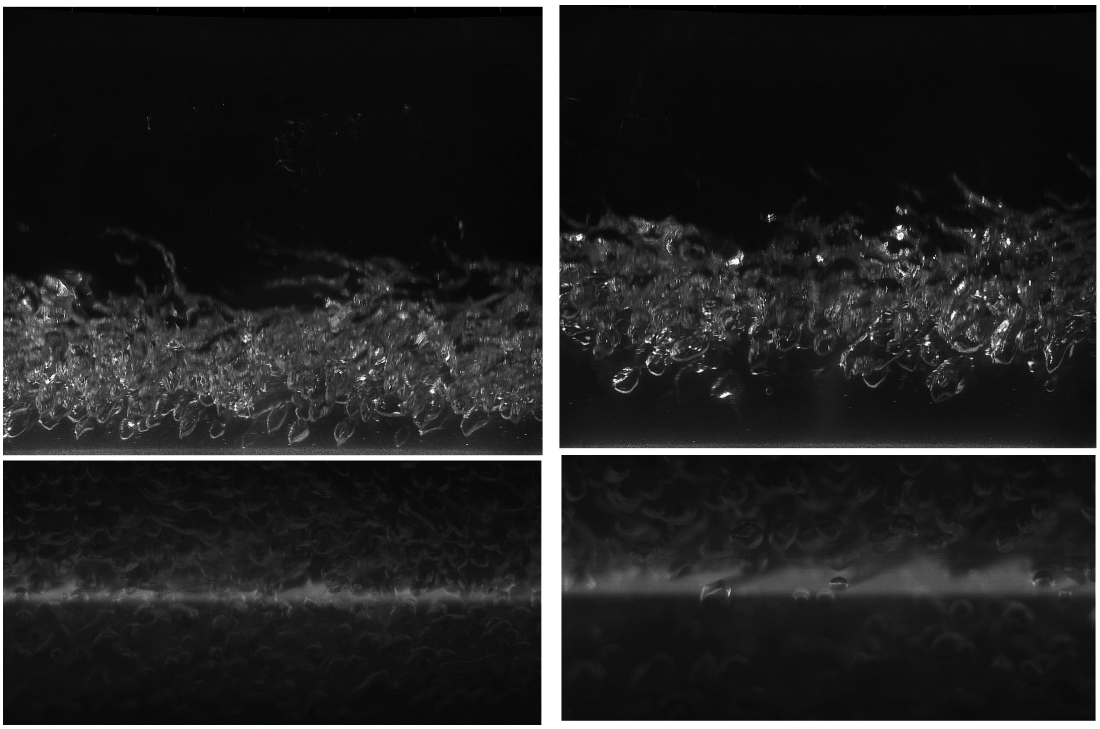


Figure 6.15: Vapour bubble velocity u_b versus superficial mixture velocity u_m for slug flow. The different heat flux conditions are indicated by different marker symbols and colours.

6.4 Annular flow

Annular flow occurs at high mass fluxes and vapour qualities, and is characterised by a continuous vapour core flowing inside a liquid annulus. In horizontal annular flow, the thickness of the liquid film is larger at the bottom of the pipe than the top due to gravity. In this work, film thickness variations in other flow patterns were shown to affect heat transfer, so it is reasonable to assume this will also be the case in annular flow, which has the added complexity of film asymmetry around the pipe circumference. Thus, as a first step to understanding this film behaviour, the advanced optical diagnostic methods and processing techniques described in Sections 3.5 and 3.6.3 were applied to annular flows with the conditions G = 380–510 kg/m^2.s, q = 21–29 kW/m^2 to investigate the bottom liquid film behaviour. These experimental conditions approached the upper limit of the capabilities of the system whilst maintaining a steady state in the flow loop for measurements.

Examples of the PLIF and BBLIF images obtained for annular flow are shown in Fig. 6.16 for two flow conditions. It is clear from the images that there are a great deal of bubbles around the interface, and this is characteristic of all the annular flow conditions investigated with these techniques. Attempts were made to achieve a flow with a smoother interface but an appropriate set of conditions could not be found within the limitations of the FLOBOF facility. The interfaces around the bubble reflect the laser light and appear



(a) (b)

Figure 6.16: Example instantaneous PLIF (top) and BBLIF (bottom) images in a stationary frame of reference for annular flow with the conditions (a) $G = 440$ kg/m^2.s, $q = 26\,\mathrm{kW/m^2}$ and (b) $G = 510$ kg/m^2.s, $q = 21\,\mathrm{kW/m^2}$.

brighter than the rest of the image in the PLIF frames, making the binarisation and area filtering technique described in Section 3.6.2 difficult to apply successfully. Also, it is unclear from the top images in Fig. 6.16 where the true vapour-liquid interface lies, as it may correspond to the top or bottom of the bubble layer, or somewhere in between that is obscured by the bubbles in the image. As such, it was not possible to apply the processing methods in Section 3.6.2 to obtain a reliable estimate of the film thickness and alternative methods need to be developed. Ideally, PLIF requires a clear line of sight to the interface, which will not always be the case with a single PLIF camera in a fixed position capturing a bubble interface. The measurement could be improved by positioning two or more PLIF cameras around the illumination plane, perhaps on either side, to ensure the film thickness around the bubbles can be recovered.

It can also be seen in the lower images in Fig. 6.16 that the bubbles overlap and obscure the band of brightness detected by the camera. The bubbles also cause focusing of the light as it reflects off the many interfaces, which results in further distortion of the brightness signal. To correct somewhat for this in the BBLIF processing as described in Section 3.6.3, a running average filter with a window size of 50 was applied to the

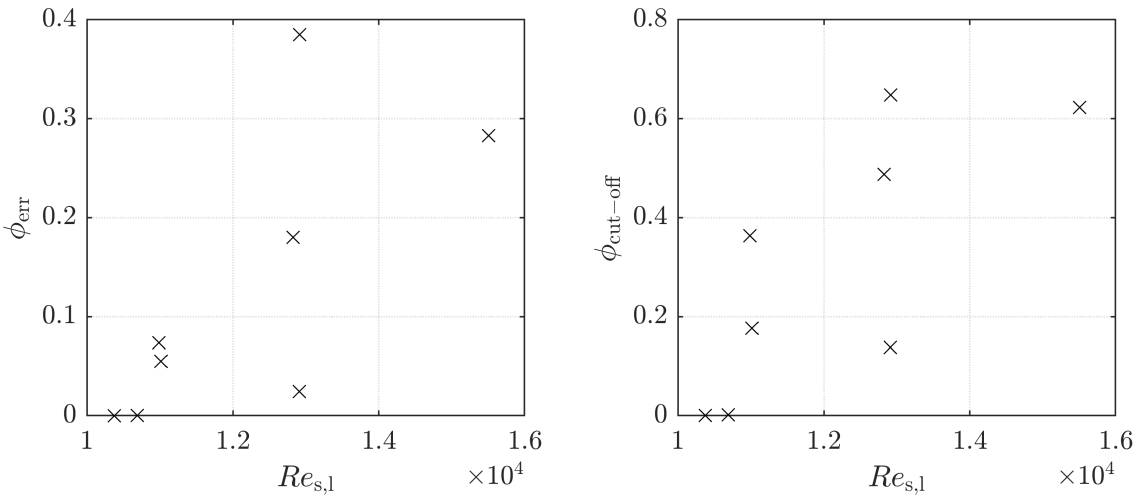


Figure 6.17: Fraction ϕ of (a) erroneous film thickness-time pairs after filtering and (b) film thickness values above the 5 mm cut-off value as functions of superficial liquid Reynolds number $Re_{\mathrm{s,l}} = G(1-x)d/\mu_{\mathrm{l}}$.

temporal records of brightness to smooth out unphysical peaks. This approach worked well for low proportions of bubbles but was less effective for flows with large numbers of bubbles where there are long areas of high intensity. The fraction of erroneous film thickness-time pairs as a function of experimental mass flux is shown in Fig. 6.17a. For most of the conditions, the fraction is well below 0.1, but is much higher for the conditions with highest mass flux where there are more bubbles at the interface.

Due to the geometrical limitations and intensity saturation as shown in Fig. 3.16, the film thickness values were capped at 5 mm for analysis. This may result in the loss of interface information for large waves, or if the mean film thickness is larger than the cut-off value. The fraction of film thickness values as a function of superficial liquid Reynolds number ($Re_{\mathrm{s,l}} = G(1-x)d/\mu_{\mathrm{l}}$) is plotted in Fig. 6.17b. For half of the cases this fraction is < 0.2, but it is much larger for the rest at up to 0.65. This may be due to the actual film thickness being greater than 5 mm, or excessive numbers of bubbles causing internal reflections and subsequent light-focussing. If Fig. 6.17a is also considered, the points with the highest fraction of erroneous pairs after filtering correspond to the points in Fig. 6.17b with the highest fraction of film thickness values above the cut-off, supporting the latter explanation.

The effect of the application of the cut-off can be seen in the plot of film thickness versus time in Fig. 6.18. This trace was extracted at the axial midpoint of the BBLIF

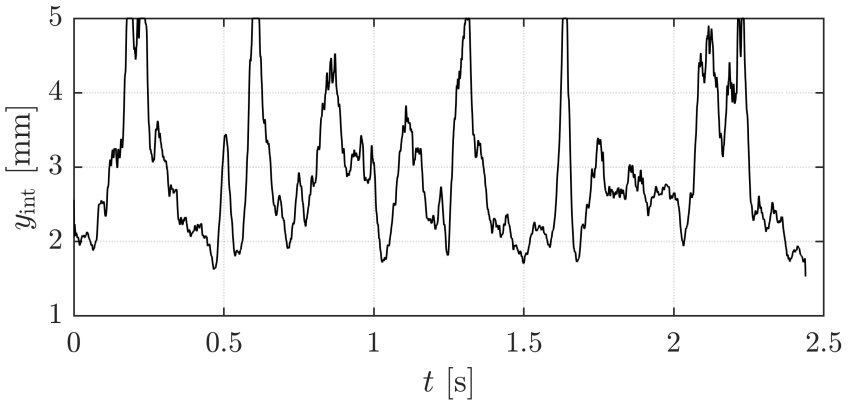


Figure 6.18: Example plot of film thickness y_{int} versus time t extracted at the midpoint of the BBLIF frame for annular flow at the conditions $G = 440$ kg/m^2.s, $q = 23$ kW/m^2.

frame for the conditions $G = 440$ kg/m^2.s, $q = 23$ kW/m^2, and the corresponding cut-off fraction was 0.1. It can be seen that some of the larger peaks are capped by the cut-off value of 5 mm, but the mean film thickness is significantly below this at 3.1 mm. The film thickness varies significantly over time, suggesting film waviness at varying amplitudes or the intermittent appearance of bubbles around the interface which cause internal reflections, resulting in a higher brightness identified by the camera and a higher corresponding film thickness measurement. In adiabatic horizontal air-water annular flows in a 26 mm ID pipe, Setyawan et al. [240] observed similar time-dependent behaviour of the bottom film thickness at comparable liquid and gas superficial velocities, with intermittent peaks of varying heights. The range of heights suggests the existence in the flow of different types of waves, e.g. small amplitude ripple waves and large amplitude disturbance waves.

Figure 6.19 displays the film thickness probability distribution functions for all the annular flow conditions investigated using BBLIF. For the lower mass flux cases ($G = 380$–390 kg/m^2.s) particularly, the peaks are mostly shifted to the left of the 5 mm cut-off value and the distribution is not significantly affected by this treatment of the data. However, in cases where the average film thickness is higher, i.e. higher mass flux and lower heat flux, the tail of the distribution on the right-hand side is lost. If these curtailed distributions were considered to be single peaked, the tails could be reconstructed based on the shape of the complete distributions. This would not be an unreasonable assumption, since left-shifted single-peaked distributions with the same shape as the complete distribution in Fig. 6.19 have been observed in downwards annular flow in pipe diameters in the range 11.7–32.4 mm [150, 194, 241]. For a given heat flux, increasing the mass flux shifts the

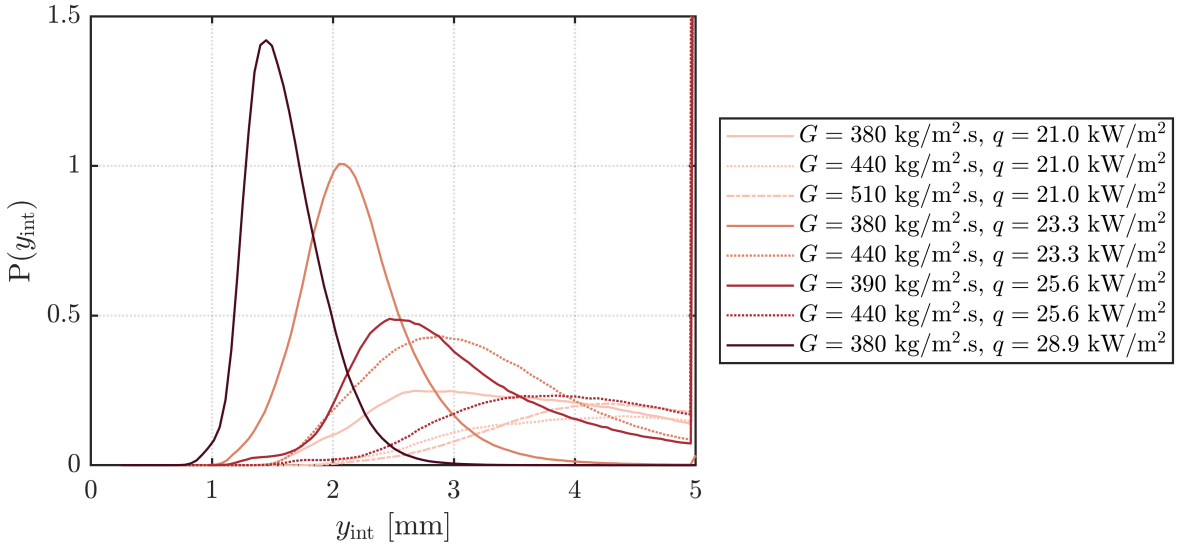


Figure 6.19: Probability density functions of the film thickness y_{int} in annular flow for all experimental conditions investigated with BBLIF, with colour grading by heat flux.

peak of the film thickness distribution in Fig. 6.19 to the right and results in a wider spread of absolute values of film thickness. Generally, increasing the heat flux at fixed mass flux results in a higher degree of evaporation, decreasing the mean film thickness height, shifting the peak to the left and narrowing the distribution.

To further assess the impact of experimental conditions on the characteristic film statistics, the mean film thickness and its standard deviation are plotted against superficial liquid Reynolds number $\text{Re}_{\text{s,l}} = G(1-x)d/\mu_{\text{l}}$ in Fig. 6.20. Different marker shapes and colours are used to show the different heat flux conditions across the data set. Despite the relatively small range of $\text{Re}_{\text{s,l}}$ conditions covered, it is clear that overall the mean film thickness increases with $\text{Re}_{\text{s,l}}$. This is shown consistently for heat flux conditions with more than one data point, and has been widely observed in both horizontal [240] and vertical [17, 241] annular flows.

The behaviour of the standard deviation is less clear from Fig. 6.20b, although it generally appears to increase with increasing $\text{Re}_{\text{s,l}}$. This trend was reported for downwards annular air-water flows in a 32.4 mm ID pipe by Cherdantsev et al. [17]. As $\text{Re}_{\text{s,l}}$ increases, the turbulence intensity in the liquid film will also increase, leading to enhanced liquid film waviness and a wider range of film thicknesses. This is in competition with the expectation that in boiling flows at a fixed heat flux, an increase in $\text{Re}_{\text{s,l}}$ will result in a decrease in the vapour quality and therefore a thicker, more stable liquid film. It might be suggested that these competing effects contribute to seemingly opposite behaviour of

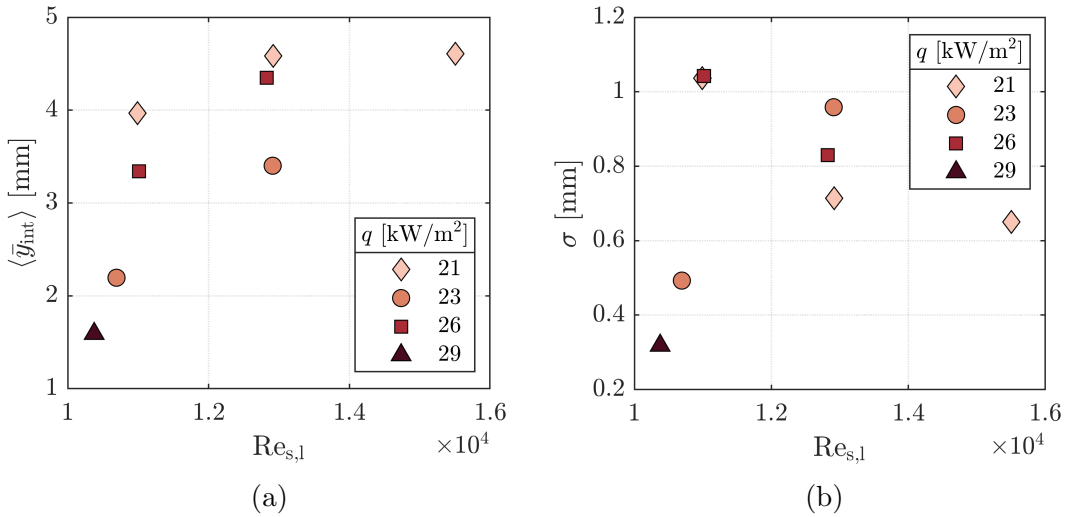


Figure 6.20: (a) Mean film thickness $\langle \bar{y}_{\mathrm{int}} \rangle$ and (b) film thickness standard deviation σ as a function of superficial liquid Reynolds number $\mathrm{Re}_{\mathrm{s,l}}$, separated by heat flux conditions, for annular flow conditions investigated using BBLIF.

the $q = 23\,\mathrm{kW/m^2}$ and $q = 21\,\mathrm{kW/m^2}$ data sets in Fig. 6.20b, although a much wider range of experimental conditions would be required to investigate this fully.

The effect of the bottom liquid film behaviour of the heat transfer is presented in Fig. 6.21, where the Stanton number $\mathrm{St} = h/Gc_{p,\mathrm{l}}$ has been used to normalise the heat transfer results by the inlet mass flux. There is a clear reduction in heat transfer performance with increasing film thickness in Fig. 6.21a both overall and for each q condition with multiple data points. This trend indicates thin-film enhancement of heat transfer as discussed in Section 6.2.2 for stratified-wavy flow. The corresponding effect of the film thickness standard deviation on heat transfer is again less defined. For stratified-wavy flows, interfacial waviness was found to enhance heat transfer due to stronger mixing and increased convective effects under waves, and this is also seen to be the case for the conditions $q = 21\,\mathrm{kW/m^2}$ and $26\,\mathrm{kW/m^2}$ in Fig. 6.21b.

6.5 Summary

Results from the application of laser-based diagnostic techniques specifically developed for boiling flows in horizontal pipes were presented in this chapter. Laser-induced fluorescence methods were employed to identify the vapour-liquid interface in different flow patterns, and particle image velocimetry was used to investigate the velocity fields inside the liquid phase of these flows.

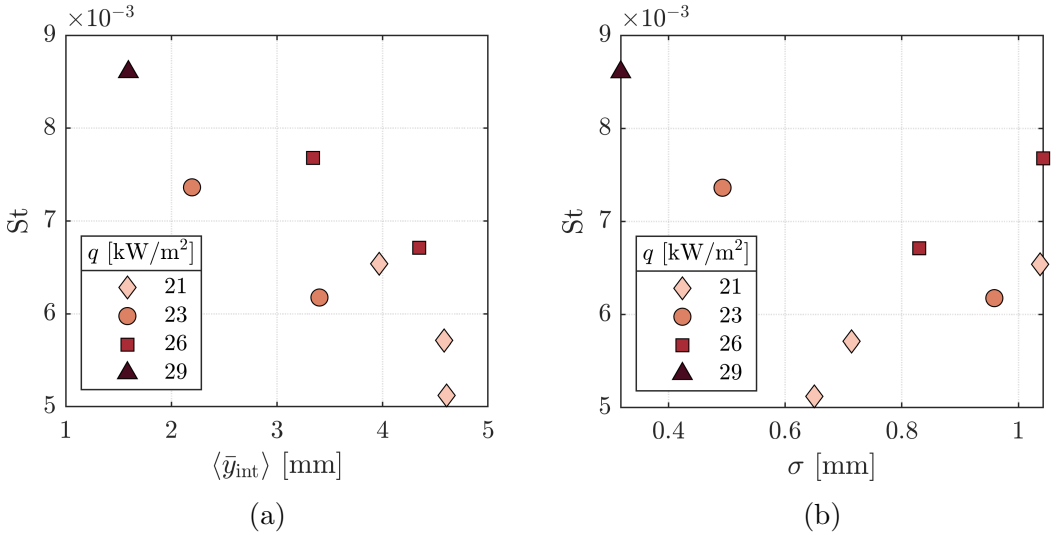


Figure 6.21: The effect of film statistics for annular flow on heat transfer, represented by Stanton number $\mathrm{St} = h/Gc_{p,\mathrm{l}}$ versus (a) mean film thickness $\langle \bar{y}_{\mathrm{int}} \rangle$ and (b) film thickness standard deviation σ, separated by heat flux conditions.

In stratified flows, the streamwise velocity profiles for laminar inlet conditions conformed to theoretical predictions, whilst the heat transfer coefficient was found to increase with decreasing interface height due to thin film effects. A corrective correlation for the stratified angle in the Wojtan et al. [37] method for predicting heat transfer coefficient was proposed which improved the prediction accuracy by 16 percentage points. The presence of interfacial waves was found to enhance heat transfer in stratified-wavy flows when compared to stratified flows, but the stratified-wavy flows investigated did not exhibit large disturbance waves or the corresponding recirculation flows in the liquid phase. Secondary flows with a non-zero vertical velocity component were observed below waves and troughs, which were characterised using an ensemble averaging technique. Inspection of the liquid-phase velocity fields in slug flow revealed disturbances in both the slug nose and tail, with higher velocity magnitudes observed in the nose. The near-wall velocity field close to the bottom of the pipe did not change significantly in direction or magnitude as the vapour bubble passed. The slug frequency for the set of slug flow conditions investigated was determined from the interface information and was predicted to a satisfactory level using literature correlations. Similarly, vapour bubble velocities were calculated and found to increase linearly with mixture velocity, where the gradient increased with heat flux.

Laser-based diagnostic techniques were developed for investigation of the liquid film at the bottom of the pipe in annular flow. The presence of large numbers of bubble at the vapour-liquid interface made reliable interface detection using the planar laser-

induced fluorescence processing methods applied to stratified, stratified-wavy, and slug flows challenging. Film thickness data was obtained using a brightness-based laser induced fluorescence technique, but an upper limit of 5 mm was imposed on the measurable film thickness based on the geometry of the camera and saturation of the intensity in the recorded images. The bubbles around the interface also caused internal reflections and local light-focussing, resulting in bright spots that did not necessarily correspond to thicker films. Despite these challenges, film thickness statistics were computed and the observed trends were in accordance with previous investigations of annular flows. The mean film thickness increased with superficial liquid Reynolds number, whilst the corresponding standard deviation increased or decreased with $Re_{s,l}$ depending on the heat flux condition. Heat transfer performance decreased markedly with increasing film thickness for all conditions studied, but increased with film thickness standard deviation for some of the conditions. This heat transfer behaviour corresponds to that observed in stratified-wavy flow.

These detailed spatio-temporally resolved measurements in boiling flows represent an important contribution to the literature and can provide insights into the interaction of hydrodynamic and heat transfer phenomena in these systems, and improve our understanding of boiling in many important applications, including refrigeration and heat-pump systems, waste-heat recovery and conversion systems and concentrating solar power technology. The data can also be used for advanced multiphase model development and validation.

Chapter 7

Numerical Simulations Towards Flow Boiling

From a computational perspective, the flow studied experimentally in Chapters 5 and 6 poses a complex problem. A subcooled liquid flow is heated before starting to undergo evaporation, resulting in a multiphase flow in which the flow in both phases is turbulent for most of the experimental conditions studied. The bubble nucleation as boiling begins, and some of the two-phase flow structures that develop as more of the liquid boils, occur at a much smaller scale than that of the pipe geometry which at 12.6 mm falls into the macro-scale category. A fine mesh resolution is typically required to resolve these phenomena accurately, which can become very computationally expensive for a flow at this scale.

As such, the approach of working towards a full flow boiling model by building layers of complexity on established computational techniques was taken. First, a multiphase flow model used to successfully simulate flow of elongated bubbles in micro-channels [165] was applied to such flows in larger channels where the effects of buoyancy and inertia became significant. Then, a phase change model developed by Ferrari et al. [155] for slug flow boiling in square micro-channels was validated for circular cross-sections. This phase change model was then used to obtain preliminary results involving the simulation of laminar flow boiling in the experimental geometry used in this work. The results of these steps are presented in the subsequent sections of this chapter.

7.1 Inertial and buoyancy effects on flow of elongated bubbles in horizontal pipes

In this section, the results of a numerical study of the effect of buoyancy and inertial forces on the dynamics of an elongated bubble, and of the liquid film surrounding it, are presented based on the work published in Moran et al. [242]. The development of a theoretical model extending existing models to the conditions studied in this work is first presented in Section 7.1.1. Validation of the numerical model is then presented in Section 7.1.2. Gravitational effects are studied in Section 7.1.3 by systematically varying the Bond number, $\mathrm{Bo} = \rho_\mathrm{l} g r^2/\gamma$, but fixing the Reynolds number to a small value, $\mathrm{Re_l} = \rho_\mathrm{l} U_\mathrm{l} d/\mu = 1$. The capillary number is defined as $\mathrm{Ca_l} = \mu_\mathrm{l} U_\mathrm{l}/\gamma$ such that the Weber number of the flow $\mathrm{We_l} = \mathrm{Ca_l}\,\mathrm{Re_l} \ll 1$. This allows the isolation of the effects of buoyancy from those of inertia. The analysis of the inertial regime is outlined in Section 7.1.4, where simulations were run by systematically varying the Reynolds number for selected values of the Bond and capillary numbers.

7.1.1 Theoretical predictions

In this section, existing predictive models are further developed for the liquid film thickness, bubble speed and liquid drainage velocities. These models provide a useful benchmark for the computational data presented in the next section.

7.1.1.1 Liquid film thickness

The equations derived theoretically by Jensen et al. [168], Eqs. (2.27), (2.28a) and (2.28b), apply as long as $\mathrm{Ca_b} \lesssim 10^{-3}$. In order to extend their validity to larger capillary numbers, the approach of Aussillous and Quéré [161] is followed, assuming that the radius of curvature of the bubble nose on the top/bottom of the channel is reduced from r to $r - 2.5h^{\pm}$ to account for the presence of a thick film. This modifies Eq. (2.27), valid for $\mathrm{Bo} < 1$, into:

$$\frac{h^{\pm}}{r} = \frac{1.34{\mathrm{Ca_b}}^{2/3}}{1 + 3.35{\mathrm{Ca_b}}^{2/3} \pm \mathrm{Bo}} \tag{7.1}$$

and Eq. (2.28a), valid for the top film thickness when Bo > 1, into:

$$\frac{h^+}{r} = \frac{1.34\mathrm{Ca_b}^{2/3}}{2\sqrt{\mathrm{Bo}} + 3.35\mathrm{Ca_b}^{2/3}} \tag{7.2}$$

Note that the two equations above yield predictions for the top film thickness that converge at Bo = 1. On the other hand, Eq. (7.1) for the bottom film thickness diverges to ∞ as $\mathrm{Bo} \to 1 + 3.35\mathrm{Ca_b}^{2/3}$, and therefore should not be used when Bo is close to unity.

The correction of Eq. (2.28b) to account for a thick film at the bottom of the channel is done by replacing r (b in Eq. (2.28b)) with $r - 2.5h_{AQ}$, where h_{AQ} is the film thickness in the absence of gravitational effects estimated via the Aussillous and Quéré [161] correlation (Eq. (2.25)), thus leading to:

$$\frac{h^-}{r} = 2\frac{\sqrt{\mathrm{Bo}} - 1}{\sqrt{\mathrm{Bo}}\left(1 + 3.35\mathrm{Ca_b}^{2/3}\right)} \tag{7.3}$$

This introduces the effect of the capillary number to the prediction of the bottom film thickness for Bo > 1, which was otherwise absent in Eq. (2.28b). Note that Eq. (7.3) yields $h^- \to 0$ as $\mathrm{Bo} \to 1^+$, and therefore should not be used for Bond numbers close to unity.

7.1.1.2 Bubble advancing speed and liquid drainage velocities

A useful relationship linking liquid film thickness, streamwise bubble and liquid average velocities is provided by a material balance of the liquid in a control-volume containing the bubble [159]. In a reference frame moving with the bubble, the liquid displaced by the advancing bubble must match the liquid bypassing the bubble through the liquid film, thus leading to:

$$\frac{U_\mathrm{b}}{U_\mathrm{l}} = \frac{1}{(1-H)^2} \tag{7.4}$$

where $H = h/r$ is the axisymmetric film thickness, or a cross-sectional average film thickness $\overline{H}$ in the case of asymmetric film. In the latter case, $\overline{H}$ can be estimated as $\overline{H} = (H^+ + H^- + 2H^\mathrm{h})/4$, with H^+ from Eq. (7.1) (Bo < 1) or Eq. (7.2) (Bo > 1), H^- from Eq. (7.1) (Bo < 1) or Eq. (7.3) (Bo > 1), and the horizontal film thickness H^h from the Aussillous and Quéré [161] correlation, Eq. (2.25), under the assumption that the horizontal film thickness does not deviate significantly from the buoyancy-free

configuration.

For the cross-sectional liquid drainage velocity, i.e. the circumferential velocity of liquid averaged radially across the film at a certain angle θ (see Fig. 4.1b), Leung et al. [170] proposed a fluid dynamics model based on the solution of the Navier-Stokes equations in the film. Under the assumption that the cross-section of the bubble remains circular, their model led to the following expression for the average drainage velocity U_d as a function of the circumferential position:

$$U_\mathrm{d}(\theta) = \frac{\Delta\rho g h^2}{3\mu}\left(1 - \frac{3}{8}\frac{h}{r}\right)\sin\theta \tag{7.5}$$

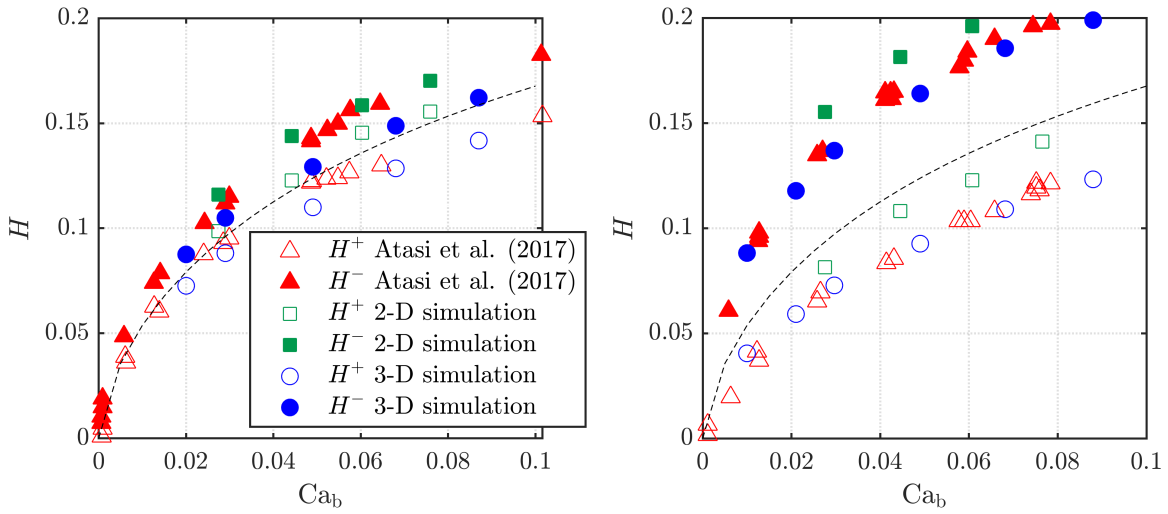
where $h \equiv h(\theta)$ and θ indicates the angle measured from the top. Note that $\theta = \pi/2$ identifies the horizontal centreline of the cross-section (the $x-$axis in Fig. 4.1), irrespective of the actual bubble elevation above it. Equation (7.5) is rendered dimensionless by scaling U_d on U_l and by making use of the definitions of Bo and $\mathrm{Ca_l}$:

$$\frac{U_\mathrm{d}(\theta)}{U_\mathrm{l}} = \frac{1}{3}\frac{\mathrm{Bo}}{\mathrm{Ca_l}}H^2\left(1 - \frac{3}{8}H\right)\sin\theta \tag{7.6}$$

where $H = h(\theta)/r$. Leung et al. [170] simplified Eq. (7.6) by neglecting the cubic term and neglecting the circumferential changes of H, thus expressing H as a function of the capillary number alone using Eq. (2.25). There seems to be an error in their final formula (Eq. 10 in Leung et al. [170]), however, where the constant in the numerator should be 0.15 instead of 0.45.

7.1.2 Model validation

Simulations were performed for elongated bubble flow in a horizontal pipe at conditions designed to match those of the experiments by Atasi et al. [169] ($\mathrm{We_l} \ll 1$), with cases run in both 2-D and 3-D geometries to assess the most appropriate configuration. The experimental film thickness values are plotted against the results from both 2-D and 3-D simulations in Fig. 7.1a for Bo = 0.11 and 0.42, along with the predictions obtained using Eq. (2.25), i.e. the Bo = 0 case. For all of the plotted data sets, film thickness increases with $\mathrm{Ca_b}$ as expected from traditional thin-film theory. The bottom film thickness H^- is larger than that at the top of the bubble H^+, because buoyancy causes the bubble to rise upwards in the channel. As Bo increases, H^+ and H^- diverge more from the



(a) Bo = 0.11 (b) Bo = 0.42

Figure 7.1: Comparison of the effect of the bubble capillary number and Bond number on the top and bottom film thicknesses with the experimental work of Atasi et al. [169]. The results of both 2-D and 3-D numerical simulations are reported. The dashed line represents the prediction of H using the Aussillous and Quéré [161] correlation, Eq. (2.25), i.e. in the Bo = 0 case.

Bo = 0 theoretical prediction, with larger values of H^- and smaller values of H^+. It can be seen from Fig. 7.1 that the film thickness is over-predicted by the 2-D simulations, more significantly so at the top of the bubble than the bottom. It was also observed that bubbles were not inclined in the 2-D simulations, because bubble inclination is caused by film drainage from the top of the bubble around its sides to the bottom. This drainage flow is perpendicular to the main flow direction, so cannot be captured by a 2-D simulation. Thus, whilst more computationally expensive, 3-D simulations are required to accurately model elongated bubble flow in the presence of buoyancy effects.

The 3-D simulations match the experimental results very well, with a maximum deviation of 4 % for Bo = 0.42 and 10 % for Bo = 0.11, detected at lower values of Ca_b. Atasi et al. [169] reported a maximum experimental error of 14 % at the lowest Ca_b and 5 % for all other measurements, and the 3-D computational results fall within these margins.

7.1.3 Buoyancy effects

A parametric study of the effect of buoyancy on elongated bubble flow with negligible inertia (i.e. $We_l \ll 1$) was performed for a range of Ca_l and Bo values, with results reported in this section for $Ca_l = 0.024$ and 0.051 and Bo = 0.11 to 3.5.

A representative case is visualised in Fig. 7.2, for $Ca_l = 0.024$ and Bo = 0.42. Three cross-sections along the bubble, the locations of which are indicated on Fig. 7.2a, are shown in Fig. 7.2b-d. The white space at the centre represents the volume occupied by the gas phase and the ovalisation of the bubble cross-section can be clearly seen. This is an important observation, since the cross-sectional view of the bubble is very difficult to obtain experimentally. The coloured regions of Fig. 7.2b-d show the y-component of the velocity, U_y, in the liquid film, scaled by the average bubble velocity in the z-direction. It can be seen that U_y is negative around the sides of the bubble, with the largest magnitude corresponding to the widest point of the bubble, confirming film drainage from the top to the bottom of the bubble as suggested by Leung et al. [170]. The magnitude of this drainage velocity is larger near the bubble nose and decreases towards the rear. This may be ascribed to the progressive thinning of the liquid film at the top and sides of the bubble as the rear is approached, which is apparent in Fig. 7.2b-d, and this reduces the drainage flow rate.

The bubble inclination that is characteristic of buoyancy-affected elongated bubble flows can be clearly seen in Fig. 7.2e, along with a well-defined rounded bubble nose and tail, which is typical in capillary flows. This figure is not to scale to allow for better visualisation of the aforementioned effects. The film thicknesses at location F for this case were calculated to be $H^+ = 0.073$ and $H^- = 0.137$, whilst the inclination angles are $\alpha^+ = 1.2 \times 10^{-3}$ rad and $\alpha^- = 2.9 \times 10^{-3}$ rad.

7.1.3.1 Bubble shape

The effect of buoyancy (i.e. increasing Bo) on the bubble shape is studied in Fig. 7.3. Figure 7.3a reveals that, with increasing Bo, the bubble lengthens and moves higher up in the channel, and the top film thins while the bottom film becomes thicker. Also, the front and rear menisci progressively lose the typical spherical shapes characteristic of long bubbles propagating in capillary channels, and for Bo = 3 it is actually difficult to distinguish between the nose and rear of the bubble since their shapes are very similar.

Figure 7.3b provides insight into the cross-sectional shape of the bubble when varying the Bond number and emphasises the process of bubble ovalisation. As Bo $\to$ 0, the bubble cross-section tends towards a circular shape, but with increasing Bo it becomes less axisymmetric, and as Bo $>$ 1 the bubble shape is far from being circular. Also, it can

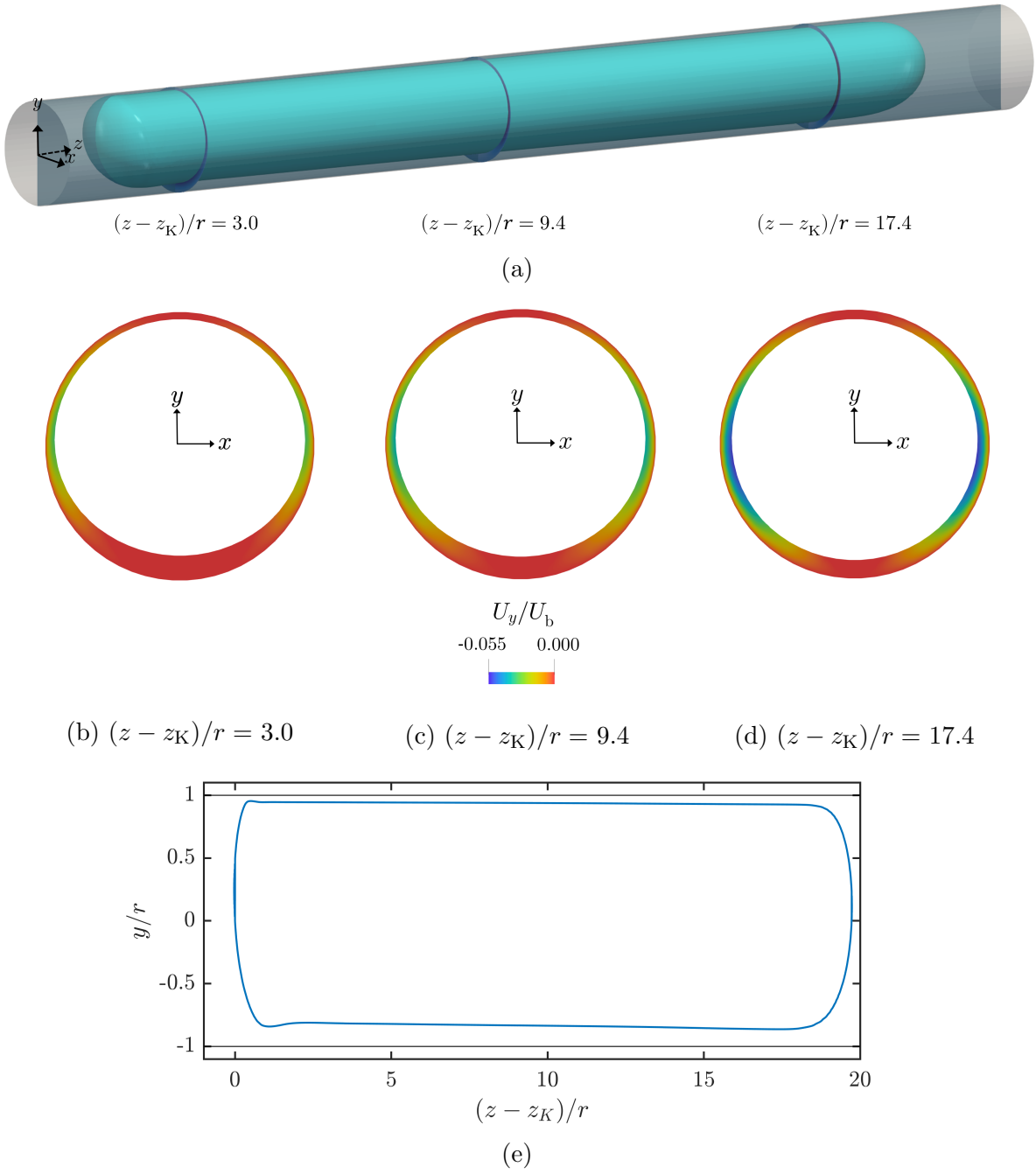


Figure 7.2: (a) Profile of an elongated bubble obtained with a numerical simulation for $Ca_l = 0.024$ and $Bo = 0.42$ ($We_l \ll 1$), flow is from left to right; (b-d) corresponding contour plots of the vertical component of the velocity in the liquid film, at selected cross-sections along the bubble; (e) corresponding bubble profile (not to scale) in the $x = 0$ plane.

be seen that the upper half of the bubble cross-section remains relatively circular whilst the lower half becomes more oval in shape with increasing Bo. Such deformations of the bubble cross-section due to buoyancy effects were reported in channels with rectangular cross-sections by de Lózar et al. [243] who attributed this effect to the pressure balance

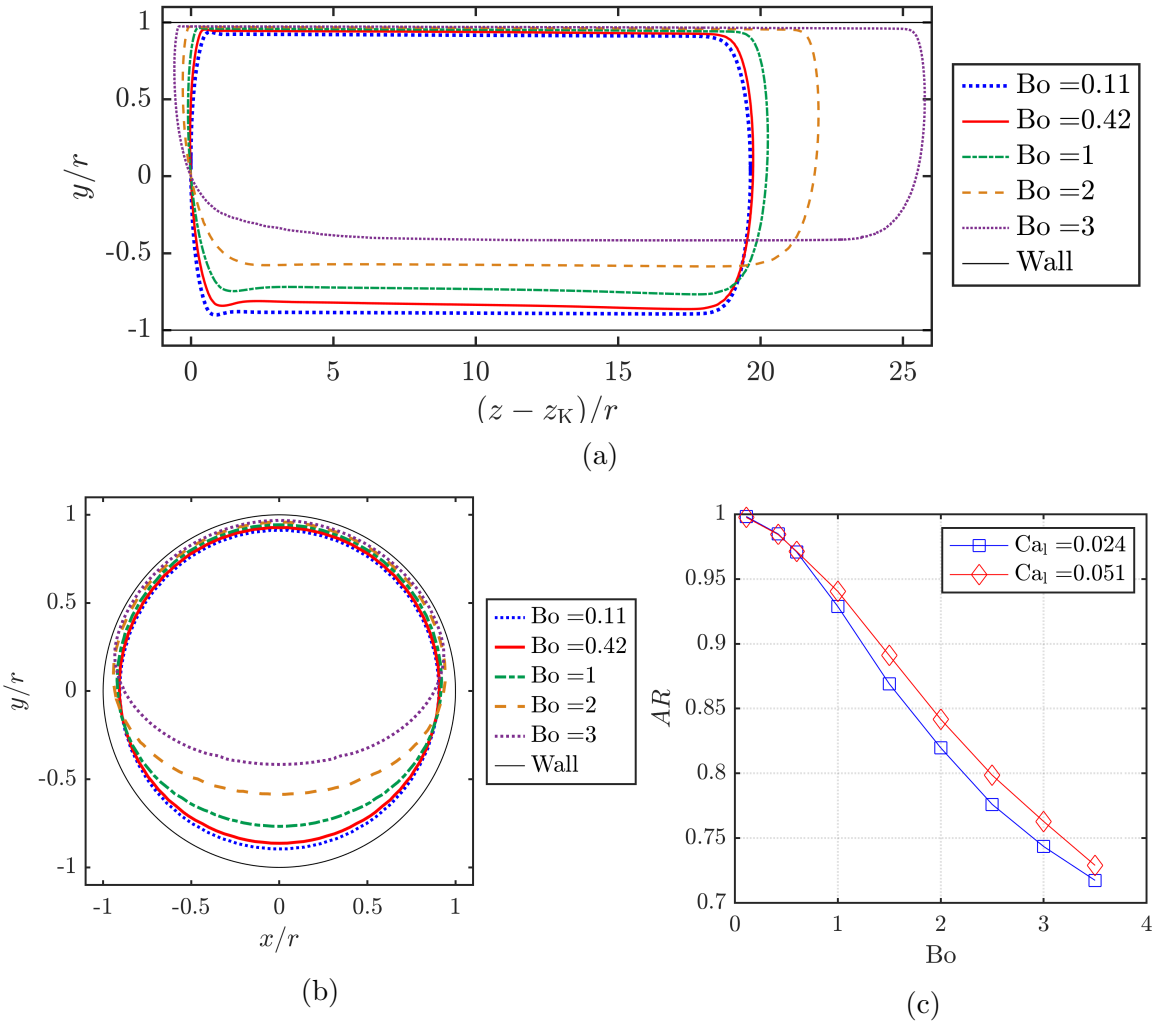


Figure 7.3: Systematic analysis of the impact of the Bond number for the negligible inertia case ($We_l \ll 1$) on the (a) bubble profile on a vertical centreline plane ($x = 0$), (b) on the bubble cross-sectional shape at the location F (see Fig. 4.1), and (c) on the bubble cross-sectional aspect-ratio AR measured at the same location. In (a), flow is from left to right. The capillary number of the liquid in (a) and (b) is $Ca_l = 0.024$.

in the liquid film. The hydrostatic pressure in the liquid film increases linearly with distance from the top of the channel, and when the flow is subjected to a transverse gravitational force, this pressure must be balanced with the pressure drop across the interface to maintain a constant pressure inside the bubble, resulting in a decrease in interface curvature with distance from the top of the channel.

The aspect-ratio of the bubble cross-sectional shape, calculated as indicated in Fig. 4.1, is reported as a function of the Bond number in Fig. 7.3c. The trends of the deformation of the bubble cross-section are similar for the two values of Ca_l presented. Generally, AR decreases with increasing Bo, meaning the vertical extent of the bubble cross-section becomes smaller compared to the horizontal extent, and the bubble cross-section becomes

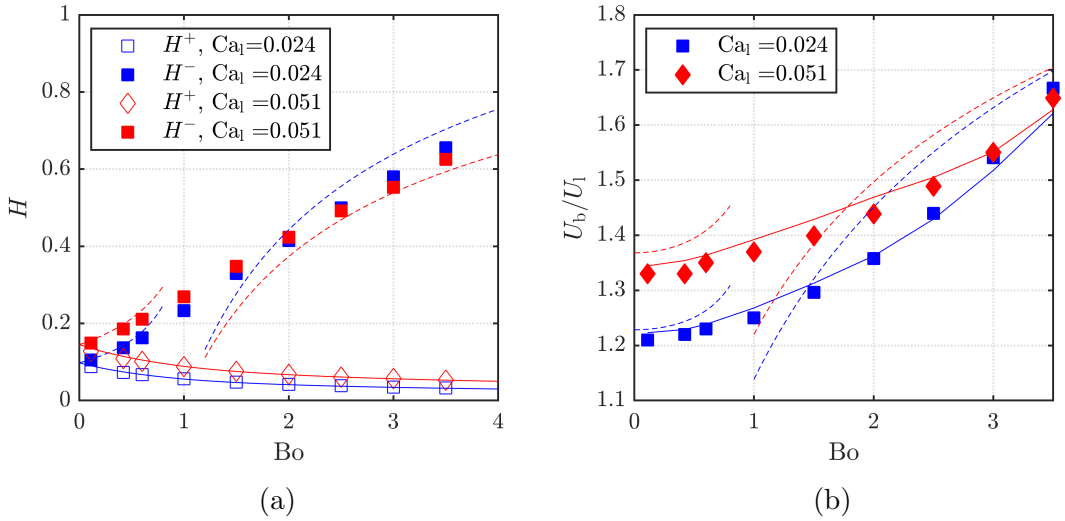


Figure 7.4: Impact of the Bond and capillary numbers ($We_l \ll 1$) on the (a) top (H^+) and bottom (H^-) liquid film thicknesses and (b) bubble advancing speed. In (a), the solid lines represent the predictions for the top film thickness given by Eqs. (7.1) and (7.2), while the dashed lines identify the predictions for the bottom thickness obtained with Eqs. (7.1) and (7.3). In (b), the lines identify the predictions extracted by applying Eq. (7.4) with $\overline{H}$ calculated based on the simulation data (solid lines), and with $\overline{H}$ predicted based on Eqs. (7.1)−(7.3) for H^+ and H^-, and Aussillous and Quéré [161] correlation for H^h (dashed lines).

less circular in shape. When Bo $>$ 1, the relative difference of vertical and horizontal extensions of the bubble cross-section rises above 10 %. The decreasing trend of AR with Bo is slightly more pronounced for the lower Ca_l case. As derived by Magnini et al. [166] for the flow of long bubbles in vertical channels, the gravitational force acting on the liquid film scales as Bo/Ca, and therefore the impact of buoyancy is expected to be more significant at lower Ca_l, thus explaining the steeper curve at $Ca_l = 0.024$ in Fig. 7.3c.

7.1.3.2 Film thickness and bubble speed

The effects of buoyancy on liquid film thickness and advancing speed of the bubble for flow with negligible inertia are displayed in Fig. 7.4. All the values of the film thickness in Fig. 7.4a are measured near the bubble nose at location F in Fig. 4.1. As a general trend, H^- increases with Bo, as observed in Fig. 7.3, whilst H^+ decreases with Bo as buoyancy pushes the bubble further up in the channel. The gravitational effects are more pronounced in the bottom film where the film is thicker, due to the combined effect of the rise of the bubble and of the cross-sectional bubble deformation. The film thickness behaviour is similar for the two values of Ca_l, although the slope of the H^- curve is larger

for the smaller Ca_l because the buoyancy effects are more impactful as explained in the previous section, so that eventually when Bo > 2 the bottom film for $Ca_l = 0.024$ is thicker than that for $Ca_l = 0.051$. Notably, the top and bottom film thicknesses at the largest Bond numbers tested may differ by more than one order of magnitude.

Figure 7.4a also includes the predictions for the top and bottom film thicknesses estimated with Eqs. (7.1)−(7.3). As a first approximation, the input value of Ca_b in Eqs. (7.1)−(7.3) was estimated by iterating between the Aussillous and Quéré [161] correlation (Eq. (2.25)) and the material balance Eq. (7.4) (with H from Eq. (2.25)), and thus it does not account for the impact of Bo on the bubble velocity. The model predicts the top film thickness very well across the range of conditions studied, and performs well for the bottom film thickness when Bo ≤ 0.6 and Bo > 1.5. In the Bo < 1 range, the mean absolute error on the prediction of top and bottom film thicknesses is 4.8%, whereas the model of Atasi et al. [169] yields an 8% error. For the entire data set, excluding the bottom film thicknesses for Bo $= 1$ and 1.5, the error is 4.6%, compared to 20.4% with Atasi et al. [169]. However, the large error with Atasi et al. [169] is to be expected since the model is only valid for Bo < 1, and does not account for the ovalisation of the bottom of the bubble.

The bubble velocity (Fig. 7.4b) increases monotonically with the Bond number. As Bo $\to 0$, U_b converges to the value for negligible gravity, which is an increasing function of Ca_l. However, as Bo increases, the bubble velocity rises owing to its reduced cross-sectional area, and the simulation data for different Ca_l seem to converge as Bo ≥ 3. Notably, for the same liquid flow rate (i.e. same Ca_l), the bubble travels 50 % faster when Bo ≥ 3 compared to the Bo $= 0$ case. The bubble speed trends are closely related to those for the bottom film thickness presented in Fig. 7.4a. Since bubble speed and cross-sectional area are related via the material balance of the liquid flow, Eq. (7.4), and at large Bo the extension of the cross-sectional area is mostly determined by H^- (as is clear from Fig. 7.3b), the trends for H^- and U_b as a function of Bo and Ca_l have to be similar. Figure 7.4b also includes two different sets of predictions obtained using Eq. (7.4). When using simulation data for H^+, H^- and H^h in $\overline{H} = (H^+ + H^- + 2H^h)/4$, the bubble velocity is predicted very well, thus emphasising the validity of the material balance also in situations with large buoyancy effects. When evaluating $\overline{H}$ based on the set of Eqs. (7.1)−(7.3) for H^+ and H^-, and on Eq. (2.25) for H^h, the predictions are still

relatively good except when Bo ≈ 1.

Additional data illustrating the streamwise pressure profiles along the channel for this set of Bond and capillary numbers are included in Appendix B.

7.1.3.3 Liquid film drainage velocity and bubble inclination angle

Leung et al. [170] and Atasi et al. [169] demonstrated that the inclination of the bubble originates from the drainage flow from the top to the bottom of the channel, and thus the trends of drainage velocity and bubble inclination angle are expected to be correlated. This is confirmed by the results obtained from this computational study, which are presented in Fig. 7.5. The drainage velocity U_d is calculated on the tube cross-section at the location F, by taking the mean value of the y-component of the velocity in the liquid film, U_y, in the horizontal plane where E_x and H^h are measured (see Fig. 4.1). The values of bubble inclination reported in Fig. 7.5b are measured by taking the average slope of the top and bottom profiles of the bubble (on the plane $x = 0$), in a region $4d$ long around the bubble centre. The data in Fig. 7.5 show that both drainage velocity and bubble inclination initially increase with the Bond number, owing to the initiation of draining flows as the liquid in the film begins moving downward under the effect of

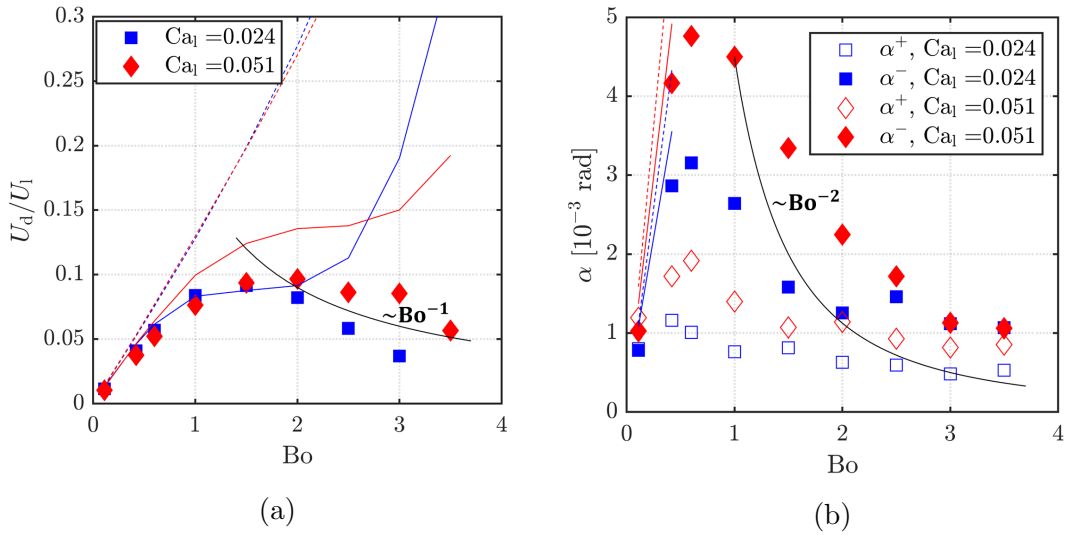


Figure 7.5: Impact of the Bond and capillary numbers (We$_\mathrm{l} \ll 1$) on the (a) average liquid film drainage velocity and (b) top (α^+) and bottom (α^-) bubble inclination angles. Red and blue lines identify the predictions obtained using (a) Eq. (7.6) with $\sin\theta = 1$, and (b) Eq. (2.29), with H^h based on simulation data (solid lines) or Aussillous and Quéré [161] correlation (dashed lines). The black solid lines identify the scaling laws extracted from the analysis of the minimum film thickness trends in Fig. 7.6.

gravity. Both U_d and α increase linearly with Bo when Bo < 1, which is consistent with the scalings $U_d \sim \mathrm{Bo}\, H^2$ and $\alpha \sim \mathrm{Bo}\, H^3$ arising, respectively, from Eqs. (7.6) and (2.29), with $H \equiv H^{\mathrm{h}}$ being approximately constant in this regime (see cross-sectional profiles in Fig. 7.3b).

When Bo > 1, the simulation data show that both U_d and α drop as the Bond number is further increased. This declining trend at large Bo was not observed in previous studies, which were limited to the Bo < 1 regime. Figure 7.3b reveals that, as Bo > 1, the bubble cross-section becomes oval and the film thickness on the top half of the bubble reduces. In this regime, the $\sim H^2$ and $\sim H^3$ terms in Eqs. (7.6) and (2.29) become dominant and the drainage flow rate reduces because there is very little liquid available to drain from the top film region. Figure 7.5 includes the predictions of U_d and α obtained using the existing theory based on Eqs. (7.6) and (2.29). While the theory works well as long as the bubble cross-section is circular (Bo < 1), it fails when Bo > 1 because the bubble cross-section becomes oval and H^{h} is no longer representative of the actual gap available between the bubble interface and the wall through which the liquid can flow, which is actually much smaller. At a first glance, the top film thickness H^+ may seem a more suitable parameter to calculate the drainage flow rate. However, Eq. (7.2) yields $H^+ \sim 1/\sqrt{\mathrm{Bo}}$ as Bo $\gg 1$. This would give $U_d \sim \mathrm{Bo}\, (H^+)^2 \sim 1$, i.e. constant U_d at large Bo, which does not match the present data. Hence, the gap available for the draining liquid to flow must decrease as Bo increases, at a faster rate than H^+ does.

In order to investigate the perimetral evolution of the liquid film more in detail, Fig. 7.6a displays the cross-sectional film thickness for the interface profiles depicted in Fig. 7.3b, $\mathrm{Ca_l} = 0.024$, plotted as a function of the circumferential coordinate θ. It can be seen that as the Bond number increases above 1, the top ($\theta = 0$) and bottom ($\theta = \pi$) film thicknesses diverge. This leads to the creation of a constriction in the film, at the matching point between the thin film at the top and the thick liquid lobe at the bottom. This constriction, whose circumferential location is constant along the bubble body and converges to $\theta = 1$ rad as Bo increases, identifies a minimum value of the liquid film thickness $H_{min} = h_{min}/r$. A liquid film constriction with very similar morphological features has been reported for the film profile around long bubbles translating in square channels, at the matching point between the thin film at the cross-section centre and the thick liquid lobes at the corners [167, 244, 245]. Figure 7.6b displays the values of both H^+

and H_{min} measured at the location F and indicates that the deviation between H^+ and H_{min} increases with Bo, with H^+ obeying a scaling law $H^+ \sim \mathrm{Bo}^{-1/2}$ (in agreement with Eq. (7.2)), whereas $H_{min} \sim \mathrm{Bo}^{-1}$. Interestingly, these two scalings yield $H_{min} \sim (H^+)^2$, which is the same law obtained theoretically by Wong et al. [244] for flow in square channels, where $H \sim \mathrm{Ca}^{2/3}$ at the centre and $H_{min} \sim \mathrm{Ca}^{4/3}$ at the constriction. Using the minimum film thickness as the characteristic length scale for evaluating the draining flow rate, the scaling laws $U_d \sim \mathrm{Bo}\ (H_{min})^2 \sim 1/\mathrm{Bo}$ and $\alpha \sim \mathrm{Bo}\ (H_{min})^3 \sim 1/\mathrm{Bo}^2$ are obtained. These laws capture the trends of the average drainage velocity and bubble inclination angle well for $\mathrm{Bo} > 1$, as indicated in Fig. 7.5.

Figure 7.5b also shows that the inclination angle of the bubble at the top α^+ is systematically smaller than that at the bottom α^-, as was observed experimentally by Atasi et al. [169], and that α increases with the capillary number, due to the development of thicker films which are subject to more copious draining flows.

7.1.4 Inertial effects

A parametric study of the effect of inertia on elongated bubble flows with non-negligible buoyancy effects is presented in this section for a range of values of Bo, $\mathrm{Ca_l}$ and $\mathrm{Re_l}$.

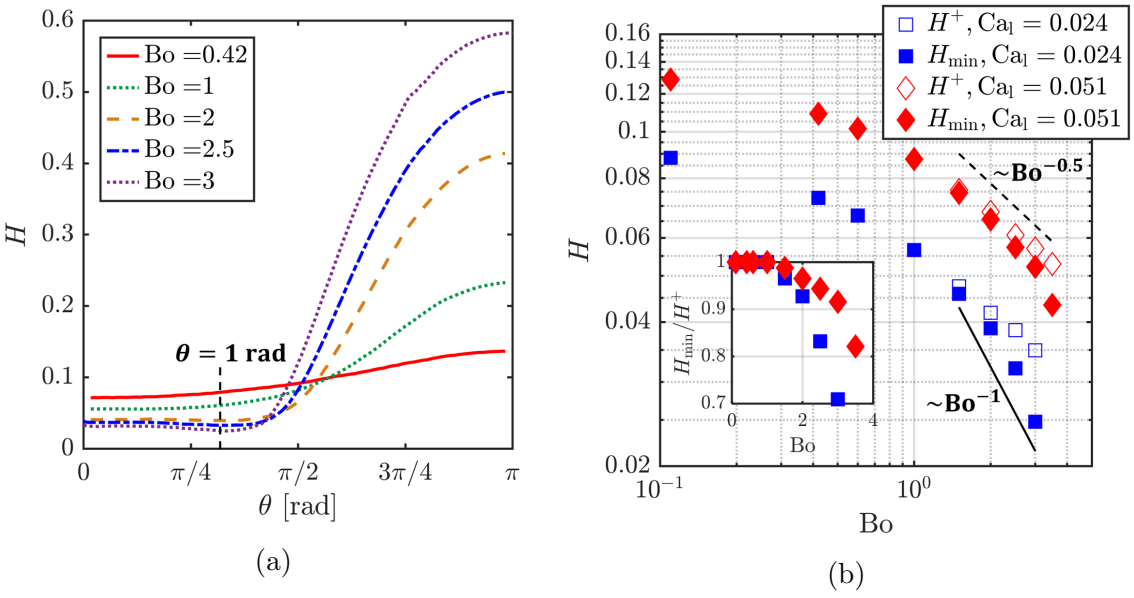


Figure 7.6: (a) Circumferential evolution of the liquid film thickness on the channel cross-section at the location F for $\mathrm{Ca_l} = 0.024$ and different Bond numbers ($\mathrm{We_l} \ll 1$), and (b) top and minimum liquid film thickness at F as a function of Bond and capillary numbers. In (a), $\theta = 0$ corresponds to the top of the channel, see Fig. 4.1.

7.1.4.1 Bubble shape

The impact of inertial and buoyancy forces on the bubble profile can be studied by means of Fig. 7.7, which reports the geometrical features of the bubbles for a fixed value of Ca_l =0.024, two values of the Bond number, Bo = 0.42 and 1, and a range of Reynolds numbers Re_l = 1–750. Figure 7.7a shows that the bubble nose elongates and its cross-section shrinks as the Reynolds number increases, which is in accordance with the literature concerning flows in the absence of buoyancy [162, 163]. Interestingly, as the bubble cross-section reduces the liquid film around it does not thicken uniformly around the tube perimeter. Only the bottom film becomes substantially thicker, while the top film thickness is unchanged such that inertial effects further elevate the bubble above the channel axis. Inertial effects are known to be responsible for the appearance of interfacial undulations near the tail of long bubbles when $We_l \geq 1$ [208]. It can be seen in Fig. 7.7a that these appear only on the bottom profile at intermediate values of Re_l, whereas the profile on the top stays smooth. This can be explained by considering that the impact of inertia on the free-surface profile is better described by the Reynolds number calculated based on the actual film thickness, rather than the channel diameter which has little impact on the film dynamics. Since the bottom film is more than twice as thick as the top film, its Reynolds number is larger and undulations are expected to appear earlier. These numerical simulations reveal that the interfacial undulations become less evident as Re_l is increased towards $Re_l = 750$ and the bubble dynamics become time-dependent, which is consistent with the large Weber number of the flow, $We_l = 18$ [208]. The bubble profiles on the channel cross-section depicted in Fig. 7.7b show that the increase of the Reynolds number is responsible for a more apparent bubble ovalisation, and thus the cross-sectional bubble aspect-ratio decreases monotonically as Re_l increases, as shown in Fig. 7.7c for two different values of Bo.

Additional data for the dynamics of bubbles in the presence of non-negligible inertial effects at another value of the capillary number, $Ca_l = 0.051$, are presented in Fig. 7.8. The trends are similar in shape to those observed for $Ca_l = 0.024$ in Fig. 7.7. Inertia causes the bubble to elongate and elevate further above the centreline of the channel, with the bubble cross-section becoming progressively more deformed. Note that simulations at this capillary number were run up to a maximum Reynolds number of 500, which corresponds to a maximum Weber number of 25, above which profiles begin to exhibit time-dependent

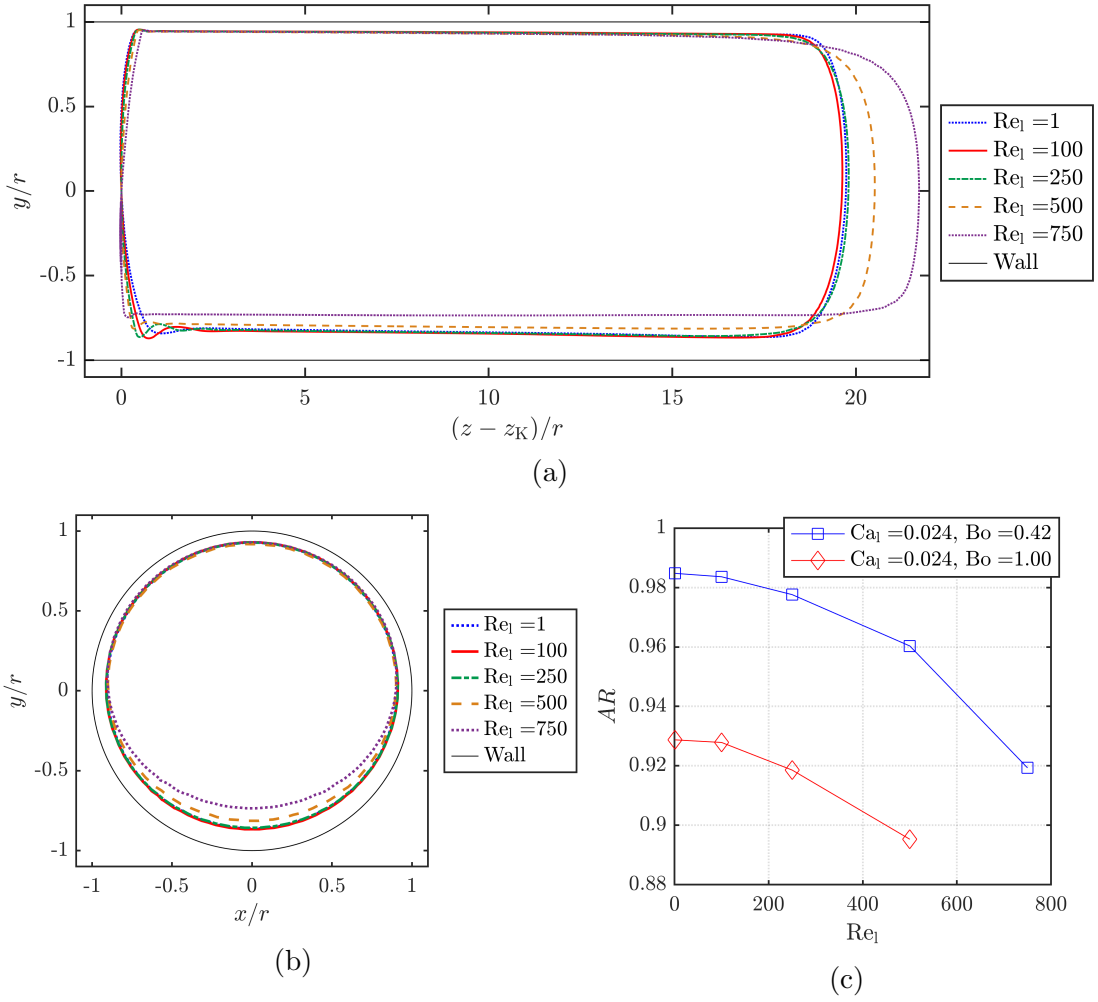


Figure 7.7: Systematic analysis of the impact of the Reynolds number on the (a) bubble profile on a vertical centreline plane ($x = 0$), (b) on the bubble cross-sectional shape at the location F, and (c) on the bubble cross-sectional aspect-ratio measured at the same location. In (a) and (b), conditions are $\mathrm{Ca_l} = 0.024$ and $\mathrm{Bo} = 0.42$.

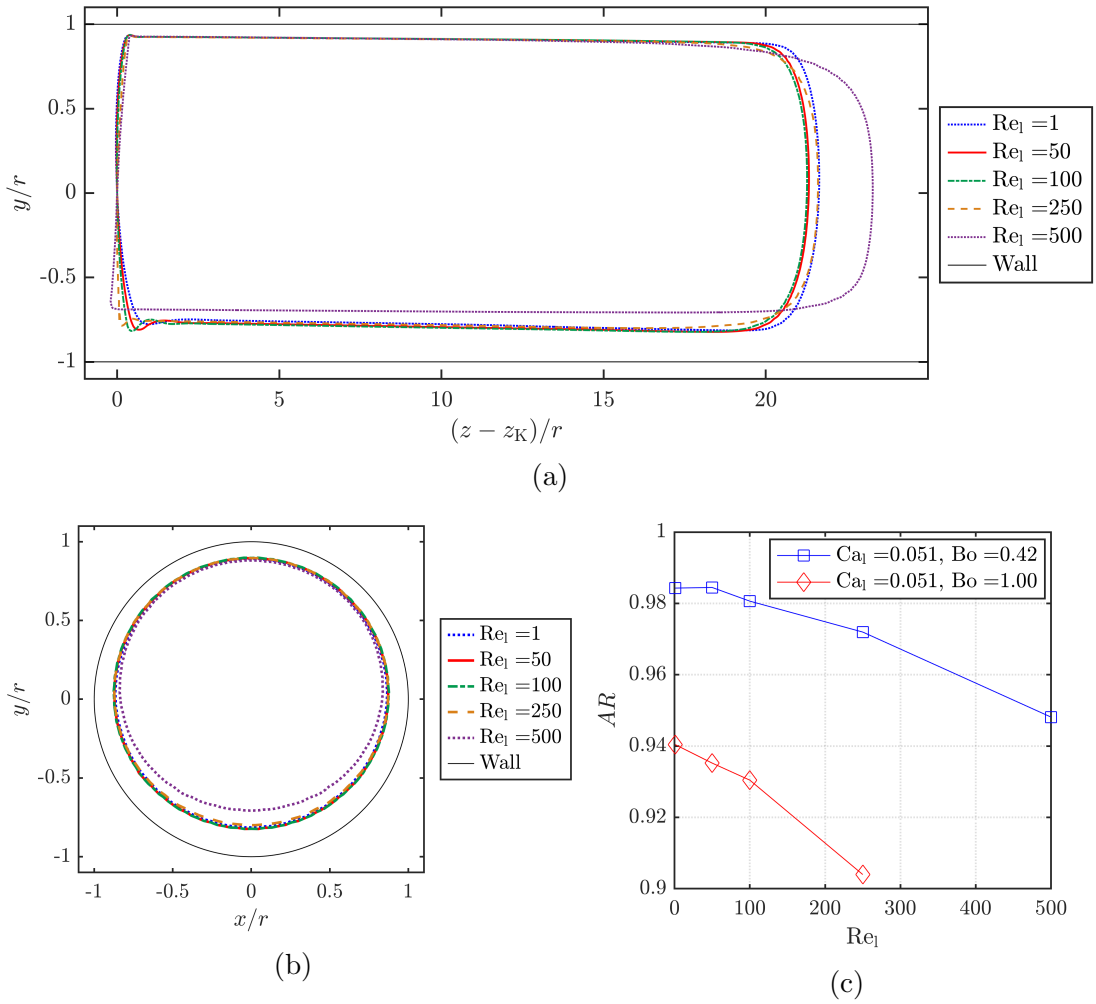
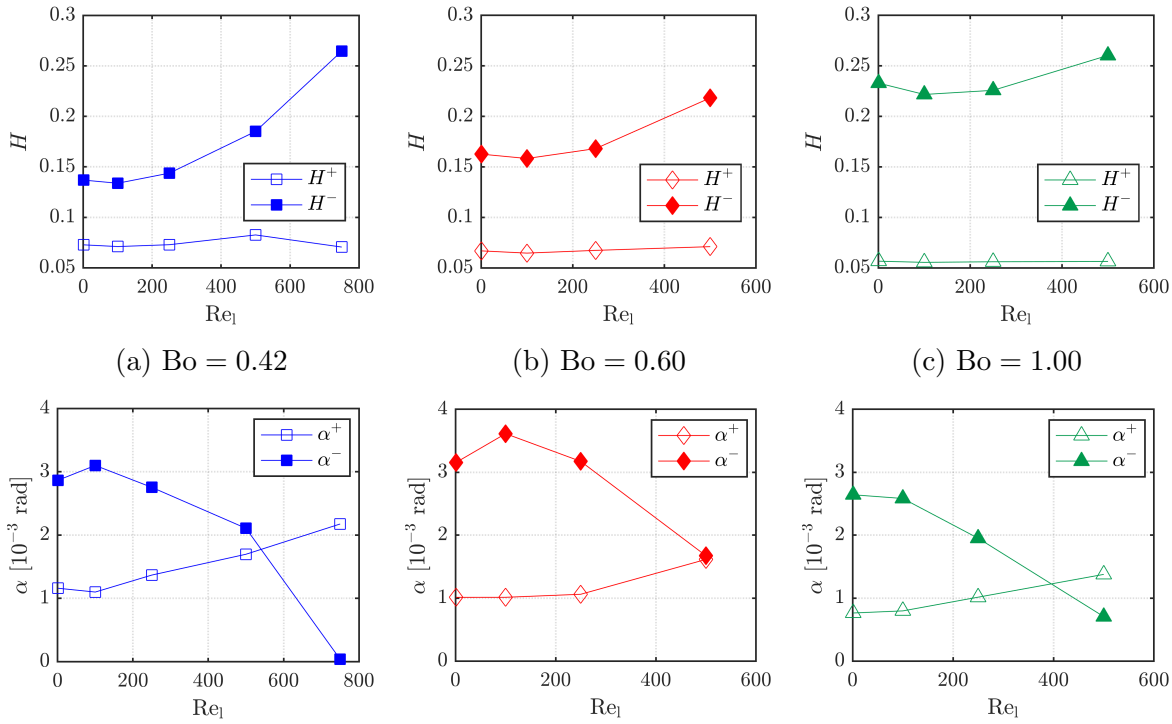


Figure 7.8: Systematic analysis of the impact of the Reynolds number on the (a) bubble profile on a vertical centreline plane ($x = 0$), (b) on the bubble cross-sectional shape at the location F, and (c) on the bubble cross-sectional aspect-ratio measured at the same location. In (a) and (b), conditions are $\mathrm{Ca_l} = 0.051$ and $\mathrm{Bo} = 0.42$.

patterns.

7.1.4.2 Film thickness and inclination angle

Figure 7.9 shows the combined impact of inertia and buoyancy on the liquid film thickness and bubble inclination angle in elongated bubble flow. The inclination angles were assessed using different lengths of the central region of the bubble to ensure the reported values are independent of nose or tail behaviour. It can been seen from Fig. 7.9a-c that the bottom film thickness increases with Bo as discussed in Section 7.1.3, and it increases with $\mathrm{Re_l}$ as shown by the profiles in Fig. 7.7. The impact of $\mathrm{Re_l}$ on H^- is more apparent for the $\mathrm{Bo} = 1.00$ case because H^- is already substantially thicker than the gravity-free case at the same $\mathrm{Re_l}$, and hence the thicker film is more sensitive to inertial forces for



(a) Bo = 0.42 (b) Bo = 0.60 (c) Bo = 1.00

(d) Bo = 0.42 (e) Bo = 0.60 (f) Bo = 1.00

Figure 7.9: Systematic analysis of the effect of the Reynolds number on the (a-c) top and bottom liquid film thickness, and (d-f) on the top and bottom bubble inclination. The liquid capillary number is fixed to $\mathrm{Ca_l} = 0.024$.

the reasons explained in the previous section. Accordingly, the top film thickness is only weakly dependent on $\mathrm{Re_l}$ in the range of Reynolds numbers studied, because this thinner film is less sensitive to the inertial effects until much larger values of $\mathrm{Re_l}$ are achieved.

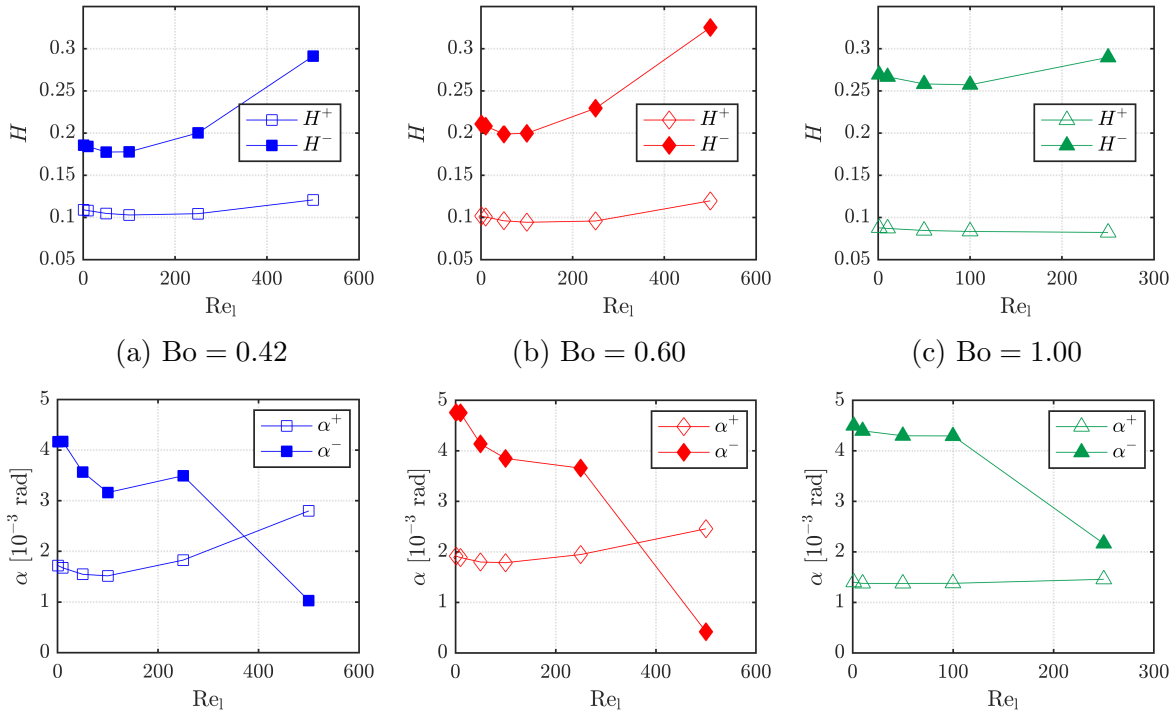
The bubble inclinations plotted in Fig. 7.9d-f show that generally α^- decreases and α^+ increases with increasing $\mathrm{Re_l}$, although the effect is again more pronounced at the bottom of the bubble. This effect was also apparent in Fig. 7.7a, where the bottom profiles of the bubble become less inclined as $\mathrm{Re_l}$ increases. Figure 7.7b shows that the shape of top half of the bubble cross-section is very similar across the different values of $\mathrm{Re_l}$, so that the top (H^+) and horizontal (H^h) film thicknesses change by less than 5 % on average, suggesting that the drainage flow rate is near constant with $\mathrm{Re_l}$. However, since the bottom film becomes substantially thicker and thus contains more liquid as $\mathrm{Re_l}$ increases, it is expected that the incoming flow rate from the thin film induces a smaller relative change on the bottom film volume, and thus on α^-.

Figure 7.10 displays the results for the top and bottom film thicknesses and inclination angles when varying both $\mathrm{Re_l}$ and Bo at $\mathrm{Ca_l} = 0.051$. The trends closely follow those

observed in Fig. 7.9 for $Ca_l = 0.024$. The bottom film thickness is more sensitive to changes of Re_l compared to the top film thickness. However, when compared to the $Ca_l = 0.024$ case, H^+ shows some more apparent changes with Re_l, due to the fact that the film is thicker and thus more sensitive to inertial effects. The trends for the bubble inclination are similar to those for $Ca_l = 0.024$, with α^+ increasing and α^- decreasing upon increase of Re_l. The sharp drop of α^- observed at all values of Bo for $Re_l = 500$ is due to a substantial flattening of the bottom profile of the bubble, as seen in Fig. 7.8a, which is also promoted by the onset of unsteady dynamics of the bubble tail.

7.1.5 Film thickness predictive method comparison to experimental data

The slug flow investigated experimentally in Section 6.3 has many similar characteristics to the elongated bubble flow presented in this section: a long vapour bubble flows in a continuous liquid phase with a very thin liquid film between the bubble and the top of the pipe, and a much thicker liquid film at the bottom of the pipe (see Fig. 6.10b). In the



(a) Bo = 0.42 (b) Bo = 0.60 (c) Bo = 1.00

(d) Bo = 0.42 (e) Bo = 0.60 (f) Bo = 1.00

Figure 7.10: Systematic analysis of the effect of the Reynolds number on the (a-c) top and bottom liquid film thickness, and (d-f) on the top and bottom bubble inclination. The liquid capillary number is fixed to $Ca_l = 0.051$.

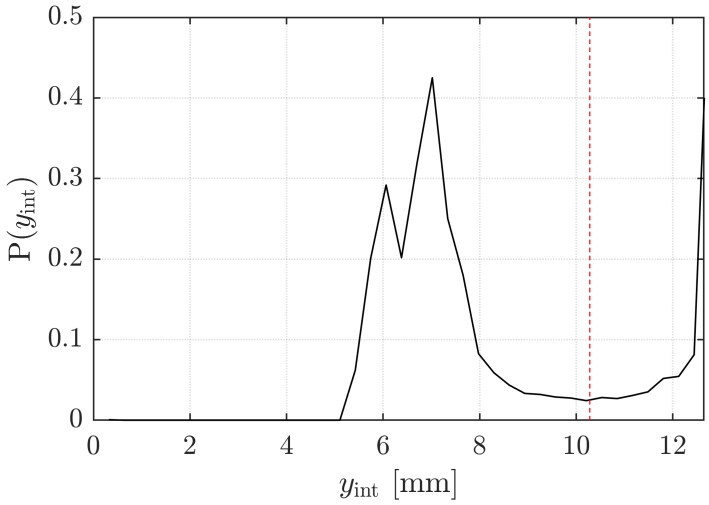


Figure 7.11: Probability density function of interface height y_{int} corresponding to Fig. 6.11a for slug flow at the conditions $G = 460$ kg/m^2.s, $q = 7.9\,\mathrm{kW/m^2}$. The red dashed line indicates the rightmost local minimum, below which the probability density function is integrated to estimate the film thickness under the vapour bubble, h^-.

central region of the bubble, away from the nose and tail, the film thickness is relatively constant and is not disturbed by large waves. However, because of the larger pipe size in the experiments and high mass flux required to achieve slug flow in the facility, the average superficial liquid Reynolds number for the slug flow experiments was $\mathrm{Re_{s,l}} = 12000$ whilst the average Bond number was $\mathrm{Bo} = 39$. These values are much larger than those for which the predictive method described in Section 7.1.1.1 has been validated computationally in this work so inaccuracies may be expected, but bottom film thickness were extracted from the experimental data and compared to predictions made using Eq. (7.3). The prediction of film thickness around slug flows is particularly important to flow boiling applications, since the film thickness typically governs the heat transfer coefficient [246].

To estimate the bottom film thickness from the experiments, a probability density function of the interface height trace for each condition (e.g. Fig. 6.11a) was constructed as shown in Fig. 7.11. There are two clear peaks in the distribution of the interface height, one at the pipe diameter (12.6 mm) which corresponds to the liquid slugs between vapour bubbles, and one at around 7 mm that represents the film thickness under the vapour bubbles. This distribution was cut off at the local minimum between the two peaks, and the mean of the data to the left of the cut-off taken as the film thickness. The resulting film thickness for Fig. 7.11 is 6.9 mm, which corresponds to the interface height displayed on the velocity field for the same conditions in Fig. 6.10b.

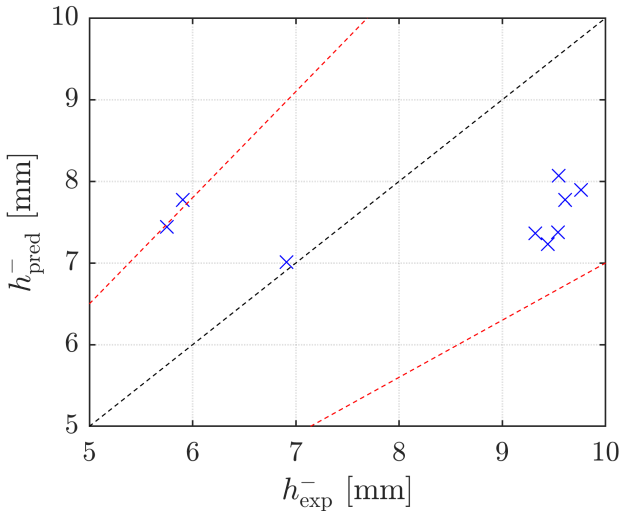


Figure 7.12: Predictions of film thickness under vapour bubbles, h^-, using Eq. (7.3) against the corresponding experimental film thicknesses in slug flow at the conditions $G = 300$–460 kg/m^2.s, $q = 5.3$–7.9 kW/m^2. The black dashed line represents $h^-_{\text{pred}} = h^-_{\text{exp}}$, whilst the red dashed lines indicate $h^-_{\text{pred}} = h^-_{\text{exp}} \pm 30\,\%$.

Film thickness predictions were made for each set of experimental slug flow conditions using Eq. (7.3), with the bubble velocity calculated as described in Section 6.3.3. The two film thicknesses are compared in Fig. 7.12. The experimental bottom film thickness is mostly underpredicted by Eq. (7.3), which is to be expected as it was shown in Fig. 7.9 that increasing the Reynolds number results in an increase in film thickness above the negligible inertia case for which the equation was developed. However, Eq. (7.3) predicts the experimental film thickness to within $\pm$ 30 % for almost all of the slug flow conditions, which is of comparable accuracy to many of the heat transfer coefficient and pressure drop predictive methods assessed in Chapter 6. However, it is much larger than the 4.8 % error reported in Section 7.1.3.2 for smaller values of Bo, so the model could be improved to account for inertial effects. It would also be of interest to compare experimental and predicted film thickness values across a larger range of conditions to assess the comparability of the trends with different variables.

7.2 Flow boiling model development

After considering the effects of buoyancy and inertia on elongated bubble flow, the next step towards a complete model of flow boiling is the inclusion of heat transfer and phase change, i.e. evaporation. In this section, the model described in Section 4.2.2, which is

a development of the *interFoam* solver in OpenFOAM 2.3.1, is first validated for boiling flows in micro-channels before being extended to a preliminary simulation of a set of experimental conditions for a stratified, laminar flow.

7.2.1 Phase change model validation in micro-channels

To validate the phase change model for boiling flow, the dynamics of a single small vapour bubble nucleating at the wall of a heated micro-channel were investigated. The model described in Section 4.2.2 was employed with the conditions set out in Section 4.2.3.1 to emulate the experimental and numerical conditions of Mukherjee et al. [152], in which water at 1 atm boils as it flows through a square micro-channel of size 229 µm. The water enters the channel under saturation conditions at a mass flux of $G = 123$ kg/m^2.s, which corresponds to a Reynolds number of 100 and a capillary number of 0.0006. The bottom and side walls are maintained at 375.25 K, whilst an adiabatic condition is applied to the top. A small spherical bubble is initiated at the wall one channel-width downstream from the inlet, as shown in Fig. 7.13, with an initial radius of 25 µm and a contact angle of 30° which is characteristic of hydrophilic surfaces. A range of initial temperature conditions were employed, as detailed in Table 7.1. The linear profile for cases 1 and 3 corresponds to that used by Mukherjee et al. [152] in their numerical study, where the temperature profile decays linearly from 375.25 K at the bottom wall to 373.15 K (the saturation temperature) at the top wall. Mukherjee et al. [152] did not report whether a thermal boundary layer was initialised around the bubble, but this is necessary to avoid an initial exponential evaporation rate. An arbitrarily large thermal boundary layer (simulation 1 in Table 7.1) and a layer three cells thick (simulation 3) were trialled. Since the linear profile is not particularly realistic, cases were trialled in which the initial temperature was set to T_{sat} everywhere (simulation 2), and with an initial temperature field obtained by running a liquid-only simulation to the point of full thermal development (simulation 4) with the *icoTempFoam* solver compiled in OpenFOAM 2.3.1.

Comparing simulations 1 and 3 to simulation 4 in Fig. 7.13 demonstrates the differences in the temperature field and the inaccuracy of a linear profile initial temperature condition. The linear temperature decay in simulations 1 and 3 results in the hot region, indicated by the red-coloured area, extending further upwards than in simulation 4. Because of this, outside the thermal boundary layer the bubble in 4 is mostly surrounded by liquid

Table 7.1: Initial temperature conditions for different simulation test cases in a 229 µm channel. In the thermal boundary layer the condition $T = T_{\text{sat}}$ is set. The bottom and side walls of the channel are subject to the condition $T_{\text{wall}} = 375.25\,\text{K}$.

Simulation	Initial temperature field	Thermal boundary layer thickness [µm]
1	Linear profile from T_{wall} to T_{sat}	50
2	Uniform $T = T_{\text{sat}}$	-
3	Linear profile from T_{wall} to T_{sat}	7
4	Fully developed T field	7

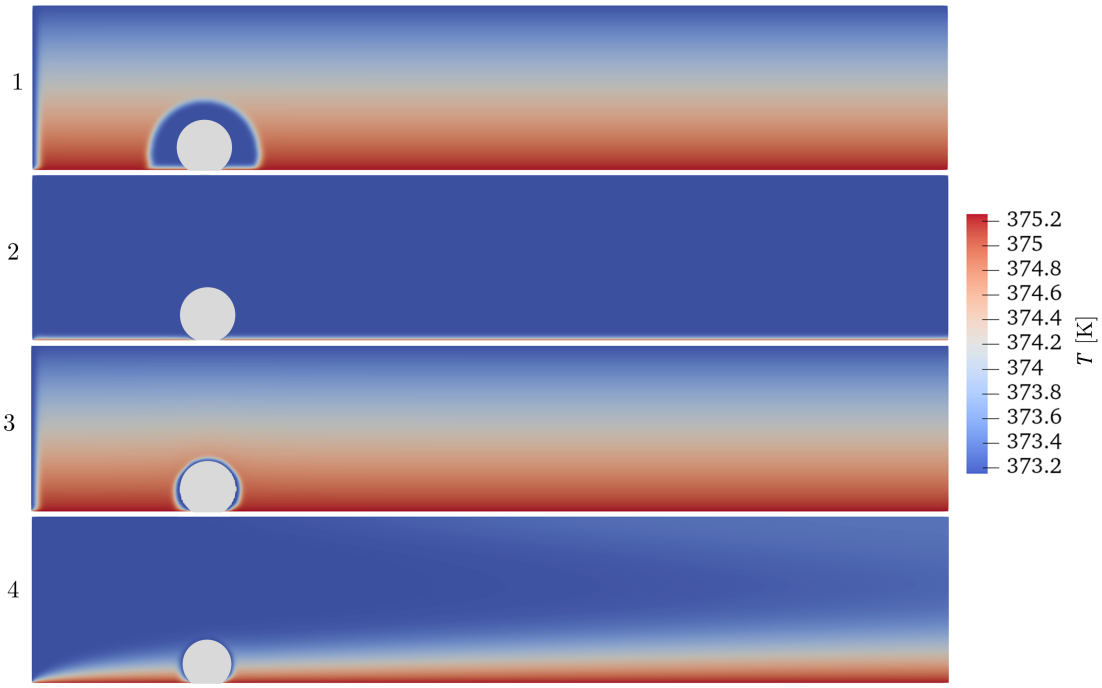


Figure 7.13: Initial temperature conditions extracted along the central $x = 0$ plane for 4 different simulations as described in Table 7.1.

at, or just above, saturation temperature, whilst the bubble in 3 is surrounded by liquid at least 1.2 K hotter than than the saturation temperature. The effect of this on bubble growth can be clearly seen in Fig. 7.14, which compares experimental [152] and numerical results in terms of the equivalent diameter of the bubble, i.e. the diameter of a sphere of equivalent volume, versus time.

The final growth rate of the bubble, shown by the gradient of the lines in Fig. 7.14 towards the upper right-hand corner of the plot, is approximately the same across all the cases, and is well matched to the experimental data [152]. However, the magnitude of the final bubble diameter differs between simulations due to the variations in initial growth of the bubble, which is highly dependent on the initial conditions. In simulation 1 the bubble initially grows steadily and spherically since the large thermal boundary layer shields it from the high temperatures of the surrounding liquid. Just after 1 ms the bubble outgrows the thermal boundary layer and begins to elongate at which point the evaporation rate increases slightly before settling when dry patches start to form at the walls. In simulation 3, which is the same as 1 except for the size of the initial thermal boundary layer, the initial growth rate is significantly faster as the bubble very quickly comes into contact with the hot liquid. Because of this fast growth, the bubble diameter quickly reaches the width of the channel and bubble elongation begins at approximately 0.5 ms with the growth rate after 1 ms equalling that of the other simulations after 1.5–2 ms.

Since the initial liquid temperature around the bubble nucleation site in simulation 2 is much lower than that in the other simulations the bubble grows steadily at the initial rate for much longer, only beginning to elongate at around 1.8 ms. In contrast, the bubble in simulation 4 grows at a faster rate than in 2 and 3 for a short initial period, after which the proportion of the bubble volume in the hot region of the liquid is smaller and the growth rate decreases. At approximately 1.2 ms the bubble begins to elongate at a steady rate equal to that of the other simulations. This case is probably the most realistic, and matches the experimental data of Mukherjee et al. [152] well. It is worth noting that the liquid-phase simulation used to obtain the developed temperature field was run for 15 ms, so the temperature field in simulations 1 to 3 would not become fully developed in the time elapsed in Fig. 7.14.

The bubble growth for simulation 4 is also illustrated by the bubble visualisation in Fig. 7.15, where the colouring of the bubble surfaces indicates the evaporation rate. The

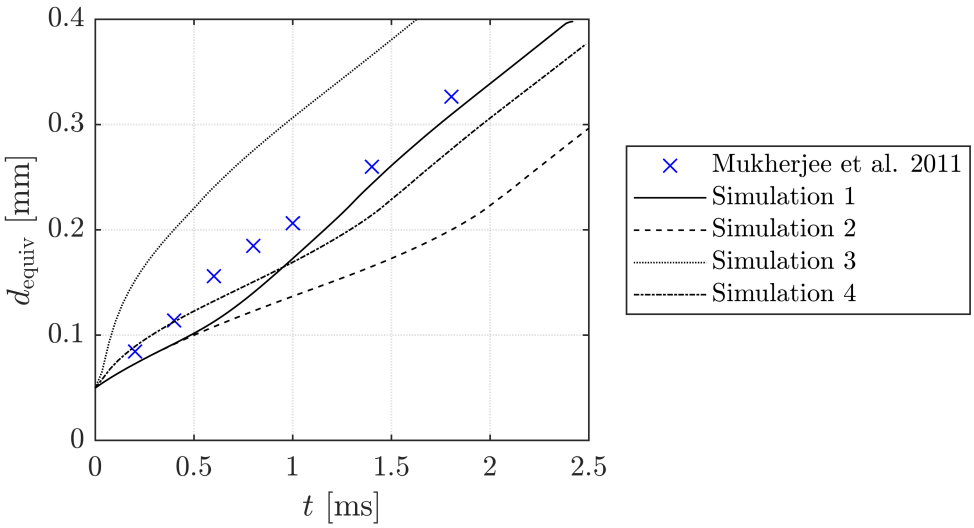


Figure 7.14: Development of equivalent bubble diameter d_{equiv} from boiling in a 229 µm square micro-channel with time t for cases with different initial temperature conditions, as described in Table 7.1, with comparison to the experimental data of Mukherjee et al. [152] (blue crosses). The flow conditions are $\text{Re}_\text{l} = 100$ and $\text{Ca}_\text{l} = 0.0006$.

spherical growth of the bubble is clear up to 1.0 ms, after which the bubble diameter approaches the width of the channel and the bubble begins to elongate. As it grows further, the bubble comes into contact with the wall and dry patches appear on all four walls, indicated by the empty regions of the bubbles in Fig. 7.15 that first appear at 2 ms. From then, the bubble increases in length up to 2.5 ms, with the dry regions also growing. It can be seen in the later time steps that the highest evaporation rates occur at the triple solid-liquid-vapour contact line, where the temperature is highest.

To complete the validation of the numerical phase change model a mesh independence study was completed using the initial conditions of simulation 4 (see Table. 7.1), with the boundary layer maintained at a thickness of 3 cells in each case. The different mesh and cell sizes investigated are shown in Table 7.2, and the effect of the different mesh resolutions on bubble growth is shown by plotting equivalent bubble diameter against time in Fig. 7.16.

The initial growth of the equivalent bubble diameter in Fig. 7.16 shows very little variation between the different meshes. Similarly, the final equivalent bubble diameter and gradient of the line towards 2.5 ms match well for most of the meshes, with the coarse mesh deviating slightly from the rest. Between 1 ms and 2 ms the fine and coarser cases deviate more from the base and coarse cases. This is predominantly caused by the variation in the thickness of the initial boundary layer. In the fine mesh, 3 cells have a

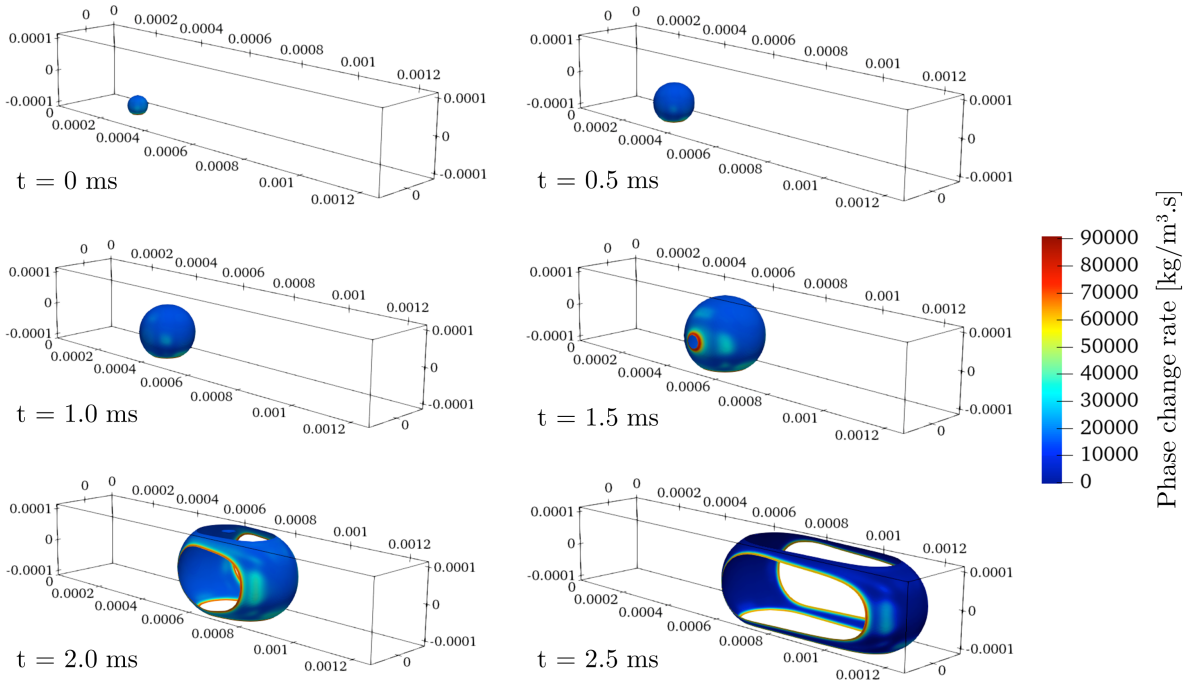


Figure 7.15: Visualisation of bubble growth from boiling in a 229 µm square micro-channel for simulation 4 (see Table. 7.1 and Fig. 7.13), coloured by the local evaporation rate. Channel dimensions are in metres and empty regions within the bubble identify dry vapour regions. The flow conditions are $Re_l = 100$ and $Ca_l = 0.0006$.

Table 7.2: Mesh parameters.

Mesh	Cell size [µm]	Number of cells
Coarser	4.6	0.34×10^6
Coarse	3.4	0.80×10^6
Base	2.3	1.05×10^6
Fine	1.5	9.28×10^6

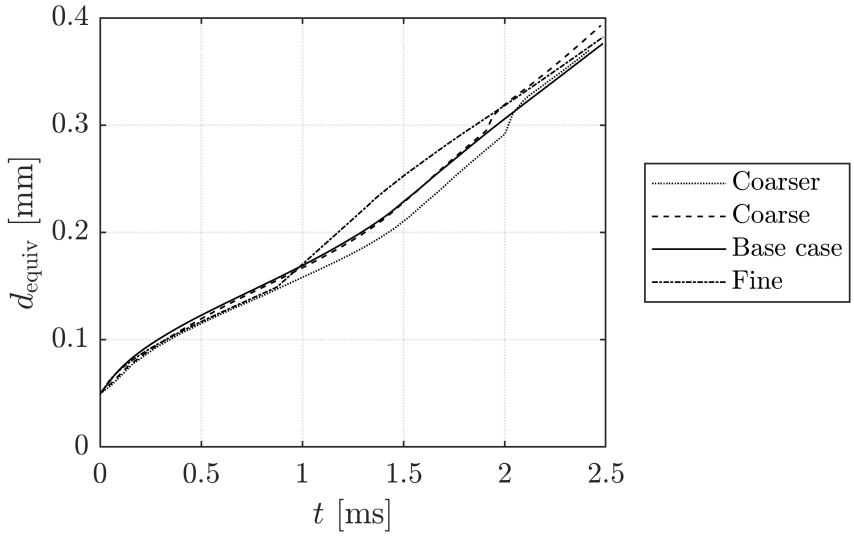


Figure 7.16: Development of equivalent bubble diameter d_{equiv} from boiling in a 229 µm square micro-channel with time t for different computational meshes, as described in Table 7.2. The flow conditions are $\text{Re}_{\text{l}} = 100$ and $\text{Ca}_{\text{l}} = 0.0006$ and the initial temperature condition corresponds to simulation 4 in Table 7.1.

width of 4.6 µm compared to 13.7 µm in the coarser mesh. Therefore in the fine mesh the bubble outgrows the thermal boundary layer sooner and comes into contact with liquid above the saturation temperature, altering the evaporation rate. Apart from this small deviation the results from the base case mesh match those of the fine mesh well, and there is no need for further refinement from the base case. The coarse and coarser meshes show some strange behaviour towards the end of the simulation time as the bubble approaches the end of the channel, so the base case mesh was selected as modelling the boiling phenomena best.

7.2.2 Simulation of experimental conditions

Following on from the validation of the phase change model in the previous section, a simulation was constructed according to the experimental geometry described in Section 3.2.2 to perform a preliminary assessment of the model performance against experimental data. Conditions were selected to correspond to an experimental data point for stratified flow where the liquid phase was in the laminar regime. The case selected had the conditions $G = 32$ kg/m^2.s, $q = 1.9\,\text{kW/m}^2$ and $x = 0.21$, which were translated into inlet and boundary conditions for the simulation as described in Section 4.2.3.2. The superficial liquid and vapour Reynolds numbers were $\text{Re}_{\text{s,l}} = 850$ and $\text{Re}_{\text{s,v}} = 7100$. Instead of mod-

elling the full test-section, the inlet conditions used in the simulation were those measured at the inlet to the visualisation section in the experiment so that direct comparisons to measurements in that section could be made.

7.2.2.1 Velocity fields and interface information

The simulated boiling flow is visualised in Fig. 7.17. The contour surface indicates the location of the vapour-liquid interface, whilst the streamwise liquid-phase velocity field in the plane along the centreline of the channel, i.e. the plane equivalent to that captured by the high-speed camera in the laser-based diagnostic techniques described in Section 3.5, is shown below that. The interface height in Fig. 7.17 increases slightly towards the outlet of the computational domain but is relatively constant locally. Some small waves are evident at the interface, despite a smooth stratified flow being observed experimentally at these conditions. The standard deviation of the interface height for the simulation and experiment were 0.54 mm and 0.24 mm respectively. The standard deviation is larger in the simulation due to the increased waviness, and is more similar in value to that of a stratified wavy flow which was 0.45 mm on average experimentally.

The streamwise liquid-phase velocity is consistently high close to the interface, as observed experimentally for stratified flows in Fig. 6.1. The velocity decreases towards the outlet of the computational domain where the interface height increases and the liquid must decelerate to accommodate this. Such behaviour towards the outlet does not correspond to experimental observations so further development of the outlet boundary conditions is required. Due to this outlet behaviour and the potential impact of any entrance effects at the inlet, average simulation values reported subsequently have been calculated over the central region of the domain discarding a length of 2 diameters (0.025 m) at each end.

Figure 7.18 shows how the mean interface height from the simulation develops over time with a comparison to the experimental average from PLIF measurements. This interface height is initiated based on the experimental void fraction calculated using the Steiner [44] formulation ((3.14)) of the Rouhani and Axelsson [45] drift flux void fraction correlation, which does not correspond directly to the measured interface height. The simulation interface height rises initially with an oscillation that deteriorates as the simulation stabilises. The height then decreases gradually from its maximum value of 3.40 mm

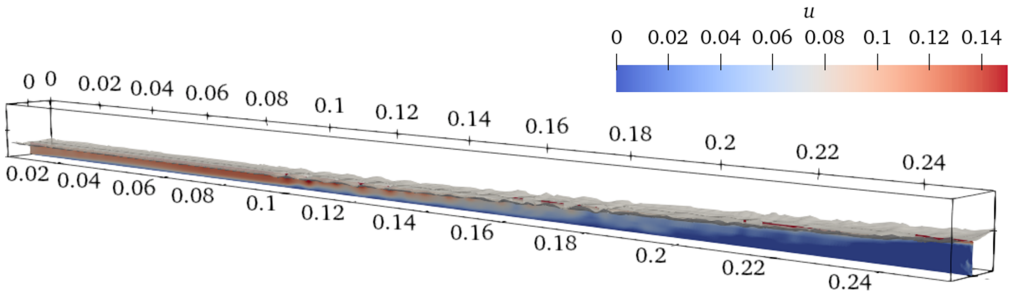


Figure 7.17: Visualisation of simulation of flow boiling in a 12.6 mm pipe at the conditions $G = 32$ kg/m^2.s, $q = 1.9$ kW/m^2 after 4.5 s of simulation time. Flow is from left to right. The contour of the vapour liquid interface is shown above the liquid-phase streamwise velocity field along the central plane of the pipe. The axial coordinate is in m and velocity u is in m/s.

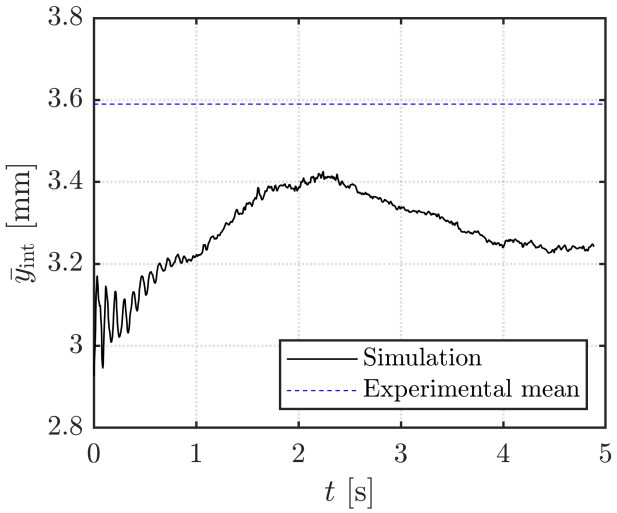


Figure 7.18: Spatially averaged interface height, $\bar{y}_{\text{int}}$, development with time t from the flow boiling simulation (solid black line) compared to the experimental mean interface height (dashed blue line) for stratified flow at the conditions $G = 32$ kg/m^2.s, $q = 1.9$ kW/m^2.

towards a constant value of approximately 3.25 mm, which is less than 10 % lower than the experimental value of 3.59 mm.

Another interesting comparison between the computational and experimental results is that of the velocity field. Figure 7.19 shows the streamwise velocity profiles averaged along the axial direction and in the time domain from both the simulation and the experiment, along with the corresponding mean interface heights. The resolution and accuracy of the computational data is better towards the wall and interface where the experimental data is affected by glow from the FEP pipe and internal reflections at the interface.

The shape of the two profiles in Fig. 7.19 is quite similar; in both, the velocity increases

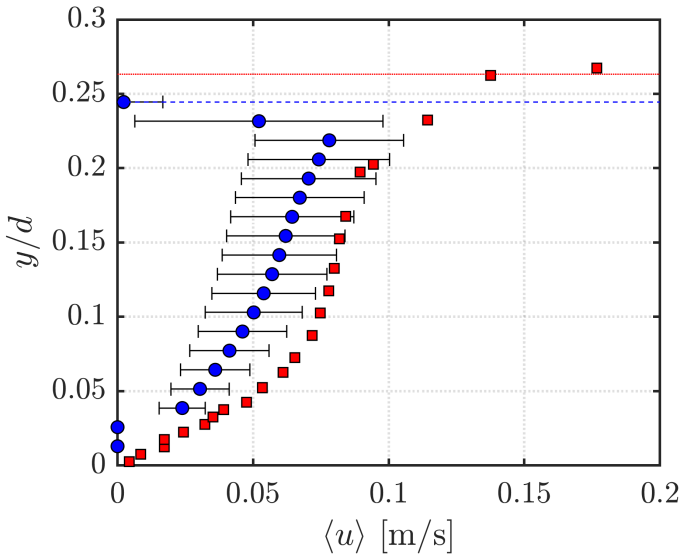


Figure 7.19: Temporally and spatially averaged streamwise velocity profiles from the experiment (blue circles) and simulation (red squares) with the conditions $G = 32\ \mathrm{kg/m^2.s}$, $q = 1.9\,\mathrm{kW/m^2}$. The horizontal lines indicate the mean interface height from the experiment (blue dashed line) and the simulation (red dotted line).

from 0 m/s at the wall before the profile experiences a decrease in gradient just under $y/d = 0.1$. Then, the velocity profile flattens somewhat before increasing again at around $y/d = 0.2$, close to the interface. The increase towards the interface was observed in both instantaneous and averaged measurements in both the computational and experimental results, so it not an artefact of spatial or temporal averaging. A similar effect was observed by Ayati et al. [227] in an air-water stratified flow. However, the particularly high velocity values observed on and just above the interface in the simulation results may in fact be related to the vapour phase. Then, ignoring those values, the maximum velocity in the simulation is almost within the error bar of that from the experiment. The absolute values of the simulated velocities are consistently higher than those of the experimental velocities which is most likely due to the initial and boundary conditions. Also, the lower interface in the simulations for an equal liquid mass flux will result in a higher liquid velocity. Therefore more consideration should be given to the most appropriate translation of the experimental conditions into boundary conditions for simulations. It is also worth noting that the phase change model employed is currently not validated for turbulent flow, so no turbulence model was employed. Therefore the vapour phase, which has a superficial Reynolds number of 7100, may not be appropriately modelled which will impact the velocity field in the liquid phase close to the interface.

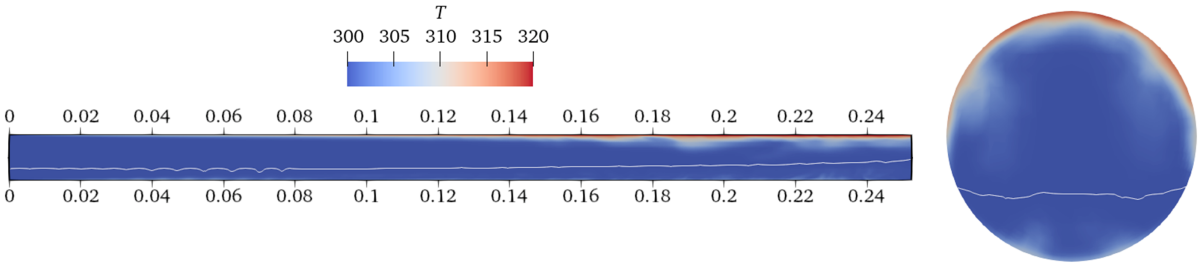


Figure 7.20: Temperature field extracted along the central plane of the pipe (left) and in the cross-section at the $z = 16d$ location (right) after 4.5 s of simulation time for stratified flow at the conditions $G = 32$ kg/m^2.s, $q = 1.9$ kW/m^2. The interface is shown by the white contour line. The axial coordinate is in metres and temperature, T, is in K.

7.2.2.2 Heat transfer

For most flow boiling applications, accurate prediction of heat transfer performance will be a key deliverable for simulations. Temperature fields extracted after 4.5 s of simulation time are shown in Fig. 7.20 for the plane along the centre of the channel, i.e. the PIV and PLIF measurement plane, and a cross-section at $16d$ (0.20 m) from the inlet. The white line indicates the vapour-liquid interface location. Temperature fields are of particular interest since they are not part of the experimental results and in the existing set-up would be very challenging to measure.

It is clear from the temperature fields in Fig. 7.20 that the bulk of the fluid in both the liquid and vapour phases is at the saturation temperature $T_{\text{sat}} = 300$ K. There are some warmer sections close to the wall, with small elevations in temperature close to the bottom wall but much higher temperatures at the top of the pipe. The top of the pipe is occupied by the vapour phase which removes heat less effectively than the liquid phase, resulting in a higher wall temperature and a lower heat transfer coefficient.

The temperature field changes somewhat along the length of the channel. The condition imposed at the inlet is that of uniform $T = T_{\text{sat}}$, so the temperature field must always develop from this condition. Such a condition is not realistic and could be a large source of discrepancy between computational and experimental results. In the experiment, the fluid at the inlet of the test section is a subcooled liquid, so it is feasible, particularly at low heat flux conditions, that some of the liquid may still be subcooled at the measurement point.

Experimentally, heat transfer performance is expressed in terms of the heat transfer coefficient (HTC), so information regarding the simulations results expressed in this way

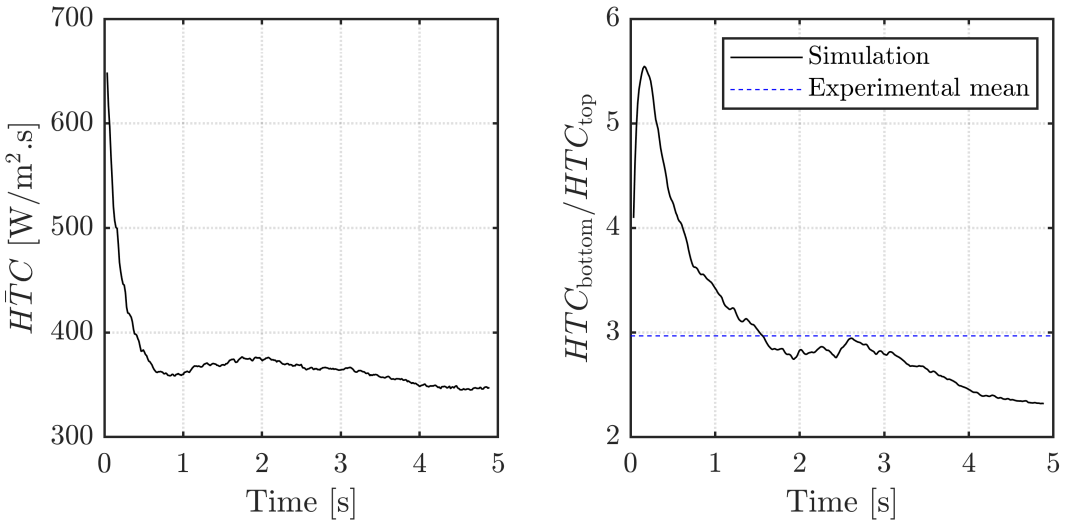


Figure 7.21: Temporal development of (a) the mean heat transfer coefficient and (b) the ratio of the heat transfer coefficients at the bottom and top of the pipe in simulations of stratified flow at the conditions $G = 32$ kg/m^2.s, $q = 1.9$ kW/m^2. In (b) the blue dashed line indicates the mean heat transfer coefficient ratio obtained in the corresponding experiment.

is shown in Fig. 7.21. Figure 7.21a shows the development of the mean heat transfer coefficient in the simulation with time. This value was obtained by averaging the heat transfer coefficient around the pipe wall. At the start of the simulation the heat transfer coefficient decreases drastically before rising slightly then settling to a value of approximately 360 W/m^2.K. The mean experimental heat transfer coefficient for the same conditions was 1200 W/m^2.K, over 3 times that of the simulation. This large discrepancy is likely to be due to the way in which the temperature condition at the wall is dealt with in the simulation compared to the experiment.

Despite the discrepancy between the absolute values of the experimental and computational heat transfer coefficients, the ratio of heat transfer coefficient at the top and bottom of the pipe is comparable between the two, as shown in Fig. 7.21b. This ratio is important in boiling applications where stratified flow may occur, since it relates to the difference in wall temperature induced between the top and bottom of the pipe. If large, this difference can cause pipe bending, potentially resulting in damage to the pipe and connecting components, and subsequent plant downtime.

7.2.2.3 Model limitations

There are various assumptions and simplifications made in the boiling model that may limit its ability to simulate experimental conditions accurately. In the simulation, a constant uniform temperature gradient is imposed at the wall to emulate the uniform heat flux condition. However, this approach neglects the conjugate heat transfer problem in the wall of the pipe. Experimentally, the outside wall temperature was measured and the inside wall temperature required for calculation of the heat transfer coefficient was estimated by solving a 1-D conduction equation in the pipe wall. This assumes uniform heat generation and negligible heat transfer in the axial and circumferential directions. The validity of these assumptions could be tested by also modelling the conjugate transfer in the wall, which would also improve the predictive capability of the simulation.

The volume fraction boundary condition at the wall could also be improved through better characterisation of the contact angle through tuning the simulation or measuring it experimentally. The value of the contact angle affects the way the liquid film forms at the pipe walls, which will in turn impact the heat transfer. Mukherjee [178] found that smaller contact angles resulted in improved heat transfer at the wall in the case of flow boiling of a bubble due to the formation of a thin liquid layer between the vapour bubble and the pipe wall.

Also, the lack of a turbulence model in the simulation will have a significant effect on the heat transfer coefficient, since hot fluid is moved away from the wall more efficiently in turbulent flow, enhancing the heat transfer. Therefore, this is also likely to have contributed to the low value of the heat transfer coefficient reported in the simulations.

In the model, fluid properties are assumed to be constant across the domain. In the majority of the domain, this assumption is valid since the bulk temperature of both the vapour and liquid is within 1 K of the saturation point. However, close to the walls the degree of superheating can reach 20 K resulting in variations in the phase viscosities and interfacial tension of up to 25 %, and changes in the vapour density of up to 90 %. Errors in the value of the interfacial tension used to carry out the simulations can result in unphysical interface behaviour, whilst errors in the vapour density will affect the kinetic mobility as calculated by Eq. (4.14) and subsequently the interphase mass flux (see Eq. (4.13)). The kinetic mobility calculation is also dependent on the accommodation coefficient, the appropriate value of which is much contested in the literature although

non-polar liquid are typically found to have an accommodation coefficient close to unity [247, 248]. This value could be tuned to experimental data to more accurately characterise the evaporative resistance.

7.3 Summary

A systematic study of the effects of buoyancy and inertia on the flow of elongated bubbles in horizontal channels of circular cross-section has been performed. Results are reported from direct numerical simulations with capillary, Bond, and Reynolds numbers in the ranges $0.024 < \mathrm{Ca_l} < 0.051$, $0.11 < \mathrm{Bo} < 3.5$, and $1 < \mathrm{Re_l} < 750$. The simulations were conducted by adopting the Volume-Of-Fluid method as included in the *interFoam* solver of OpenFOAM. This work demonstrates that the cross-section of the bubble undergoes large deformations as $\mathrm{Bo} > 1$, with the circular shape becoming progressively more oval, and the width and height of the bubble cross-section differing by more than 25 % as $\mathrm{Bo} \geq 3$.

Due to buoyancy, the bubble elevates above the channel centreline. The top and bottom film thicknesses diverge as $\mathrm{Bo} > 0$ and their difference grows to one order of magnitude and above as $\mathrm{Bo} > 3$, with the bubble travelling 50 % faster compared to the gravity-free case at the same liquid flow rate. Bubble inclination with respect to the channel axis was observed, with the tail being higher than the nose, and this effect is shown to be induced by the downward liquid flow that drains liquid from the top to the bottom film region. However, the bubble inclination does not increase monotonically with the Bond number, due to the formation of a localised constriction in the thin film on the top half of the bubble, whose thickness decreases with $\sim 1/\mathrm{Bo}$. As the top liquid film becomes thinner, viscous drag overcomes gravity, the flow rate of the draining flow reduces, and thus the bubble inclination becomes less apparent at the largest Bond numbers tested. Inertial forces tend to shrink the bubble cross-section and further lift the bubble above the channel centreline, so that the bottom film thickness increases significantly with the Reynolds number whereas the top film thickness is less sensitive to it.

New prediction models for the top and bottom film thicknesses and the bubble speed are proposed which incorporate the effects of the capillary and Bond numbers. These models compare well with the presented simulation data for Bo up to 3.5, although the

convergence of the bottom film thickness predictions as Bo $\rightarrow$ 1 can be improved. The existing models for the liquid film draining flows and the bubble inclination perform well as long as Bo $<$ 1 and the bubble cross-section remains circular, but the bubble deformation cannot be neglected in order to extend the predictive capability of these models to Bond numbers larger than unity. The new model for bottom film thickness was compared to experimental data for boiling in the slug flow regime. Despite the Bond and Reynolds numbers being much higher in the experiments than the validated range for the model, predicted values of the film thickness were within 30 % of most of the experimental values. Accurate prediction of the film thickness is important for heat transfer applications, since it is a dominating factor in the local heat transfer coefficient.

Results obtained from numerical simulations of flow boiling in a square micro-channel were presented. These simulations were conducted using the in-built *interFoam* solver of OpenFOAM with heat transfer and phase change introduced via external subroutines based on the Hertz-Knudsen-Schrage relationship. These numerical results showed good agreement with experimental data in the literature [152]. Realistic evaporation rates were achieved regardless of the initial temperature conditions of the simulation, although the initial conditions had a significant impact on the bubble size reached within the simulation time. Using the same solver, simulations of the experimental geometry of FLOBOF were performed at conditions corresponding to an experimental data point for stratified flow. The resulting simulation achieved an average vapour-liquid interface height and streamwise velocity profile similar to those measured experimentally, although larger waves were observed at the interface in the simulation. The average wall heat transfer coefficient in the simulation was approximately 3 times smaller than that in the experiment, although the ratio of bottom-to-top heat transfer coefficient was similar. This simulation method therefore has good potential for modelling of flow boiling in macro-scale channels but some further development is required, particularly with respect to initial and boundary conditions, and to account for the conjugate heat transfer in the pipe walls.

Chapter 8

Conclusion

This chapter gives an overview of the main findings of this work and their impact. Then, recommendations for further work are made.

8.1 Overview of thesis achievements

Experimental and numerical investigations of flow boiling in horizontal pipes have been carried out and the results presented in this thesis. A bespoke experimental facility has been constructed, commissioned and validated for the characterisation of flow boiling of R245fa in a 12.6 mm inside diameter horizontal pipe. An experimental database has been compiled including pressure drop and heat transfer measurements, and both qualitative and quantitative flow visualisations. The integral experimental measurements of pressure drop, heat transfer and flow pattern were compared to predictive methods in the literature, as such methods are not well-validated for the fluid, geometry and experimental conditions investigated in this work. A combination of existing flow pattern maps were able to describe the experimental observations well, but some modification to individual transition lines for the specific fluid and geometry may be required. Several predictive methods for pressure drop were considered, with the most accurate predictions at high vapour qualities by the Müller-Steinhagen and Heck [71] and Xu and Fang [72] methods. However, accurate predictions of the experimental data at very low vapour qualities were not made by any of the tested methods. Correlations for heat transfer coefficient were more accurate across the dataset, with the Shah [92] method proving the most consistently accurate, followed by the flow pattern-based model of Wojtan et al. [37]. The applicability of pool boiling

correlations to flow conditions in the nucleate boiling dominant zone was assessed, but empirical constants and fluid-specific parameters within many of these correlations require tuning to R245fa in the investigated geometry.

Laser-induced fluorescence methods were employed to identify the vapour-liquid interface in different flow patterns, whilst particle image velocimetry was used to investigate the velocity fields inside the liquid phase of these flows. In stratified flows, the streamwise velocity profiles for laminar inlet conditions conformed to theoretical predictions, whilst the heat transfer coefficient was found to increase with decreasing interface height due to thin film effects. A corrective correlation for the stratified angle in the Wojtan et al. [37] method for predicting heat transfer coefficient was proposed. The presence of interfacial waves was found to enhance heat transfer in stratified-wavy flows when compared to stratified flows, but the stratified-wavy flows investigated did not exhibit large disturbance waves or the corresponding recirculation flows in the liquid phase. Flow disturbances were observed in slug flow measurements in the nose and tail of the liquid slug with higher velocity magnitudes in the former. The vapour bubble velocity in slug flow was found to increase linearly with mixture velocity, where the gradient increased with heat flux.

A brightness-based laser-induced fluorescence technique was developed for measurement of the film thickness at the bottom of the pipe in annular flows. The mean film thickness increased with superficial liquid Reynolds number, whilst the corresponding standard deviation increased or decreased depending on the heat flux condition. Heat transfer performance decreased markedly with increasing film thickness for all conditions studied, but increased with film thickness standard deviation for some of the conditions, which corresponds to the behaviour observed in stratified-wavy flow.

The detailed spatio-temporally resolved measurements taken in this work represent an important contribution to the literature and can provide insights into the interaction of hydrodynamic and heat transfer phenomena in boiling flows. This could improve the design and operation of boiling systems including refrigeration and heat-pump systems, waste-heat recovery and conversion systems and concentrating solar power technology. The data can also be used for advanced multiphase model development and validation, as has been initiated in this work.

Numerical simulation methods towards a full model of boiling flow in macro-scale pipes

were developed. First, a parametric study of the effects of buoyancy and inertia on the flow of elongated bubbles in horizontal channels of circular cross-section was performed using the Volume-Of-Fluid method as included in the *interFoam* solver of OpenFOAM. With increasing Bond number, the bubble was found to elevate above the channel centreline and undergo deformation of its cross-section from circular to oval in shape. Consequently, film thickness asymmetry was observed around the bubble, with the top and bottom film thicknesses differing by up to one order of magnitude for high Bond numbers. Inertial forces tended to shrink the bubble cross-section and further lift the bubble above the channel centreline, so that the bottom film thickness increased significantly with the Reynolds number.

New prediction models for the top and bottom film thicknesses and the bubble speed were proposed which incorporate the effects of the capillary and Bond numbers. These models predicted the simulation data well. Existing models for liquid film drainage velocity and bubble inclination performed well for small Bond numbers for which the bubble cross-section remained circular, but consideration of the bubble deformation is required for accurate film thickness prediction where buoyancy effects are more significant. The new model for bottom film thickness was also compared to experimental data for boiling in the slug flow regime. Despite higher Bond and Reynolds numbers in the experiments than the validated range for the model, predicted values of the film thickness were within 30 % of most of the experimental values. Accurate prediction of the film thickness is important for heat transfer applications, since it is a dominating factor in the local heat transfer coefficient.

Numerical simulations of bubble growth in a heated square micro-channel were conducted using the in-built *interFoam* solver of OpenFOAM with heat transfer and phase change introduced via external subroutines. The numerical results showed good agreement with experimental data in the literature and realistic evaporation rates were achieved regardless of the initial temperature conditions, although these conditions had a significant impact on the bubble size reached within the simulation time. Using the same solver, simulations of the experimental geometry investigated in this work were performed at conditions corresponding to an experimental data point for stratified flow. The resulting simulation achieved an average vapour-liquid interface height and streamwise velocity profile similar to those measured experimentally, although larger waves were observed at

the interface in the simulation. The average wall heat transfer coefficient in the simulation was approximately 3 times smaller than that in the experiment, although the ratio of bottom-to-top heat transfer coefficient was similar. This simulation method therefore has good potential for modelling of flow boiling in macro-scale channels but some further development is required, particularly with respect to initial and boundary conditions, and to account for the conjugate heat transfer in the pipe walls. The high level of detail in the experimental results allows validation of numerical results with a high degree of accuracy.

8.2 Recommendations for future work

This work has addressed a number of challenges in the application of experimental techniques and computational methods to boiling flows in macro-scale pipes, and provides many learnings for further development of these approaches. It also provides an interesting starting point for further research, suggestions for which are given in this section.

The experimental database developed in this work could be enhanced through the addition of more data points across fixed heat and mass flux conditions, and particularly around flow pattern transition boundaries. Investigations with other test fluids would add a further dimension to the database and aid in the identification of suitable predictive methods for flow boiling in these geometries. Further modifications and improvements could be made to existing predictive methods for flow pattern, pressure drop and heat transfer coefficient based on the experimental database, and validated against other flow boiling data in the literature. It would also be of interest to applications such as concentrating solar power to investigate the effect of non-uniformity of heat flux around the circumference of the pipe, and the dynamic behaviour associated with transient heat flux conditions.

There is significant scope for further development of advanced optical measurement techniques for boiling flows. Firstly, capturing the velocity fields in both the vapour and liquid phases would give further insights into the interaction of the phases, particularly across the interface. Examination of the flow in the pipe cross-section would allow more accurate determination of the experimental void fraction and dry angle, and would aid further improvement of predictive methods for heat transfer coefficient, pressure drop and flow pattern. It would also be of great interest to extend the application of the

experimental methods presented here to a wider range of conditions for all flow patterns to form a more complete picture of the phenomena observed in this work. Another natural next step would be the corresponding measurement of spatio-temporally resolved wall and fluid temperatures, rather than integral point measurements, for comparison to the space- and time-resolved interface and velocity field information.

Ensemble averaging techniques similar to those applied to stratified-wavy flow could be utilised to examine the velocity field behaviour in liquid slugs, particularly in the nose and tail where mixing and secondary flows occur. The laser-induced fluorescence techniques applied to annular flow in this work require further development to produce reliable film thickness estimates. The geometry of the laser plane and camera could be manipulated to increase the maximum measurable film thickness, and further attempts should be made to achieve annular flow conditions in which the interface is not obscured by bubbles. If the latter is not possible, a post-processing technique should be developed to account for the presence of bubbles as best as possible. It would also be interesting to measure the film thickness at the top of the pipe to investigate film asymmetry, whilst particle image velocimetry in the liquid phase may reveal interesting flow structures.

The validation of the numerical phase change model for simulation of flow boiling in micro-channels would be well-complemented by a systematic analysis of the impact of the wetting conditions and channel aspect ratio on bubble growth. The solver requires the addition of a turbulence model and subsequent step-wise validation of the results from laminar flow in a square micro-channel to turbulent flow in a macro-scale horizontal pipe. It would also be beneficial to consider conduction in the pipe walls to solve the conjugate heat transfer problem and better emulate experimental conditions. Further work is also required in the translation of experimental conditions into initial and boundary conditions in the simulation. Ideally, a similar experiment would be designed with this in mind, setting or measuring the inlet conditions such that they are well-defined. Experimental measurement of the temperature field using infrared imaging or thermal PLIF techniques would provide insights into the thermohydraulic flow behaviour and an additional reference point for comparison to numerical simulations.

The research tasks proposed in this section will require advanced experimental and numerical techniques to address and all present significant challenges in their implementation. However, the resulting data and models will significantly improve the current

knowledge of boiling flows, which could translate to more effective design and operation of applications based on flow boiling heat transfer.

Bibliography

[1] Galloni, E., Fontana, G., and Staccone, S., "Design and experimental analysis of a mini ORC (organic Rankine cycle) power plant based on R245fa working fluid," *Energy*, vol. 90, 768–775, 2015. DOI: 10.1016/j.energy.2015.07.104.

[2] Kang, S. H., "Design and experimental study of ORC (organic Rankine cycle) and radial turbine using R245fa working fluid," *Energy*, vol. 41 (1), 514–524, 2012. DOI: 10.1016/j.energy.2012.02.035.

[3] Freeman, J., Guarracino, I., Kalogirou, S. A., and Markides, C. N., "A small-scale solar organic Rankine cycle combined heat and power system with integrated thermal energy storage," *Applied Thermal Engineering*, vol. 127, 1543–1554, 2017. DOI: 10.1016/j.applthermaleng.2017.07.163.

[4] Ramos, A., Chatzopoulou, M. A., Freeman, J., and Markides, C. N., "Optimisation of a high-efficiency solar-driven organic Rankine cycle for applications in the built environment," *Applied Energy*, vol. 228, 755–765, 2018. DOI: 10.1016/j.apenergy.2018.06.059.

[5] Pantaleo, A. M., Simpson, M., Rotolo, G., Distaso, E., Oyewunmi, O. A., Sapin, P., De Palma, P., and Markides, C. N., "Thermoeconomic optimisation of small-scale organic Rankine cycle systems based on screw vs. piston expander maps in waste heat recovery applications," *Energy Conversion and Management*, vol. 200, 112053, 2019. DOI: 10.1016/j.enconman.2019.112053.

[6] Chatzopoulou, M. A., Lecompte, S., De Paepe, M., and Markides, C. N., "Off-design optimisation of organic Rankine cycle (ORC) engines with different heat exchangers and volumetric expanders in waste heat recovery applications," *Applied Energy*, vol. 253, 113442, 2019. DOI: 10.1016/j.apenergy.2019.113442.

[7] Song, J., Li, X., Wang, K., and Markides, C. N., "Parametric optimisation of a combined supercritical CO2 (S-CO2) cycle and organic Rankine cycle (ORC) system for internal combustion engine (ICE) waste-heat recovery," *Energy Conversion and Management*, vol. 218, 112999, 2020. DOI: 10.1016/j.enconman.2020.112999.

[8] Tchanche, B. F., Quoilin, S., Declaye, S., Papadakis, G., and Lemort, V., "Economic feasibility study of a small scale organic rankine cycle system in waste heat recovery application," in *ASME 2010 10th Biennial Conference on Engineering Systems Design and Analysis, ESDA2010*, vol. 1, American Society of Mechanical Engineers Digital Collection, 2010, 249–256. DOI: 10.1115/ESDA2010-24828.

[9] White, M. T., Oyewunmi, O. A., Chatzopoulou, M. A., Pantaleo, A. M., Haslam, A. J., and Markides, C. N., "Computer-aided working-fluid design, thermodynamic optimisation and thermoeconomic assessment of ORC systems for waste-heat recovery," *Energy*, vol. 161, 1181–1198, 2018. DOI: 10.1016/j.energy.2018.07.098.

[10] Kleef, L. M. T. van, Oyewunmi, O. A., and Markides, C. N., "Multi-objective thermo-economic optimization of organic Rankine cycle (ORC) power systems in waste-heat recovery applications using computer-aided molecular design techniques," *Applied Energy*, vol. 251, 112513, 2019. DOI: 10.1016/j.apenergy.2019.01.071.

[11] Fernández-García, A., Zarza, E., Valenzuela, L., and Pérez, M., "Parabolic-trough solar collectors and their applications," *Renewable and Sustainable Energy Reviews*, vol. 14 (7), 1695–1721, 2010. DOI: 10.1016/j.rser.2010.03.012.

[12] Odeh, S. D., Behnia, M., and Morrison, G. L., "Hydrodynamic analysis of direct steam generation solar collectors," *Journal of Solar Energy Engineering*, vol. 122 (1), 14, 2000. DOI: 10.1115/1.556273.

[13] Ajona, J. I., Herrmann, U., Sperduto, F., and Farinha-Mendes, J., "Main achievements within ARDISS (Advanced Receiver for Direct Solar Steam Production in parabolic trough solar power plants) project," in *Components, tools, facilities and measurement techniques. - (Solar thermal concentrating technologies : proceedings of the 8th international symposium, October, 6 - 11, 1996, Köln, Germany ; Vol. 2)*, M. Becker, Ed., 1996, 733–754.

[14] Kandlikar, S. G. and Grande, W. J., "Evolution of microchannel flow passages–thermohydraulic performance and fabrication technology," *Heat Transfer Engineering*, vol. 24 (1), 3–17, 2003. DOI: 10.1080/01457630304040.

[15] Zadrazil, I. and Markides, C. N., "An experimental characterization of liquid films in downwards co-current gas-liquid annular flow by particle image and tracking velocimetry," *International Journal of Multiphase Flow*, vol. 67, 42–53, 2014. DOI: 10.1016/j.ijmultiphaseflow.2014.08.007.

[16] Charogiannis, A., An, J. S., and Markides, C. N., "A simultaneous planar laser-induced fluorescence, particle image velocimetry and particle tracking velocimetry technique for the investigation of thin liquid-film flows," *Experimental Thermal and Fluid Science*, vol. 68, 516–536, 2015. DOI: 10.1016/j.expthermflusci.2015.06.008.

[17] Cherdantsev, A. V., An, J. S., Charogiannis, A., and Markides, C. N., "Simultaneous application of two laser-induced fluorescence approaches for film thickness measurements in annular gas-liquid flows," *International Journal of Multiphase Flow*, vol. 119, 237–258, 2019. DOI: 10.1016/J.IJMULTIPHASEFLOW.2019.07.013.

[18] Collier, J. G. and Thome, J. R., Convective boiling and condensation, 3rd ed. Clarendon Press, 1994. DOI: 10.1017/S0022112095233160.

[19] Alves, G. E., "Cocurrent liquid-gas flow in a pipe-line contactor," *Chemical Engineering Progress*, vol. 50 (9), 449–456, 1954.

[20] Bergelin, O. P. and Gazeley, C. J., "Cocurrent gas-liquid flow. I. Flow in horizontal tubes," *ASME Process Heat Transfer and Fluid Mechanics Institute*, 5–18, 1949.

[21] Kosterin, S. I., "An investigation of the influence of the diameter and inclination of a tube on the hydraulic resistance and flow structure of gas-liquid mixtures," *Izvestiza Akademii Nauk SSSR Otdelema Tekhnicheskikh*, vol. 12 (1824), 1949.

[22] Baker, O., "Simultaneous flow of oil and gas," *Oil and Gas Journal*, vol. 53, 185–195, 1954.

[23] Hoogendoorn, C. J., "Gas-liquid flow in horizontal pipes," *Chemical Engineering Science*, vol. 9 (4), 205–217, 1959. DOI: 10.1016/0009-2509(59)85003-X.

[24] Hoogendoorn, C. J. and Buitelaar, A. A., "The effect of gas density and gradual vaporization on gas-liquid flow in horizontal pipes," *Chemical Engineering Science*, vol. 16 (3-4), 208–221, 1961. DOI: 10.1016/0009-2509(61)80032-8.

[25] Scott, D. S., "Properties of cocurrent gas-liquid flow," in *Advances in Chemical Engineering*, 1964, 199–277. DOI: 10.1016/S0065-2377(08)60241-0.

[26] Mandhane, J. M., Gregory, G. A., and Aziz, K., "A flow pattern map for gas-liquid flow in horizontal pipes," *International Journal of Multiphase Flow*, vol. 1 (4), 537–553, 1974. DOI: 10.1016/0301-9322(74)90006-8.

[27] Taitel, Y. and Dukler, A. E., "A model for predicting flow regime transitions in horizontal and near horizontal gas-liquid flow," *AIChE Journal*, vol. 22 (1), 47–55, 1976.

[28] Hashizume, K., "Flow pattern, void fraction and pressure drop of refrigerant two-phase flow in a horizontal pipe," *International Journal of Multiphase Flow*, vol. 9 (4), 399–410, 1983. DOI: 10.1016/0301-9322(83)90096-4.

[29] Dukler, A. E. and Taitel, Y., "Flow Pattern Transitions in Gas-Liquid Systems, chap. 3; Modelling Two-Phase Annular Flow, chap. 5 and Modelling Upward Gas-Liquid Flow, chap. 7," in *Two-Phase Gas-Liquid Flow: a Short Course on Principles of Modelling Gas-Liquid Flow and on Modern Measuring Methods*, Houston, TX: University of Houston, 1991.

[30] Steiner, D., "Wärmeübergang beim Strömungsverdampfen von Reinstoffen und von Mischungen," Ph.D. dissertation, University of Karlsruhe, 1996.

[31] Kattan, N., Thome, J. R., and Favrat, D., "Flow boiling in horizontal tubes: Part 1—Development of a diabatic two-phase flow pattern map," *Journal of Heat Transfer*, vol. 120 (1), 140–147, 1998. DOI: 10.1115/1.2830037.

[32] Kattan, N., Thome, J. R., and Favrat, D., "Flow boiling in horizontal tubes: Part 2—New heat transfer data for five refrigerants," *Journal of Heat Transfer*, vol. 120 (1), 148–155, 1998. DOI: 10.1115/1.2830038.

[33] Kattan, N., Thome, J. R., and Favrat, D., "Flow boiling in horizontal tubes: Part 3—Development of a new heat transfer model based on flow pattern," *Journal of Heat Transfer*, vol. 120 (1), 156–165, 1998. DOI: 10.1115/1.2830039.

[34] Zürcher, O., Favrat, D., and Thome, J. R., "Development of a diabatic two-phase flow pattern map for horizontal flow boiling," *International Journal of Heat and Mass Transfer*, vol. 45 (2), 291–301, 2002. DOI: 10.1016/S0017-9310(01)00146-6.

[35] Thome, J. R. and El Hajal, J., "Two-phase flow pattern map for evaporation in horizontal tubes: latest version," *Heat Transfer Engineering*, vol. 24 (6), 3–10, 2003. DOI: 10.1080/01457630390232681.

[36] Wojtan, L., Ursenbacher, T., and Thome, J. R., "Investigation of flow boiling in horizontal tubes: Part I - A new diabatic two-phase flow pattern map," *International Journal of Heat and Mass Transfer*, vol. 48 (14), 2955–2969, 2005. DOI: 10.1016/j.ijheatmasstransfer.2004.12.012.

[37] Wojtan, L., Ursenbacher, T., and Thome, J. R., "Investigation of flow boiling in horizontal tubes: Part II - Development of a new heat transfer model for stratified-wavy, dryout and mist flow regimes," *International Journal of Heat and Mass Transfer*, vol. 48 (14), 2970–2985, 2005. DOI: 10.1016/j.ijheatmasstransfer.2004.12.013.

[38] Cheng, L., Ribatski, G., Moreno Quibén, J., and Thome, J. R., "New prediction methods for CO2 evaporation inside tubes: Part I – A two-phase flow pattern map and a flow pattern based phenomenological model for two-phase flow frictional pressure drops," *International Journal of Heat and Mass Transfer*, vol. 51 (1-2), 111–124, 2008. DOI: 10.1016/J.IJHEATMASSTRANSFER.2007.04.002.

[39] Grauso, S., Mastrullo, R., Mauro, A. W., Thome, J. R., and Vanoli, G. P., "Flow pattern map, heat transfer and pressure drops during evaporation of R-1234ze(E) and R134a in a horizontal, circular smooth tube: Experiments and assessment of predictive methods," *International Journal of Refrigeration*, vol. 36 (2), 478–491, 2013. DOI: 10.1016/J.IJREFRIG.2012.07.016.

[40] Govier, G. W. and Omer, M. M., "The horizontal pipeline flow of air-water mixtures," *The Canadian Journal of Chemical Engineering*, vol. 40 (3), 93–104, 1962. DOI: 10.1002/cjce.5450400303.

[41] Al-Sheikh, J. N., Saunders, D. E., and Brodkey, R. S., "Prediction of flow patterns in horizontal two-phase pipe flow," *The Canadian Journal of Chemical Engineering*, vol. 48 (1), 21–29, 1970. DOI: 10.1002/cjce.5450480105.

[42] Yin, S., Zhang, J., Tong, L., Yao, Y., and Wang, L., "Experimental study on flow patterns for water boiling in horizontal heated tubes," *Chemical Engineering Science*, vol. 102, 577–584, 2013. DOI: 10.1016/J.CES.2013.08.026.

[43] Kundu, A., Kumar, R., and Gupta, A., "Heat transfer characteristics and flow pattern during two-phase flow boiling of R134a and R407C in a horizontal smooth tube," *Experimental Thermal and Fluid Science*, vol. 57, 344–352, 2014. DOI: 10.1016/J.EXPTHERMFLUSCI.2014.05.020.

[44] Steiner, D., "H3. 1 flow patterns in evaporator tubes," *Verein Deutscher Ingenieure. VDI Heat Atlas:*, 2010.

[45] Rouhani, S. Z. and Axelsson, E., "Calculation of void volume fraction in the subcooled and quality boiling regions," *International Journal of Heat and Mass Transfer*, vol. 13 (2), 383–393, 1970. DOI: 10.1016/0017-9310(70)90114-6.

[46] Biberg, D., "An explicit approximation for the wetted angle in two-Phase stratified pipe flow," *The Canadian Journal of Chemical Engineering*, vol. 77 (6), 1221–1224, 1999. DOI: 10.1002/cjce.5450770619.

[47] Kutateladze, S. S., "On the transition to film boiling under natural convection," *Kotloturbostroenie*, vol. 3, 10–12, 1948.

[48] Nasr, M., Akhavan-Behabadi, M. A., Momenifar, M. R., and Hanafizadeh, P., "Heat transfer characteristic of R-600a during flow boiling inside horizontal plain tube," *International Communications in Heat and Mass Transfer*, vol. 66, 93–99, 2015. DOI: 10.1016/J.ICHEATMASSTRANSFER.2015.05.024.

[49] Zürcher, O., Thome, J. R., and Favrat, D., "Evaporation of ammonia in a smooth horizontal tube: Heat transfer measurements and predictions," *Journal of Heat Transfer*, vol. 121 (1), 89–101, 1999. DOI: 10.1115/1.2825974.

[50] Ong, C. L. and Thome, J. R., "Macro-to-microchannel transition in two-phase flow: Part 1 - Two-phase flow patterns and film thickness measurements," *Experimental Thermal and Fluid Science*, vol. 35 (1), 37–47, 2011. DOI: 10.1016/j.expthermflusci.2010.08.004.

[51] Costa-Patry, E. and Thome, J. R., "Flow pattern-based flow boiling heat transfer model for microchannels," *International Journal of Refrigeration*, vol. 36 (2), 414–420, 2013. DOI: 10.1016/j.ijrefrig.2012.12.006.

[52] Barbieri, P. E. L., Jabardo, J. M. S., and Filho, E. P. B., "Flow patterns in convective boiling of refrigerant R-134a in smooth tubes of several diameters," in *5th European Thermal-Sciences Conference*, 2008.

[53] Cicchitti, A., Lombardi, C., Silvestri, M., Soldaini, G., and Zavattarelli, R., "Two-phase cooling experiments: Pressure drop, heat transfer and burnout measurements," *Energia Nuclear*, vol. 7, 407–425, 1960.

[54] McAdams, W. H., Woods, W. K., and Heroman, L. C., "Vaporization inside horizontal tubes—III—benzene oil mixtures," *Transactions of the American Society of Mechanical Engineers*, vol. 64 (3), 193–200, 1942.

[55] Beggs, D. H. and Brill, J. P., "A study of two-phase flow in inclined pipes," *Journal of Petroleum Technology*, vol. 25 (05), 607–617, 1973. DOI: 10.2118/4007-PA.

[56] Awad, M. M. and Muzychka, Y. S., "Effective property models for homogeneous two-phase flows," *Experimental Thermal and Fluid Science*, vol. 33 (1), 106–113, 2008. DOI: 10.1016/J.EXPTHERMFLUSCI.2008.07.006.

[57] Cioncolini, A. and Thome, J. R., "Pressure drop prediction in annular two-phase flow in macroscale tubes and channels," *International Journal of Multiphase Flow*, vol. 89, 321–330, 2017. DOI: 10.1016/J.IJMULTIPHASEFLOW.2016.11.003.

[58] Dalkılıç, A. S., Çebi, A., Celen, A., Awad, M. M., and Wongwises, S., "Evaluation of the performance of the empirical correlations used to predict R134a's boiling frictional pressure drop inside smooth and corrugated tubes," *International Communications in Heat and Mass Transfer*, vol. 81, 8–18, 2017. DOI: 10.1016/J.ICHEATMASSTRANSFER.2016.11.010.

[59] Meyer, G. B. and Wallis, P. E., "Co-current upwards annular-mist flow," 1965.

[60] Fitzsimmons, D. E., "Two phase pressure drop in piping components," Hanford Atomic Products Operation, Richland, Washington, Tech. Rep., 1964.

[61] Martinelli, R. C. and Nelson, D. B., "Prediction of pressure drop during forced circulation boiling of water," in *ASME Annual Meeting*, 1947.

[62] Lockhart, R. W. and Martinelli, R. C., "Proposed correlation of data for isothermal two-phase, two-component flow in pipes," *Chemical Engineering Progress*, vol. 45 (1), 39–48, 1949.

[63] Grönnerud, R., "Investigation of liquid holdup, flow resistance and heat transfer in circulation type evaporators, part IV: Two-phase resistance in boiling refrigerants," *Bulletin of the International Institute Du Froid*, vol. 16 (Annexe 1), 1972–1981, 1972.

[64] Turgut, O. E., Çoban, M. T., and Asker, M., "Comparison of flow boiling pressure drop correlations for smooth macrotubes," *Heat Transfer Engineering*, vol. 37 (6), 487–506, 2016. DOI: 10.1080/01457632.2015.1060733.

[65] Hardik, B. K., Kumar, G., and Prabhu, S. V., "Boiling pressure drop, local heat transfer distribution and critical heat flux in horizontal straight tubes," *International Journal of Heat and Mass Transfer*, vol. 113, 466–481, 2017. DOI: 10.1016/J.IJHEATMASSTRANSFER.2017.05.073.

[66] Friedel, L., "Improved friction pressure drop correlations for horizontal and vertical two-phase pipe flow," *Proceedings of the European Two-Phase Flow Group Meeting, Ispra, Italy*, 1979.

[67] Whalley, P. B., "Multiphase Flow and Pressure Drop," in *Heat Exchanger Design Handbook*, Vol. 2, Washington, D.C.: Hemisphere, 1983, 2.3.2–11.

[68] Xu, Y., Fang, X. D., Xianghui, S., Zhou, Z., and Chen, W., "Evaluation of frictional pressure drop correlations for two-phase flow in pipes," *Nuclear Engineering and Design*, vol. 253, 86–97, 2012. DOI: 10.1016/j.nucengdes.2012.08.007.

[69] Yang, Z., Gong, M., Chen, G., Zou, X., and Shen, J., "Two-phase flow patterns, heat transfer and pressure drop characteristics of R600a during flow boiling inside a horizontal tube," *Applied Thermal Engineering*, vol. 120, 654–671, 2017. DOI: 10.1016/j.applthermaleng.2017.03.124.

[70] Whalley, P. B., Two-phase flow and heat transfer. Oxford University Press, 199, 1996.

[71] Müller-Steinhagen, H. and Heck, K., "A simple friction pressure drop correlation for two-phase flow in pipes," *Chemical Engineering and Processing: Process Intensification*, vol. 20 (6), 297–308, 1986. DOI: 10.1016/0255-2701(86)80008-3.

[72] Xu, Y. and Fang, X., "A new correlation of two-phase frictional pressure drop for evaporating flow in pipes," *International Journal of Refrigeration*, vol. 35 (7), 2039–2050, 2012. DOI: 10.1016/j.ijrefrig.2012.06.011.

[73] Hardik, B. K. and Prabhu, S. V., "Boiling pressure drop and local heat transfer distribution of water in horizontal straight tubes at low pressure," *International Journal of Thermal Sciences*, vol. 110, 65–82, 2016. DOI: 10.1016/j.ijthermalsci.2016.06.025.

[74] Fang, X., Xu, Y., and Zhou, Z., "New correlations of single-phase friction factor for turbulent pipe flow and evaluation of existing single-phase friction factor correlations," *Nuclear Engineering and Design*, vol. 241 (3), 897–902, 2011. DOI: 10.1016/j.nucengdes.2010.12.019.

[75] Chawla, J. M., "Frictional pressure drop on the flow of liquid/gas mixtures in horizontal pipes," *Chemie Ingenieur Technik*, vol. 44 (1-2), 58–63, 1972. DOI: 10.1002/cite.330440111.

[76] V.D.I., VDI-Wärmeatlas (VDI Heat Atlas). 1974.

[77] Olujic, Z., "Predicting two-phase-flow friction loss in horizontal pipes," *Chemical Engineering (New York)*, vol. 92, 45–50, 1985.

[78] Ferguson, M. E. G. and Spedding, P. L., "Measurement and prediction of pressure drop in two-phase flow," *Journal of Chemical Technology AND Biotechnology*, vol. 63 (3), 262–278, 1995. DOI: 10.1002/jctb.280630311.

[79] Bandel, J., Druckverlust und Wärmeübergang bei der verdampfung siendender Kältemittel im Durchströmten Waagerechten Rohr. University Karlsruhe, 1973.

[80] Quibén, J. and Thome, J. R., "Flow pattern based two-phase frictional pressure drop model for horizontal tubes, Part II: New phenomenological model," *International Journal of Heat and Fluid Flow*, vol. 28 (5), 1060–1072, 2007. DOI: 10.1016/j.ijheatfluidflow.2007.01.004.

[81] Quibén, J. and Thome, J. R., "Flow pattern based two-phase frictional pressure drop model for horizontal tubes. Part I: Diabatic and adiabatic experimental study," *International Journal of Heat and Fluid Flow*, vol. 28, 1049–1059, 2007. DOI: 10.1016/j.ijheatfluidflow.2007.01.003.

[82] Hirsch, T., Feldhoff, J. F., Hennecke, K., and Pitz-Paal, R., "Advancements in the field of direct steam generation in linear solar concentrators-a review," *Heat Transfer Engineering*, vol. 35 (3), 258–271, 2014. DOI: 10.1080/01457632.2013.825172.

[83] Stephan, K. and Abdelsalam, M., "Heat-transfer correlations for natural convection boiling," *International Journal of Heat and Mass Transfer*, vol. 23 (1), 73–87, 1980. DOI: 10.1016/0017-9310(80)90140-4.

[84] Halon, S., Gil, B., Bialko, B., and Zajaczkowski, B., "Influence of saturation temperature and heat flux on pool boiling of R245fa," *Experimental Heat Transfer*, 1–18, 2020. DOI: 10.1080/08916152.2020.1795009.

[85] Gorenflo, D., "Pool boiling," in *VDI Heat Atlas*, Düsseldorf, Germany: VDI-Verlag, 1993.

[86] Gorenflo, D. and Kenning, D., "Pool Boiling," in *VDI Heat Atlas*, Springer Berlin Heidelberg, 2009, ch. H2, 757–792. DOI: 10.1007/978-3-540-77877-6_45.

[87] Cooper, M. G., "Heat flow rates in saturated nucleate pool boiling-A wide-ranging examination using reduced properties," *Advances in Heat Transfer*, vol. 16 (C), 157–239, 1984. DOI: 10.1016/S0065-2717(08)70205-3.

[88] Ribatski, G. and Jabardo, J. M. S., "Experimental study of nucleate boiling of halocarbon refrigerants on cylindrical surfaces," *International Journal of Heat and Mass Transfer*, vol. 46 (23), 4439–4451, 2003. DOI: 10.1016/S0017-9310(03)00252-7.

[89] Mostinski, I., "Application of the rule of corresponding states for calculation of heat transfer and critical heat flux," *Teploenergetika*, vol. 4 (4), 66–71, 1963.

[90] Jung, D., Kim, Y., Ko, Y., and Song, K., "Nucleate boiling heat transfer coefficients of pure halogenated refrigerants," *International Journal of Refrigeration*, vol. 26, 240–248, 2003. DOI: 10.1016/S0140-7007(02)00040-3.

[91] Chen, J. C., "Correlation for boiling heat transfer to saturated fluids in convective flow," *Industrial and Engineering Chemistry Process Design and Development*, vol. 5 (3), 322–329, 1966. DOI: 10.1021/i260019a023.

[92] Shah, M. M., "Chart correlation for saturation boiling heat transfer: Equation and further study," *ASHREA Transactions*, vol. 88 (1), 185–196, 1982.

[93] Guo, Q., Li, M., and Tian, X., "Experimental study on flow boiling heat transfer characteristics of R134a, R245fa and R134a/R245fa mixture at high saturation temperatures," *International Journal of Thermal Sciences*, vol. 150, 106195, 2020. DOI: 10.1016/j.ijthermalsci.2019.106195.

[94] Liu, S., Song, M., Dai, B., Tian, Y., Song, M., and Mao, N., "Experimental study on R245fa condensation heat transfer in horizontal smooth tube and enhanced tube," in *Energy Procedia*, vol. 142, Elsevier Ltd, 2017, 4169–4175. DOI: 10.1016/j.egypro.2017.12.342.

[95] Kandlikar, S. G., "A general correlation for saturated two-phase flow boiling heat transfer inside horizontal and vertical tubes," *Journal of Heat Transfer*, vol. 112 (1), 219–228, 1990. DOI: 10.1115/1.2910348.

[96] Saiz Jabardo, J. M., Bandarra Filho, E. P., and Da Silva Lima, C. U., "New correlation for convective boiling of pure halocarbon refrigerants flowing in horizontal tubes," *Revista Brasileira de Ciencias Mecanicas/Journal of the Brazilian Society of Mechanical Sciences*, vol. 21 (2), 245–258, 1999.

[97] Greco, A. and Vanoli, G. P., "Flow boiling heat transfer with HFC mixtures in a smooth horizontal tube. Part II: Assessment of predictive methods," *Experimental Thermal and Fluid Science*, vol. 29 (2), 199–208, 2005. DOI: 10.1016/j.expthermflusci.2004.03.004.

[98] Kim, J. yong and Ghajar, A. J., "A general heat transfer correlation for non-boiling gas-liquid flow with different flow patterns in horizontal pipes," *International Journal of Multiphase Flow*, vol. 32 (4), 447–465, 2006. DOI: 10.1016/j.ijmultiphaseflow.2006.01.002.

[99] Gungor, K. E. and Winterton, R. H. S., "A general correlation for flow boiling in tubes and annuli," *International Journal of Heat and Mass Transfer*, vol. 29 (3), 351–358, 1986. DOI: 10.1016/0017-9310(86)90205-X.

[100] Liu, Z. and Winterton, R. H. S., "A general correlation for saturated and subcooled flow boiling in tubes and annuli, based on a nucleate pool boiling equation," *International Journal of Heat and Mass Transfer*, vol. 34 (11), 2759–2766, 1991. DOI: 10.1016/0017-9310(91)90234-6.

[101] Wattelet, J. P., Chato, J. C., Christoffersen, B. R., Gaibel, J. A., Ponchner, M., Kenney, P. J., Shimon, R. L., Villaneuva, T. C., Rhines, N. L., Sweeney, K. A., Allen, D. G., and Hershberger, T. T., "Heat transfer flow regimes of refrigerants in a horizontal-tube evaporator," Air Conditioning and Refrigeration Center, Univeristy of Illinois, Urbana, IL, Tech. Rep., 1994.

[102] Yuan, S., Cheng, W. L., Nian, Y. L., Zhong, Q., Fan, Y. F., and He, J., "Evaluation of prediction methods for heat transfer coefficient of annular flow and a novel correlation," *Applied Thermal Engineering*, vol. 114, 10–23, 2017. DOI: 10.1016/j.applthermaleng.2016.11.170.

[103] Guo, C., Wang, J., Du, X., and Yang, L., "Experimental flow boiling characteristics of R134a/R245fa mixture inside smooth horizontal tube," *Applied Thermal Engineering*, vol. 103, 901–908, 2016. DOI: 10.1016/j.applthermaleng.2016.04.162.

[104] Lee, H. S., Yoon, J. I., Kim, J. D., and Bansal, P., "Evaporating heat transfer and pressure drop of hydrocarbon refrigerants in 9.52 and 12.70 mm smooth tube," *International Journal of Heat and Mass Transfer*, vol. 48 (12), 2351–2359, 2005. DOI: 10.1016/J.IJHEATMASSTRANSFER.2005.01.012.

[105] Wang, S., Gong, M. Q., Chen, G. F., Sun, Z. H., and Wu, J. F., "Two-phase heat transfer and pressure drop of propane during saturated flow boiling inside a horizontal tube," *International Journal of Refrigeration*, vol. 41, 200–209, 2014. DOI: 10.1016/J.IJREFRIG.2013.03.019.

[106] Thome, J. R., Cheng, L., Ribatski, G., and Vales, L. F., "Flow boiling of ammonia and hydrocarbons: A state-of-the-art review," *International Journal of Refrigeration*, vol. 31 (4), 603–620, 2008. DOI: 10.1016/J.IJREFRIG.2007.11.010.

[107] Steiner, D. and Taborek, J., "Flow boiling heat transfer in vertical tubes correlated by an asymptotic model," *Heat Transfer Engineering*, vol. 13 (2), 43–69, 1992. DOI: 10.1080/01457639208939774.

[108] Balachander, P., Raja, B., and Lal, D. M., "Evaporative heat transfer characteristics of R404a and R134a under varied heat flux conditions," *Experimental Heat Transfer*, vol. 25, 254–265, 2012. DOI: 10.1080/08916152.2011.623820.

[109] Zhang, L., Fan, L., Hua, M., Zhu, Z., Wu, Y., Yu, Z., Hu, Y., Fan, J., and Cen, K., "An indoor experimental investigation of the thermal performance of a TPLT-based natural circulation steam generator as applied to PTC systems," *Applied Thermal Engineering*, vol. 62 (2), 330–340, 2014. DOI: 10.1016/J.APPLTHERMALENG.2013.09.045.

[110] Passos, J. C., Kuser, V. F., Haberschill, P., and Lallemand, M., "Convective boiling of R-407c inside horizontal microfin and plain tubes," *Experimental Thermal and Fluid Science*, vol. 27 (6), 705–713, 2003. DOI: 10.1016/S0894-1777(02)00308-4.

[111] Jung, D. S., McLinden, M., and Radermacher, R., "Measurement techniques for horizontal flow boiling heat transfer with pure and mixed refrigerants," *Experimental Heat Transfer*, vol. 2 (3), 237–255, 1989. DOI: 10.1080/08916158908946367.

[112] Cho, K. and Tae, S. J., "Condensation heat transfer for R-22 and R-407C refrigerant-oil mixtures in a microfin tube with a U-bend," *International Journal of Heat and Mass Transfer*, vol. 44 (11), 2043–2051, 2001. DOI: 10.1016/S0017-9310(00)00253-2.

[113] Shin, J. Y., Kim, M. S., and Ro, S. T., "Experimental study on forced convective boiling heat transfer of pure refrigerants and refrigerant mixtures in a horizontal tube," *International Journal of Refrigeration*, vol. 20 (4), 267–275, 1997. DOI: 10.1016/S0140-7007(97)00004-2.

[114] Landelle, A., Tauveron, N., Haberschill, P., Revellin, R., and Colasson, S., "Organic Rankine cycle design and performance comparison based on experimental database," *Applied Energy*, vol. 204, 1172–1187, 2017. DOI: 10.1016/j.apenergy.2017.04.012.

[115] Charnay, R., Revellin, R., and Bonjour, J., "Flow pattern characterization for R-245fa in minichannels: Optical measurement technique and experimental results," *International Journal of Multiphase Flow*, vol. 57, 169–181, 2013. DOI: 10.1016/j.ijmultiphaseflow.2013.05.015.

[116] Tibiriçá, C. B., Ribatski, G., and Tibiri, C. B., "Two-phase frictional pressure drop and flow boiling heat transfer for R245fa in a 2.32-mm tube," *Heat Transfer Engineering*, vol. 32 (13=14), 1139–1149, 2011. DOI: 10.1080/01457632.2011.562725.

[117] Kanizawa, F. T., Tibiriçá, C. B., and Ribatski, G., "Heat transfer during convective boiling inside microchannels," *International Journal of Heat and Mass Transfer*, vol. 93, 566–583, 2016. DOI: 10.1016/j.ijheatmasstransfer.2015.09.083.

[118] Huang, H. and Thome, J. R., "Local measurements and a new flow pattern based model for subcooled and saturated flow boiling heat transfer in multi-microchannel evaporators," *International Journal of Heat and Mass Transfer*, vol. 103, 701–714, 2016. DOI: 10.1016/j.ijheatmasstransfer.2016.07.074.

[119] Pike-Wilson, E. A. and Karayiannis, T. G., "Flow boiling of R245fa in 1.1mm diameter stainless steel, brass and copper tubes," *Experimental Thermal and Fluid Science*, vol. 59, 166–183, 2014. DOI: 10.1016/j.expthermflusci.2014.02.024.

[120] Liu, S., Dai, B., Zhang, W., and Li, X., "Experimental study on R245fa condensation heat transfer properties in horizontal tube," *Energy Procedia*, vol. 104, 419–424, 2016. DOI: 10.1016/j.egypro.2016.12.071.

[121] Kedzierski, M. A., Carr, M. A., and Brown, J. S., "Measurement and prediction of vapor-space condensation of refrigerants on trapezoidal-finned and turbo-C geometries," *Journal of Enhanced Heat Transfer*, vol. 20 (1), 59–71, 2013. DOI: 10.1615/JEnhHeatTransf.2013006779.

[122] Jung, D. S., Mclinden, M., Radermachert, R., and Didion, D., "Horizontal flow boiling heat transfer experiments with a mixture of R22 / R114," *International Journal of Heat and Mass Transfer*, vol. 32 (1), 131–145, 1989.

[123] Jung, D. S., McLinden, M., Radermacher, R., and Didion, D., "A study of flow boiling heat transfer with refrigerant mixtures," *International Journal of Heat and Mass Transfer*, vol. 32 (9), 1751–1764, 1989. DOI: 10.1016/0017-9310(89)90057-4.

[124] Wang, C.-c. and Chiang, C.-s., "Two-phase heat transfer characteristics for R-22/R-407C in a 6.5-mm smooth tube," *International Journal of Heat and Fluid Flow*, vol. 18 (6), 550–558, 1997. DOI: 10.1016/S0142-727X(97)00017-9.

[125] Choi, T. Y., Kim, Y. J., Kim, M. S., and Ro, S. T., "Evaporation heat transfer of R-32, R-134a, R-32/134a, and R-32/125/134a inside a horizontal smooth tube," *International Journal of Heat and Mass Transfer*, vol. 43 (19), 3651–3660, 2000. DOI: 10.1016/S0017-9310(00)00005-3.

[126] Boissieux, X., Heikal, M. R., and Johns, R. A., "Two-phase heat transfer coefficients of three HFC refrigerants inside a horizontal smooth tube, part I: evaporation," *International Journal of Refrigeration*, vol. 23 (4), 269–283, 2000. DOI: 10.1016/S0140-7007(99)00056-0.

[127] Bandarra Filho, E. P., Saiz Jabardo, J. M., da Silva Lima, C. U., Bandarra, E. P., Saiz, J. M., and Silva, C. U. da, "Heat transfer under convective boiling of refrigerants R-404A and R-407C in a horizontal copper tube electrically heated," *International Refrigeration and Air Conditioning Conference*, 25–32, 2000.

[128] Greco, A., "Convective boiling of pure and mixed refrigerants: An experimental study of the major parameters affecting heat transfer," *International Journal of Heat and Mass Transfer*, vol. 51 (3-4), 896–909, 2008. DOI: 10.1016/J.IJHEATMASSTRANSFER.2007.11.002.

[129] Del Col, D., "Flow boiling of halogenated refrigerants at high saturation temperature in a horizontal smooth tube," *Experimental Thermal and Fluid Science*, vol. 34 (2), 234–245, 2010. DOI: 10.1016/J.EXPTHERMFLUSCI.2009.10.035.

[130] Qiu, J., Zhang, H., Yu, X., Qi, Y., Lou, J., and Wang, X., "Experimental investigation of flow boiling heat transfer and pressure drops characteristic of R1234ze(E), R600a, and a mixture of R1234ze(E)/R32 in a horizontal smooth tube," *Advances in Mechanical Engineering*, vol. 7 (9), 168781401560631, 2015. DOI: 10.1177/1687814015606311.

[131] Yang, Z.-Q., Chen, G.-F., Zhuang, X.-R., Song, Q.-L., Deng, Z., Shen, J., and Gong, M.-Q., "A new flow pattern map for flow boiling of R1234ze(E) in a horizontal tube," *International Journal of Multiphase Flow*, vol. 98, 24–35, 2018. DOI: 10.1016/J.IJMULTIPHASEFLOW.2017.08.015.

[132] Dorao, C. A., Fernandez, O. B., and Fernandino, M., "Experimental study of horizontal flow boiling heat transfer of R134a at a saturation temperature of 18.6 °C," *Journal of Heat Transfer*, vol. 139 (11), 111510, 2017. DOI: 10.1115/1.4037153.

[133] Celen, A. and Dalkılıç, A. S., "A complete evaluation method for the experimental data of flow boiling in smooth tubes," *International Communications in Heat and Mass Transfer*, vol. 89, 108–121, 2017. DOI: 10.1016/j.icheatmasstransfer.2017.09.024.

[134] Garcia Pabon, J., Khosravi, A., Nunes, R., and Machado, L., "Experimental investigation of pressure drop during two-phase flow of R1234yf in smooth horizontal tubes with internal diameters of 3.2 mm to 8.0 mm," *International Journal of Refrigeration*, vol. 104, 426–436, 2019. DOI: 10.1016/j.ijrefrig.2019.05.019.

[135] Wang, D., Zhao, L., Nie, X., Lu, Y., and Deng, S., "Experimental study on flow boiling characteristics of R-245fa in circular tube under non-uniform heat flux," *International Journal of Heat and Mass Transfer*, vol. 143, 118570, 2019. DOI: 10.1016/j.ijheatmasstransfer.2019.118570.

[136] Lillo, G., Mastrullo, R., Mauro, A. W., and Viscito, L., "Flow boiling of R32 in a horizontal stainless steel tube with 6.00 mm ID. Experiments, assessment of correlations and comparison with refrigerant R410A," *International Journal of Refrigeration*, vol. 97, 143–156, 2019. DOI: 10.1016/j.ijrefrig.2018.09.024.

[137] Liu, J., Liu, J., and Xu, X., "Diabatic visualization study of R245fa two phase flow pattern characteristics in horizontal smooth and microfin tube," *International Journal of Heat and Mass Transfer*, vol. 152, 119513, 2020. DOI: 10.1016/j.ijheatmasstransfer.2020.119513.

[138] Jassim, E. W., Newell, T. A., and Chato, J. C., "Probabilistic determination of two-phase flow regimes in horizontal tubes utilizing an automated image recognition technique," *Experiments in Fluids*, vol. 42 (4), 563–573, 2007. DOI: 10.1007/s00348-007-0264-8.

[139] Ursenbacher, T., Wojtan, L., and Thome, J. R., "Interfacial measurements in stratified types of flow. Part I: New optical measurement technique and dry angle measurements," *International Journal of Multiphase Flow*, vol. 30 (2), 107–124, 2004. DOI: 10.1016/j.ijmultiphaseflow.2003.11.010.

[140] Estrada-Perez, C. E. and Hassan, Y. A., "PTV experiments of subcooled boiling flow through a vertical rectangular channel," *International Journal of Multiphase Flow*, vol. 36 (9), 691–706, 2010. DOI: 10.1016/J.IJMULTIPHASEFLOW.2010.05.005.

[141] Hassan, Y. A., Estrada-Perez, C. E., and Yoo, J. S., "Measurement of subcooled flow boiling using Particle Tracking Velocimetry and infrared thermographic tech-

nique," *Nuclear Engineering and Design*, vol. 268, 185–190, 2014. DOI: 10.1016/J.NUCENGDES.2013.04.044.

[142] Su, G. Y., Wang, C., Zhang, L., Seong, J. H., Kommajosyula, R., Phillips, B., and Bucci, M., "Investigation of flow boiling heat transfer and boiling crisis on a rough surface using infrared thermometry," *International Journal of Heat and Mass Transfer*, vol. 160, 120134, 2020. DOI: 10.1016/j.ijheatmasstransfer.2020.120134.

[143] Kossolapov, A., Phillips, B., and Bucci, M., "Experimental investigation of subcooled flow boiling and CHF at high pressure using high-resolution diagnostics," in *18th International Topical Meeting on Nuclear Reactor Thermal Hydraulics, NURETH 2019*, American Nuclear Society, 2019, 307–318.

[144] Duan, X., Phillips, B., McKrell, T., and Buongiorno, J., "Synchronized high-speed video, infrared thermometry, and particle image velocimetry data for validation of interface-tracking simulations of nucleate boiling phenomena," *Experimental Heat Transfer*, vol. 26 (2-3), 169–197, 2013. DOI: 10.1080/08916152.2012.736837.

[145] Voulgaropoulos, V., Aguiar, G. M., Bucci, M., and Markides, C. N., "Simultaneous laser- and infrared-based measurements of the life cycle of a vapour bubble during pool boiling," in *Advances in Heat Transfer and Thermal Engineering*, Singapore: Springer Singapore, 2021, 169–173. DOI: 10.1007/978-981-33-4765-6_31.

[146] Schubring, D., Ashwood, A. C., Shedd, T. A., and Hurlburt, E. T., "Planar laser-induced fluorescence (PLIF) measurements of liquid film thickness in annular flow. Part I: Methods and data," *International Journal of Multiphase Flow*, vol. 36 (10), 815–824, 2010. DOI: 10.1016/J.IJMULTIPHASEFLOW.2010.05.007.

[147] Seitzman, J. M., Kychakoff, G., and Hanson, R. K., "Instantaneous temperature field measurements using planar laser-induced fluorescence," *Optics Letters*, vol. 10 (9), 439, 1985. DOI: 10.1364/OL.10.000439.

[148] Crimaldi, J. P., "Planar laser induced fluorescence in aqueous flows," *Experiments in Fluids*, vol. 44 (6), 851–863, 2008. DOI: 10.1007/s00348-008-0496-2.

[149] Morgan, R. G., Markides, C. N., Zadrazil, I., and Hewitt, G. F., "Characteristics of horizontal liquid-liquid flows in a circular pipe using simultaneous high-speed laser-

induced fluorescence and particle velocimetry," *International Journal of Multiphase Flow*, vol. 49, 99–118, 2013. DOI: 10.1016/j.ijmultiphaseflow.2012.09.004.

[150] Zadrazil, I., Matar, O. K., and Markides, C. N., "An experimental characterization of downwards gas-liquid annular flow by laser-induced fluorescence: Flow regimes and film statistics," *International Journal of Multiphase Flow*, vol. 60, 87–102, 2014. DOI: 10.1016/j.ijmultiphaseflow.2013.11.008.

[151] Charogiannis, A., Zadrazil, I., and Markides, C. N., "Thermographic particle velocimetry (TPV) for simultaneous interfacial temperature and velocity measurements," *International Journal of Heat and Mass Transfer*, vol. 97, 589–595, 2016. DOI: 10.1016/j.ijheatmasstransfer.2016.02.050.

[152] Mukherjee, A., Kandlikar, S. G., and Edel, Z. J., "Numerical study of bubble growth and wall heat transfer during flow boiling in a microchannel," *International Journal of Heat and Mass Transfer*, vol. 54 (15-16), 3702–3718, 2011. DOI: 10.1016/J.IJHEATMASSTRANSFER.2011.01.030.

[153] Suh, Y., Lee, W., and Son, G., "Bubble dynamics, flow, and heat transfer during flow boiling in parallel microchannels," *Numerical Heat Transfer, Part A: Applications*, vol. 544, 390–405, 2008. DOI: 10.1080/10407780802164561.

[154] Magnini, M. and Thome, J. R., "Computational study of saturated flow boiling within a microchannel in the slug flow regime," *Journal of Heat Transfer*, vol. 138 (2), 021502, 2015. DOI: 10.1115/1.4031234.

[155] Ferrari, A., Magnini, M., and Thome, J. R., "Numerical analysis of slug flow boiling in square microchannels," *International Journal of Heat and Mass Transfer*, vol. 123, 928–944, 2018. DOI: 10.1016/J.IJHEATMASSTRANSFER.2018.03.012.

[156] Magnini, M., Beisel, A. M., Ferrari, A., and Thome, J. R., "Pore-scale analysis of the minimum liquid film thickness around elongated bubbles in confined gas-liquid flows," *Advances in Water Resources*, vol. 109, 84–93, 2017. DOI: 10.1016/j.advwatres.2017.08.020.

[157] Karayiannis, T. G. and Mahmoud, M. M., "Flow boiling in microchannels: Fundamentals and applications," *Applied Thermal Engineering*, vol. 115, 1372–1397, 2017. DOI: 10.1016/j.applthermaleng.2016.08.063.

[158] Dirker, J., Juggurnath, D., Kaya, A., Osowade, E. A., Simpson, M., Lecompte, S., Abadi, S. M. A. N. R., Voulgaropoulos, V., Adelaja, A. O., Dauhoo, M. Z., Khoodaruth, A., Obayopo, S. O., Olakoyejo, O. T., Elahee, M. K., De Paepe, M., Meyer, J. P., and Markides, C. N., "Thermal energy processes in direct steam generation solar systems: Boiling, condensation and energy storage," *Frontiers in Energy Research*, vol. 6, 147, 2019. DOI: 10.3389/fenrg.2018.00147.

[159] Bretherton, F. P., "The motion of long bubbles in tubes," *Journal of Fluid Mechanics*, vol. 10 (02), 166–188, 1961. DOI: 10.1017/S0022112061000160.

[160] Taylor, G. I., "Deposition of a viscous fluid on the wall of a tube," *Journal of Fluid Mechanics*, vol. 10 (2), 161–165, 1961. DOI: 10.1017/S0022112061000159.

[161] Aussillous, P. and Quéré, D., "Quick deposition of a fluid on the wall of a tube," *Physics of Fluids*, vol. 12 (10), 2367–2371, 2000. DOI: 10.1063/1.1289396.

[162] Kreutzer, M. T., Kapteijn, F., Moulijn, J. A., Kleijn, C. R., and Heiszwolf, J. J., "Inertial and interfacial effects on pressure drop of Taylor flow in capillaries," *AIChE Journal*, vol. 51 (9), 2428–2440, 2005. DOI: 10.1002/aic.10495.

[163] Heil, M., "Finite Reynolds number effects in the Bretherton problem," *Physics of Fluids*, vol. 13 (9), 2517–2521, 2001. DOI: 10.1063/1.1389861.

[164] Han, Y. and Shikazono, N., "Measurement of the liquid film thickness in micro tube slug flow," *International Journal of Heat and Fluid Flow*, vol. 30 (5), 842–853, 2009. DOI: 10.1016/j.ijheatfluidflow.2009.02.019.

[165] Khodaparast, S., Magnini, M., Borhani, N., and Thome, J. R., "Dynamics of isolated confined air bubbles in liquid flows through circular microchannels: an experimental and numerical study," *Microfluidics and Nanofluidics*, vol. 19, 209–234, 2015. DOI: 10.1007/s10404-015-1566-4.

[166] Magnini, M., Khodaparast, S., Matar, O. K., Stone, H. A., and Thome, J. R., "Dynamics of long gas bubbles rising in a vertical tube in a cocurrent liquid flow," *Physical Review Fluids*, vol. 4 (2), 023601, 2019. DOI: 10.1103/PhysRevFluids.4.023601.

[167] Hazel, A. L. and Heil, M., "The steady propagation of a semi-infinite bubble into a tube of elliptical or rectangular cross-section," *Journal of Fluid Mechanics*, vol. 470, 91–114, 2002. DOI: 10.1017/S0022112002001830.

[168] Jensen, M. H., Libchaber, A., Pelce, P., and Zocchi, G., "Effect of gravity on the saffman-taylor meniscus: Theory and experiments," *Physical Review A*, vol. 35 (5), 2221–2227, 1987. DOI: 10.1103/physreva.35.2221.

[169] Atasi, O., Khodaparast, S., Scheid, B., and Stone, H. A., "Effect of buoyancy on the motion of long bubbles in horizontal tubes," *Physical Review Fluids*, vol. 2 (9), 094304, 2017. DOI: 10.1103/PhysRevFluids.2.094304.

[170] Leung, S. S. Y., Gupta, R., Fletcher, D. F., and Haynes, B. S., "Gravitational effect on Taylor flow in horizontal microchannels," *Chemical Engineering Science*, vol. 69 (1), 553–564, 2012. DOI: 10.1016/J.CES.2011.11.016.

[171] Rek, Z. and Zun, I., "CFD based mini- vs. micro-system delineation in elongated bubble flow regime," *International Journal of Multiphase Flow*, vol. 59, 73–83, 2014. DOI: 10.1016/j.ijmultiphaseflow.2013.10.013.

[172] Gupta, R., Fletcher, D. F., and Haynes, B. S., "On the CFD modelling of Taylor flow in microchannels," *Chemical Engineering Science*, vol. 64 (12), 2941–2950, 2009. DOI: 10.1016/J.CES.2009.03.018.

[173] Fukagata, K., Ua-arayaporn, P., and Himeno, T., "Numerical simulation of gas–liquid two-phase flow and convective heat transfer in a micro tube," *International Journal of Heat and Fluid Flow*, vol. 28 (1), 72–82, 2007. DOI: 10.1016/J.IJHEATFLUIDFLOW.2006.04.010.

[174] Lakehal, D., Larrignon, G., and Narayanan, C., "Computational heat transfer and two-phase flow topology in miniature tubes," *Microfluidics and Nanofluidics*, vol. 4 (4), 261–271, 2008. DOI: 10.1007/s10404-007-0176-1.

[175] Gupta, R., Fletcher, D. F., and Haynes, B. S., "CFD modelling of flow and heat transfer in the Taylor flow regime," *Chemical Engineering Science*, vol. 65 (6), 2094–2107, 2010. DOI: 10.1016/J.CES.2009.12.008.

[176] He, Q., Hasegawa, Y., and Kasagi, N., "Heat transfer modelling of gas–liquid slug flow without phase change in a micro tube," *International Journal of Heat and Fluid Flow*, vol. 31 (1), 126–136, 2010. DOI: 10.1016/J.IJHEATFLUIDFLOW.2009.11.004.

[177] Mukherjee, A. and Kandlikar, S. G., "Numerical simulation of growth of a vapor bubble during flow boiling of water in a microchannel," *Microfluidics and Nanofluidics*, vol. 1 (2), 137–145, 2005. DOI: 10.1007/s10404-004-0021-8.

[178] Mukherjee, A., "Contribution of thin-film evaporation during flow boiling inside microchannels," *International Journal of Thermal Sciences*, vol. 48 (11), 2025–2035, 2009. DOI: 10.1016/J.IJTHERMALSCI.2009.03.006.

[179] Magnini, M., "CFD Modeling of Two-Phase Boiling Flows in the Slug Flow Regime with an Interface Capturing Technique," Ph.D. dissertation, Università di Bologna, 2012.

[180] Magnini, M., Pulvirenti, B., and Thome, J., "Numerical investigation of hydrodynamics and heat transfer of elongated bubbles during flow boiling in a microchannel," *International Journal of Heat and Mass Transfer*, vol. 59, 451–471, 2013. DOI: 10.1016/J.IJHEATMASSTRANSFER.2012.12.010.

[181] Hardt, S. and Wondra, F., "Evaporation model for interfacial flows based on a continuum-field representation of the source terms," *Journal of Computational Physics*, vol. 227 (11), 5871–5895, 2008. DOI: 10.1016/j.jcp.2008.02.020.

[182] Scriven, L. E., "On the dynamics of phase growth," *Chemical Engineering Science*, vol. 10 (1-2), 1–13, 1959. DOI: 10.1016/0009-2509(59)80019-1.

[183] Magnini, M. and Matar, O. K., "Numerical study of the impact of the channel shape on microchannel boiling heat transfer," *International Journal of Heat and Mass Transfer*, vol. 150, 119322, 2020. DOI: 10.1016/j.ijheatmasstransfer.2020.119322.

[184] Eck, M. and Steinmann, W.-D., "Modelling and design of direct solar steam generating collector fields," *Journal of Solar Energy Engineering*, vol. 127 (3), 371, 2005. DOI: 10.1115/1.1849225.

[185] Zarza, E., Valenzuela, L., León, J., Weyers, H.-D., Eickhoff, M., Eck, M., and Hennecke, K., "The DISS Project: Direct steam generation in parabolic trough systems. Operation and maintenance experience and update on project status," *Journal of Solar Energy Engineering*, vol. 124 (2), 126, 2002. DOI: 10.1115/1.1467645.

[186] Rodriguez-Sanchez, D. and Rosengarten, G., "Improving the concentration ratio of parabolic troughs using a second-stage flat mirror," *Applied Energy*, vol. 159, 620–632, 2015. DOI: 10.1016/j.apenergy.2015.08.106.

[187] Wright, S. F., Zadrazil, I., and Markides, C. N., "A review of solid–fluid selection options for optical-based measurements in single-phase liquid, two-phase liquid–liquid and multiphase solid–liquid flows," *Experiments in Fluids*, vol. 58 (9), 1–39, 2017. DOI: 10.1007/s00348-017-2386-y.

[188] Morgan, R. G., Ibarra, R., Zadrazil, I., Matar, O. K., Hewitt, G. F., and Markides, C. N., "On the role of buoyancy-driven instabilities in horizontal liquid–liquid flow," *International Journal of Multiphase Flow*, vol. 89, 123–135, 2017. DOI: 10.1016/j.ijmultiphaseflow.2016.07.009.

[189] Bell, I. H., Wronski, J., Quoilin, S., and Lemort, V., "Pure and pseudo-pure fluid thermophysical property evaluation and the open-source thermophysical property library coolprop," *Industrial & Engineering Chemistry Research*, vol. 53 (6), 2498–2508, 2014. DOI: 10.1021/ie4033999. eprint: http://pubs.acs.org/doi/pdf/10.1021/ie4033999.

[190] Moffat, R. J., "Describing the uncertainties in experimental results," *Experimental Thermal and Fluid Science*, vol. 1 (1), 3–17, 1988. DOI: 10.1016/0894-1777(88)90043-X.

[191] C. Tropea, A. L. Yarin, and J. F. Foss, Eds., Springer Handbook of Experimental Fluid Mechanics. Springer Berlin Heidelberg, 2007. DOI: 10.1007/978-3-540-30299-5.

[192] Hudaya, A. Z., Widyatama, A., Dinaryanto, O., Juwana, W. E., Indarto, and Deendarlianto, "The liquid wave characteristics during the transportation of air-water stratified co-current two-phase flow in a horizontal pipe," *Experimental Thermal and Fluid Science*, vol. 103, 304–317, 2019. DOI: 10.1016/j.expthermflusci.2019.01.021.

[193] Alekseenko, S. V., Cherdantsev, A. V., Heinz, O. M., Kharlamov, S. M., and Markovich, D. M., "Analysis of spatial and temporal evolution of disturbance waves and ripples in annular gas-liquid flow," *International Journal of Multiphase Flow*, vol. 67 (S), 122–134, 2014. DOI: 10.1016/j.ijmultiphaseflow.2014.07.009.

[194] Alekseenko, S., Cherdantsev, A., Heinz, O., Kharlamov, S., and Markovich, D., "Analysis of spatial and temporal spectra of liquid film surface in annular gas-liquid flow," *Experiments in Fluids*, vol. 54 (9), 1–12, 2013. DOI: 10.1007/s00348-013-1590-7.

[195] Alekseenko, S., Cherdantsev, A., Cherdantsev, M., Isaenkov, S., Kharlamov, S., and Markovich, D., "Application of a high-speed laser-induced fluorescence technique for studying the three-dimensional structure of annular gas-liquid flow," *Experiments in Fluids*, vol. 53 (1), 77–89, 2012. DOI: 10.1007/s00348-011-1200-5.

[196] Cherdantsev, A. V., Hann, D. B., and Azzopardi, B. J., "Study of gas-sheared liquid film in horizontal rectangular duct using high-speed LIF technique: Three-dimensional wavy structure and its relation to liquid entrainment," *International Journal of Multiphase Flow*, vol. 67, 52–64, 2014. DOI: 10.1016/j.ijmultiphaseflow.2014.08.003.

[197] Fritz, W., "Maximum volume of vapor bubbles," *Phyische. Zeitschrift [German]*, vol. 11, 379, 1935.

[198] Hamzekhani, S., Maniavi Falahieh, M., and Akbari, A., "Bubble departure diameter in nucleate pool boiling at saturation: Pure liquids and binary mixtures," *International Journal of Refrigeration*, vol. 46, 50–58, 2014. DOI: 10.1016/J.IJREFRIG.2014.07.003.

[199] Chae, H. B., Schmidt, J. W., and Moldover, M. R., "Alternative refrigerants R123a, R134, R141 b, R142b, and R152a: Critical temperature, refractive index, surface tension, and estimates of liquid, vapor, and critical densities," *Journal of Physical Chemistry*, vol. 94, 8840–8845, 1990. DOI: 10.1021/j100388a018.

[200] Cachadiña, I., Mulero, A., and Tian, J., "Surface tension of refrigerants: A new correlation using the boiling point as reference," *Fluid Phase Equilibria*, vol. 442, 68–80, 2017. DOI: 10.1016/j.fluid.2017.03.017.

[201] Schmidt, J. W., Carillo-Nava, E., and Moldover, M. R., "Partially halogenated hydrocarbons CHFCl-CF3, CF3-CH3, CF3-CHF-CHF2, CF3-CH2-CF3, CHF2-CF2-CH2F, CF3-CH2-CHF2, CF3-0-CHF2: critical temperature, refractive indices, surface tension and estimates of liquid, vapor and critical densities," *Fluid Phase Equilibria*, vol. 122 (1-2), 187–206, 1996. DOI: 10.1016/0378-3812(96)03044-0.

[202] ASHRAE, "Thermophysical Properties of Refrigerants," in *2009 ASHRAE Handbook-Fundamentals (SI)*, vol. 718, 2009, ch. 30, 30.1–30.75. DOI: 10.1007/978-3-662-02608-3.

[203] Meyer, J. P., Everts, M., Coetzee, N., Grote, K., and Steyn, M., "Heat transfer coefficients of laminar, transitional, quasi-turbulent and turbulent flow in circular tubes," *International Communications in Heat and Mass Transfer*, vol. 105, 84–106, 2019. DOI: 10.1016/j.icheatmasstransfer.2019.03.016.

[204] Deshpande, S. S., Anumolu, L., and Trujillo, M. F., "Evaluating the performance of the two-phase flow solver interfoam," *Computational Science & Discovery*, vol. 5 (1), 014016, 2012. DOI: 10.1088/1749-4699/5/1/014016.

[205] Brackbill, J. U., Kothe, D. B., and Zemach, C., "A continuum method for modeling surface tension," *Journal of Computational Physics*, vol. 100 (2), 335–354, 1992. DOI: 10.1016/0021-9991(92)90240-Y.

[206] Ferrari, A., Magnini, M., and Thome, J. R., "A flexible Coupled Level Set and Volume of Fluid (flexCLV) method to simulate microscale two-phase flow in non-uniform and unstructured meshes," *International Journal of Multiphase Flow*, vol. 91, 276–295, 2017. DOI: 10.1016/J.IJMULTIPHASEFLOW.2017.01.017.

[207] Issa, R. I., "Solution of the implicitly discretised fluid flow equations by operator-splitting," *Journal of Computational Physics*, vol. 62 (1), 40–65, 1986. DOI: 10.1016/0021-9991(86)90099-9.

[208] Magnini, M., Ferrari, A., Thome, J. R., and Stone, H. A., "Undulations on the surface of elongated bubbles in confined gas-liquid flows," *Physical Review Fluids*, vol. 2 (8), 084001, 2017. DOI: 10.1103/PhysRevFluids.2.084001.

[209] Schrage, R. W., A Theoretical Study of Interphase Mass Transfer. Columbia University Press, 1953. DOI: 10.7312/schr90162.

[210] Tanasawa, I., "Advances in condensation heat transfer," in, ser. Advances in Heat Transfer, J. P. Hartnett, T. F. Irvine, and Y. I. Cho, Eds., vol. 21, Elsevier, 1991, 55–139. DOI: 10.1016/S0065-2717(08)70334-4.

[211] Kunkelmann, C., "Numerical Modeling and Investigation of Boiling Phenomena," Ph.D Thesis, Technische Universität Darmstadt, 2011.

[212] Moran, H. R., Zogg, D., Voulgaropoulos, V., Van den Bergh, W. J., Dirker, J., Meyer, J. P., Matar, O. K., and Markides, C. N., "An experimental study of the thermohydraulic characteristics of flow boiling in horizontal pipes: Linking spatiotemporally resolved and integral measurements," *Applied Thermal Engineering*, 117085, 2021. DOI: 10.1016/j.applthermaleng.2021.117085.

[213] Billiet, M., Ameel, B., Charnay, R., Revellin, R., and De Paepe, M., "Flow regime based heat transfer correlation for R245fa in a 3 mm tube," *International Journal of Heat and Mass Transfer*, vol. 117, 1304–1311, 2018. DOI: 10.1016/J.IJHEATMASSTRANSFER.2017.10.062.

[214] Kew, P. A. and Cornwell, K., "Correlations for the prediction of boiling heat transfer in small-diameter channels," *Applied Thermal Engineering*, vol. 17 (8-10), 705–715, 1997. DOI: 10.1016/s1359-4311(96)00071-3.

[215] Shao, J., Li, X., Guo, Z., Ma, T., Liu, R., and Tian, X., "Flow pattern, pressure drop and heat transfer coefficient during two-phase flow boiling of R134a in pump-assisted separate heat pipe," *Experimental Thermal and Fluid Science*, vol. 85, 240–247, 2017. DOI: 10.1016/j.expthermflusci.2017.03.007.

[216] Tribbe, C. and Müller-Steinhagen, H. M., "An evaluation of the performance of phenomenological models for predicting pressure gradient during gas-liquid flow in horizontal pipelines," *International Journal of Multiphase Flow*, vol. 26 (6), 1019–1036, 2000. DOI: 10.1016/S0301-9322(99)00070-1.

[217] Lee, H.-S., Yoon, J.-I., Kim, J.-D., and Bansal, P. K., "Characteristics of condensing and evaporating heat transfer using hydrocarbon refrigerants," *Applied Thermal Engineering*, vol. 26 (10), 1054–1062, 2006. DOI: 10.1016/J.APPLTHERMALENG.2005.10.002.

[218] Fang, X., Zhuang, F., Chen, C., Wu, Q., Chen, Y., Chen, Y., and He, Y., "Saturated flow boiling heat transfer: review and assessment of prediction methods," *Heat and Mass Transfer*, vol. 55, 197–222, 2019. DOI: 10.1007/s00231-018-2432-1.

[219] Yiantsios, S. G. and Higgins, B. G., "Linear stability of plane Poiseuille flow of two superposed fluids.," *Physics of Fluids*, vol. 31 (11 , Nov. 1988), 3225–3238, 1988. DOI: 10.1063/1.866933.

[220] Yao, W., Bestion, D., Coste, P., and Boucker, M., "A three-dimensional two-fluid modeling of stratified flow with condensation for pressurized thermal shock investigations," *Nuclear Technology*, vol. 152 (1), 129–142, 2005. DOI: 10.13182/NT05-A3665.

[221] Morgan, R. G., "Studies of Liquid-Liquid Two-Phase Flows Using Laser-Based Methods," Ph.D. dissertation, Imperial College London, 2012.

[222] Markides, C. N., Mathie, R., and Charogiannis, A., "An experimental study of spatiotemporally resolved heat transfer in thin liquid-film flows falling over an inclined heated foil," *International Journal of Heat and Mass Transfer*, vol. 93, 872–888, 2016. DOI: 10.1016/j.ijheatmasstransfer.2015.10.062.

[223] Mathie, R., Nakamura, H., and Markides, C. N., "Heat transfer augmentation in unsteady conjugate thermal systems - Part II: Applications," *International Journal of Heat and Mass Transfer*, vol. 56 (1-2), 819–833, 2013. DOI: 10.1016/j.ijheatmasstransfer.2012.09.017.

[224] Schagen, A., Modigell, M., Dietze, G., and Kneer, R., "Simultaneous measurement of local film thickness and temperature distribution in wavy liquid films using a luminescence technique," *International Journal of Heat and Mass Transfer*, vol. 49 (25-26), 5049–5061, 2006. DOI: 10.1016/j.ijheatmasstransfer.2006.06.010.

[225] Schagen, A. and Modigell, M., "Local film thickness and temperature distribution measurement in wavy liquid films with a laser-induced luminescence technique," *Experiments in Fluids*, vol. 43 (2-3), 209–221, 2007. DOI: 10.1007/s00348-007-0289-z.

[226] Birvalski, M., Tummers, M. J., Delfos, R., and Henkes, R. A., "PIV measurements of waves and turbulence in stratified horizontal two-phase pipe flow," *International Journal of Multiphase Flow*, vol. 62, 161–173, 2014. DOI: 10.1016/j.ijmultiphaseflow.2014.03.001.

[227] Ayati, A. A., Kolaas, J., Jensen, A., and Johnson, G. W., "A PIV investigation of stratified gas-liquid flow in a horizontal pipe," *International Journal of Multiphase Flow*, vol. 61, 129–143, 2014. DOI: 10.1016/j.ijmultiphaseflow.2014.01.008.

[228] Lee, S., Euh, D. J., Kim, S., and Song, C. H., "Quantitative observation of co-current stratified two-phase flow in a horizontal rectangular channel," *Nuclear Engineering and Technology*, vol. 47 (3), 267–283, 2015. DOI: 10.1016/j.net.2014.11.007.

[229] Denner, F., Charogiannis, A., Pradas, M., Markides, C. N., Van Wachem, B. G., and Kalliadasis, S., "Solitary waves on falling liquid films in the inertia-dominated regime," *Journal of Fluid Mechanics*, vol. 837, 491–519, 2018. DOI: 10.1017/jfm.2017.867.

[230] Xu, K. W., Zhang, Y., Liu, D., Azman, A. N., and Kim, H. B., "Slug flow development study in a horizontal pipe using particle image velocimetry," *International Journal of Heat and Mass Transfer*, vol. 162, 120267, 2020. DOI: 10.1016/j.ijheatmasstransfer.2020.120267.

[231] Czapp, M., Utschick, M., Rutzmoser, J., and Sattelmayer, T., "Investigations on slug flow in a horizontal pipe using stereoscopic particle image velocimetry and CFD simulation with volume of fluid method," in *International Conference on Nuclear Engineering, Proceedings, ICONE*, vol. 3, American Society of Mechanical Engineers (ASME), 2012, 477–486. DOI: 10.1115/ICONE20-POWER2012-54591.

[232] Frank, T., "Numerical simulation of slug flow regime for an air-water two-phase flow in horizontal pipes," in *International Topical Meeting on Nuclear Reactor Thermal Hydraulics*, Avignon, France, 2005, 1–13.

[233] Pineda-Pérez, H., Kim, T., Pereyra, E., and Ratkovich, N., "CFD modeling of air and highly viscous liquid two-phase slug flow in horizontal pipes," *Chemical Engineering Research and Design*, vol. 136, 638–653, 2018. DOI: 10.1016/j.cherd.2018.06.023.

[234] Dukler, A. E. and Hubbard, M. G., "A model for gas-liquid slug flow in horizontal and near horizontal tubes," *Industrial and Engineering Chemistry Fundamentals*, vol. 14 (4), 337–347, 1975. DOI: 10.1021/i160056a011.

[235] Gregory, G. A. and Scott, D. S., "Correlation of liquid slug velocity and frequency in horizontal cocurrent gas-liquid slug flow," *AIChE Journal*, vol. 15 (6), 933–935, 1969. DOI: 10.1002/aic.690150623.

[236] Al-Safran, E. M., "Probabilistic modeling of slug frequency in gas/liquid pipe flow using the Poisson probability theory," *Journal of Petroleum Science and Engineering*, vol. 138, 88–96, 2016. DOI: 10.1016/j.petrol.2015.12.008.

[237] Schmidt, J., Giesbrecht, H., and Geld, C. W. van der, "Phase and velocity distributions in vertically upward high-viscosity two-phase flow," *International Journal of Multiphase Flow*, vol. 34 (4), 363–374, 2008. DOI: 10.1016/j.ijmultiphaseflow.2007.10.013.

[238] Al-Safran, E., "Investigation and prediction of slug frequency in gas/liquid horizontal pipe flow," *Journal of Petroleum Science and Engineering*, vol. 69 (1-2), 143–155, 2009. DOI: 10.1016/j.petrol.2009.08.009.

[239] Nicklin, D. J., Wilkes, J. O., and Davidson, J. F., "Two-phase flow in vertical tubes," *Transactions of the Institution of Chemical Engineers*, vol. 40 (1), 61–68, 1962.

[240] Setyawan, A., Indarto, and Deendarlianto, "Experimental investigations of the circumferential liquid film distribution of air-water annular two-phase flow in a horizontal pipe," *Experimental Thermal and Fluid Science*, vol. 85, 95–118, 2017. DOI: 10.1016/j.expthermflusci.2017.02.026.

[241] Voulgaropoulos, V., Patapas, A., Lecompte, S., Charogiannis, A., Matar, O. K., De Paepe, M., and Markides, C. N., "Simultaneous laser-induced fluorescence and capacitance probe measurement of downwards annular gas-liquid flows," *International Journal of Multiphase Flow*, vol. 142, 103665, 2021. DOI: 10.1016/j.ijmultiphaseflow.2021.103665.

[242] Moran, H. R., Magnini, M., Markides, C. N., and Matar, O. K., "Inertial and buoyancy effects on the flow of elongated bubbles in horizontal channels," *International Journal of Multiphase Flow*, vol. 135, 103468, 2021. DOI: 10.1016/j.ijmultiphaseflow.2020.103468.

[243] de Lózar, A., Juel, A., and Hazel, A. L., "The steady propagation of an air finger into a rectangular tube," *Journal of Fluid Mechanics*, vol. 614, 173–195, 2008. DOI: 10.1017/S0022112008003455.

[244] Wong, H., Radke, C. J., and Morris, S., "The motion of long bubbles in polygonal capillaries. Part 1. Thin films," *Journal of Fluid Mechanics*, vol. 292, 71–94, 1995. DOI: 10.1017/S0022112095001443.

[245] Magnini, M. and Matar, O. K., "Morphology of long gas bubbles propagating in square capillaries," *International Journal of Multiphase Flow*, vol. 120, 103353, 2020. DOI: 10.1016/j.ijmultiphaseflow.2020.103353.

[246] Thome, J. R., Dupont, V., and Jacobi, A. M., "Heat transfer model for evaporation in microchannels. Part I: Presentation of the model," *International Journal of Heat and Mass Transfer*, vol. 47 (14-16), 3375–3385, 2004. DOI: 10.1016/j.ijheatmasstransfer.2004.01.006.

[247] Paul, B., "Compilation of evaporation coefficients," *American Rocket Society Journal*, vol. 32 (9), 1321–1328, 1962. DOI: 10.2514/8.6277.

[248] Marek, R. and Straub, J., "Analysis of the evaporation coefficient and the condensation coefficient of water," *International Journal of Heat and Mass Transfer*, vol. 44 (1), 39–53, 2001. DOI: 10.1016/S0017-9310(00)00086-7.

[249] Markides, C. N., "Autoignition in turbulent flows," Ph.D. Thesis, University of Cambridge, 2005.

[250] Fotache, C. G., Kreutz, T. G., Zhu, D. L., and Law, C. K., "An experimental study of ignition in nonpremixed counterflowing hydrogen versus heated air," *Combustion Science and Technology*, vol. 109 (1-6), 373–393, 1995. DOI: 10.1080/00102209508951910.

[251] Collis, D. C. and Williams, M. J., "Two-dimensional convection from heated wires at low Reynolds numbers," *Journal of Fluid Mechanics*, vol. 6 (3), 357–384, 1959. DOI: 10.1017/S0022112059000696.

[252] Mastorakos, E., "Turbulent combustion in opposed jet flows," Ph.D. Thesis, Imperial College London, 1993.

[253] Maranzana, G., Perry, I., and Maillet, D., "Mini- and micro-channels: Influence of axial conduction in the walls," *International Journal of Heat and Mass Transfer*, vol. 47 (17-18), 3993–4004, 2004. DOI: 10.1016/j.ijheatmasstransfer.2004.04.016.

Appendix A

Temperature Measurement Corrections and Calculations

A.1 Thermocouple response times

A thermocouple measures the temperature of its immediate environment, but when this temperature changes, the temperature of the thermocouple itself must also change for it to identify this. There is thus a time constant associated with the response time of a thermocouple, i.e. the time delay between the environmental temperature changing and this change being detected in the thermocouple output signal. This time constant determines what temporal variations in the temperature measurement can be considered significant and physical.

The method described by Markides [249] was used to estimate the time constants, τ, associated with the thermocouples in the facility. In these experiments the Biot number, $\mathrm{Bi} = (\mathrm{Nu}/2)(k_{\mathrm{fluid}}/k_{\mathrm{metal}})$, where Nu is the Nusselt number and k_{fluid}, k_{metal} are the thermal conductivities of the fluid and thermocouple metal respectively, obeys $\mathrm{Bi} \leq\sim 10^{-2}$. This satisfies the condition $\mathrm{Bi} \ll 1$, allowing the assumption of temperature uniformity in the thermocouple bead [250]. Since the experimental temperatures are not high ($T_{\mathrm{exp,max}} = 55\,^{\circ}\mathrm{C}$), radiative heat transfer can be neglected in comparison to the convective and conductive contributions and the overall time constant of the thermocouple wire is:

$$\tau_{\mathrm{wire}} = \tau_{\mathrm{conv}} \left[1 + \frac{4\epsilon\sigma_{\mathrm{SB}} T_{\mathrm{wire}}^3 d_{\mathrm{wire}}}{k_{\mathrm{fluid}} \mathrm{Nu}} \right]^{-1} \tag{A.1}$$

where τ_{conv} is the convective time constant, ϵ is the emissivity of the thermocouple wire, and σ_{SB} is the Stefan-Boltzmann constant. The empirical relation proposed by Collis and Williams [251] for forced-convective heat transfer from the wire gives:

$$\text{Nu} = 0.24 + 0.56\text{Re}_{\text{wire}}^{0.45} \tag{A.2}$$

and this value of Nu was also used to calculate τ_{conv} according to the method described by Mastorakos [252]:

$$\tau_{\text{conv}} = \frac{\rho_{\text{wire}} c_{p,\text{wire}} d_{\text{wire}}^2}{4 k_{\text{fluid}} \text{Nu}} \tag{A.3}$$

Based on the experimental conditions and corresponding fluid parameters, the thermocouple time constants are in the range 0.2–1.1 s. This is insufficient to accurately capture the temporal behaviour of, e.g., wave or slug dynamics and as such only temporally averaged temperature based data is reported.

A.2 Thermocouple conduction errors

When using thermocouple measurements of temperature, the heat transfer along the thermocouple itself is often ignored. However, depending on the experimental conditions this heat transfer due to conduction may be non-negligible and the recorded temperature T_{raw} may not be representative of the temperature at the thermocouple tip, T_{corr}, and a correction may be required.

Markides [249] proposed that the normalized conduction correction ΔT_{cond} can be obtained from the following solution of the 1-D conduction equation:

$$\frac{\Delta T_{\text{cond}}}{T_{\text{corr}}} = \frac{T_{\text{corr}} - T_{\text{raw}}}{T_{\text{corr}}} = \frac{1 - c}{1 + g_{\text{cond}}^{-1}} \tag{A.4}$$

$$g_{\text{cond}} = \{[\cosh m L_{\text{tc}} + (\frac{h}{m k_{\text{metal}}}) \sinh m L_{\text{tc}}] - 1\}^{-1} \tag{A.5}$$

where c is a constant of proportionality defined as $c \approx T_{\text{wall}}/T_{\infty}$, which due to the small temperature range experienced by the experimental equipment is is always $\sim 10^{-1}$–10^{1}. The parameter m is defined as $m = 2\sqrt{h/(k_{\text{metal}} d_{\text{tc}})}$, where h is the heat transfer coefficient $h = (k_{\text{metal}}/d_{\text{tc}})\text{Nu}$, d_{tc} is the thermocouple diameter and L_{tc} is its immersed length.

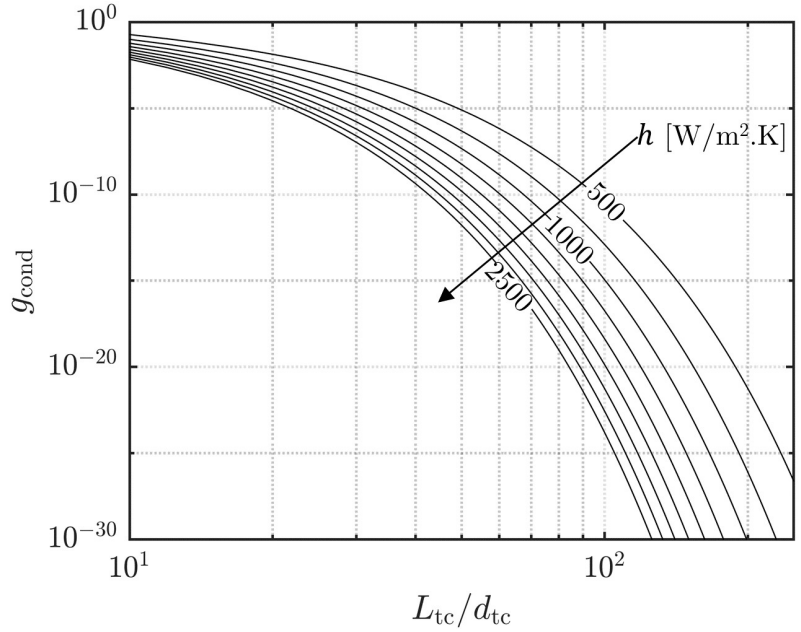


Figure A.1: Errors in raw thermocouple temperature readings due to conduction heat losses along the thermocouple wire.

From Eq. (A.2), the heat transfer coefficient to the thermocouple is estimated to be in the range $h \cong 500$–2500 W/m^2.K. Assessing g_{cond} across this range for h gives the lines plotted in Fig. A.1. The in-flow thermocouples are introduced to the flow via a long fitting, so the immersed length ratio $L_{\mathrm{tc}}/d_{\mathrm{tc}} \approx 200$. The wall thermocouples are laid along the pipe wall, so the 'immersed' length may be considered to be the contact length and $L_{\mathrm{tc}}/d_{\mathrm{tc}} \approx 250$. For these conditions, $g_{\mathrm{cond}} < 10^{-20}$ from Fig. A.1 and $\Delta T_{\mathrm{cond}}/T_{\mathrm{corr}}$ from Eq. (A.5) is vanishingly small, so conductivity errors in the thermocouple measurements may be neglected.

A.3 Calibration

All thermocouples in the facility, including in-flow and wall temperature thermocouples, were calibrated using the same method with the reference temperature provided by a digital thermometer with a 5-point UKAS calibration. The thermometer was placed in an agitated water bath with the thermocouples arranged concentrically around it with a spacing of 10 mm, as illustrated in Fig. A.2. Insulation was placed over the top of the water bath to minimise heat losses to the ambient. The temperature of the water bath was increased in 5 °C intervals from 20 °C to 70 °C, with thermocouple readings recorded for 5 min at each interval and digital thermometer readings taken every 30 s during this

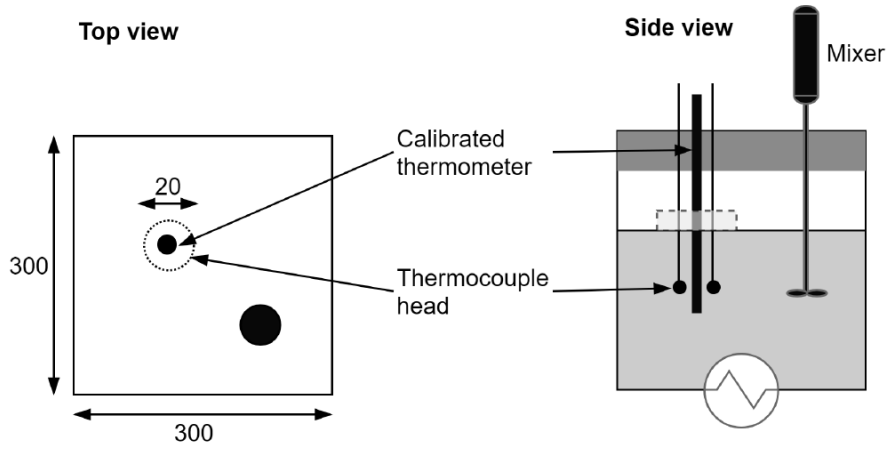


Figure A.2: Diagram of thermal bath set-up for thermocouple calibration. Measurements are in mm.

time.

The recorded thermocouple data was then fitted to the thermometer readings using linear regression and the corresponding corrections applied within the LabView interface. An example of the data and fitting for one of the thermocouples is shown in Fig. A.3. It should be noted that the fit and confidence intervals shown in this plot are calculated based on the whole calibration temperature range.

After calibration of all thermocouples in the facility, the average 95 % confidence intervals was found to be $\pm 0.25\,\mathrm{K}$.

A.4 Inside wall temperature calculation

The measured wall temperature in the experimental facility described in Section 3.2.2 is the outside wall temperature, $T_{\mathrm{w,o}}$, but the inside wall temperature, $T_{\mathrm{w,i}}$, is required for calculation of an experimental heat transfer coefficient. To find $T_{\mathrm{w,i}}$, analysis of the conjugate heat transfer between the convection/boiling in the fluid and the conduction in the pipe walls was performed.

Generally, axial conduction in the pipe walls can be neglected when the walls are thin. Maranzana et al. [253] proposed evaluation of a dimensionless axial conduction number M_{c} to determine the significance of axial conduction in the wall compared to convective heat transfer in the flow. They found that axial heat conduction in the wall could be

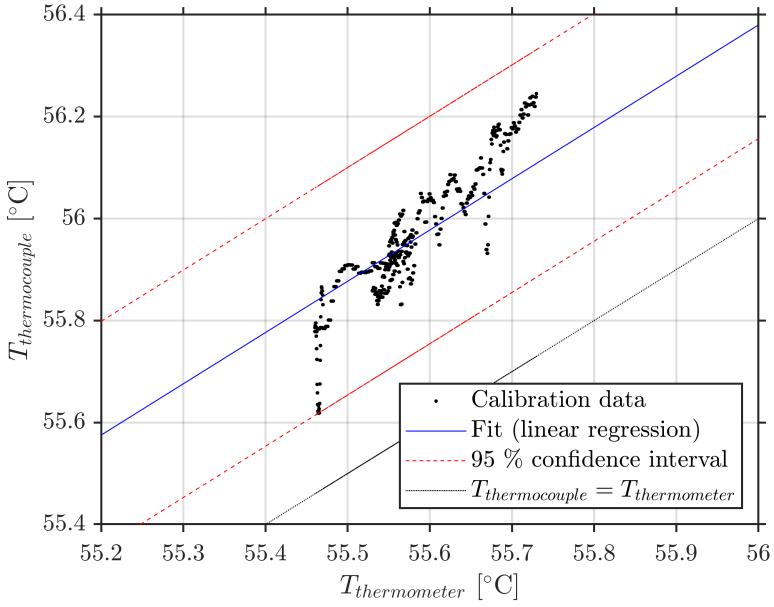


Figure A.3: Thermocouple calibration data at one recorded temperature alongside the fitted line and 95 % confidence intervals as applied to the whole calibration temperature range.

considered negligible for $M_\mathrm{c} < 0.01$, with

$$M_\mathrm{c} = \frac{4k_\mathrm{w}(d_\mathrm{o} - d_\mathrm{i})(1 + \frac{d_\mathrm{o}-d_\mathrm{i}}{d_\mathrm{i}}}{k_\mathrm{l}\mathrm{Pe}L_\mathrm{ht}} \tag{A.6}$$

where Pe is the Peclet number given by

$$Pe = \frac{ud_\mathrm{i}\rho_\mathrm{l}c_{p,\mathrm{l}}}{k_\mathrm{l}} \tag{A.7}$$

For the experimental conditions, $10^{-6} < M_\mathrm{c} < 10^{-4}$, so axial heat conduction in the pipe wall can confidently be neglected.

Then, the heat transfer must only be solved in the radial direction to determine $T_{\mathrm{w,i}}$. This was assessed by considering the control volume presented in Fig. A.4. Performing an energy balance across the control volume gives

$$Q_r + Q^{'''}\mathrm{d}V = Q_{r+\mathrm{d}r} \tag{A.8}$$

$$Q_{r+\mathrm{d}r} - Q_r = Q^{'''}\mathrm{d}V \tag{A.9}$$

$$\mathrm{d}Q = Q^{'''}\mathrm{d}V \tag{A.10}$$

By Fourier's law, $Q_r = -kA\frac{\mathrm{d}T}{\mathrm{d}r}$, and for the control volume $A = 2\pi rL$. Substituting

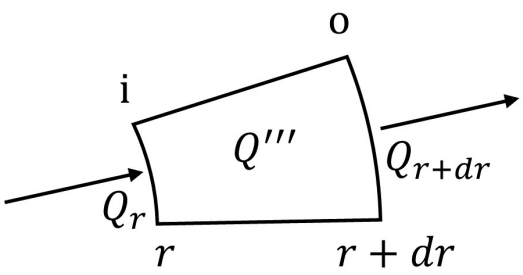


Figure A.4: Control volume evaluated for solution of one-dimensional heat transfer in pipe walls. Q is heat flow measured in W, and Q''' is the heat input per unit volume, V.

this into the energy balance gives

$$-\,\mathrm{d}(2\pi r L k \frac{\mathrm{d}T}{\mathrm{d}r}) = Q''' 2\pi r \mathrm{dr} \mathrm{L} \tag{A.11}$$

Integrating once and rearranging gives

$$-kr\frac{\mathrm{d}T}{\mathrm{d}r} = \frac{Q''' r^2}{2} + C \tag{A.12}$$

$$\frac{\mathrm{d}T}{\mathrm{d}r} = -\frac{Q''' r}{2k} - \frac{C}{kr} \tag{A.13}$$

where C is a constant of integration. Then integrating again

$$T = -\frac{Q''' r^2}{4k} - \frac{C}{k}\ln r + D \tag{A.14}$$

where D is a second constant of integration.

If negligible heat losses are assumed, then $\left(\frac{\mathrm{d}T}{\mathrm{d}r}\right)_{r=r_\mathrm{o}}$ and

$$0 = -\frac{Q''' r_\mathrm{o}}{2k} - \frac{C}{k r_\mathrm{o}} \tag{A.15}$$

$$C = -\frac{Q''' r_\mathrm{o}^2}{2} \tag{A.16}$$

$$T = -\frac{Q''' r^2}{4k} + \frac{Q''' r_\mathrm{o}^2}{2k}\ln r + D \tag{A.17}$$

Also, $T_{r=r_o} = T_{w,o}$, so

$$D = T_{w,o} + \frac{Q''' r_o^2}{4k} - \frac{Q''' r_o^2}{2k} \ln r_o \tag{A.18}$$

$$T = T_{w,o} + \frac{Q''' r_o^2}{4k} - \frac{Q''' r^2}{4k} + \frac{Q''' r_o^2}{2k} \ln r - \frac{Q''' r_o^2}{2k} \ln r_o \tag{A.19}$$

$$= T_{w,o} + \frac{Q'''}{2k} \left(\frac{r_o^2 - r^2}{2} + r_o^2 \ln \frac{r}{r_o} \right) \tag{A.20}$$

Evaluating this equation at $r = r_i$, and considering that $Q''' = \frac{Q_{in}}{\pi r_o^2 L_{ht}}$ gives the equation given in Chapter 3

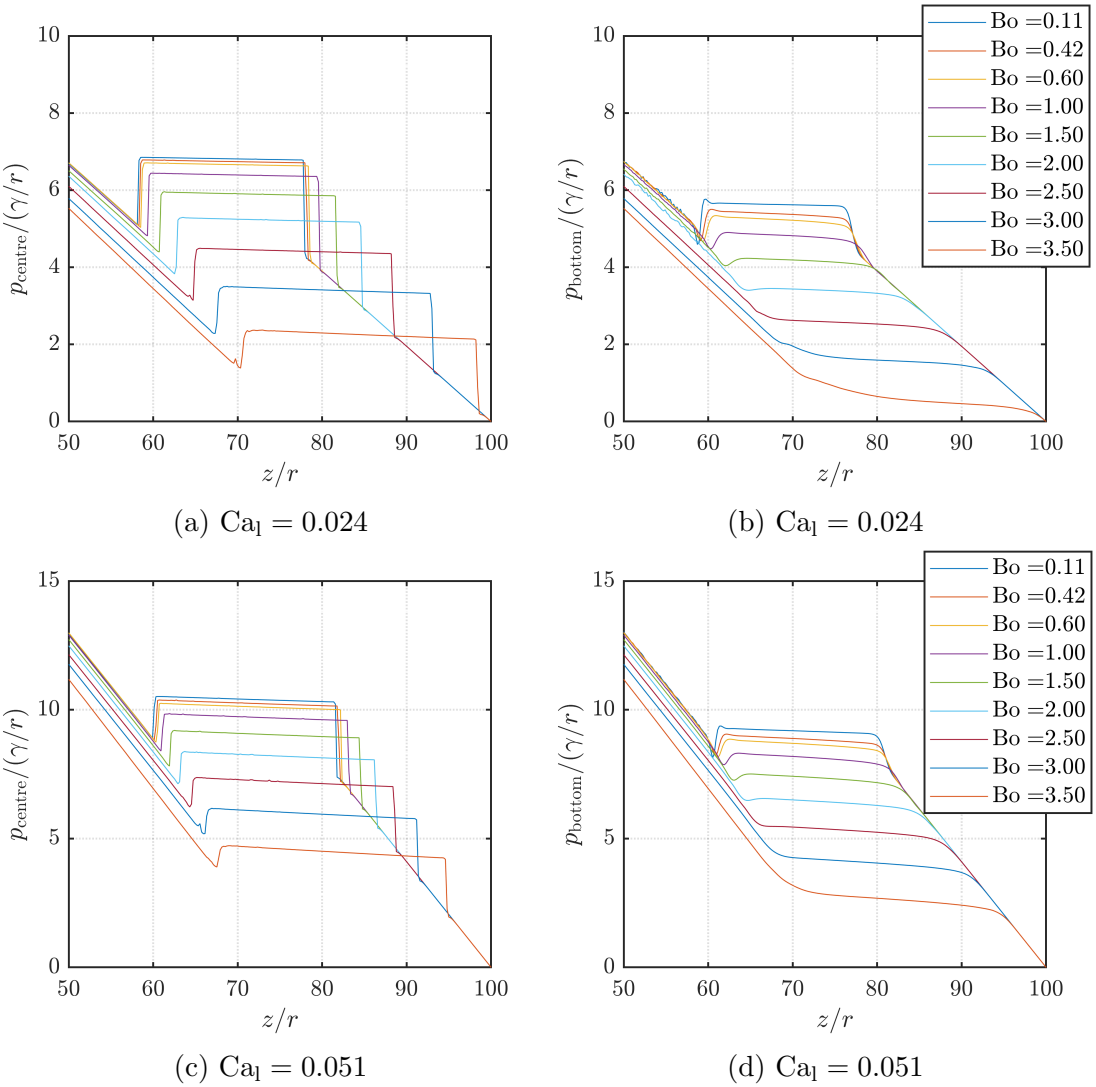
$$T_{w,i} = T_{w,o} + \frac{Q_{in}}{2\pi k_{pipe} L_{ht} (r_o^2 - r_i^2)} \left(\frac{r_o^2 - r_i^2}{2} + r_o^2 \ln \frac{r_i}{r_o} \right) \tag{A.21}$$

Appendix B

Supplementary Material for Computational Results

B.1 Pressure profiles for the inertia-free case

Fig. B.1 shows the streamwise profiles of pressure extracted along the channel axis and the channel bottom for the $We_l \ll 1$ cases. The profiles along the channel axis (a,c) show that there is always a pressure discontinuity associated with the Laplacian pressure jump across the nose and tail of the bubble, with the pressure jump being larger at the nose owing to its larger curvature. The pressure drop induced by the bubble, whose values are reported in Fig. B.2, increases with increasing Bo, in particular when $Bo > 1$. The streamwise pressure profiles extracted along the bottom wall, see Fig. B.1b and d, exhibit a change in their trends as the Bond number increases. In the $Bo < 1$ regime, there is still an apparent rise in the pressure at the wall along the bubble region, owing to the Laplace jump in pressure at the interface (of magnitude $\approx \gamma/r$). However, as Bo is progressively increased above 1, the pressure discontinuity at the nose and bubble rear disappears because the bottom half of the bubble flattens, thus causing a reduction (and disappearance) of the Laplacian pressure jump across the bottom interface.



(a) $\text{Ca}_\text{l} = 0.024$ (b) $\text{Ca}_\text{l} = 0.024$

(c) $\text{Ca}_\text{l} = 0.051$ (d) $\text{Ca}_\text{l} = 0.051$

Figure B.1: Streamwise pressure profiles along the (a,c) channel axis and (b,d) channel bottom ($x = 0$, $y = -r$).

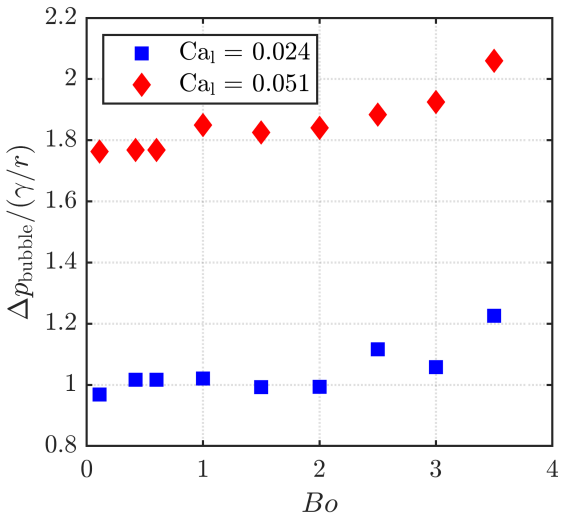


Figure B.2: Streamwise pressure drop induced by the bubble, calculated along the channel axis. As a reference, Bretherton's theoretical model in the absence of gravity (Bo = 0) predicts $\Delta p/(\gamma/r) = 4.52(3\mathrm{Ca})^{2/3} = 0.89$ and 1.57 for, respectively, bubble capillary numbers $\mathrm{Ca} = 0.029$ ($\mathrm{Ca_l} = 0.024$) and $\mathrm{Ca} = 0.068$ ($\mathrm{Ca_l} = 0.051$).